# IMAGING EXTENDED REFLECTORS IN WAVEGUIDES

A DISSERTATION
SUBMITTED TO THE DEPARTMENT OF
MATHEMATICS & APPLIED MATHEMATICS
OF UNIVERSITY OF CRETE
FOR THE DEGREE OF
DOCTOR OF PHILOSOPHY
IN MATHEMATICS


Symeon Papadimitropoulos

July 2018

*To my family*

# Contents

# Introduction

In this thesis, we consider the problem of detecting and imaging *extended* reflectors that are embedded in a waveguide using acoustic waves. The term 'extended' refers to reflectors that are comparable in size to the probing wavelength. A schematic of the problem setup that we consider is illustrated in Figure 1. To image we use a vertical array of transducers that records the response of the medium, *i.e.* the reflected echoes corresponding to one or more known insonifications. These recorded data are subsequently used to create an image that allows us to locate the reflector and retrieve its support. Imaging in waveguides is of particular interest in underwater acoustics [14, 17, 21, 34, 36, 46, 50, 62] where one wants to characterize sound speed inhomogeneities in shallow ocean environments with applications in sonar, marine ecology, seabed imaging, etc. Moreover, imaging in waveguides also finds applications in inspections of underground pipes using acoustic waves [43, 49] as well as in non-destructive evaluation of materials where elastic wave propagation should be considered [13].

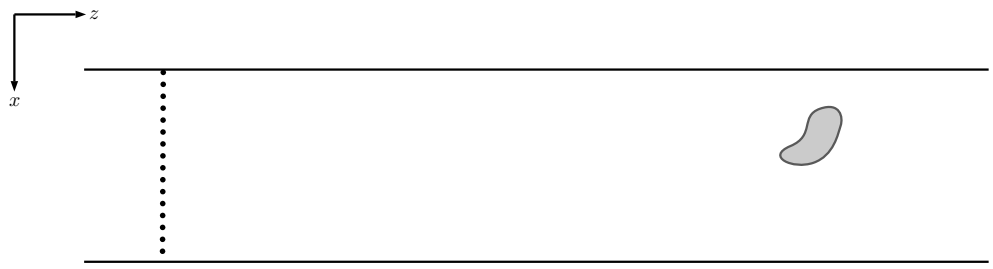


Figure 1: Schematic of active imaging setup.

To be more specific, the vertical array that we consider in this thesis consists of $N$ transducers that can play the role of sources and receivers. The array may span the whole cross-section of the waveguide, or part of it. One array element emits a pulse and the echoes are recorded at all the receivers along the array. By repeating this process for all the array

elements, acting as sources, an $N \times N$ matrix is created. Let $\widehat{\Pi}$ denote this matrix and we shall refer to it as the *array response matrix*. We work here with the array response matrix for the *scattered* field created by subtracting the data for the *incident* field, *i.e.* the solution of the wave equation in the absence of the reflector, from the *total* field, *i.e.* the associated solution in the presence of the reflector. We assume here that the forward problems that we need to solve in order to create the response matrix in each case are well-posed.

Assuming that we have in our disposal the data that are tabulated in the form of the array response matrix, we want to create images of the medium that will assist us to determine whether a reflector is present in it. The imaging process can be described as follows: We select a bounded subdomain of the waveguide, called the *search domain*, which we discretize using some grid. Next, we compute the values of an appropriate imaging functional at each grid point of the search domain. Ideally, this functional should have the property that its values, when graphically displayed, attain their maxima on the reflector. Examples of widely used imaging methods include the *Kirchhoff Migration* (KM) (see [7, §9]), the *matched field* (see [39]), the linear sampling [14,15,43] and the factorization method [3].

We consider first the *full aperture* case, *i.e.* when the array spans the whole vertical cross-section of the waveguide, and propose an imaging functional that consists in back-propagating a weighted projection of the array response matrix on the *propagating* modes. Let $\widehat{\mathbb{P}}$ denote this projected array response matrix. The idea of formulating the inverse scattering problem in terms of the propagating modes has been considered by several authors in the past; indicatively we refer to the relatively recent works [14, 21, 48]. In [21] the problem of reconstructing weak inhomogeneities located in an infinite strip is addressed and the solution of the linearized inverse scattering problem is obtained using the spectral decomposition of the far-field matrix. We note that in this case the measurements consist of both the transmitted and the reflected (backscattered) field. In [48] the problem of selective focusing on small scatterers in two dimensional acoustic waveguides is considered and the spectral decomposition of the time-reversal operator is analyzed in this setting. In [14] the authors establish a modal formulation for the Linear Sampling Method (LSM) [20] for imaging extended reflectors in waveguides. The extension to the case of anisotropic scatterers that may touch the waveguide boundaries is carried out in [43] where both the LSM and the Reciprocity Gap Method (RGM) [19] are studied theoretically and numerically. The case of imaging cracks in acoustic waveguides is considered in [15] using LSM and the

factorization method [38]. In all the aforementioned works the waveguide geometry is infinite in one-dimension.

Moreover, we consider the problem of *selective* imaging, *i.e.* creating images that focus selectively on specific parts of the reflector. To do so we propose to back-propagate instead of $\widehat{\mathbb{P}}$, projections of $\widehat{\mathbb{P}}$ onto selected subspaces created using its singular value decomposition. We follow here the approach of [10], where the authors used the so-called *subspace projection* method in order to perform selective imaging of extended reflectors in free space. We refer also to [12] for selective imaging in clutter, *i.e.*, propagation medium with inhomogeneities that are unknown, cannot be estimated in detail, and, are modelled as random processes. Note that the concept of selective imaging of extended scatterers has been motivated by the concept of *selective focusing*, where for multiple point scatterers present in the medium, we wish to create an image that focuses on a specific subset of them. Related works include [51], where Prada and Fink introduced the well-known DORT method in order to achieve selective focusing on individual scatterers, [46, 50]; see also [32] where DORT was analysed with mathematical rigor in the free-space, and [48] for a waveguide problem.

The thesis is organized as follows. In Chapter 1, we present the two waveguide geometries that we examine in this work: the *infinite* and the *terminating* waveguide. The infinite waveguide refers to a waveguide that is infinite in the range direction ($z \to \pm\infty$), while in the terminating waveguide there is a vertical boundary on the right side of the waveguide at $z = R$. We present the scalar acoustic wave equation which describes wave propagation for our problem and derive the corresponding Green's function. Finally, we present some identities and properties that will prove useful in the course of the thesis. Specifically, we present the Dirichlet-to-Neumann (DtN) map, the reciprocity property of the Green's function and the Kirchhoff-Helmholtz identity. Let us note that we will work in the infinite waveguide setting in Chapters 2 to 5, while we will consider the terminating waveguide problem in Chapter 6.

Next, in Chapter 2 we introduce the concepts of *passive* and *active* imaging and describe the structure of the array response matrix in both cases. Then, we present the Kirchhoff migration imaging functional, and introduce our imaging functional that is based on the modal projection of the array response matrix. We close the chapter by presenting our selective imaging methodology.

In Chapter 3 we consider a model problem where the scatterer is a 'screen', *i.e.* a one-dimensional perfect reflector of length $b$ that is vertically placed into an infinite strip

with horizontal boundaries, and which is filled with a homogeneous medium. In this case the array response matrix may be evaluated analytically using the Born approximation. First, we consider an array that spans the whole vertical cross-section of the waveguide. In this case, it turns out that the projected array response matrix at a single frequency $\omega$, $\widehat{\mathbb{P}}(\omega)$, possesses the special structure of a Toeplitz-minus-Hankel matrix. Then we fully characterize the spectral properties of $\widehat{\mathbb{P}}(\omega)$ and exploit them in order to derive a relation between the number of 'significant' singular values of $\widehat{\mathbb{P}}(\omega)$ and the size of the screen. Specifically, we show that this number, that may be seen as the effective rank of the matrix $\widehat{\mathbb{P}}(\omega)$, is roughly equal to $[2b/\lambda]$, where $\lambda$ is the wavelength. In other words, the number of significant singular values of $\widehat{\mathbb{P}}(\omega)$ equals the size of the scatterer divided by the array resolution. This is known to hold in the free-space case, [10], but is a new result for a waveguide. Moreover, we derive analytic expressions for the singular vectors of $\widehat{\mathbb{P}}(\omega)$, and for the selective imaging functional. In particular, we investigate the relation of the matrix $\widehat{\mathbb{P}}(\omega)$ with the well-known *prolate matrix*, and of its singular vectors with the so-called *discrete prolate spheroidal sequences*. The latter are discrete analogues of the *prolate spheroidal wave functions*, which have been studied in a series of papers by Slepian, Pollak and Landau, [40, 41, 55, 56, 58]. The above ingredients allow us to conclude that when we selectively image using the projection of $\widehat{\mathbb{P}}(\omega)$ onto its first singular vector we get an image that focuses at the midpoint of the screen, while by projecting $\widehat{\mathbb{P}}(\omega)$ onto the singular vector that corresponds to the last significant singular value the resulting image exhibits focusing at the endpoints of the screen.

Next, we consider the more realistic case of an array with partial aperture, *i.e.* it covers only part of the vertical cross-section of the waveguide. In this case, the main difficulty lies in the definition of the weighted modal projection of the array response matrix, since now the modes are no longer orthonormal along the array. We adequately modify the construction of the matrix $\widehat{\mathbb{P}}(\omega)$ in order to preserve all the good properties that we have observed in the full-array case. Our numerical experiments indicate that our method allows to successfully image the screen even with an array that spans just 10% of the vertical cross-section of the waveguide. Moreover, we numerically assess the performance of our imaging approach under the presence of additive noise, and for another one-dimensional scatterer that has the shape of a semicircle. We close this chapter by formulating an algorithm that we will use for imaging in both the full and partial array cases.

Chapter 4 is devoted to the resolution analysis of the proposed imaging functional, which

is the study of the point spread function (PSF), *i.e.* the image that is created for a point source or a point scatterer. As in the previous chapter, the waveguide is assumed to be a homogeneous infinite strip. We first consider the case of a single frequency. The analysis is carried out by deriving analytic expressions for the point spread function only for a point source. This is enough, since it emerges that the imaging functional for a point scatterer is the square of the functional for a point source. We end up with analytical expressions for the resolution in range and cross-range that show that the image resolution is equal to $2\lambda$ in range, and $\lambda/2$ in cross-range ($\lambda$ being the wavelength). We also examine the effect that the use of multiple frequencies brings upon the quality of the image. Our analytical results show that the cross-range resolution does not depend on the bandwidth that we use, and is in fact determined by the central frequency, while the *Signal-to-Noise Ratio* (SNR) of the image improves as the bandwidth increases. As far as the range resolution is concerned, numerical evidence indicates that both resolution and SNR are significantly improved as the bandwidth increases. We close this chapter by proving a result that concerns the partial array case and states that, under certain circumstances, the projected response matrix $\widehat{\mathbb{P}}$ for the partial aperture case is the same as for the full aperture case.

In Chapter 5 we assess the robustness of the proposed imaging functional for more realistic scatterer geometries with data that are generated by a full wave model. Specifically, we consider two scatterer shapes: a square and a disc-shaped scatterer. In order to construct the array response matrix for each case, we compute numerically the solution of the related initial/boundary value problems for the wave equation. To this end, we use Montjoie [44], a high-order finite element C++ code developed at INRIA. At first, we consider a single frequency and a full-aperture array, and we compare the results of the square and the disc-shaped scatterers with their respective one-dimensional ones for the screen and the semicircle. Although the analysis that we have performed in Chapter 3 concerns the ideal model problem of the screen, our extensive numerical experiments indicate that the properties that we have observed for the model problems carry over to these more realistic examples. Next, we examine the partial array-aperture case and demonstrate the major improvement that the use of multiple frequencies brings upon the performance of the method. For example, our numerical experiments suggest that we can obtain quite good images that locate the position of the scatterer even if we use an array that spans only 5% of the vertical cross-section of the waveguide. We conclude the chapter by briefly presenting numerical results for a waveguide which has a cross-range dependent sound-speed profile.

Lastly, in Chapter 6, we consider the problem of imaging extended reflectors in a terminating waveguide. We consider this waveguide geometry to check whether we can obtain more information about the support and the shape of the extended reflector compared to the infinite waveguide geometry. As one may intuitively expect, the multiple-scattering reflections that bounce off the terminating boundary of the waveguide they should in principle assist in providing multiple views of the reflector that are not in general available in the infinite waveguide case. To benefit from this multipathing we need to know or determine the boundary of the waveguide prior to imaging the reflector. Here, we consider that the waveguide's boundary is known. The case of a terminating waveguide as the one considered here was first studied in our knowledge in [9] for electromagnetic waves in three dimensions. In particular in [9] the forward data model was derived using Maxwell's equations and two imaging methods were formulated: reverse time migration (the corresponding one in the frequency domain is phase conjugation) that is obtained by applying the adjoint of the forward operator to the data, and an $l_1$-sparsity promoting optimization method.

In this chapter we present the formulation of the problem for our current waveguide geometry and describe our imaging methodology, that is inspired by phase conjugation, for both passive and active imaging. We also carry out a resolution analysis for single and multiple frequency imaging. Our analysis suggests that both range and cross-range resolution is equal to $\lambda/2$. Moreover, when we use multiple frequencies, the resolution is determined by the central frequency, while the bandwidth does not affect the resolution but it markedly improves the SNR of the image. In all numerical experiments that we consider in this chapter we verify a significant improvement in the reconstruction in the terminating waveguide as compared to the infinite one. We also assess the robustness of the proposed method for different array apertures that range from full to one fourth of the waveguide's vertical cross-section. Of course, the quality of the image deteriorates as the length of the array decreases but our imaging results remain very satisfactory even with an array-aperture equal to one fourth of the waveguide's vertical cross-section. Moreover, we test our method with synthetic array data that are obtained with a single transmit/receive element. Although the data that now we have in our disposal is limited compared to those contained in a multistatic array response matrix we again obtain good reconstructions of the scatterer, albeit for larger array apertures that cover at least half of the waveguide's width in the vertical direction. Finally, we present some very promising preliminary results of our approach in imaging of an extended scatterer in a three-dimensional terminating

waveguide with a bounded rectangular cross-section.

# Chapter 1

# The forward problem

In this work, we consider the problem of detecting and imaging extended scatterers embedded in a waveguide environment, using acoustic waves. Specifically, we will work in a two-dimensional setup in Cartesian coordinates $(z, x)$, where $z$ denotes the *range* variable and $x$ the *cross-range* variable, which is taken to be positive downward. We assume that in our waveguide, denoted by $\Omega$, there exists a single extended scatterer $\mathcal{O}$ where the term 'extended' indicates that the typical size of the scatterer is comparable to the acoustic wavelength.

In this chapter, we will introduce the waveguide environments that we will work in, present the equations that govern the wave propagation in the medium in the time and in the frequency domain and introduce useful identities and properties of the wave equation in the waveguide. Namely, we will introduce the Dirichlet-to-Neumann map, the reciprocity property of the Green's function, and the Kirchhoff-Helmholtz identity.

## 1.1 The waveguide environment

We will consider two cases for our waveguide setup: the *infinite* and the *terminating* waveguide.

The infinite waveguide allows waves to travel infinitely in both directions in range, namely as $z \to \pm\infty$. An example of an infinite waveguide containing an extended scatterer is depicted in Figure 1.1. We define two points in range, $z = L^-$ and $z = L^+$, and the

subdomain $\Omega_L$ of our waveguide $\Omega$,

$$\Omega_L = \{\vec{\boldsymbol{x}} = (z, x) \in \Omega \ : \ L^- < z < L^+\}.$$

Let us note here that throughout this work, vectors representing points in $\Omega$, are denoted by boldface characters with an overscript arrow. A key assumption for the waveguide is that all the inhomogeneities of the medium and the scatterer $\mathcal{O}$, are contained in $\Omega_L$, while the rest of the waveguide, *i.e.* $\Omega \setminus \Omega_L$, is composed of two semi-infinite strips of constant width that are filled with a homogenous medium. We may relax the assumption of a constant wave speed, by allowing the speed to depend on the cross-range variable $x$. However, throughout this work we will consistently assume that $\Omega \setminus \Omega_L$ is filled with a homogeneous medium, unless stated otherwise.

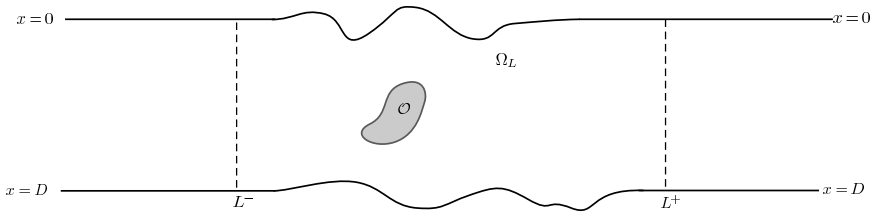


Figure 1.1: Schematic representation of an infinite waveguide.

The second type of waveguide geometry that we are going to deal with is the terminating waveguide. In this case, as can be seen in Figure 1.2, we have an additional boundary on the right side of the waveguide, thus the waves are allowed to propagate infinitely only as $z \to -\infty$. Similarly to the infinite waveguide, we define two subdomains: the bounded domain

$$\Omega_{L^+} = \{\vec{\boldsymbol{x}} = (z, x) \in \Omega \ : \ z > L\}$$

and the semi-infinite strip of constant cross-range width $D$,

$$\Omega_{L^-} = \{\vec{\boldsymbol{x}} = (z, x) \in \Omega \ : \ z < L, \ 0 < x < D\}.$$

In this setup, we assume that all the inhomogeneities, including the scatterer, are included in $\Omega_{L^+}$, while $\Omega_{L^-}$ is filled with a medium that is either homogeneous or it has a wave speed that depends on $x$.

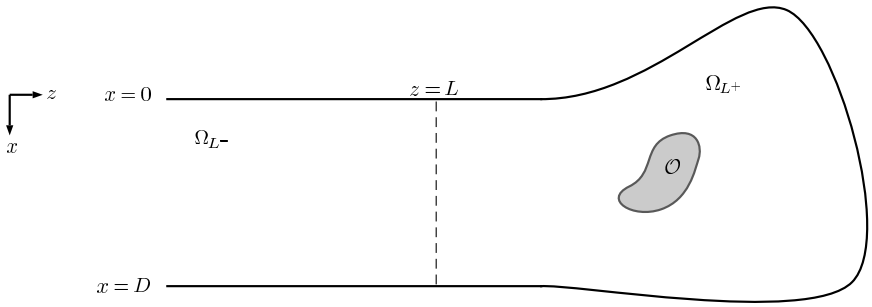


Figure 1.2: Schematic representation of a terminating waveguide.

## 1.2 The wave equation

The propagation of waves in the waveguide $\Omega$ is described by the scalar acoustic wave equation, which is given by

$$\Delta p(t,\vec{\boldsymbol{x}}) - \frac{1}{c^2(\vec{\boldsymbol{x}})}\frac{\partial^2 p(t,\vec{\boldsymbol{x}})}{\partial t^2} = f(t,\vec{\boldsymbol{x}}). \tag{1.1}$$

Here $\vec{\boldsymbol{x}} = (z,x) \in \Omega$ is a point in the waveguide, $c(\vec{\boldsymbol{x}})$ denotes the sound speed and $f(t,\vec{\boldsymbol{x}})$ models a point-like source with time-harmonic dependence located at $\vec{\boldsymbol{x}}_s \in \Omega$. The equation is supplemented by homogeneous Dirichlet boundary conditions on the waveguide's boundaries and appropriate radiation conditions at infinity.

In the absence of a scatterer $\mathcal{O}$, the acoustic pressure field, called the incident field, satisfies the following initial boundary value problem,

$$\begin{aligned}
&\Delta p^{\text{inc}}(t,\vec{\boldsymbol{x}}) - \frac{1}{c^2(\vec{\boldsymbol{x}})}\frac{\partial^2 p^{\text{inc}}(t,\vec{\boldsymbol{x}})}{\partial t^2} = f(t,\vec{\boldsymbol{x}}), \quad \vec{\boldsymbol{x}} \in \Omega,\ t > 0 \\
&p^{\text{inc}}(0,\vec{\boldsymbol{x}}) = 0, && \vec{\boldsymbol{x}} \in \Omega, \\
&p^{\text{inc}}(t,\vec{\boldsymbol{x}}) = 0, && \vec{\boldsymbol{x}} \in \partial\Omega, \\
&p^{\text{inc}}(t,\vec{\boldsymbol{x}}) \text{ is outgoing as } z \to \pm\infty.
\end{aligned} \tag{1.2}$$

In the presence of a scatterer $\mathcal{O}$, the acoustic pressure field is called the *total* field, and is denoted by $p^{\text{tot}}$. In this work, we will impose a homogeneous Neumann boundary condition on the boundary $\partial\mathcal{O}$, to model a sound-hard impenetrable scatterer. Therefore, the total

field satisfies the equation

$$\begin{aligned}
&\Delta p^{\mathrm{tot}}(t,\vec{\boldsymbol{x}}) - \frac{1}{c^2(\vec{\boldsymbol{x}})}\frac{\partial^2 p^{\mathrm{tot}}(t,\vec{\boldsymbol{x}})}{\partial t^2} = f(t,\vec{\boldsymbol{x}}), \quad \vec{\boldsymbol{x}} \in \Omega \setminus \overline{\mathcal{O}},\ t>0,\\
&p^{\mathrm{tot}}(0,\vec{\boldsymbol{x}}) = 0, && \vec{\boldsymbol{x}} \in \Omega,\\
&p^{\mathrm{tot}}(t,\vec{\boldsymbol{x}}) = 0, && \vec{\boldsymbol{x}} \in \partial\Omega,\\
&\frac{\partial}{\partial \nu} p^{\mathrm{tot}}(t,\vec{\boldsymbol{x}}) = 0, && \vec{\boldsymbol{x}} \in \partial\mathcal{O},\\
&p^{\mathrm{tot}}(t,\vec{\boldsymbol{x}}) \text{ is outgoing as } z \to \pm\infty,
\end{aligned} \tag{1.3}$$

where $\nu$ is the outward-pointing unit normal vector.

We are interested in working with the *scattered* field, denoted by $p^{\mathrm{sc}}$. If we know the total and the incident field then we may create this field, simply by subtracting the incident from the total field, *i.e.* $p^{\mathrm{sc}} = p^{\mathrm{tot}} - p^{\mathrm{inc}}$.

## 1.3 The Helmholtz equation

In the previous section we presented the time-dependent wave equation. However, we are interested in working in the frequency domain. To achieve that, we use the Fourier transform

$$\widehat{p}(\omega,\vec{\boldsymbol{x}}) = \int \mathrm{e}^{\mathrm{i}\omega t} p(t,\vec{\boldsymbol{x}})\, dt,$$

on (1.1), and we obtain the Helmholtz equation

$$-\Delta\widehat{p}(\omega,\vec{\boldsymbol{x}}) - k^2\eta(\vec{\boldsymbol{x}})\widehat{p}(\omega,\vec{\boldsymbol{x}}) = \widehat{f}(\omega,\vec{\boldsymbol{x}}), \tag{1.4}$$

where $\omega$ is the angular frequency, $k = \omega/c_0$ is the (real) wavenumber, $c_0$ is the reference wave speed and $\eta(\vec{\boldsymbol{x}}) = c_0^2/c^2(\vec{\boldsymbol{x}})$ is the index of refraction.

Similar to the time domain equivalent, the incident field $\widehat{p}^{\mathrm{inc}}(\omega,\vec{\boldsymbol{x}})$ in the frequency domain comes as the solution of the following boundary value problem (BVP), supplemented

with appropriate radiation conditions at infinity:

$$\begin{aligned} &-\Delta\widehat{p}^{\text{inc}}(\omega,\vec{\boldsymbol{x}}) - k^2\eta(\vec{\boldsymbol{x}})\widehat{p}^{\text{inc}}(\omega,\vec{\boldsymbol{x}}) = \widehat{f}(\omega,\vec{\boldsymbol{x}}), \qquad \vec{\boldsymbol{x}} \in \Omega, \\ &\widehat{p}^{\text{inc}}(\omega,\vec{\boldsymbol{x}}) = 0, \qquad\qquad\qquad\qquad\qquad \vec{\boldsymbol{x}} \in \partial\Omega, \\ &\widehat{p}^{\text{inc}}(\omega,\vec{\boldsymbol{x}}) \text{ is outgoing as } z \to \pm\infty, \end{aligned} \tag{1.5}$$

while the total field $\widehat{p}^{\text{tot}}$ satisfies

$$\begin{aligned} &-\Delta\widehat{p}^{\text{tot}}(\omega,\vec{\boldsymbol{x}}) - k^2\eta(\vec{\boldsymbol{x}})\widehat{p}^{\text{tot}}(\omega,\vec{\boldsymbol{x}}) = \widehat{f}(\omega,\vec{\boldsymbol{x}}), \quad \vec{\boldsymbol{x}} \in \Omega \setminus \overline{\mathcal{O}}, \\ &\widehat{p}^{\text{tot}}(\omega,\vec{\boldsymbol{x}}) = 0, \qquad\qquad\qquad\qquad\qquad \vec{\boldsymbol{x}} \in \partial\Omega, \\ &\frac{\partial}{\partial\nu}\widehat{p}^{\text{tot}}(\omega,\vec{\boldsymbol{x}}) = 0, \qquad\qquad\qquad\qquad\qquad \vec{\boldsymbol{x}} \in \partial\mathcal{O}, \\ &\widehat{p}^{\text{tot}}(\omega,\vec{\boldsymbol{x}}) \text{ is outgoing as } z \to \pm\infty. \end{aligned} \tag{1.6}$$

Finally, as before, the scattered field is the difference between the total and the incident field, that is $\widehat{p}^{\text{sc}} = \widehat{p}^{\text{tot}} - \widehat{p}^{\text{inc}}$.

**Remark 1** *The initial/boundary value problems (1.2), (1.3) and the BVP's (1.5), (1.6) were presented for the infinite waveguide. In the case of the terminating waveguide as the one described previously, see also Figure 1.2, the radiation conditions are adjusted accordingly, stating that 'p is outgoing as $z \to -\infty$'.*

## 1.4 The Green's function

Next, we will introduce the so-called Green's function for the Helmholtz equation. The Green's function is the solution of (1.4), with the specified boundary and radiation conditions, where we replace the source term $\widehat{f}(\omega,\vec{\boldsymbol{x}})$ with a point source of unit strength, described by a Dirac delta function $\delta(\vec{\boldsymbol{x}} - \vec{\boldsymbol{x}}_s)$, where $\vec{\boldsymbol{x}}_s = (z_s, x_s)$ is the location of the source. We will denote with $\widehat{G}(\vec{\boldsymbol{x}},\vec{\boldsymbol{x}}_s;\omega)$ the Green's function for the Helmholtz equation and the associated boundary and radiation conditions, which is the field recorded at a point $\vec{\boldsymbol{x}}$ due to a point source located at $\vec{\boldsymbol{x}}_s \in \Omega$ for a single frequency $\omega$ and is given as a solution

to

$$-\Delta\widehat{G}(\vec{\boldsymbol{x}},\vec{\boldsymbol{x}}^{\,\mathrm{s}};\omega)-k^2\eta(\vec{\boldsymbol{x}})\widehat{G}(\vec{\boldsymbol{x}},\vec{\boldsymbol{x}}_s;\omega)=\delta(\vec{\boldsymbol{x}}-\vec{\boldsymbol{x}}_s). \tag{1.7}$$

In the following subsection we present the derivation of the Green's function in the case where the waveguide is an infinite strip with homogeneous Dirichlet boundary conditions on its boundaries.

### 1.4.1 The Green's function for a homogeneous infinite waveguide

Let us assume that we have a waveguide that is an infinite strip, that is it has flat horizontal boundaries and, therefore, has a constant width $D$, as shown in Figure 1.3 , filled with a homogeneous medium, *i.e.* $\eta(\vec{\boldsymbol{x}})=1$.


Figure 1.3: Schematic representation of an infinite strip.

As in the previous cases, we impose homogeneous Dirichlet boundary conditions on its boundaries. Then, the Green's function for this waveguide is given as a solution to the equation

$$\Delta\widehat{G}(\vec{\boldsymbol{x}},\vec{\boldsymbol{x}}_s)+k^2\widehat{G}(\vec{\boldsymbol{x}},\vec{\boldsymbol{x}}_s)=-\delta(\vec{\boldsymbol{x}}-\vec{\boldsymbol{x}}_s), \tag{1.8}$$

which satisfies the boundary and radiation conditions

$$\widehat{G}(z,0)=\widehat{G}(z,D)=0,$$

$$\widehat{G}\text{ is outgoing as } z\to\pm\infty.$$

Here, and for the rest of this work, whenever we refer to a single frequency, we suppress the parameter $\omega$ to simplify the notation. The dependence on $\omega$ will be recalled when we are going to use the Green's function for multiple frequencies.

Under the previous assumptions, we may perform a separation of variables and write the Green's function as

$$\widehat{G}(\vec{\boldsymbol{x}},\vec{\boldsymbol{x}}_s)=Z(z)X(x). \tag{1.9}$$

Substituting (1.9) into the homogeneous version of (1.8), we get

$$Z''(z)X(x) + Z(z)X''(x) + k^2 Z(z)X(x) = 0$$

and by separating the variables we get

$$\frac{Z''(z)}{Z(z)} + k^2 + \frac{X''(x)}{X(x)} = 0.$$

From this we recover the vertical eigenvalue problem

$$X''(x) + \mu X(x) = 0, \quad X(0) = X(D) = 0, \tag{1.10}$$

whose solutions are the eigenfunctions

$$X_n(x) = \sqrt{\frac{2}{D}} \sin(\sqrt{\mu_n} x), \quad \mu_n = \frac{n^2\pi^2}{D^2}. \tag{1.11}$$

Let us assume that there exists an index $M$ such that

$$\mu_M < k^2 < \mu_{M+1}.$$

The index $M$ indicates the number of *propagating modes* in the waveguide. Having defined the eigenpairs $\{\mu_n, X_n\}_{n=1}^{\infty}$, (1.9) can be written as

$$\widehat{G}(\vec{\boldsymbol{x}}, \vec{\boldsymbol{x}}_s) = \sum_{n=1}^{\infty} Z_n(z) X_n(x), \tag{1.12}$$

which when substituted into (1.8) now gives

$$\begin{aligned}
&\sum_{n=1}^{\infty} Z_n'' X_n + Z_n X_n'' + k^2 Z_n X_n = -\delta(\vec{\boldsymbol{x}} - \vec{\boldsymbol{x}}_s) \\
\Rightarrow &\sum_{n=1}^{\infty} Z_n'' X_n - \mu_n Z_n X_n + k^2 Z_n X_n = -\delta(\vec{\boldsymbol{x}} - \vec{\boldsymbol{x}}_s) \\
\Rightarrow &\sum_{n=1}^{\infty} \left(Z_n'' + (k^2 - \mu_n) Z_n\right) X_n = -\delta(\vec{\boldsymbol{x}} - \vec{\boldsymbol{x}}_s).
\end{aligned}$$

We multiply the previous relation by $X_m$ and integrate with respect to $x$ from 0 to $D$, to get

$$\sum_{n=1}^{\infty} \left(Z_n'' + (k^2 - \mu_n)Z_n\right) \int_0^D X_n X_m = -\delta(z - z_s) \int_0^D \delta(x - x_s) X_m$$

Using the orthonormality of the eigenfunctions $X_n$ along the cross-range and the sifting property of the Dirac function, which states that $\int \delta(x - x_s) f(x) = f(x_s)$, we end up with

$$Z_m'' + (k^2 - \mu_m)Z_m = -\delta(z - z_s)X_m(x_s). \tag{1.13}$$

Therefore, we seek a continuous function $Z_l$, whose derivative has a jump discontinuity of magnitude $X_m(x_s)$ at $z = z_s$. Hence

$$Z_m(z) = \frac{i}{2\beta_m} \mathrm{e}^{\mathrm{i}\beta_m |z - z_s|} X_m(x_s),$$

where

$$\beta_m = \begin{cases} \sqrt{k^2 - \mu_m}, & m = 1, \ldots, M \\ i\sqrt{\mu_m - k^2}, & m \geq M + 1. \end{cases} \tag{1.14}$$

Finally, we have that the expression for the Green's function in our waveguide is given by

$$\widehat{G}(\vec{\boldsymbol{x}}, \vec{\boldsymbol{x}}_s) = \frac{i}{2} \sum_{m=1}^{\infty} \frac{\mathrm{e}^{\mathrm{i}\beta_m |z - z_s|}}{\beta_m} X_m(x) X_m(x_s). \tag{1.15}$$

Let us note here that in the case of a wave speed that depends on the cross-range, *i.e.* $c = c(x)$, we can follow the same approach as before, *i.e.* use the separation of variables and compute the eigenpairs $(\mu_n, X_m)$ of the corresponding (1.10) numerically and subsequently determine the horizontal wavenumbers $\beta_m$.

### 1.4.2 The Green's function for a homogeneous terminating waveguide

In this subsection we present the derivation of the Green's function $\widehat{G}$ for the Helmholtz operator when the waveguide $\Omega$ is a homogeneous ($\eta(\vec{\boldsymbol{x}}) = 1$) semi-infinite strip of width $D$, terminated by a vertical boundary at $z = R$. Specifically, $\Omega = (-\infty, R) \times (0, D)$, as depicted in Figure 1.4 .

In order to derive an analytic expression for $\widehat{G}(\cdot, \vec{\boldsymbol{x}}_s)$ we will use the method of images [18]. With reference to Figure 1.5, we assume an infinite strip and we add a source at the

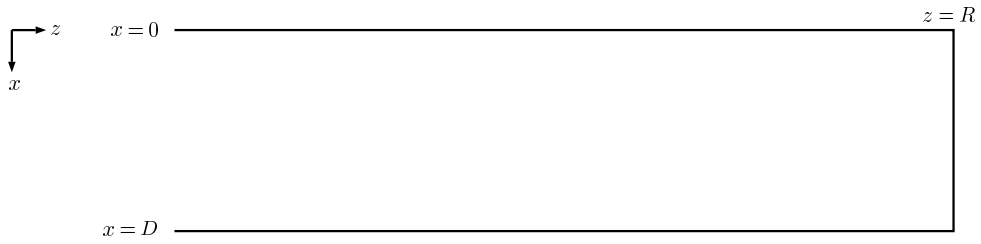


Figure 1.4: Schematic representation of a semi-infinite strip.

point $\vec{\boldsymbol{x}}_s'$ that is symmetric to $\vec{\boldsymbol{x}}_s$ with respect to $\Gamma_R$, *i.e.* $\vec{\boldsymbol{x}}_s' = (2R - z_s, x_s)$.

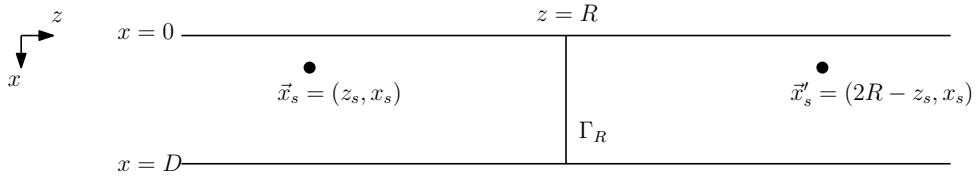


Figure 1.5: Two sources placed symmetrically with respect to $\Gamma_R$

We then compute the field at a point $\vec{\boldsymbol{y}} = (z, x) \in \Omega$ as

$$\widehat{G}(\vec{\boldsymbol{y}}, \vec{\boldsymbol{x}}_s) = \widehat{G}^0(\vec{\boldsymbol{y}}, \vec{\boldsymbol{x}}_s) - \widehat{G}^0(\vec{\boldsymbol{y}}, \vec{\boldsymbol{x}}_s'), \tag{1.16}$$

where $\widehat{G}^0(\vec{\boldsymbol{y}}, \vec{\boldsymbol{x}}_s)$ denotes the Green's function for the infinite waveguide, given by (1.15).

Then, (1.16) implies that

$$\begin{aligned}\widehat{G}(\vec{\boldsymbol{y}}, \vec{\boldsymbol{x}}_s) &= \frac{i}{2}\sum_{m=1}^{\infty} \frac{\mathrm{e}^{i\beta_m|z-z_s|}}{\beta_m} X_m(x)X_m(x_s) - \frac{i}{2}\sum_{n=1}^{\infty} \frac{\mathrm{e}^{i\beta_n|z-2R+z_s|}}{\beta_n} X_n(x)X_n(x_s) \\ &= \frac{i}{2}\sum_{m=1}^{\infty} \frac{\mathrm{e}^{i\beta_m|z-z_s|} - \mathrm{e}^{i\beta_m|z+z_s-2R|}}{\beta_m} X_m(x)X_m(x_s),\end{aligned}$$

where $z < R$ and $0 \le x \le D$. Since $z < R$ and $z_s < R$ it turns out that $z + z_s - 2R < 0$,

hence

$$\begin{aligned}\widehat{G}(\vec{\boldsymbol{y}},\vec{\boldsymbol{x}}_s) &= \frac{i}{2}\sum_{m=1}^{\infty}\frac{\mathrm{e}^{i\beta_m|z-z_s|}-\mathrm{e}^{-i\beta_m(z+z_s-2R)}}{\beta_m}X_m(x)X_m(x_s)\\ &= \begin{cases}\displaystyle\sum_{m=1}^{\infty}\frac{i}{2\beta_m}\left(\mathrm{e}^{i\beta_m(z-z_s)}-\mathrm{e}^{-i\beta_m(z+z_s-2R)}\right)X_m(x)X_m(x_s), & z>z_s,\\ \displaystyle\sum_{m=1}^{\infty}\frac{i}{2\beta_m}\left(\mathrm{e}^{-i\beta_m(z-z_s)}-\mathrm{e}^{-i\beta_m(z+z_s-2R)}\right)X_m(x)X_m(x_s), & z<z_s.\end{cases}\end{aligned} \tag{1.17}$$

Notice that

$$\begin{aligned}\mathrm{e}^{i\beta_m(z-z_s)}-\mathrm{e}^{-i\beta_m(z+z_s-2R)} &= \mathrm{e}^{i\beta_m(R-z_s)}\left(\mathrm{e}^{i\beta_m(z-R)}-\mathrm{e}^{-i\beta_m(z-R)}\right)\\ &= -2i\,\mathrm{e}^{i\beta_m(R-z_s)}\,\sin\beta_m(R-z),\end{aligned}$$

and, similarly,

$$\mathrm{e}^{-i\beta_m(z-z_s)}-\mathrm{e}^{-i\beta_m(z+z_s-2R)} = -2i\,\mathrm{e}^{i\beta_m(R-z)}\,\sin\beta_m(R-z_s).$$

Therefore, (1.17) may also be written as

$$\widehat{G}(\vec{\boldsymbol{y}},\vec{\boldsymbol{x}}_s) = \begin{cases}\displaystyle\sum_{m=1}^{\infty}\frac{1}{\beta_m}\,\mathrm{e}^{i\beta_m(R-z_s)}\,\sin\beta_m(R-z)\,X_m(x)\,X_m(x_s), & z>z_s,\\ \displaystyle\sum_{m=1}^{\infty}\frac{1}{\beta_m}\,\mathrm{e}^{i\beta_m(R-z)}\,\sin\beta_m(R-z_s)\,X_m(x)\,X_m(x_s), & z<z_s.\end{cases} \tag{1.18}$$

## 1.5 The Dirichlet-to-Neumann (DtN) map

In this section, we present the *Dirichlet-to-Neumann* (DtN) method [27] which consists in reformulating a problem posed in an infinite domain, to an equivalent problem posed in a bounded domain. The method relies on the introduction of artificial boundaries, on which non-reflecting boundary conditions are imposed, called the DtN boundary conditions because they make use of a map that connects the Dirichlet data with the Neumann data.

### 1.5.1 The DtN map for an infinite waveguide

Let $\Omega$ be the infinite waveguide depicted in Figure 1.6. We define a subdomain $\Omega_L$ of our waveguide, such that $\Omega_L = \{\vec{\boldsymbol{x}} = (z, x) \in \Omega \ : \ L^- < z < L^+\}$. We assume that all the inhomogeneities of the medium are contained in $\Omega_L$ and that the wave speed is constant in $\Omega \setminus \Omega_L$.

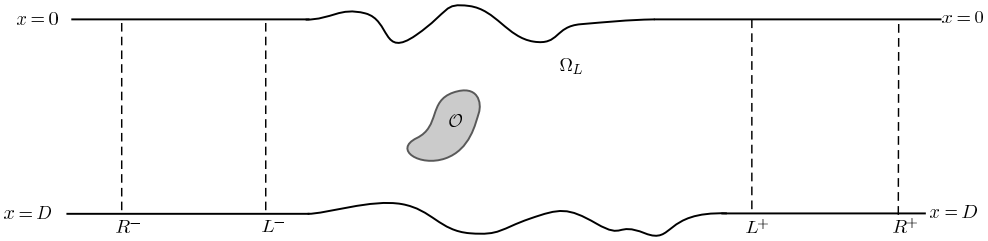


Figure 1.6: Schematic representation of an infinite waveguide.

For any $R^- < L^-$, let $\Gamma_{R^-} = \{(R^-, x) : \ 0 \le x \le D\}$ be the corresponding cross-section. Similarly, for $R^+ > L^+$ we define $\Gamma_{R^+} = \{(R^+, x) : \ 0 \le x \le D\}$. Now let us define the bounded domain $\Omega_R = \{\vec{\boldsymbol{x}} = (z, x) \in \Omega \ : \ R^- \le z \le R^+\}$. Then, the eigenpairs $\{\mu_n, X_n\}$, given by (1.11), allow us to define a *Dirichlet-to-Neumann (DtN)* map, denoted by $T$, such that for each function $u$ in a suitable function space

$$Tu(z, x) := \sum_{n=1}^{\infty} i\beta_n u_n(z) X_n(x) = T_1 u(z, x) + T_2 u(z, x), \tag{1.19}$$

where

$$T_1 u(z, x) = i \sum_{n=1}^{M} \sqrt{k^2 - \mu_n}\, u_n(z) X_n(x), \tag{1.20}$$

$$T_2 u(z, x) = - \sum_{n=M+1}^{\infty} \sqrt{\mu_n - k^2}\, u_n(z) X_n(x), \tag{1.21}$$

and

$$u_n(z) := \int_0^D u(z, x)\, X_n(x)\, dx, \tag{1.22}$$

are the Fourier coefficients of $u$ with respect to the orthonormal basis $\{X_n\}_{n=1,2,\ldots}$.

**Remark 2**

1. *On the artificial boundaries $\Gamma_{R^\pm}$ we may define the following norms of fractional order:*

$$\|u\|_{X^s(\Gamma_{R^\pm})} := \left(\sum_{n=1}^{\infty}(\mu_n)^s|u_n(R^\pm)|^2\right)^{1/2} < \infty,$$

*The spaces $X^s(\Gamma_{R^\pm})$, $s \geq 0$, are then defined as the domain of $(-d^2/dx^2)^{s/2}$, while the space of negative order $X^{-s}(\Gamma_{R^\pm})$ may be identified with the dual of $X^s(\Gamma_{R^\pm})$. The notation is adopted from [5].*

*The function space $X^s(\Gamma_{R^\pm})$ coincides with $H^s(\Gamma_{R^\pm})$ for $0 < s < 1/2$. For $s = 1/2$, $X^{1/2}(\Gamma_{R^\pm})$ may be identified with $H_{00}^{1/2}(\Gamma_{R^\pm})$, the subspace of functions of $H^{1/2}(\Gamma_{R^\pm})$ which when extended by zero belong to $H^{1/2}(\partial\Omega_R)$. For $1/2 < s \leq 1$, $X^s(\Gamma_{R^\pm}) = \overset{0}{H}{}^s(\Gamma_{R^\pm})$, (see [5, 42]). Then $T$ is a bounded linear operator from $X^{1/2}(\Gamma_{R^\pm})$ to $X^{-1/2}(\Gamma_{R^\pm})$.*

2. *It is easy to show the following properties of the DtN operator. First,*

$$\int_{\Gamma_{R^\pm}} Tu\, v = \int_{\Gamma_{R^\pm}} Tv\, u, \tag{1.23}$$

*and second, letting*

$$\begin{aligned} & T^*u(z,x) = T_1^*u(z,x) + T_2u(z,x), \\ \textit{where} \qquad & T_1^*u(z,x) = -i\textstyle\sum_{n=1}^{\infty}\sqrt{k^2-\mu_n}\, u_n(z)X_n(x), \end{aligned} \tag{1.24}$$

*it holds that*

$$\overline{Tu} = T^*\overline{u}. \tag{1.25}$$

Now let $\widehat{G}(\cdot, \vec{\boldsymbol{x}}_s)$ denote the Green's function for the Helmholtz operator with Dirichlet conditions on the boundary $\partial\Omega$ due to a point source located at $\vec{\boldsymbol{x}}_s = (z_s, x_s) \in \Omega_L$ for a fixed single frequency. (Here we consider a single frequency so when we refer to the Green's

function we omit writing dependence on frequency.) Thus $\widehat{G}(\cdot, \vec{\boldsymbol{x}}_s)$ solves the problem

$$-\Delta\widehat{G}(\cdot, \vec{\boldsymbol{x}}_s) - k^2\eta(\cdot)\,\widehat{G}(\cdot, \vec{\boldsymbol{x}}_s) = \delta(\cdot - \vec{\boldsymbol{x}}_s) \text{ in } \Omega_R, \tag{1.26}$$

$$\widehat{G}(\cdot, \vec{\boldsymbol{x}}_s) = 0 \text{ on } \partial\Omega_R \setminus \Gamma_{R^\pm}, \tag{1.27}$$

$$\partial_\nu\widehat{G}(\cdot, \vec{\boldsymbol{x}}_s) = T\widehat{G}(\cdot, \vec{\boldsymbol{x}}_s) \text{ on } \Gamma_{R^\pm}, \tag{1.28}$$

where $\nu$ is the outward unit normal on $\Gamma_{R^\pm}$ and the last boundary condition, which is imposed on the artificial boundaries $\Gamma_{R^\pm}$, accounts for the radiation condition.

### 1.5.2 The DtN map for a terminating waveguide

Let us also consider the equivalent setup for a terminating waveguide, as shown in Figure 1.7. We now define the domains $\Omega_{L^+} = \{\vec{\boldsymbol{x}} = (z, x) \in \Omega \ : \ z > L\}$ and $\Omega_R = \{\vec{\boldsymbol{x}} = (z, x) \in \Omega \ : \ z > R^-\}$ and the artificial boundary $\Gamma_{R^-} = \{(R^-, x) : \ 0 \le x \le D\}$. Then, $\widehat{G}(\cdot, \vec{\boldsymbol{x}}_s)$ solves the problem

$$-\Delta\widehat{G}(\cdot, \vec{\boldsymbol{x}}_s) - k^2\eta(\cdot)\,\widehat{G}(\cdot, \vec{\boldsymbol{x}}_s) = \delta(\cdot - \vec{\boldsymbol{x}}_s) \text{ in } \Omega_R, \tag{1.29}$$

$$\widehat{G}(\cdot, \vec{\boldsymbol{x}}_s) = 0 \text{ on } \partial\Omega_R \setminus \Gamma_{R^-}, \tag{1.30}$$

$$\partial_\nu\widehat{G}(\cdot, \vec{\boldsymbol{x}}_s) = T\widehat{G}(\cdot, \vec{\boldsymbol{x}}_s) \text{ on } \Gamma_{R^-}. \tag{1.31}$$

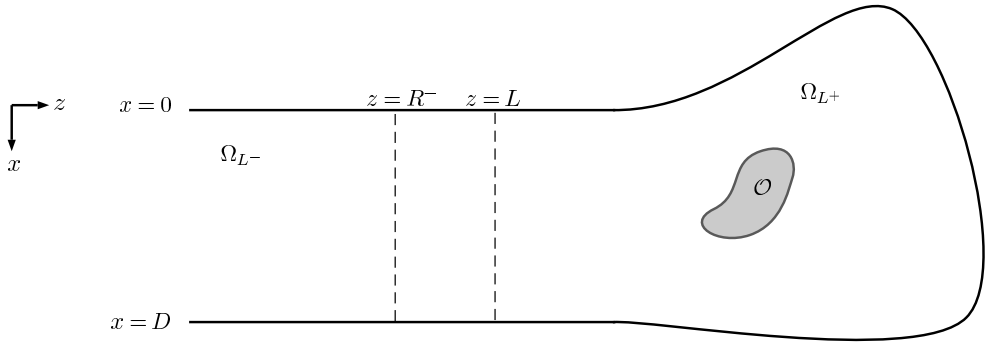


Figure 1.7: Schematic representation of a terminating waveguide.

## 1.6 Reciprocity of the Green's function

Having introduced the Dirichlet-to-Neumann map, we may prove the following proposition:

**Proposition 1 (Reciprocity relation)** *For any $\vec{\boldsymbol{x}}_1, \vec{\boldsymbol{x}}_2 \in \Omega_R$ it holds that*

$$\widehat{G}(\vec{\boldsymbol{x}}_1, \vec{\boldsymbol{x}}_2) = \widehat{G}(\vec{\boldsymbol{x}}_2, \vec{\boldsymbol{x}}_1). \tag{1.32}$$

Here, we will present the proof of the reciprocity relation for the infinite waveguide case. The proof for the terminating waveguide is completely analogous so we do not present it here.

*Proof.* Let $\vec{\boldsymbol{x}}_i \in \Omega_R$, $i = 1, 2$. Since $\widehat{G}(\cdot, \vec{\boldsymbol{x}}_i)$ satisfies (1.26) we have for every $\vec{\boldsymbol{y}} = (z, x) \in \Omega_R$ that

$$\begin{aligned}
\Delta\widehat{G}(\vec{\boldsymbol{y}}, \vec{\boldsymbol{x}}_2) + k^2\eta(\vec{\boldsymbol{y}})\,\widehat{G}(\vec{\boldsymbol{y}}, \vec{\boldsymbol{x}}_2) &= -\delta(\vec{\boldsymbol{y}} - \vec{\boldsymbol{x}}_2), \\
\Delta\widehat{G}(\vec{\boldsymbol{y}}, \vec{\boldsymbol{x}}_1) + k^2\eta(\vec{\boldsymbol{y}})\,\widehat{G}(\vec{\boldsymbol{y}}, \vec{\boldsymbol{x}}_1) &= -\delta(\vec{\boldsymbol{y}} - \vec{\boldsymbol{x}}_1).
\end{aligned}$$

We multiply the first equation by $\widehat{G}(\vec{\boldsymbol{y}}, \vec{\boldsymbol{x}}_1)$, the second by $\widehat{G}(\vec{\boldsymbol{y}}, \vec{\boldsymbol{x}}_2)$, subtract and integrate the resulting equation over $\Omega_R$ to obtain that

$$\begin{aligned}
&\int_{\Omega_R} \Big(\Delta\widehat{G}(\vec{\boldsymbol{y}}, \vec{\boldsymbol{x}}_2)\,\widehat{G}(\vec{\boldsymbol{y}}, \vec{\boldsymbol{x}}_1) - \widehat{G}(\vec{\boldsymbol{y}}, \vec{\boldsymbol{x}}_2)\,\Delta\widehat{G}(\vec{\boldsymbol{y}}, \vec{\boldsymbol{x}}_1)\Big) \\
&= \int_{\Omega_R} \Big(\delta(\vec{\boldsymbol{y}} - \vec{\boldsymbol{x}}_1)\,\widehat{G}(\vec{\boldsymbol{y}}, \vec{\boldsymbol{x}}_2) - \delta(\vec{\boldsymbol{y}} - \vec{\boldsymbol{x}}_2)\,\widehat{G}(\vec{\boldsymbol{y}}, \vec{\boldsymbol{x}}_1)\Big) \\
&\Rightarrow \int_{\Omega_R} \Big(\Delta\widehat{G}(\vec{\boldsymbol{y}}, \vec{\boldsymbol{x}}_2)\widehat{G}(\vec{\boldsymbol{y}}, \vec{\boldsymbol{x}}_1) - \widehat{G}(\vec{\boldsymbol{y}}, \vec{\boldsymbol{x}}_2)\Delta\widehat{G}(\vec{\boldsymbol{y}}, \vec{\boldsymbol{x}}_1)\Big) = \widehat{G}(\vec{\boldsymbol{x}}_1, \vec{\boldsymbol{x}}_2) - \widehat{G}(\vec{\boldsymbol{x}}_2, \vec{\boldsymbol{x}}_1).
\end{aligned}$$

Using the second Green's identity, and the Dirichlet boundary conditions (1.27), the equation above may be written as

$$\begin{aligned}
\widehat{G}(\vec{\boldsymbol{x}}_1, \vec{\boldsymbol{x}}_2) - \widehat{G}(\vec{\boldsymbol{x}}_2, \vec{\boldsymbol{x}}_1) &= \int_{\partial\Omega_R} \Big(\frac{\partial\widehat{G}}{\partial\nu}(\vec{\boldsymbol{y}}, \vec{\boldsymbol{x}}_2)\widehat{G}(\vec{\boldsymbol{y}}, \vec{\boldsymbol{x}}_1) - \widehat{G}(\vec{\boldsymbol{y}}, \vec{\boldsymbol{x}}_2)\frac{\partial\widehat{G}}{\partial\nu}(\vec{\boldsymbol{y}}, \vec{\boldsymbol{x}}_1)\Big) \\
&= \int_{\Gamma_{R^-}} \Big(\frac{\partial\widehat{G}}{\partial z}(\vec{\boldsymbol{y}}, \vec{\boldsymbol{x}}_2)\widehat{G}(\vec{\boldsymbol{y}}, \vec{\boldsymbol{x}}_1) - \widehat{G}(\vec{\boldsymbol{y}}, \vec{\boldsymbol{x}}_2)\frac{\partial\widehat{G}}{\partial z}(\vec{\boldsymbol{y}}, \vec{\boldsymbol{x}}_1)\Big)\, dx \\
&\quad + \int_{\Gamma_{R^+}} \Big(\frac{\partial\widehat{G}}{\partial z}(\vec{\boldsymbol{y}}, \vec{\boldsymbol{x}}_2)\widehat{G}(\vec{\boldsymbol{y}}, \vec{\boldsymbol{x}}_1) - \widehat{G}(\vec{\boldsymbol{y}}, \vec{\boldsymbol{x}}_2)\frac{\partial\widehat{G}}{\partial z}(\vec{\boldsymbol{y}}, \vec{\boldsymbol{x}}_1)\Big)\, dx.
\end{aligned}$$

Using the DtN conditions (1.28), we get that

$$\begin{aligned}&\int_{\Gamma_{R^-}} \Big(\frac{\partial \widehat{G}}{\partial z}(\vec{\boldsymbol{y}},\vec{\boldsymbol{x}}_2)\widehat{G}(\vec{\boldsymbol{y}},\vec{\boldsymbol{x}}_1) - \widehat{G}(\vec{\boldsymbol{y}},\vec{\boldsymbol{x}}_2)\frac{\partial \widehat{G}}{\partial z}(\vec{\boldsymbol{y}},\vec{\boldsymbol{x}}_1)\Big)\, dx \\ =&\int_{\Gamma_{R^-}} \Big(T\widehat{G}((R^-,x),\vec{\boldsymbol{x}}_2)\,\widehat{G}((R^-,x),\vec{\boldsymbol{x}}_1) - \widehat{G}((R^-,x),\vec{\boldsymbol{x}}_2)\,T\widehat{G}((R^-,x),\vec{\boldsymbol{x}}_1)\Big)\, dx \overset{(1.23)}{=} 0\end{aligned}$$

Similarly, we may prove that

$$\int_{\Gamma_{R^+}} \Big(\frac{\partial \widehat{G}}{\partial z}(\vec{\boldsymbol{y}},\vec{\boldsymbol{x}}_2)\widehat{G}(\vec{\boldsymbol{y}},\vec{\boldsymbol{x}}_1) - \widehat{G}(\vec{\boldsymbol{y}},\vec{\boldsymbol{x}}_2)\frac{\partial \widehat{G}}{\partial z}(\vec{\boldsymbol{y}},\vec{\boldsymbol{x}}_1)\Big)\, dx = 0.$$

Hence $\widehat{G}(\vec{\boldsymbol{x}}_1,\vec{\boldsymbol{x}}_2) - \widehat{G}(\vec{\boldsymbol{x}}_2,\vec{\boldsymbol{x}}_1) = 0$. □

## 1.7 The Kirchhoff-Helmholtz identity

Now, by using the DtN map and the reciprocity relation of the Green's function in the waveguide, we are in a position to prove the following Kirchhoff-Helmholtz identity.

**Proposition 2 (Kirchhoff-Helmholtz identity in the infinite waveguide)** *Let $\vec{\boldsymbol{x}}_1, \vec{\boldsymbol{x}}_2 \in \Omega_R$. Then*

$$\widehat{G}(\vec{\boldsymbol{x}}_1,\vec{\boldsymbol{x}}_2) - \overline{\widehat{G}(\vec{\boldsymbol{x}}_1,\vec{\boldsymbol{x}}_2)} = \int_{\Gamma_{R^-}\cup\Gamma_{R^+}} \Big(\overline{\widehat{G}(\vec{\boldsymbol{y}},\vec{\boldsymbol{x}}_1)}\nabla\widehat{G}(\vec{\boldsymbol{y}},\vec{\boldsymbol{x}}_2) - \widehat{G}(\vec{\boldsymbol{y}},\vec{\boldsymbol{x}}_2)\overline{\nabla\widehat{G}(\vec{\boldsymbol{y}},\vec{\boldsymbol{x}}_1)}\ \Big)\cdot\nu\, dx. \tag{1.33}$$

*Moreover we can prove that,*

$$\begin{aligned}\widehat{G}(\vec{\boldsymbol{x}}_1,\vec{\boldsymbol{x}}_2) - \overline{\widehat{G}(\vec{\boldsymbol{x}}_1,\vec{\boldsymbol{x}}_2)} = {}& 2i\sum_{n=1}^{M}\beta_n\,\overline{\widehat{G}_n(R^-,\vec{\boldsymbol{x}}_1)}\,\widehat{G}_n(R^-,\vec{\boldsymbol{x}}_2) \\ &+ 2i\sum_{n=1}^{M}\beta_n\,\overline{\widehat{G}_n(R^+,\vec{\boldsymbol{x}}_1)}\,\widehat{G}_n(R^+,\vec{\boldsymbol{x}}_2),\end{aligned} \tag{1.34}$$

*where $\widehat{G}_n(R^\pm,\cdot)$, $n=1,\dots,M$, denote the first $M$ Fourier coefficients of the Green's function (which correspond to the propagating modes) with respect to the orthonormal basis of $L^2(0,D)$ that is formed by the vertical eigenfunctions $X_n$, i.e.*

$$\widehat{G}_n(R^\pm,\cdot) = \int_0^D \widehat{G}((R^\pm,x'),\cdot)\,X_n(x')\,dx'. \tag{1.35}$$

**Proof**

Since $\widehat{G}(\cdot,\vec{\boldsymbol{x}}_1)$ solves (1.26)–(1.28) it is immediate to show that $\overline{\widehat{G}(\cdot,\vec{\boldsymbol{x}}_1)}$ solves the problem

$$-\Delta\overline{\widehat{G}(\cdot,\vec{\boldsymbol{x}}_1)} - k^2\eta(\cdot)\,\overline{\widehat{G}(\cdot,\vec{\boldsymbol{x}}_1)} = \delta(\cdot-\vec{\boldsymbol{x}}_1) \text{ in } \Omega_R, \tag{1.36}$$

$$\overline{\widehat{G}(\cdot,\vec{\boldsymbol{x}}_1)} = 0 \text{ on } \partial\Omega_R \setminus \Gamma_{R^\pm}, \tag{1.37}$$

$$\partial_\nu\overline{\widehat{G}(\cdot,\vec{\boldsymbol{x}}_1)} = T^*\overline{\widehat{G}(\cdot,\vec{\boldsymbol{x}}_1)} \text{ on } \Gamma_{R^\pm}. \tag{1.38}$$

Hence, for every $\vec{\boldsymbol{y}} = (z,x) \in \Omega_R$ we have that

$$\Delta\widehat{G}(\vec{\boldsymbol{y}},\vec{\boldsymbol{x}}_2) + k^2\eta(\vec{\boldsymbol{y}})\,\widehat{G}(\vec{\boldsymbol{y}},\vec{\boldsymbol{x}}_2) = -\delta(\vec{\boldsymbol{y}}-\vec{\boldsymbol{x}}_2),$$
$$\Delta\overline{\widehat{G}(\vec{\boldsymbol{y}},\vec{\boldsymbol{x}}_1)} + k^2\eta(\vec{\boldsymbol{y}})\,\overline{\widehat{G}(\vec{\boldsymbol{y}},\vec{\boldsymbol{x}}_1)} = -\delta(\vec{\boldsymbol{y}}-\vec{\boldsymbol{x}}_1),$$

Now, we multiply the first equation by $\overline{\widehat{G}(\vec{\boldsymbol{y}},\vec{\boldsymbol{x}}_1)}$, the second by $\widehat{G}(\vec{\boldsymbol{y}},\vec{\boldsymbol{x}}_2)$, subtract, and integrate over $\Omega_R$ to obtain that:

$$\begin{aligned}&\int_{\Omega_R}\left(\Delta\widehat{G}(\vec{\boldsymbol{y}},\vec{\boldsymbol{x}}_2)\overline{\widehat{G}(\vec{\boldsymbol{y}},\vec{\boldsymbol{x}}_1)} - \widehat{G}(\vec{\boldsymbol{y}},\vec{\boldsymbol{x}}_2)\Delta\overline{\widehat{G}(\vec{\boldsymbol{y}},\vec{\boldsymbol{x}}_1)}\right)\\ &= \int_{\Omega_R}\left(\delta(\vec{\boldsymbol{y}}-\vec{\boldsymbol{x}}_1)\widehat{G}(\vec{\boldsymbol{y}},\vec{\boldsymbol{x}}_2) - \delta(\vec{\boldsymbol{y}}-\vec{\boldsymbol{x}}_2)\overline{\widehat{G}(\vec{\boldsymbol{y}},\vec{\boldsymbol{x}}_1)}\right) = \widehat{G}(\vec{\boldsymbol{x}}_1,\vec{\boldsymbol{x}}_2) - \overline{\widehat{G}(\vec{\boldsymbol{x}}_2,\vec{\boldsymbol{x}}_1)}.\end{aligned}$$

Then, from the reciprocity property (1.32) we get that

$$\int_{\Omega_R}\left(\Delta\widehat{G}(\vec{\boldsymbol{y}},\vec{\boldsymbol{x}}_2)\overline{\widehat{G}(\vec{\boldsymbol{y}},\vec{\boldsymbol{x}}_1)} - \widehat{G}(\vec{\boldsymbol{y}},\vec{\boldsymbol{x}}_2)\Delta\overline{\widehat{G}(\vec{\boldsymbol{y}},\vec{\boldsymbol{x}}_1)}\right) = \widehat{G}(\vec{\boldsymbol{x}}_1,\vec{\boldsymbol{x}}_2) - \overline{\widehat{G}(\vec{\boldsymbol{x}}_1,\vec{\boldsymbol{x}}_2)}.$$

Using the second Green's identity and the boundary conditions (1.27) and (1.37), we end up with

$$\widehat{G}(\vec{\boldsymbol{x}}_1,\vec{\boldsymbol{x}}_2) - \overline{\widehat{G}(\vec{\boldsymbol{x}}_1,\vec{\boldsymbol{x}}_2)} = \int_{\partial\Omega_R}\left(\overline{\widehat{G}(\vec{\boldsymbol{y}},\vec{\boldsymbol{x}}_1)}\nabla\widehat{G}(\vec{\boldsymbol{y}},\vec{\boldsymbol{x}}_2) - \widehat{G}(\vec{\boldsymbol{y}},\vec{\boldsymbol{x}}_2)\overline{\nabla\widehat{G}(\vec{\boldsymbol{y}},\vec{\boldsymbol{x}}_1)}\right)\cdot\nu\,dx,$$

and (1.33) is proven. Now, having proven (1.33), the DtN conditions (1.28) and (1.38) allow

us to write

$$
\begin{aligned}
&\widehat{G}(\vec{\boldsymbol{x}}_1,\vec{\boldsymbol{x}}_2)-\overline{\widehat{G}(\vec{\boldsymbol{x}}_1,\vec{\boldsymbol{x}}_2)}\\
&= \int_{\Gamma_{R^-}}\Big(\overline{\widehat{G}((R^-,x),\vec{\boldsymbol{x}}_1)}T\widehat{G}((R^-,x),\vec{\boldsymbol{x}}_2)-\widehat{G}((R^-,x),\vec{\boldsymbol{x}}_2)T^*\overline{\widehat{G}((R^-,x),\vec{\boldsymbol{x}}_1)}\Big)\,dx\\
&+ \int_{\Gamma_{R^+}}\Big(\overline{\widehat{G}((R^+,x),\vec{\boldsymbol{x}}_1)}T\widehat{G}((R^+,x),\vec{\boldsymbol{x}}_2)-\widehat{G}((R^+,x),\vec{\boldsymbol{x}}_2)T^*\overline{\widehat{G}((R^+,x),\vec{\boldsymbol{x}}_1)}\Big)\,dx\\
&\overset{(1.23)}{=} \int_{\Gamma_{R^-}}\Big(T\overline{\widehat{G}((R^-,x),\vec{\boldsymbol{x}}_1)}-T^*\overline{\widehat{G}((R^-,x),\vec{\boldsymbol{x}}_1)}\Big)\widehat{G}((R^-,x),\vec{\boldsymbol{x}}_2)\,dx.\\
&+ \int_{\Gamma_{R^+}}\Big(T\overline{\widehat{G}((R^+,x),\vec{\boldsymbol{x}}_1)}-T^*\overline{\widehat{G}((R^+,x),\vec{\boldsymbol{x}}_1)}\Big)\widehat{G}((R^+,x),\vec{\boldsymbol{x}}_2)\,dx. \qquad (1.39)
\end{aligned}
$$

Therefore, in view of (1.20) and (1.24), we deduce that

$$
T\overline{\widehat{G}((R^\pm,x),\vec{\boldsymbol{x}}_1)}-T^*\overline{\widehat{G}((R^\pm,x),\vec{\boldsymbol{x}}_1)}=2i\sum_{n=1}^{M}\beta_n\,\overline{\widehat{G}_n(R^\pm,\vec{\boldsymbol{x}}_1)}\,X_n(x).
$$

Inserting the above in (1.39) we conclude that

$$
\begin{aligned}
\widehat{G}(\vec{\boldsymbol{x}}_1,\vec{\boldsymbol{x}}_2)-\overline{\widehat{G}(\vec{\boldsymbol{x}}_1,\vec{\boldsymbol{x}}_2)} &= 2i\int_0^D\sum_{n=1}^{M}\beta_n\,\overline{\widehat{G}_n(R^-,\vec{\boldsymbol{x}}_1)}\,X_n(x)\,\widehat{G}((R^-,x),\vec{\boldsymbol{x}}_2)\,dx\\
&\quad+2i\int_0^D\sum_{n=1}^{M}\beta_n\,\overline{\widehat{G}_n(R^+,\vec{\boldsymbol{x}}_1)}\,X_n(x)\,\widehat{G}((R^+,x),\vec{\boldsymbol{x}}_2)\,dx\\
&=2i\sum_{n=1}^{M}\beta_n\,\overline{\widehat{G}_n(R^-,\vec{\boldsymbol{x}}_1)}\int_0^D\widehat{G}((R^-,x),\vec{\boldsymbol{x}}_2)\,X_n(x)\,dx\\
&\quad+2i\sum_{n=1}^{M}\beta_n\,\overline{\widehat{G}_n(R^+,\vec{\boldsymbol{x}}_1)}\int_0^D\widehat{G}((R^+,x),\vec{\boldsymbol{x}}_2)\,X_n(x)\,dx\\
&=2i\sum_{n=1}^{M}\beta_n\,\overline{\widehat{G}_n(R^-,\vec{\boldsymbol{x}}_1)}\,\widehat{G}_n(R^-,\vec{\boldsymbol{x}}_2)\\
&\quad+2i\sum_{n=1}^{M}\beta_n\,\overline{\widehat{G}_n(R^+,\vec{\boldsymbol{x}}_1)}\,\widehat{G}_n(R^+,\vec{\boldsymbol{x}}_2),
\end{aligned}
$$

which completes the proof. □

As with the reciprocity relation, the proof of the Kirchhoff-Helmholtz identity for the terminating waveguide follows in a completely analogous manner to the infinite waveguide case,

where again we only consider the integrals over $\Gamma_{R^-}$. Therefore, the Kirchhoff-Helmholtz identity in the terminating case, states that

**Proposition 3 (Kirchhoff-Helmholtz identity in the terminating waveguide)** *Let $\vec{\boldsymbol{x}}_1, \vec{\boldsymbol{x}}_2 \in \Omega_{\mathcal{A}}$. Then we can prove that,*

$$\widehat{G}(\vec{\boldsymbol{x}}_1, \vec{\boldsymbol{x}}_2) - \overline{\widehat{G}(\vec{\boldsymbol{x}}_1, \vec{\boldsymbol{x}}_2)} = 2i \sum_{n=1}^{M} \beta_n \, \overline{\widehat{G}_n(R^-, \vec{\boldsymbol{x}}_1)} \, \widehat{G}_n(R^-, \vec{\boldsymbol{x}}_2). \tag{1.40}$$

# Chapter 2

# Imaging problem

The imaging problem that we consider in this dissertation consists in determining the support of an extended source or scatterer located in a waveguide environment. Wave propagation is modelled using the scalar wave equation and our data is the acoustic pressure field collected on an array of receivers that may or may not span the whole vertical cross-section of the waveguide.

In this chapter, we first describe the data structures that are collected on the array and depend on whether we search for a source or a scatterer. Then we present the well known *Kirchhoff migration* imaging functional and introduce an alternative imaging functional that is based on the projection of the data on the propagating modes. We also discuss selective imaging and its implementation in a waveguide using both imaging functionals.

## 2.1 Array imaging data structures

In what follows we consider two different array setups for imaging: i) The *passive* case, where we seek to locate a source. ii) The *active* case, where we seek to locate a scatterer.

### 2.1.1 Passive array setup

In the passive setup, the array records the pressure field generated by an extended source located in the waveguide. Specifically, as shown in Figure 2.1, assume that an extended source with support $\mathcal{O}$ is located in the waveguide. Every point in the support of the source emits a delta-function pulse in time and the data are collected on a vertical array, denoted

by $\mathcal{A}$, located at $z = z_a$. The array consists of $N$ receivers, that record the pressure field at each receiver location $\vec{\boldsymbol{x}}_r = (z_r, x_r)$.

Then, for a single frequency $\omega$, the data is an $N \times 1$ vector called the *array response vector*, denoted by $\widehat{\Pi}$ with components $\widehat{\Pi}(\vec{\boldsymbol{x}}_r; \omega)$, $r = 1, \ldots, N$. The element $\widehat{\Pi}(\vec{\boldsymbol{x}}_r; \omega)$ corresponds to the Fourier transform of the time trace of the pressure field recorded at the receiver located at $\vec{\boldsymbol{x}}_r$, evaluated at frequency $\omega$.

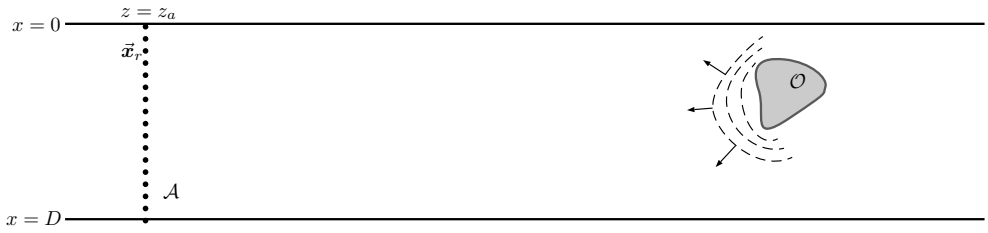


Figure 2.1: Passive imaging setup for an extended source.

### 2.1.2 Active array setup

The other setup we consider, is the active array case. Here, as shown in Figure 2.2, we wish to image an extended scatterer which, slightly abusing notation, we denote again as $\mathcal{O}$, using again a vertical array $\mathcal{A}$ located at $z = z_a$. The array now consists of $N$ transducers that can act both as sources and receivers.


Figure 2.2: Active imaging setup in an infinite strip.

In the active case the data is the array response matrix for the scattered field. For a single frequency this is an $N \times N$ matrix, whose element $\widehat{\Pi}(\vec{\boldsymbol{x}}_r, \vec{\boldsymbol{x}}_s; \omega)$ corresponds to the Fourier transform of the recorded time trace of the pressure field at receiver $\vec{\boldsymbol{x}}_r \in \mathcal{A}$, due to a delta-function pulse send from the source located at $\vec{\boldsymbol{x}}_s \in \mathcal{A}$, evaluated at frequency $\omega$. As usual, the data for the *scattered* field are obtained by subtracting the incident field from the total field.

**Remark 3** *In this work, the array may span the whole, or part of the waveguide's cross-section. For the rest of this chapter we assume that the array spans the whole cross-section, we refer to this case as the full-aperture array case. We will examine the partial-aperture array case and make the necessary adjustments to our imaging methods in the next chapter.*

## 2.2 Imaging functionals

Given the data for the passive or the active case as described in the previous section, we now want to create an image of the waveguide that would assist us to decide whether a source or a scatterer is present in it. We first define a search domain $\mathcal{S}$, which is discretized using a (usually rectangular) grid, as shown in Figure 2.3. Then, on each point $\vec{\boldsymbol{y}}^{\mathrm{s}} \in \mathcal{S}$, we compute the value of an appropriate imaging functional. It is expected that the values of the imaging functional, when they are graphically displayed in the search domain, should exhibit peaks that indicate the presence of the source or the scatterer.

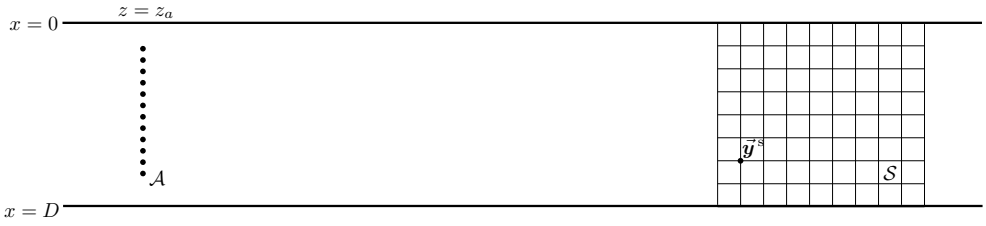


Figure 2.3: Search domain, discretized using a rectangular grid.

### 2.2.1 The Kirchhoff-migration imaging functional

The first imaging functional we will discuss, is the *Kirchhoff migration* functional [8, 11]. Kirchhoff migration is widely used in seismic imaging and exploration geophysics, applications for which the arrays are very large and so is the bandwidth. Although our final goal is to image extended reflectors, we will first start with the passive imaging case for a point source, to provide a derivation of the imaging functional that follows one's intuition.

#### Passive case

Let us assume that a point source of unit strength, located at the point $\vec{\boldsymbol{x}}^{\star} = (z^{\star}, x^{\star}) \in \Omega$, emits a signal that is recorded on a vertical array $\mathcal{A} = \{\vec{\boldsymbol{x}}_r = (z_a, x_r)\}_{r=1}^{N}$ as illustrated in Figure 2.4. In this case, the array response vector has the form

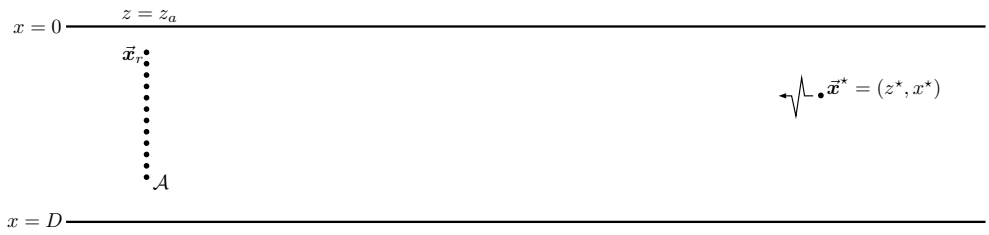


Figure 2.4: Passive imaging setup for a point source.

$$\widehat{\Pi}(\vec{\boldsymbol{x}}_r;\omega) = \widehat{G}(\vec{\boldsymbol{x}}_r, \vec{\boldsymbol{x}}^\star), \tag{2.1}$$

where $\widehat{G}$ is the Green's function.

The imaging functional that we propose to use is based on the concept of phase conjugation, which may be physically interpreted by virtue of the Huygen's principle. As pointed out in [35], Huygen's principle states that a propagating wave may be viewed as superposition of wavelets reemitted from a fictitious surface with amplitudes proportional to those of the original wave. In phase conjugation, which may be seen as the equivalent of time reversal [25] in the frequency domain, the reemitted wavelets' amplitudes are proportional to the complex conjugate of the corresponding ones in the original wave. These remarks lead naturally one to define the following imaging functional

$$\mathcal{I}(\vec{\boldsymbol{y}}^s) = \int_{\mathcal{A}} \overline{\widehat{\Pi}(\vec{\boldsymbol{x}}_r, \omega)} \widehat{G}(\vec{\boldsymbol{y}}^s, \vec{\boldsymbol{x}}_r) dx, \tag{2.2}$$

where $\vec{\boldsymbol{x}}_r = (z_a, x) \in \mathcal{A}$, $\vec{\boldsymbol{y}}^s \in \mathcal{S}$ and overline denotes complex conjugation.

The expression shown in (2.2) concerns an ideal case, where we have a continuous array. However, as mentioned in our previous description of the array setup, we have a discrete array that consists of $N$ transducers. Therefore, instead of working with (2.2), we will use its discrete analogue, namely we define the imaging functional

$$\mathcal{I}^{\mathrm{KM}}(\vec{\boldsymbol{y}}^s, \omega) = \sum_{r=1}^{N} \overline{\widehat{\Pi}(\vec{\boldsymbol{x}}_r;\omega)} \widehat{G}(\vec{\boldsymbol{y}}^s, \vec{\boldsymbol{x}}_r), \tag{2.3}$$

where we use the superscript KM as an abbreviation for Kirchhoff migration.

### Extension to active case

We now turn back to the active imaging problem, where we wish to image a scatterer, with a setup as the one shown in Figure 2.2. Then, as stated earlier, our data may be cast in the form of the array response matrix $\widehat{\Pi}(\vec{\boldsymbol{x}}_s, \vec{\boldsymbol{x}}_r; \omega)$. As such, a natural generalization of the imaging functional for the passive case given by (2.3), is the following active imaging functional

$$\mathcal{I}^{\mathrm{KM}}(\vec{\boldsymbol{y}}^s, \omega) = \sum_{r=1}^{N} \sum_{s=1}^{N} \overline{\widehat{\Pi}(\vec{\boldsymbol{x}}_s, \vec{\boldsymbol{x}}_r; \omega)} \widehat{G}(\vec{\boldsymbol{y}}^s, \vec{\boldsymbol{x}}_r) \widehat{G}(\vec{\boldsymbol{y}}^s, \vec{\boldsymbol{x}}_s). \tag{2.4}$$

We also define the imaging functional for multiple frequencies, as a simple addition over frequencies, specifically

$$\mathcal{I}^{\mathrm{KM}}(\vec{\boldsymbol{y}}^s) = \sum_{\omega} \mathcal{I}^{\mathrm{KM}}(\vec{\boldsymbol{y}}^s, \omega). \tag{2.5}$$

### Imaging Examples

In order to provide to the reader a sense of how $\mathcal{I}^{\mathrm{KM}}$ behaves, we will consider the simple case of imaging in a homogeneous infinite waveguide that forms an infinite strip, i.e. $\Omega = (-\infty, \infty) \times (0, D)$. We will examine three simplified cases for the scatterers' shapes: a point scatterer, an one-dimensional vertical scatterer (which we will call the *screen*), and a semicircular scatterer. In all cases, the response matrix $\widehat{\Pi}$ is computed by means of the Born approximation.

Specifically, the array response matrix for a point scatterer is given by

$$\widehat{\Pi}(\vec{\boldsymbol{x}}_s, \vec{\boldsymbol{x}}_r; \omega) = k^2 \widehat{G}(\vec{\boldsymbol{x}}^\star, \vec{\boldsymbol{x}}_s) \widehat{G}(\vec{\boldsymbol{x}}_r, \vec{\boldsymbol{x}}^\star),$$

where $\widehat{G}$ in the infinite strip is given by (1.15). In what follows we suppress the multiplicative constant $k^2$, hence we assume that

$$\widehat{\Pi}(\vec{\boldsymbol{x}}_s, \vec{\boldsymbol{x}}_r; \omega) = \widehat{G}(\vec{\boldsymbol{x}}^\star, \vec{\boldsymbol{x}}_s) \widehat{G}(\vec{\boldsymbol{x}}_r, \vec{\boldsymbol{x}}^\star). \tag{2.6}$$

Next, if we view an one-dimensional extended scatterer $\mathcal{T}$ – which in our case is the screen or the semicircle – as a collection of point scatterers, the response matrix is then given by

$$\widehat{\Pi}(\vec{\boldsymbol{x}}_s, \vec{\boldsymbol{x}}_r; \omega) = \int_{\mathcal{T}} \widehat{G}(\vec{\boldsymbol{y}}, \vec{\boldsymbol{x}}_s) \widehat{G}(\vec{\boldsymbol{x}}_r, \vec{\boldsymbol{y}}) \, d\vec{\boldsymbol{y}}, \tag{2.7}$$

where $\vec{\boldsymbol{y}} \in \mathcal{T}$.

The exact formulas for the response matrix in all three cases, are given in Appendix A. Having an expression for the response matrix for each case, we may proceed in computing the $\mathcal{I}^{\mathrm{KM}}$ image, which in this work is the modulus of equation (2.5).

We assume a reference wavenumber $k_0 = \pi/10$ that corresponds to a reference wavelength $\lambda_0$, and take $D = 10\lambda_0$. We use a bandwidth around a single central frequency $f_c$ that corresponds to a wavenumber $k = 0.975k_0$, with $B \simeq 0.14f_c$, *i.e.* $B = [f_c - B/2, f_c + B/2]$. Finally our search domain is $\mathcal{S} = [11.5, 26.5] \times [0, 10]$, where all distances are expressed in terms of the reference wavelength $\lambda_0$. Let us remark that since horizontal wavenumbers $\beta_n$ appear in the denominator of the Green's function and are descending in order, we have to be careful not to divide by a very small number. Therefore, before computing an image for each frequency, we check the minimum $\beta_n$ for that frequency and, if it lies below a certain threshold, we exclude this frequency from the computations of our imaging functional. For the creation of the $\mathcal{I}^{\mathrm{KM}}$ images, we have employed a threshold of $8 \cdot 10^{-2}$.

In Figure 2.5, we plot the $\mathcal{I}^{\mathrm{KM}}$ image for a point scatterer, located at $\vec{\boldsymbol{x}}^{\star} = (19, 5)\lambda_0$ in the left subplot, a vertical screen of size $b = 2\lambda_0$, centered at $\vec{\boldsymbol{x}}^{\star} = (19, 5)\lambda_0$ in the middle, and a semicircular scatterer centered at $\vec{\boldsymbol{x}}^{\star} = (19, 5)\lambda_0$ with diameter $b = 2\lambda_0$ in the right. We seem to have a very good reconstruction for the point scatterer. For the screen, we observe that the image has deteriorated in quality compared to the point scatterer but we again have a quite good reconstruction of the scatterer's support. One way to measure the quality of an image is with what we call the peak to side lobe ratio, which is the maximum value in the vicinity of the scatterer, divided by the maximum value in an area away from it. Lastly, for the semicircle, the noise level of the image is relatively high, but we seem to recover most of the scatterer's support, while we do not reconstruct the upper and lower edges of the semicircle.

### 2.2.2 An active imaging functional based on modal projection

The Kirchhoff migration imaging functional we just presented backpropagates our data, the response matrix $\widehat{\Pi}$, from each receiver element of the array to a point in our search domain and then back to a source element of the array. An alternative way to create an image in a waveguide environment, is to backpropagate instead the propagating modes (see [14,21,48]).

A first step towards that is to project our data, the array response matrix $\widehat{\Pi}$, on the vertical eigenfunctions $X_n$, that form an orthonormal basis of $L^2[0, D]$. We thus define the

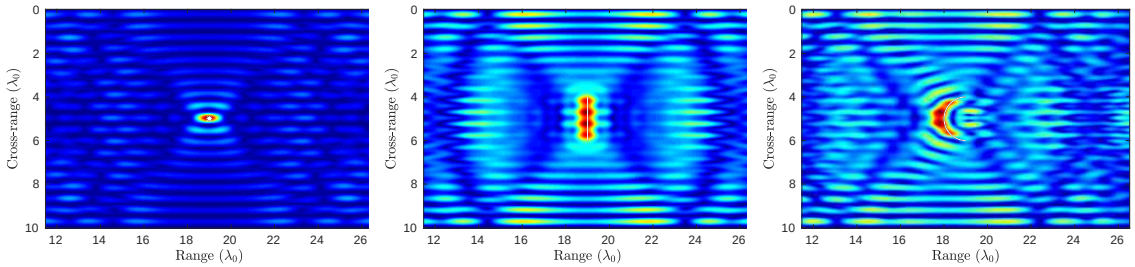


Figure 2.5: Imaging with $\mathcal{I}^{\mathrm{KM}}$ for a point scatterer, located at $\vec{\boldsymbol{x}}^{\star} = (19, 5)\lambda_0$ (left), a vertical screen of size $b = 2\lambda_0$, centered at $\vec{\boldsymbol{x}}^{\star} = (19, 5)\lambda_0$ (middle) and a semicircular scatterer centered at $\vec{\boldsymbol{x}}^{\star} = (19, 5)\lambda_0$ with diameter $b = 2\lambda_0$ (right). We use frequencies $f \in [f_c - B/2, f_c + B/2]$ with $f_c = 0.975k_0$ and $B = 0.14f_c$.

matrix $\widehat{\mathbb{Q}}$, whose $mn-$th element is given by

$$\widehat{\mathbb{Q}}_{mn}(\omega) = \int_0^D \mathrm{d}x_s \int_0^D \mathrm{d}x_r \, \widehat{\Pi}(\vec{\boldsymbol{x}}_s, \vec{\boldsymbol{x}}_r, \omega) X_m(x_s) X_n(x_r), \quad m = 1, \ldots, M, n = 1, \ldots, M, \tag{2.8}$$

where $M$ is the number of propagating modes in $\Omega \setminus \Omega_L$, for a waveguide as the one depicted in Figure 1.1.

Moreover, we will use a weighted modal projection and define the matrix $\widehat{\mathbb{P}}$ as

$$\begin{aligned} \widehat{\mathbb{P}}_{mn} &= \beta_m \beta_n \int_0^D \mathrm{d}x_s \int_0^D \mathrm{d}x_r \, \widehat{\Pi}(\vec{\boldsymbol{x}}_s, \vec{\boldsymbol{x}}_r, \omega) X_m(x_s) X_n(x_r) \\ &= \beta_m \beta_n \widehat{\mathbb{Q}}_{mn}, \quad m = 1, \ldots, M, n = 1, \ldots, M. \end{aligned} \tag{2.9}$$

The matrix $\widehat{\mathbb{P}}$ has nice properties regarding selective imaging as we will see in the next chapter. We also need to introduce the projection of the Green's function on the propagating modes

$$\widehat{G}_n(z_a, \cdot) = \int_0^D \widehat{G}((z_a, x'), \cdot) \, X_n(x') \, dx', \quad n = 1, \ldots, M \tag{2.10}$$

and the weighted projection

$$\begin{aligned} \widetilde{G}_n(z_a, \cdot) &= \beta_n \int_0^D \widehat{G}((z_a, x'), \cdot) \, X_n(x') \, dx'. \\ &= \beta_n \widehat{G}_n(z_a, \cdot), \quad n = 1, \ldots, M \end{aligned} \tag{2.11}$$

The $\widetilde{G}_n(z_a, \cdot)$, $n = 1, \ldots, M$, denote the first $M$ Fourier coefficients of the Green's function (which correspond to the propagating modes) with respect to the orthonormal basis

of $L^2(0, D)$ that is formed by the vertical eigenfunctions $X_n$, weighted by the horizontal wavenumbers $\beta_n$.

Mimicking (2.4), we define the functional

$$\widetilde{\mathcal{I}}^{\mathrm{KM}}(\vec{\boldsymbol{y}}^{\mathrm{s}}, \omega) = \sum_{m,n=1}^{M} \overline{\widehat{\mathbb{P}}_{mn}(\omega)} \widetilde{G}_n(\vec{\boldsymbol{x}}_s, \vec{\boldsymbol{y}}^{\mathrm{s}}) \widetilde{G}_n(\vec{\boldsymbol{x}}_r, \vec{\boldsymbol{y}}^{\mathrm{s}}). \tag{2.12}$$

We also define the multiple frequency version of $\widetilde{\mathcal{I}}^{\mathrm{KM}}$ in the same way as we did for $\mathcal{I}^{\mathrm{KM}}$, namely we simply add over frequencies, hence

$$\widetilde{\mathcal{I}}^{\mathrm{KM}}(\vec{\boldsymbol{y}}^{\mathrm{s}}) = \sum_{\omega} \widetilde{\mathcal{I}}^{\mathrm{KM}}(\vec{\boldsymbol{y}}^{\mathrm{s}}, \omega). \tag{2.13}$$

**Remark 4** *A key assumption for the definition of the projected response matrix, is that the array spans the whole vertical cross-section. In the case of partial array aperture, we lose the orthonormality of the vertical eigenfunctions $X_n$ along the array. The necessary modifications to the projection and the imaging functional for the partial array case are presented in the next chapter.*

### Imaging results

Now, let us compare the imaging results of $\mathcal{I}^{\mathrm{KM}}$ and $\widetilde{\mathcal{I}}^{\mathrm{KM}}$. On the top row of Figure 2.6 we display again the $\mathcal{I}^{\mathrm{KM}}$ images from Figure 2.5, while on the bottom row we show the corresponding $\widetilde{\mathcal{I}}^{\mathrm{KM}}$ images, for the same setup. As with the $\mathcal{I}^{\mathrm{KM}}$ case, the $\widetilde{\mathcal{I}}^{\mathrm{KM}}$ images are the modulus of (2.12).

First, on the left column, we consider the case of the point scatterer. Next, on the middle column, we show the images for the vertical screen and on the right column we consider the semicircular scatterer. In all cases, we observe a clear gain in terms of peak to side lobe ratio when imaging with $\widetilde{\mathcal{I}}^{\mathrm{KM}}$. We also observe a slightly better resolution for $\mathcal{I}^{\mathrm{KM}}$ in the range direction. The usual way to assess the quality of an imaging method, is to perform a resolution and an SNR analysis. This is typically done by computing the point-spread function (PSF), which is the analytical expression of the image obtained for a point scatterer. A resolution analysis for $\widetilde{\mathcal{I}}^{\mathrm{KM}}$ will be performed in Chapter 4.

As illustrated in the rightmost images, for the semicircle we obtain a rather poor reconstruction of the scatterer's support, with the image being essentially supported in the

central part (bulk) of the object. In hopes of recovering more information about the object's size and shape, we will use the concept of *selective imaging*, which will be discussed in the next section.

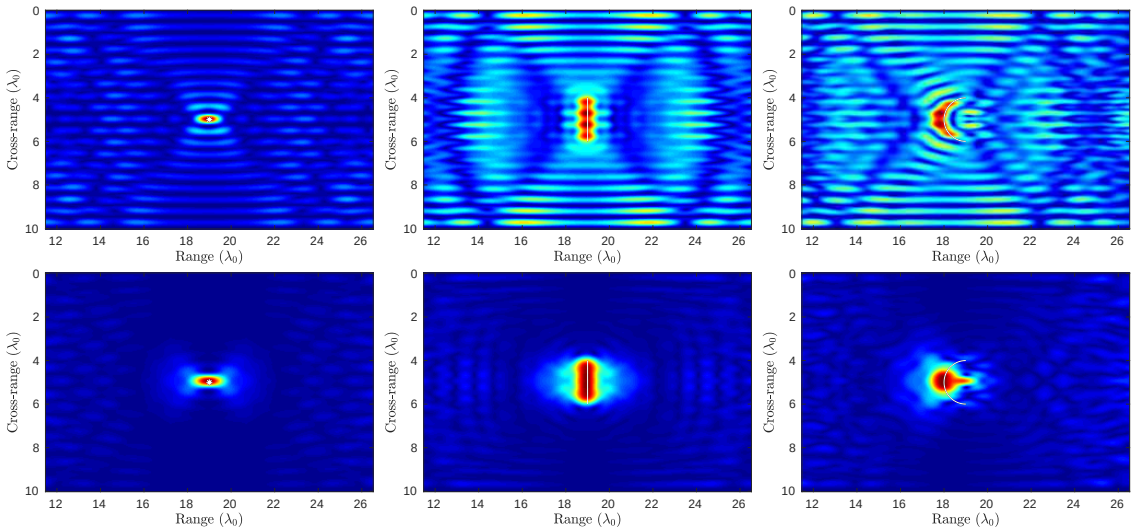


Figure 2.6: Imaging with $\mathcal{I}^{\mathrm{KM}}$ (top) and $\widetilde{\mathcal{I}}^{\mathrm{KM}}$ (bottom) for a point scatterer (left), a vertical screen (middle) and a semiricle (right), centered at $\vec{\boldsymbol{x}}^{\star} = (19, 5)\lambda_0$. We use frequencies $f \in [f_c - B/2, f_c + B/2]$ with $f_c = 0.975k_0$ and $B = 0.14f_c$.

## 2.3 Selective imaging

In this section, we will discuss the concept of *selective imaging*, in which we are interested in reconstructing specific parts of the scatterer. It has been motivated by *selective focusing*, where we have multiple point-like scatterers and we wish to create images that focus on each scatterer separately. This can be achieved with the DORT method (DORT is an acronym for 'decomposition of the time reversal operator' in French), introduced by Prada and Fink [51]. DORT uses the singular value decomposition (SVD) of the array response matrix to achieve selective focusing. Under the assumption that the scatterers are located far enough from each other, the experimental results in [51] suggest that the number of non-zero singular values equals the number of scatterers present in the medium. That means that there is an one-to-one correspondence between the singular values and vectors of the array response matrix and the scatterers. Therefore, we can create an image that focuses on a single scatterer by back-propagating the projection of the response matrix on the space generated

by the singular vector that corresponds to that scatterer. Related works include [46, 50]. To the best of our knowledge, the first rigorous mathematical justification of DORT has been given in [32], where the propagation medium is the free space $\mathbb{R}^3$. For the analysis of DORT in a waveguide environment we refer to the work of Pinçon and Ramdani [48].

The method that we will use for selective imaging of extended reflectors, is called the *subspace projection method* [10], which, much like DORT, is based on the SVD of the array response matrix. To present the general idea behind this method, we will denote the array response matrix $\mathcal{P}$, with $\mathcal{P} = \widehat{\Pi}$ when using $\mathcal{I}^{\text{KM}}$ and $\mathcal{P} = \widehat{\mathbb{P}}$ for $\widetilde{\mathcal{I}}^{\text{KM}}$. The SVD of $\mathcal{P}$ is a factorization of the form (see, for example, [29, §2.5])

$$\mathcal{P} = \mathcal{U}\Sigma\mathcal{V}^*,$$

where $\Sigma$ is a matrix that contains the singular values $\sigma_i$ along its diagonal in descending order, and $\mathcal{U}$, $\mathcal{V}$ are unitary matrices containing the left and right singular vectors, respectively. Also, $\mathcal{V}^*$ denotes the complex conjugate transpose of the matrix $\mathcal{V}$.

We may also write the SVD of $\mathcal{P}$ as a sum of the form:

$$\mathcal{P} = \sum_{i=1}^{\rho} \sigma_i \, \mathcal{U}_i \mathcal{V}_i^*,$$

where $\rho = \text{rank}(\mathcal{P})$, so that $\sigma_1 \geq \ldots \geq \sigma_\rho > \sigma_{\rho+1} = \ldots = \sigma_N = 0$, and $\mathcal{U}_i$, $\mathcal{V}_i$ are the left and right singular vectors.

As shown in [10] for the free space case, the reflections from the main body of an extended scatterer correspond to the first (and larger) singular values, while the reflections coming from the edges correspond to smaller singular values. Thus, since our goal is to focus on specific parts of the scatterer, we will need to create an appropriate filtered version of $\mathcal{P}$. Having written the SVD of $\mathcal{P}$ as a sum, we may write a filtered version of the response matrix as

$$D[\mathcal{P}] = \sum_{i=1}^{\rho} d_i \sigma_i \, \mathcal{U}_i \mathcal{V}_i^*.$$

The simpler choice is that the filter weights $d_i$ may take only values 1 or 0, depending on whether we will include the $i$-th singular vector in the filtered version of the response matrix, or not.

### 2.3.1 Selective imaging with $\mathcal{I}^{\mathrm{KM}}$

Having created a filtered version of the response matrix, we will first define the selective imaging functional for $\mathcal{I}^{\mathrm{KM}}$, given by

$$\mathcal{I}^{\mathrm{KM,f}}(\vec{\boldsymbol{y}}^s,\omega)=\sum_{r=1}^{N}\sum_{s=1}^{N}\overline{D\left[\widehat{\Pi}(\vec{\boldsymbol{x}}_s,\vec{\boldsymbol{x}}_r;\omega)\right]}\widehat{G}(\vec{\boldsymbol{y}}^s,\vec{\boldsymbol{x}}_r)\widehat{G}(\vec{\boldsymbol{y}}^s,\vec{\boldsymbol{x}}_s), \tag{2.14}$$

which is essentially Equation (2.4), derived by replacing the full response matrix by its filtered version. Also, we introduce the functional

$$\mathcal{I}_J^{\mathrm{KM}}(\vec{\boldsymbol{y}}^s,\omega)=\sum_{r=1}^{N}\sum_{s=1}^{N}\overline{\left(\sigma_J\,\mathcal{U}_J\mathcal{V}_J^*\right)}_{rs}\widehat{G}(\vec{\boldsymbol{y}}^s,\vec{\boldsymbol{x}}_r)\widehat{G}(\vec{\boldsymbol{y}}^s,\vec{\boldsymbol{x}}_s), \tag{2.15}$$

which is derived from (2.14) when $d_J=1$ and $d_i=0$ for all $i\neq J$; in other words, when we consider projection on the single $J$-th singular vector of the array response matrix.

### 2.3.2 Selective imaging with $\widetilde{\mathcal{I}}^{\mathrm{KM,f}}$

We also introduce functionals for selective imaging using filtered versions of $\widehat{\mathbb{P}}$, as we have done in (2.14) and (2.15). Specifically, for a single frequency $\omega$, we define

$$\widetilde{\mathcal{I}}^{\mathrm{KM,f}}(\vec{\boldsymbol{y}}^{\mathrm{s}},\omega)=\sum_{m,n=1}^{M}\overline{\left(D[\widehat{\mathbb{P}}(\omega)]\right)}_{mn}\widetilde{G}_m(\vec{\boldsymbol{x}}_s,\vec{\boldsymbol{y}}^{\mathrm{s}})\widetilde{G}_n(\vec{\boldsymbol{x}}_s,\vec{\boldsymbol{y}}^{\mathrm{s}}). \tag{2.16}$$

and

$$\widetilde{\mathcal{I}}_J^{\mathrm{KM}}(\vec{\boldsymbol{y}}^{\mathrm{s}},\omega)=\sum_{m,n=1}^{M}\overline{\left(\sigma_J\,\mathcal{U}_J\mathcal{V}_J^*\right)}_{mn}\widetilde{G}_m(\vec{\boldsymbol{x}}_s,\vec{\boldsymbol{y}}^{\mathrm{s}})\widetilde{G}_n(\vec{\boldsymbol{x}}_s,\vec{\boldsymbol{y}}^{\mathrm{s}}), \tag{2.17}$$

where by abusing slightly the notation we now denote by $\sigma_J\,\mathcal{U}_J\mathcal{V}_J^*$ the projection on the $J$-th singular vector of $\widehat{\mathbb{P}}$.

### 2.3.3 Comparison between $\mathcal{I}_J^{\mathrm{KM}}$ and $\widetilde{\mathcal{I}}_J^{\mathrm{KM}}$

In this subsection, we will test how the two selective imaging functionals perform. We consider the case of a semicircular scatterer, as the one shown in the previous section. Recalling the results shown on the rightmost column of Figure 2.6, both $\mathcal{I}^{\mathrm{KM}}$, shown on top, and $\widetilde{\mathcal{I}}^{\mathrm{KM}}$ on the bottom, locate the scatterer but fail to recreate its whole support. We

will now use the selective imaging technique discussed earlier, in hopes of recovering more information about the scatterer.

To recall the setup, we have a semiricular scatterer, of diameter $b = 2\lambda_0$, centered at $x^\star = (19, 5)\lambda_0$ and use a bandwidth around a single frequency $f_c$ that corresponds to a wavenumber $k = 0.975k_0$, with $B \simeq 0.14f_c$. To give a sense of how the singular values of the response matrix behave, we plot on Figure 2.7 the singular values (normalized by the largest one), of the response matrix $\widehat{\Pi}$ on the left and of $\widehat{\mathbb{P}}$ on the right, for the central frequency $f_c$. We have only a few singular values that are practically non-zero. In the next chapter we will derive a relation between the size of the object and the number of non-zero singular values of $\widehat{\mathbb{P}}$ for the screen problem. Specifically, for the vertical screen problem we will show that the number of significant sv's is the size of the object divided by the size of the point-spread function, or in other words, the array's resolution length.

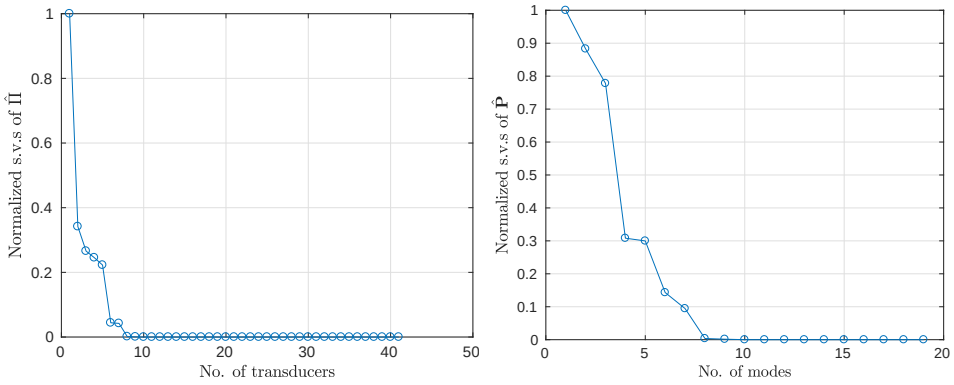


Figure 2.7: Normalized singular values of $\widehat{\Pi}$ (left subplot) and $\widehat{\mathbb{P}}$ (right subplot) for a semicircular scatterer with diameter $\delta = 40$ m, for the central frequency $f_c$.

In Figure 2.8 we present the results of selective imaging with $\mathcal{I}_J^{\mathrm{KM}}$ on the top row and $\widetilde{\mathcal{I}}_J^{\mathrm{KM}}$ on the bottom row, for $J = 1, 2, 3, 4$, shown from left to right. For $J = 1$, $\mathcal{I}_J^{\mathrm{KM}}$ appears noisy and has two main lobes near the leftmost part of the scatterer (which we will call center) and two smaller ones close to the scatterer's edges. On the other hand $\widetilde{\mathcal{I}}_J^{\mathrm{KM}}$, has a clear focus on the center. For $J = 2$, we have two similar images for both functionals, focusing close to the center. Next, for $J = 3$, imaging with $\mathcal{I}_J^{\mathrm{KM}}$ loses its target, as the maxima are located away from the scatterer, while $\widetilde{\mathcal{I}}_J^{\mathrm{KM}}$ has shifted its focus futher away from the center. Lastly, for $J = 4$, $\mathcal{I}_J^{\mathrm{KM}}$ has a clear focus on the center of the scatterer, while $\widetilde{\mathcal{I}}_J^{\mathrm{KM}}$ towards the endpoints of the vertical diameter. We do not display any images for the next singular vectors, since they do not carry any information about the object.

As a first comment, note that selective imaging with $\widetilde{\mathcal{I}}^{\mathrm{KM}}$ exhibits the behaviour presented in [10] for the free space case. Specifically, it was shown that when using a filtered version of the response matrix that corresponds to the larger singular values, the resulting image focuses mainly at the center of the scatterer, while as we use the lower singular values, the focus of the image shifts towards the scatterer's edges. This, however does not seem to be the case when imaging with $\mathcal{I}_J^{\mathrm{KM}}$.

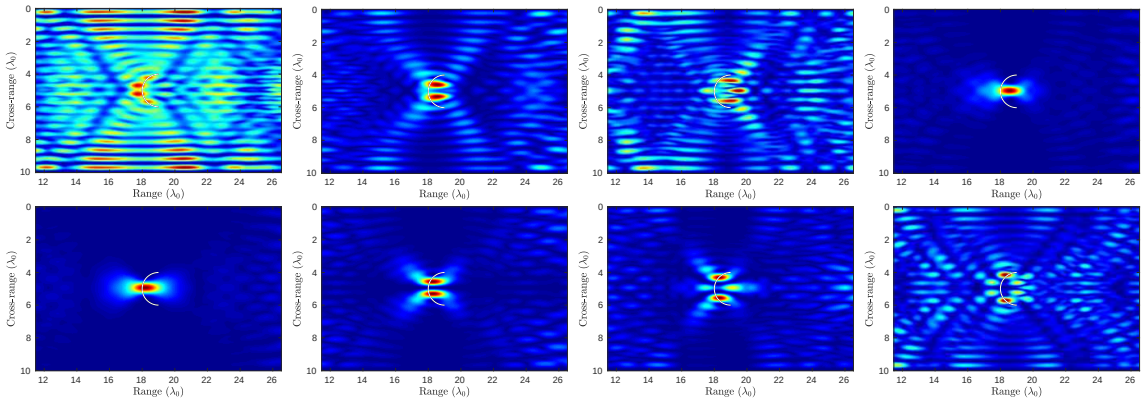


Figure 2.8: Imaging with $\mathcal{I}_J^{\mathrm{KM}}$ (top) and $\widetilde{\mathcal{I}}_J^{\mathrm{KM}}$ (bottom) for a semicircle of diameter $b = 2\lambda_0$, centered at $\vec{\boldsymbol{x}}^\star = (19, 5)\lambda_0$. We use frequencies $f \in [f_c - B/2, f_c + B/2]$ with $f_c = 0.975k_0$ and $B = 0.14f_c$. From left to right, we have $J = 1, 2, 3, 4$.

In order to get a clearer picture about the difference in behavior between the two imaging functionals, we now consider a smaller semicircle, with diameter $b = \lambda_0$. In Figure 2.9 we plot the values of $\mathcal{I}_1^{\mathrm{KM}}$ on the top row and $\widetilde{\mathcal{I}}_1^{\mathrm{KM}}$ on the bottom row. We have on the left a single frequency with $k = 0.988k_0$ and on the right $k = 1.042k_0$. We observe that in both cases, imaging with $\widetilde{\mathcal{I}}_1^{\mathrm{KM}}$ has a clear focus on the center of the scatterer, as opposed to $\mathcal{I}_1^{\mathrm{KM}}$ that focuses on the center on the left image, while it shifts its focus to the edges on the right image. This lack of robustness in the $\mathcal{I}^{\mathrm{KM}}$ images is what initially motivated us to work with $\widetilde{\mathcal{I}}^{\mathrm{KM}}$.

For the rest of this work that concerns the infinite waveguide setup, we will only consider imaging with $\widetilde{\mathcal{I}}^{\mathrm{KM}}$. In the next chapter, we will consider the imaging problem of a vertical screen, in order examine in depth the properties of the projected response matrix $\widehat{\mathbb{P}}$ and, in turn, of the imaging functional $\widetilde{\mathcal{I}}^{\mathrm{KM}}$. From the analysis we will perform, we will also understand and characterize the focusing behavior of $\widetilde{\mathcal{I}}_J^{\mathrm{KM}}$.

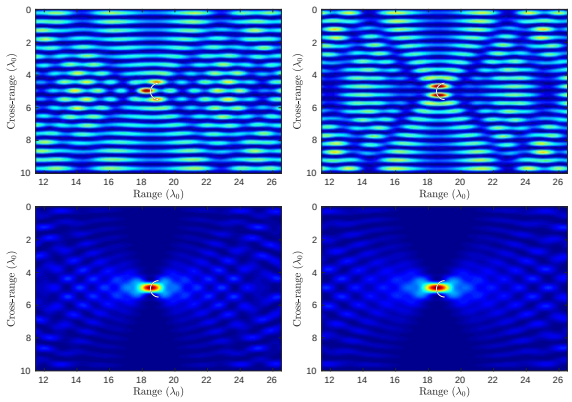


Figure 2.9: Imaging with $\mathcal{I}_1^{\mathrm{KM}}$ (top) and $\widetilde{\mathcal{I}}_1^{\mathrm{KM}}$ (bottom) for a semicircle of diameter $b = \lambda_0$, centered at $\vec{\boldsymbol{x}}^\star = (19, 5)\lambda_0$. We use a single frequency with $k = 0.988k_0$ (left) and $k = 1.042k_0$ (right).

# Chapter 3

# Model problem: Imaging a vertical screen

In the previous chapter, we described the imaging problem and presented a widely used imaging method, the Kirchhoff migration, which we denoted by $\mathcal{I}^{\text{KM}}$. We also introduced an alternative imaging method, based on the weighted modal projection of the array response matrix, denoted by $\widetilde{\mathcal{I}}^{\text{KM}}$, which seemed to outperform $\mathcal{I}^{\text{KM}}$, in terms of the image's quality. Furthermore, selective imaging with $\widetilde{\mathcal{I}}^{\text{KM}}$ allows us to better characterize the geometry and shape of the reflector since projection on the first singular vector focuses the image at the center of the reflector, while projection on subsequent singular vectors results in images that are focusing towards the edges of the reflector.

In this chapter, we consider the model problem of imaging a vertical screen. We begin with the full aperture case where the array covers the entire cross-section of the waveguide. In this case we analyze the spectral properties of the projected response matrix $\widehat{\mathbb{P}}$ and derive a relation between its singular vectors and the prolate spheroidal wave functions, that were studied in a series of papers by Slepian, Landau and Pollak, [40, 41, 55, 56, 58]. Second, we use this analysis to adequately define $\widetilde{\mathcal{I}}^{\text{KM}}$ for an array that only partially covers the waveguide's aperture. We also examine the performance of $\widetilde{\mathcal{I}}^{\text{KM}}$ with full and partial data, in another model problem where the scatterer is a semicircle.

## 3.1 Full aperture case

In this section we examine a simplified model problem in order to gain some insight about the properties of the projected response matrix $\widehat{\mathbb{P}}$, see (2.9). In a homogeneous waveguide that forms an infinite strip we assume that the array passes through the $x$ axis, and that $N$ transducers that span the whole depth of the waveguide are located equidistantly at depths $x_i = ih$, $1 \le i \le N$, where $h := D/(N+1)$. The scatterer $\mathcal{T}$ is a one-dimensional vertical mirror, a 'screen', located at range $z = L$, see Figure 3.1. Let the coordinates of its endpoints be $(L, \alpha)$ and $(L, \beta)$, hence its width equals $b = \beta - \alpha$.

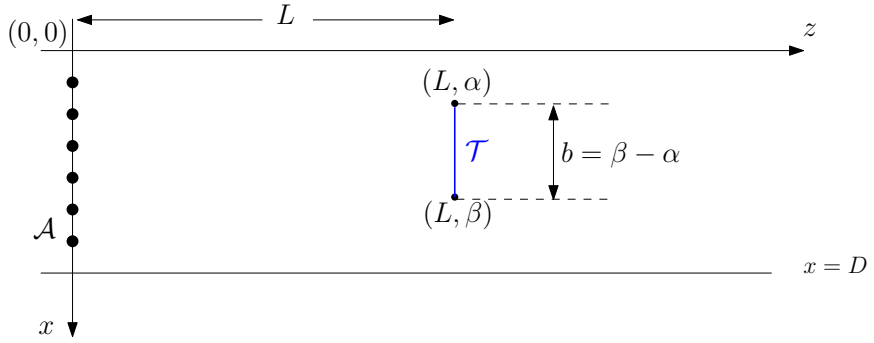


Figure 3.1: Sketch of a one-dimensional vertical scatterer ('screen') $\mathcal{T}$ and basic notation.

### 3.1.1 The weighted projected response matrix $\widehat{\mathbb{P}}$

As already seen in the previous chapter, the response matrix for the model problem is given (see (2.7)) by

$$\widehat{\Pi}(\vec{\boldsymbol{x}}_s, \vec{\boldsymbol{x}}_r; \omega) = \int_{\mathcal{T}} \widehat{G}(\vec{\boldsymbol{y}}, \vec{\boldsymbol{x}}_s) \widehat{G}(\vec{\boldsymbol{x}}_r, \vec{\boldsymbol{y}})\, d\vec{\boldsymbol{y}}. \tag{3.1}$$

We insert the expression (1.15) for the Green's function into (3.1) and we get that

$$\widehat{\Pi}(\vec{\boldsymbol{x}}_r; \vec{\boldsymbol{x}}_s, \omega) = -\frac{1}{4} \sum_{m,n=1}^{\infty} \frac{\mathrm{e}^{\mathrm{i}\beta_m L}}{\beta_m} X_m(x_s) X_n(x_r) \frac{\mathrm{e}^{\mathrm{i}\beta_n L}}{\beta_n} \int_{\alpha}^{\beta} X_m(x) X_n(x) dx. \tag{3.2}$$

However, for $L$ sufficiently large and $m \ge M+1$ it holds that

$$\mathrm{e}^{\mathrm{i}\beta_m L} = \mathrm{e}^{-\sqrt{\mu_m - k^2} L} \approx 0,$$

therefore, in practice, in each one of the infinite series shown above, only the first $M$ terms are retained, hence $\widehat{\Pi}$ can be approximated by

$$\widehat{\Pi}(\vec{\boldsymbol{x}}_r;\vec{\boldsymbol{x}}_s,\omega) = -\frac{1}{4}\sum_{m,n=1}^{M}\frac{\mathrm{e}^{\mathrm{i}\beta_m L}}{\beta_m}X_m(x_s)X_n(x_r)\frac{\mathrm{e}^{\mathrm{i}\beta_n L}}{\beta_n}\int_\beta^\alpha X_m(x)X_n(x)dx, \tag{3.3}$$

where by abuse of notation we use the same symbol $\widehat{\Pi}$ for this approximate array response matrix. Obviously $\widehat{\Pi}$ may be equivalently written as a matrix product of the form

$$\widehat{\Pi} = -\frac{1}{4}\,V\,D_\beta\,Q\,A_M\,Q\,D_\beta\,V^T, \tag{3.4}$$

where

$$D_\beta = \mathrm{diag}(1/\beta_1,\ldots,1/\beta_M), \quad Q = \mathrm{diag}(\mathrm{e}^{\mathrm{i}\beta_1 L},\ldots,\mathrm{e}^{\mathrm{i}\beta_M L}), \tag{3.5}$$

$V$ is the $N\times M$ matrix with

$$V_{k\ell} = X_\ell(x_k), \quad k=1,\ldots,N, \ell=1,\ldots,M, \tag{3.6}$$

and $A_M$ is the matrix with entries

$$a_{mn} = \int_\alpha^\beta X_m(x)X_n(x)dx, \quad m,n=1,2,\ldots,M. \tag{3.7}$$

Also, if we recall the expression for the weighted projected response matrix $\widehat{\mathbb{P}}$,

$$\widehat{\mathbb{P}}_{mn} = \beta_m\beta_n\int_0^D \mathrm{d}x_s\int_0^D \mathrm{d}x_r\,\widehat{\Pi}(\vec{\boldsymbol{x}}_s,\vec{\boldsymbol{x}}_r,\omega)X_m(x_s)X_n(x_r), \tag{3.8}$$

we may approximate the double integral by a composite trapezoidal rule to the partition of $[0,D]$ that is induced by the transducers' depths $x_i$, $i=1,\ldots,N$. Hence, in the discrete level, we define the weighted projected response matrix $\widehat{\mathbb{P}}$ as

$$\widehat{\mathbb{P}} = h^2 D_\beta^{-1}\;V^T\;\widehat{\Pi}\;V\;D_\beta^{-1}. \tag{3.9}$$

### 3.1.2 Unitary equivalence between $\widehat{\mathbb{P}}$ and $A_M$

In this subsection, we want to examine the spectral properties of the projected response matrix $\widehat{\mathbb{P}}$. We start with the following proposition:

**Proposition 4** *Let $V$ be the $N \times M$ matrix defined in (3.6), with $N \geq M$ and $h = D/(N+1)$ be the inter-element distance. Then it holds that*

$$hV^T V = I_M. \tag{3.10}$$

**Proof.** To prove (3.10), it suffices to show that

$$\begin{aligned} h\sum_{k=1}^{N} X_m(x_k)X_n(x_k) &= \delta_{mn}, \quad \forall m,n = 1,\dots,M \\ \frac{2h}{D}\sum_{k=1}^{N} \sin\left(\frac{m\pi x_k}{D}\right)\sin\left(\frac{n\pi x_k}{D}\right) &= \delta_{mn}, \quad \forall m,n = 1,\dots,M \end{aligned} \tag{3.11}$$

where $x_k = kh$, $1 \leq k \leq N$, and $h := D/(N+1)$. We add the point $x_0 = 0$ in the discretization, hence (3.11) is equivalent to

$$\frac{2}{N+1}\sum_{k=0}^{N} \sin\left(\frac{m\pi k}{N+1}\right)\sin\left(\frac{n\pi k}{N+1}\right) = \delta_{mn}. \tag{3.12}$$

The left-hand side of (3.12) may be seen as a discrete sine transform or, equivalently, as the imaginary part of a discrete Fourier transform (DFT) and therefore (3.12) results from the well-known orthogonality property of the DFT. □

Following this, if we insert (3.4) into (3.9), we have that $\widehat{\mathbb{P}}$ is related to the matrix $A_M$ as follows

$$\widehat{\mathbb{P}} = -\frac{1}{4} Q A_M Q. \tag{3.13}$$

It is trivial to check that $Q$, given by (3.5), is a unitary matrix, *i.e.* $Q^*Q = QQ^* = I_M$. Hence, up to a multiplicative constant, $\widehat{\mathbb{P}}$ is unitarily equivalent to $A_M$. Therefore, the spectral properties of $A_M$ play an important role in understanding the behavior of the imaging functional $\widetilde{\mathcal{I}}^{\text{KM}}$.

### 3.1.3 Spectral properties of $A_M$

Having proven the unitary equivalence between $\widehat{\mathbb{P}}$ and $A_M$, we wish to examine the spectral properties of $A_M$, in order to gain more insight on the behavior of $\widetilde{\mathcal{I}}^{\text{KM}}$ and $\widetilde{\mathcal{I}}_J^{\text{KM}}$. In this subsection, we will show that $A_M$ has a special structure; it is a Toeplitz-minus-Hankel matrix. This allows us to study the distribution of its singular values and its relation with

the size of the scatterer.

**The Toeplitz-minus-Hankel structure**

For $\ell, m = 1, \ldots, M$, and in view of the simple trigonometric identity $2 \sin a \sin b = \cos(a - b) - \cos(a + b)$, it holds that

$$\begin{aligned} a_{\ell m} &= \int_\alpha^\beta X_\ell(x) X_m(x) dx = \frac{2}{D} \int_\alpha^\beta \sin \frac{\ell \pi x}{D} \sin \frac{m \pi x}{D} dx \\ &= \frac{1}{D} \int_\alpha^\beta \cos \frac{(\ell - m)\pi x}{D} dx - \frac{1}{D} \int_\alpha^\beta \cos \frac{(\ell + m)\pi x}{D} dx \\ &= \frac{1}{(l-m)\pi} \left( \sin \frac{(l-m)\pi\beta}{D} - \sin \frac{(l-m)\pi\alpha}{D} \right) \\ &- \frac{1}{(l+m)\pi} \left( \sin \frac{(l+m)\pi\beta}{D} - \sin \frac{(l+m)\pi\alpha}{D} \right), \end{aligned} \tag{3.14}$$

where, of course, it is understood that for $l = m$ the term $\frac{1}{(l-m)\pi} \left( \sin \frac{(l-m)\pi\beta}{D} - \sin \frac{(l-m)\pi\alpha}{D} \right)$ takes the value $(\beta - \alpha)/D$.

Hence

$$A_M = T_M - H_M, \quad \text{where} \quad T_M := (t_{\ell - m})_{\ell,m=1}^M, \quad H_M := (t_{\ell + m})_{\ell,m=1}^M,$$

and

$$t_m = \frac{1}{D} \int_0^D \mathbb{1}_{\mathcal{T}}(x) \cos \frac{m \pi x}{D} dx, \tag{3.15}$$

where $\mathbb{1}_{\mathcal{T}}(x)$ is the indicator function of $\mathcal{T}$. Note that $\mathbb{1}_{\mathcal{T}}(x)$ is the so-called *generating function* of the matrices $A_M$, $T_M$ and $H_M$. One may immediately recognize $T_M$ as a (real symmetric) Toeplitz matrix, i.e., a matrix with constant entries along the diagonals, and $H_M$ as a Hankel matrix, i.e., a matrix with constant skew-diagonals (these are the diagonals that are perpendicular to the main diagonal). Hence $A_M$ has a special structure: It is a *Toeplitz–minus–Hankel* matrix.

**Distribution of the singular values of $A_M$**

As we shall briefly discuss next, the spectral properties of $A_M$ are determined by the Toeplitz part $T_M$. This can be seen, for example, by modifying appropriately the proofs in the work of Fasino [24], who studies the spectral properties of Toeplitz-plus-Hankel matrices, or by

tracing back to the work of Trench [59], who studies the spectral properties of the *real symmetric Toepliz* matrix

$$T_n = (t_{r-s})_{r,s=1}^{n}, \quad \text{where } t_r = \frac{1}{\pi}\int_0^{\pi} f(x)\cos rx\, dx,$$

and the generating function $f \in L^2[0,\pi]$.

Now, in the following definition we introduce some notation that is fairly standard, see *e.g.* [2, 59].

**Definition 1** *Let $\mathbb{J}$ be the flip matrix (i.e. the matrix that has ones on the secondary diagonal and zeros elsewhere). Then, a vector $\boldsymbol{x} \in \mathbb{R}^n$ is called symmetric if $\mathbb{J}\boldsymbol{x} = \boldsymbol{x}$ and skew-symmetric if $\mathbb{J}\boldsymbol{x} = -\boldsymbol{x}$. Moreover, an eigenvalue $\nu$ of a matrix $T$ is defined to be even (odd) if $T$ has a symmetric (skew-symmetric) $\nu$–eigenvector.*

Now, let $\lambda_1^{(n)} \le \lambda_2^{(n)} \le \cdots \le \lambda_n^{(n)}$ be the eigenvalues of $T_n$, and let $\nu_1^{(n)} \le \nu_2^{(n)} \le \cdots \le \nu_n^{(n)}$ be the eigenvalues of $A_n$. Since, in our case, the generating function $f$ of the matrices $A_n$, $T_n$, and $H_n$, is the indicator function of $\mathcal{T}$, its essential lower and upper bounds are simply 0 and 1, respectively. A result of Szegő [31, pp. 64-65], guarantees that:

(i) $0 \le \lambda_i^{(n)} \le 1$ for all $i = 1, \ldots, n$,

(ii) for any fixed integer $k$, $\lambda_k^{(n)} \to 0$, $\lambda_{n-k}^{(n)} \to 1$ as $n \to \infty$, and

(iii) if $G$ is any continuous function defined in [0,1], we have

$$\lim_{n\to\infty} \frac{1}{n}\sum_{i=1}^{n} G(\lambda_i^{(n)}) = \frac{1}{D}\int_0^{D} G(f(x))dx. \tag{3.16}$$

Moreover, the following theorem specializes results stated in [59] to our case, where we work on $[0, D]$, the entries of our matrix are given in (3.15), and $f = \mathbb{1}_{\mathcal{T}}$.

**Theorem 1** *(a) The odd eigenvalues $\kappa_1^{(2n+1)} \le \kappa_2^{(2n+1)} \le \cdots \le \kappa_n^{(2n+1)}$ of $T_{2n+1}$ are the eigenvalues of $A_n$ [59, Thm. 2].*

*(b) Since $f$ is bounded, the sets $\{\lambda_i^{(n)}\}_{i=1}^n$ and $\{\kappa_i^{(2n+1)}\}_{i=1}^n$ are absolutely equally distributed [59, Def. 1, Th. 5], i.e.*

$$\lim_{n\to\infty} \frac{1}{n}\sum_{i=1}^{n} \left| G\left(\kappa_i^{(2n+1)}\right) - G\left(\lambda_i^{(n)}\right)\right| = 0.$$

(c) *Since $f$ is bounded, (3.16) also holds for $\nu_i^{(n)}$ instead of $\lambda_i^{(n)}$. Moreover, if for $\epsilon > 0$ $C(\epsilon, 1-\epsilon, n)$ is the cardinality of the set $\{i : \epsilon \le \kappa_i^{(2n+1)} \le 1-\epsilon\}$, then*

$$\lim_{n\to\infty} \frac{1}{n} C(\epsilon, 1-\epsilon, n) = 0$$

[59, Lem. 2 and Thm. 6].

**Relation between the number of 'significant singular values' and size of the object**

Summarizing, the eigenvalues of the matrix $A_n$ (which are the odd eigenvalues of $T_{2n+1}$) are clustered near 0 and 1, and considering the function $G$ to be the identity on $[0,1]$, we immediately see that

$$\lim_{n\to\infty} \frac{1}{n} \sum_{i=1}^{n} \nu_i^{(n)} = \frac{1}{D} \int_0^D \mathbb{1}_{\mathcal{T}}(x)\, dx = \frac{b}{D}.$$

This indicates that asymptotically, as $n \to \infty$, the ratio of the nonzero eigenvalues of $A_n$ to the total number of eigenvalues is equal to $b/D$. In our case, where $n$ is equal to the number of propagating modes $M = \left\lfloor \frac{2D}{\lambda} \right\rfloor$, it is expected that the number of 'significant' singular values for our matrix $A_M$ is

$$\left[ M \frac{b}{D} \right] \approx \left[ \frac{2b}{\lambda} \right], \tag{3.17}$$

where $\lambda$ is the wavelength.

Therefore, we have shown that the number of nonzero singular values is related to the size of the object. In particular, by performing a standard resolution analysis (see Chapter 4), one may deduce that the cross-range resolution is $\lambda/2$, hence the rank of the matrix $A_M$ and, consequently, of $\widehat{\mathbb{P}}$, is roughly equal to the size of the object divided by the "array resolution." The same result has been obtained in the free-space case (see [10, §4.5.2]).

Moreover, if $\boldsymbol{u} = (u^1, \ldots, u^M)^T$ is an orthonormal eigenvector of $A_M$ that corresponds to an eigenvalue $\nu$, then

$$\boldsymbol{v} = 2^{-1/2} \begin{pmatrix} -\mathbb{J}\boldsymbol{u} \\ 0 \\ \boldsymbol{u} \end{pmatrix} = 2^{-1/2} (-u_M, \ldots, -u_1, 0, u_1, \ldots, u_M)^T \tag{3.18}$$

is an orthonormal skew-symmetric $\nu$–eigenvector of $T_{2M+1}$, and vice versa. We shall say that eigenvectors that correspond to eigenvalues that are close to 1 comprise the *signal subspace*, those that correspond to eigenvalues that are close to 0 comprise the *noise subspace*, and, finally, the eigenvectors that correspond to intermediate eigenvalues form the *transient subspace*.

### 3.1.4 Properties of $\widetilde{\mathcal{I}}_J^{\mathrm{KM}}$ at the correct range

Next, we consider the imaging functional $\widetilde{\mathcal{I}}_J^{\mathrm{KM}}$ evaluated at a search point $\vec{\boldsymbol{y}}^{\mathrm{s}} = (L, x^{\mathrm{s}})$ that is located at the correct range $L$. Note that the subscript $J$ indicates that for selective imaging only the $J$-th singular vector is employed in the approximation of the matrix $\widehat{\mathbb{P}}$.

Using the fact that $A_M$ is a real symmetric matrix and by evaluating (2.17) at the correct range, we have that

$$\widetilde{\mathcal{I}}_J^{\mathrm{KM}}(\vec{\boldsymbol{y}}^{\mathrm{s}}) = \sigma_J \left( \frac{1}{4h} \sum_{n=1}^{M} u_n^J X_n(x^{\mathrm{s}}) \right)^2 = (8Dh^2)^{-1} \sigma_J \left( \sum_{n=1}^{M} u_n^J \sin \frac{n\pi x^{\mathrm{s}}}{D} \right)^2, \tag{3.19}$$

where $\boldsymbol{u}^J = (u_1^J, u_2^J, \ldots, u_M^J)^T$ is the singular vector of $A_M$ that corresponds to the singular value $\sigma_J$. Hence, the $\widetilde{\mathcal{I}}_J^{\mathrm{KM}}$ functional at the correct range is in fact, up to a constant, the square of the trigonometric polynomial

$$p_J(x) = \sum_{n=1}^{M} u_n^J X_n(x) = (2/D)^{1/2} \sum_{n=1}^{M} u_n^J \sin \frac{n\pi x}{D}. \tag{3.20}$$

Moreover, we may prove the following proposition:

**Proposition 5** *The trigonometric polynomial $p_1$ that corresponds to the first singular vector $\boldsymbol{u}^1$ and, consequently, the associated image computed at the correct range $L$, exhibits the largest fractional concentration of energy in $(\alpha, \beta)$, among all polynomials $p_J$, $J = 1, \ldots, M$.*

**Proof:**

$$\frac{\|p_J\|^2_{L^2[\alpha,\beta]}}{\|p_J\|^2_{L^2[0,D]}} = \frac{\displaystyle\int_\alpha^\beta p_J^2(x)\,dx}{\displaystyle\int_0^D p_J^2(x)\,dx} \overset{(3.20)}{=} \frac{\displaystyle\int_\alpha^\beta \left(\sum_{n=1}^M u_n^J X_n(x)\right)^2 dx}{\displaystyle\int_0^D \left(\sum_{n=1}^M u_n^J X_n(x)\right)^2 dx}$$

$$= \frac{\displaystyle\sum_{m=1}^M\sum_{n=1}^M u_m^J u_n^J \int_\alpha^\beta X_m(x)X_n(x)\,dx}{\displaystyle\sum_{m=1}^M\sum_{n=1}^M u_m^J u_n^J \underbrace{\int_0^D X_m(x)X_n(x)\,dx}_{=\delta_{mn},\text{due to orthonormality}}} \overset{(3.7)}{=} \frac{\displaystyle\sum_{m=1}^M u_m^J \sum_{n=1}^M (A_M)_{mn}\, u_n^J}{\displaystyle\sum_{m=1}^M (u_m^J)^2}$$

$$= \frac{\sigma_J \displaystyle\sum_{m=1}^M (u_m^J)^2}{\displaystyle\sum_{m=1}^M (u_m^J)^2} = \sigma_J.$$

□

### 3.1.5 Connection between the singular vectors of $A_M$ and the prolate spheroidal wave functions

Now we are in a position to scrutinize the form of the singular vectors of the matrix $A_M$. In [61] we have derived some analytic expressions for those singular vectors which correspond to singular values that are close to 1. In the remaining part of the section we provide explicit characterizations for the singular vectors of $A_M$ depending on the various positions of the screen.

#### A screen attached on the top of the waveguide

**Proposition 6** *Assume that the screen is attached on the top of the waveguide, i.e.* $\mathcal{T} = \{(L,x) : \ x \in [0,b]\}$. *Then the eigenvectors of the matrix* $A_M$ *may be recovered from the skew-symmetric discrete prolate spheroidal sequence (DPSS), [56], (also known as a Slepian sequence), where we remind that skew-symmetry, according to Definition 1, implies that* $u^J_{-i} = -u^J_i$, $i = 1,\dots,M$.

**Proof:** Equation (3.14) implies that in the case where the screen is attached on the top of the waveguide, *i.e.* $\alpha = 0$ and $\beta = b$, the matrix $A_M$ has entries

$$a_{mn} = \frac{1}{(m-n)\pi} \sin \frac{(m-n)\pi b}{D} - \frac{1}{(m+n)\pi} \sin \frac{(m+n)\pi b}{D}, \tag{3.21}$$

that obviously manifest its Toeplitz-minus-Hankel structure. Therefore, from the discussion below Theorem 1, we deduce that its eigenvectors are recovered from the skew-symmetric eigenvectors of the $(2M+1) \times (2M+1)$ Toeplitz matrix $T_{2M+1}$, which satisfy

$$\sum_{n=-M}^{M} \frac{1}{(m-n)\pi} \sin \frac{(m-n)\pi b}{D} u_n^J = \nu_J u_m^J, \quad m = -M, \ldots, M.$$

Skew-symmetry implies that $u_{-i}^J = -u_i^J$, $i = 1, \ldots, M$, therefore $\{u_i^J\}_{i=-M}^M$ is identified as a skew-symmetric *discrete prolate spheroidal sequence (DPSS)*, see [56, Section 2.2], (also known as a *Slepian sequence*). □

Let us remark here that this DPSS is a discrete analog of the *prolate spheroidal wave function (PSWF)* $\psi_{2J-1}$, [58]. Specifically, $\psi_n$ is the eigenfunction that corresponds to the $n$-th eigenvalue of the Fredholm integral equation

$$\int_{-1}^{1} \frac{\sin c(x-y)}{\pi(x-y)} \psi_n(y)\, dy = \nu_n \psi_n(x), \quad x \in [-1, 1], \tag{3.22}$$

where, in our case, the so-called bandwidth parameter is $c = 2\pi b/\lambda = bk$, $k$ being the wavenumber. The PSWFs possess many interesting properties, see *e.g.* [45,57,58]. Here we just name two:

(i) The eigenvalues are discrete and form a decreasing sequence $\nu_0 > \nu_1 > \ldots$ that tends to zero as $n \to \infty$, and

(ii) the corresponding eigenfunctions $\psi_n(x)$ are even or odd with $n$.

**Remark 5** *The trigonometric polynomial $p_J(x)$ defined in (3.20) behaves like the PSWF $\psi_{2J-1}$ apart from a horizontal stretching.*

**Proof:** Consider the trigonometric polynomial $p_J(x) = (2/D)^{1/2} \sum_{n=1}^{M} u_n^J \sin \frac{n\pi x}{D}$, $x \in [0, D]$, $J = 1, 2, \ldots, M$. Letting $y_n = \frac{\lambda n}{2D}$ ($\lambda$ is the wavelength), we may interpret the

trigonometric polynomial $p_J$ as a Riemann sum that approximates the integral

$$\frac{2\sqrt{2D}}{\lambda}\int_0^1 \psi_{2J-1}(y)\sin(\xi y)\,dy = \frac{\sqrt{2D}}{i\lambda}\int_{-1}^1 \psi_{2J-1}(y)e^{i\xi y}\,dy$$
$$= \gamma_{2J-1}\psi_{2J-1}\Big(\frac{x}{b}\Big), \quad x\in[0,D],$$

where $\xi := 2\pi x/\lambda = kx$. Note that the first equality holds since $\psi_{2J-1}$ is an odd function in $[-1,1]$, while the second equality reflects the interesting property that the Fourier transform of a PSWF restricted to $[-1,1]$ is invariant except for a horizontal stretching, [57, Eq. (24)]; also notice that $\gamma_{2J-1}$ is independent of $x$. □

In order to illustrate these conclusions assume a reference wavenumber $k_0 = \pi/10$ that corresponds to a reference wavelength $\lambda_0$ and we consider a waveguide with depth equal to $D = 10\lambda_0$ and constant sound speed $c_0$. We use a single frequency with associated wavenumber $k = 0.975k_0$ and the screen's width equals $b = 2\lambda_0$. Then, $M = 19$ modes propagate in the waveguide and according to (3.17) we expect $A_M$ to possess four 'significant' singular values. Indeed, the first three lie close to 1, the fourth is approximately 0.62, the fifth one is approximately equal to 0.04, while the rest are less than $4\times10^{-4}$ and decrease rapidly to zero. In Figure 3.2 we superimpose the graph of the trigonometric polynomial $(p_J(x))^2$ on the graph of the PSWF $\Big(\psi_{2J-1}\big(\frac{x}{b}\big)\Big)^2$, both normalised with respect to their maximum values, for $x\in[0,D]$, and for $J = 1,2,\ldots,6$.

As expected, these functions for $J = 1$ to 4 are mainly supported in $[0,b] = [0,2\lambda_0]$, while for $J = 5$ and 6 they are mostly supported in the exterior of $[0,b]$.

### A screen attached on the bottom of the waveguide

In this case let $\mathcal{T} = \{(L,x) :\ x\in[D-b,D]\}$. Then it is easy to check that the entries of the matrix $A_M$ satisfy

$$a_{mn} = \int_{D-b}^{D} X_m(x)X_n(x)\,dx = (-1)^{m+n}\int_0^b X_m(x)X_n(x)\,dx,$$

and, consequently, if $\boldsymbol{u} = \big(u_i\big)_{i=1}^M$ is a $\nu$-eigenvector of $A_M$ when the screen is attached on the top of the waveguide, then one may show that $\boldsymbol{v} := \big(v_i\big)_{i=1}^M = \big((-1)^{i+1}u_i\big)_{i=1}^M$ is a $\nu$-eigenvector of $A_M$ when the screen is attached on the bottom of the waveguide. Moreover, let us denote, for the moment, $p_J^{\text{top}}(x) = \sum_{n=1}^M u_n^J X_n(x)$ to be the trigonometric

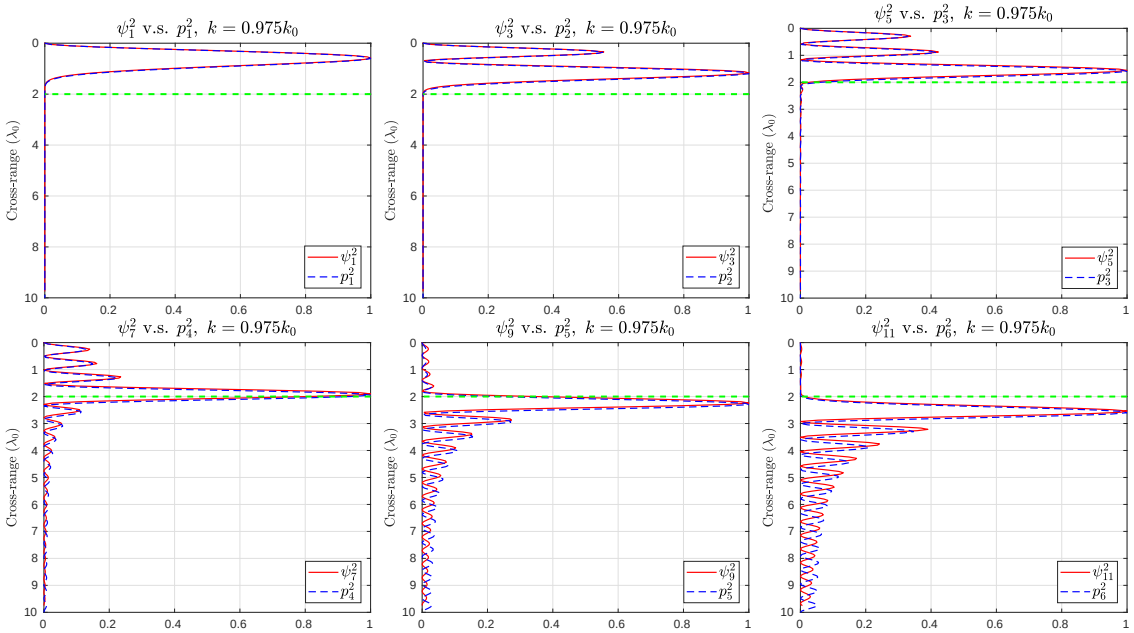


Figure 3.2: The graph of $(p_J(x))^2$ (dashed line printed in blue) superimposed on the graph of $\left(\psi_{2J-1}\left(\frac{x}{b}\right)\right)^2$ (solid line printed in red), for $x \in [0, 10\lambda_0]$. (Both are normalised with respect to their maximum values.) Top row: $J = 1, 2, 3$, bottom row: $J = 4, 5, 6$. The wavenumber $k = 0.975k_0$, and the width of the screen $b = 2\lambda_0$.

polynomial for a screen attached on the top of the waveguide, and $p_J^{\text{bot}}(x) = \sum_{n=1}^{M} v_n^J X_n(x)$ to be the corresponding trigonometric polynomial for a screen attached on the bottom of the waveguide. Then it is easy to show that

$$p_J^{\text{bot}}(x) = p_J^{\text{top}}(D - x),$$

which implies that the image created by the imaging functional $\widetilde{\mathcal{I}}_J^{\text{KM}}$, at the correct range $L$, is determined by the graph of the PSWF $\left(\psi_{2J-1}\left(\frac{D-x}{b}\right)\right)^2$, $x \in [0, D]$.

### A screen located in the interior of the waveguide

In this case let $\mathcal{T} = \{(L, x) : \ x \in [\alpha, \beta] \subset [0, D]\}$. Following the same steps as in the proof of Proposition 6, we have that the eigenvectors of $A_M$ are determined through the skew-symmetric eigenvectors of the matrix $T_{2M+1}$, and (3.14) suggests that they now satisfy

the system of equations

$$\sum_{n=-M}^{M} \frac{1}{(m-n)\pi} \left( \sin \frac{(m-n)\pi\beta}{D} - \sin \frac{(m-n)\pi\alpha}{D} \right) u_n^J = \nu_J u_m^J, \tag{3.23}$$

for $m = -M, \ldots, M$. Equation (3.23) may be viewed as the discrete analog of the following integral equation

$$K_1 u(x) := \int_{-1}^{1} \frac{1}{\pi(x-y)} \left( \sin \frac{2\pi\beta}{\lambda}(x-y) - \sin \frac{2\pi\alpha}{\lambda}(x-y) \right) u(y)\, dy = \nu u(x), \tag{3.24}$$

for $x \in [-1, 1]$, where we have suppressed the index $J$ for notational convenience. Note that the kernel in (3.24) is more complicated than the sinc kernel appearing in (3.22) that concerns the limiting case where the screen is attached on the top of the waveguide. Equation (3.24) has been studied in [53] where the authors consider a time–frequency concentration problem for signals that have a prescribed bandwidth of the form $|w| \in [a, b]$ for $0 < a < b$; thus the frequency interval is not connected any longer. Moreover, for general values of $\alpha$ and $\beta$ ($\alpha < \beta$) the work of Morrison [47], and SenGupta et al. [53], indicates that there cannot be found a second or fourth-order self-adjoint linear differential operator with polynomial coefficients that commutes with the integral operator $K_1$ defined in (3.24). The fact that in the case of Section 3.1.5 the corresponding integral operator commutes with a quite simple second-order differential operator is crucial for the analysis conducted by Slepian and his colleagues at Bell Laboratories, [40, 41, 55, 56, 58].

Therefore we are not able to characterise completely the eigenfunctions of (3.24), as was the case with the the eigenfunctions of (3.22) that were identified as PSWF's. Nevertheless, the integral operator $K_1$ is a compact symmetric operator from $L^2[-1, 1]$ to $L^2[-1, 1]$, hence its eigenvalues $\nu_0 \geq \nu_1 \geq \cdots \geq \nu_n \geq \cdots \to 0$, as $n \to \infty$, while its corresponding eigenfunctions are complete in $L^2[-1, 1]$, [53].

Working as in Section 3.1.5 we may view the trigonometric polynomial

$$p_J(x) = (2/D)^{1/2} \sum_{n=1}^{M} u_n^J \sin \frac{n\pi x}{D}$$

as an approximation of the integral

$$\frac{\sqrt{2D}}{\lambda}\, i \int_{-1}^{1} e^{i\xi y} u(y)\, dy, \quad \xi = 2\pi x/\lambda = kx,$$

where $u$ is an *odd* eigenfunction of the integral equation (3.24) that corresponds to the eigenvalue $\sigma_J$. Interestingly enough, one may follow the lines of SenGupta et al. in [53], in order to prove that

$$\int_{-1}^{1} e^{i\xi y} u(y)\, dy = Cv(x), \quad x \in [0, D],$$

where $v$ is a $\sigma_J$–eigenfunction of the integral equation

$$K_2 v(x) := \int_{\mathcal{J}} \frac{\sin k(x-y)}{\pi(x-y)}\, v(y)\, dy = \nu v(x), \tag{3.25}$$

for $x \in \mathcal{J} := [-\beta, -\alpha] \cup [\alpha, \beta]$. Here we stress the fact that in (3.25), $\mathcal{J}$ is the disconnected interval $[-\beta, -\alpha] \cup [\alpha, \beta]$, while the kernel is a sinc function with bandwidth parameter equal to the wavenumber. Note that $K_2$ is also a compact symmetric operator from $L^2(\mathcal{J})$ to $L^2(\mathcal{J})$, that has the same eigenvalues with (3.24), and its corresponding eigenfunctions are complete in $L^2(\mathcal{J})$, [53].

Hence, the output of the imaging functional $\widetilde{\mathcal{I}}_J^{\mathrm{KM}}$ when it is evaluated at the correct range (see (3.19)) is recovered by the graph of the eigenfunction of (3.25) that corresponds to the eigenvalue $\sigma_J$. Note that the domain of the eigenfunctions $v$ is extended for values of $x$ outside $\mathcal{J}$, as usual, by using the left hand side of (3.25), that is well defined for $x \in \mathcal{J}$, in order to define $v$ for values of $x$ that lie outside $\mathcal{J}$. Specifically, let

$$v(x) = \frac{1}{\nu} \int_{\mathcal{J}} \frac{\sin k(x-y)}{\pi(x-y)}\, v(y)\, dy, \quad x \notin \mathcal{J}.$$

These remarks are illustrated in Figure 3.3 where we superimpose the graph of $p_J^2(x)$ on the graph of the square of the corresponding eigenfunction of (3.25), both normalised with respect to their $L_\infty$–norms. All the physical parameters are the same as those used in Figure 3.2, while the ordinates of the screen's endpoints are $\alpha = 3\lambda_0$, $\beta = 5\lambda_0$, thus the width of the screen is again $b = 2\lambda_0$.

As one may immediately verify there is very good agreement between the graphs of $p_J^2(x)$ and the corresponding eigenfunctions of (3.25) squared. Moreover, notice that, for example, $p_1^2(x)$ that corresponds to the largest eigenvalue (approximately equal to one)

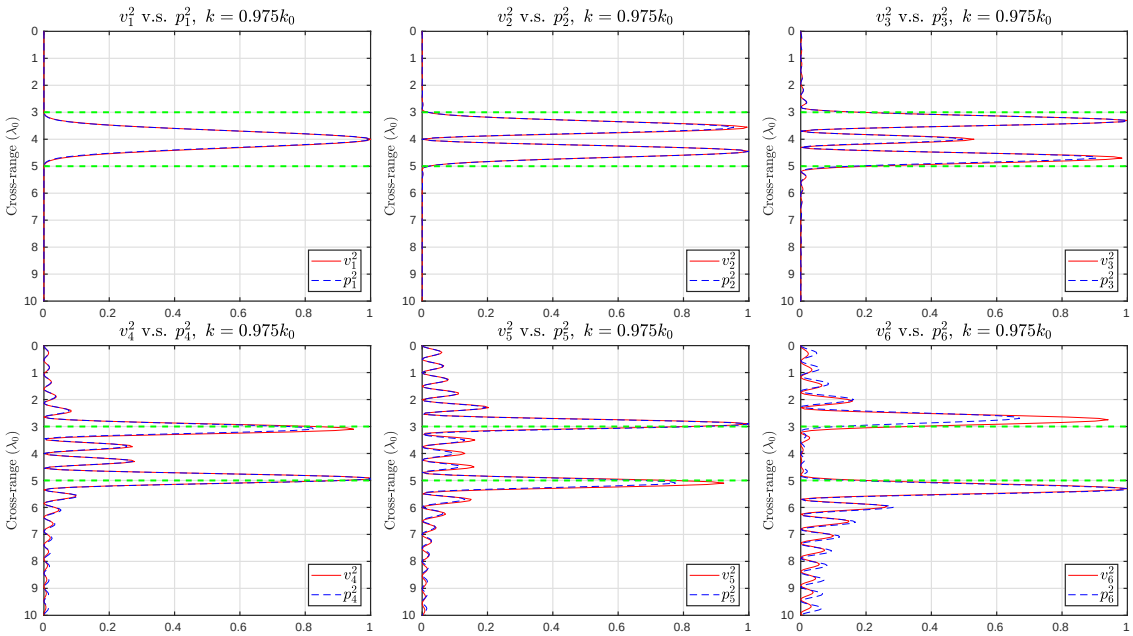


Figure 3.3: The graph of $(p_J(x))^2$ (dashed line printed in blue) superimposed on the graph of the square of the corresponding eigenfunction of (3.25) (solid line printed in red), for $x \in [0, 10\lambda_0]$. (Both are normalised with respect to their maximum values.) The ordinates $\alpha = 3\lambda_0$ and $\beta = 5\lambda_0$ are printed in green dashed lines. Top row: $J = 1, 2, 3$, bottom row: $J = 4, 5, 6$. The wavenumber $k = 0.975k_0$, and the width of the screen $b = 2\lambda_0$.

exhibits a peak around the midpoint of the screen, $p_4^2(x)$ that corresponds to an eigenvalue $\approx 0.640$ peaks near the endpoints of $\mathcal{T}$, while $p_6^2(x)$ that corresponds to an eigenvalue $\approx 0.025$ is practically supported in the exterior of $\mathcal{T}$.

**Remark 6** *We close this section with a discussion concerning possible generalizations of the theory presented here:*

1. *The theory for the considered model problem can be generalized to the three-dimensional case for a waveguide with a bounded rectangular cross-section. In this case, to allow for exploiting tensor product expressions the array should be planar and the equivalent of the one-dimensional screen would be a two-dimensional rectangular planar screen. Both the array and the screen should be perpendicular to the horizontal direction which is assumed to be the direction of propagation.*

2. *Considering a general reflector geometry is more challenging. Indeed, we can always write the matrix* $\widehat{\mathbb{P}}$ *in the form of* (3.13)*. This means that* $\widehat{\mathbb{P}}$ *can be always decomposed*

*as a product of a unitary propagator matrix $Q$ that transfers the field from the array to the range of the reflector times the matrix $A_M$ that carries information about the reflector, times the same unitary matrix $Q$ that now transfers the scattered field from the reflector to the array. Therefore, the matrix $\widehat{\mathbb{P}}$ is unitarily equivalent to the matrix $A_M$ and information about the reflector can be obtained from the singular value decomposition of $\widehat{\mathbb{P}}$. Although, the structure of the matrix $A_M$ does not have in general the exact Hankel-minus-Toeplitz form observed for the screen model problem, we expect that the conclusions drawn from the model problem carry over to more general reflector's geometries. In particular, as our numerical results suggest, information about the reflector's location and shape can be obtained from the singular vectors that correspond to the largest and intermediate singular values with the first ones focusing to the bulk of the reflector and the second ones focusing to its boundary.*

## 3.2 Partial aperture case

We have spent the previous section reviewing and analyzing the performance of the imaging functional $\widetilde{\mathcal{I}}^{\text{KM}}$ for the screen model-problem under the assumption that the array spans the whole depth of the waveguide. However, in this section we aim at imaging extended reflectors with a *partial* array. In what follows, we therefore consider the screen model-problem with an array that does not span the whole $[0, D]$. Then the vertical eigenfunctions $X_n$ are no longer orthonormal along the array, and one may immediately check that $\widehat{\mathbb{P}}$ as defined in (2.9) is no more unitarily equivalent to $A_M$. This of course affects the efficiency of $\widetilde{\mathcal{I}}_J^{\text{KM}}$ in selective imaging in the sense that we lose the usual 'ordering' of images which implies that projection of $\widehat{\mathbb{P}}$ on its first singular vector exhibits focusing at the center of the reflector, while projecting on subsequent significant singular vectors results in images that focus at the endpoints of the reflector, [10, 61]. Even if we cast aside selectivity and concentrate in creating images with $\widetilde{\mathcal{I}}^{\text{KM}}$ we will soon discover, as one would expect, that the efficiency of $\widetilde{\mathcal{I}}^{\text{KM}}$ deteriorates as we decrease the length $l_{\text{arr}}$ of the array. We illustrate this with the following example. We consider a constant sound speed $c_0$, the reference frequency is $f_0$ and corresponds to a reference wavelength $\lambda_0$ and an associated wavenumber $k_0 = \pi/10$. All the experiments shown here are performed for a single frequency with $k = 0.975k_0$, at which $M = 19$ modes propagate. The scatterer, i.e. the screen, is centered at $(L, x_0) = (22.5, 5)\lambda_0$ and its length is $b = 2\lambda_0$. The inter-element array distance $h = \lambda_0/8$,

unless stated otherwise. In the leftmost subplot of Figure 3.4 we show the image we obtain with $\widetilde{\mathcal{I}}^{\mathrm{KM}}$ for full array, while the other three subplots from left to right are created with array length $l_{\mathrm{arr}} = 0.9D,\ 0.7D$, and $0.5D$ m, respectively. In all cases the length of the array is reduced symmetrically from both ends. Moreover, to assess the noise level of an image, we define the Signal-to-Noise Ratio (SNR) by,

$$\mathrm{SNR} = \frac{\max\limits_{\vec{\boldsymbol{x}}^{\mathrm{s}} \in \mathcal{R}} |\widetilde{\mathcal{I}}^{\mathrm{KM}}(\vec{\boldsymbol{x}}^{\,\mathrm{s}})|}{\max\limits_{\vec{\boldsymbol{x}}^{\mathrm{s}} \in \mathcal{S} \setminus \mathcal{R}} |\widetilde{\mathcal{I}}^{\mathrm{KM}}(\vec{\boldsymbol{x}}^{\,\mathrm{s}})|},$$

where $\mathcal{R}$ is a subset of our search domain $\mathcal{S}$ that contains the reflector. In our tests we define $\mathcal{R}$ as a $6\lambda_0 \times 6\lambda_0$ box with the scatterer lying at its center. The SNR value can be used as a quantitative measure that corroborates the qualitative characteristics of the image. In Figure 3.4, and in what follows, the boundary of $\mathcal{R}$ is drawn in red. As it is evident from Figure 3.4, and the associated SNR values shown in the title of each subplot, the quality of the image deteriorates as $l_{\mathrm{arr}}$ decreases.

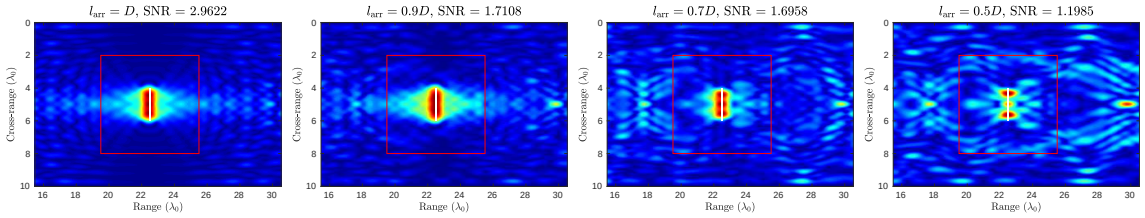


Figure 3.4: Imaging with $\widetilde{\mathcal{I}}^{\mathrm{KM}}$ for the screen. The length of the array from left to right is $l_{\mathrm{arr}} = D,\ 0.9D,\ 0.7D,\ 0.5D$, respectively, the wavenumber $k = 0.975k_0$ and the width of the screen $b = 2\lambda_0$.

Let us remark here that this is not a limitation of the particular imaging functional and, in general, a deterioration of the imaging results is expected as the array aperture decreases. Similar results not shown here are also obtained with the classical $\mathcal{I}^{\mathrm{KM}}$ imaging functional. Next, we will propose an alternative definition of the matrix $\widehat{\mathbb{P}}$ in order to preserve the nice properties that we have observed in the full array case to the case of the partial-aperture array as well.

### 3.2.1 Weighted projection of the array response matrix for the partial array case: Motivation

Now, we shall present a way to construct a weighted projection of the array response matrix in the case of the partial-aperture array. Our observations in Section 3.1 regarding the band-limited nature of the trigonometric polynomials with coefficients the eigenvectors of the matrix $A_M$ lead us to consider the $M \times M$ matrix with entries

$$(A_{\rm arr})_{mn} = \int_{\mathcal{A}} X_m(x) X_n(x) \mathrm{d}x, \quad m, n = 1, \ldots, M. \tag{3.26}$$

$A_{\rm arr}$ is a real, symmetric Toeplitz-minus-Hankel matrix and possesses all the nice properties that were described in Section 3.1. Let $\nu_j$, $j = 1, \ldots, M$, be its eigenvalues and $\boldsymbol{w}^j = (w_1^j, w_2^j, \ldots, w_M^j)^T$ be the corresponding orthonormal eigenvectors. Moreover, let $W$ be the $M \times M$ orthogonal matrix $W = (\boldsymbol{w}^1, \boldsymbol{w}^2, \ldots, \boldsymbol{w}^M)$, and $s_j$ be the trigonometric polynomial

$$s_j(x) = \sum_{i=1}^{M} w_i^j X_i(x), \quad j = 1, 2, \ldots, M, \tag{3.27}$$

where $w_i^j$ are as above.

Next, we project the array response matrix $\widehat{\Pi}$ on the $M$ trigonometric polynomials $s_n$, rather than on the first $M$ vertical eigenfunctions $X_n$. Specifically, let $\widehat{\mathbb{S}}$ be the $M \times M$ matrix with entries

$$\widehat{\mathbb{S}}_{mn} = \frac{1}{\nu_m \nu_n} \int_{\mathcal{A}} \mathrm{d}x_s \int_{\mathcal{A}} \mathrm{d}x_r \, \widehat{\Pi}(\vec{\boldsymbol{x}}_s, \vec{\boldsymbol{x}}_r, \omega) \, s_m(x_s) \, s_n(x_r), \tag{3.28}$$

where $m, n = 1, \ldots, M$. It is immediate to verify that

$$\int_{\mathcal{A}} s_k(x) X_m(x) \mathrm{d}x = \nu_k \, w_m^k, \quad k, m = 1, \ldots, M. \tag{3.29}$$

Replacing (3.3) and (3.27) into (3.28), and in view of (3.29), we arrive at the following matrix identity

$$\widehat{\mathbb{S}} = -\frac{1}{4} \, W^T D_\beta \, Q \, A_M \, Q \, D_\beta \, W. \tag{3.30}$$

As a final step, note that $W$ is an orthogonal matrix hence if we define

$$\widehat{\mathbb{P}} = D_\beta^{-1} \, W \, \widehat{\mathbb{S}} \, W^T D_\beta^{-1}. \tag{3.31}$$

we may check that

$$\widehat{\mathbb{P}} = -\frac{1}{4} D_\beta^{-1} \underbrace{W W^T}_{I_M} D_\beta Q A_M Q D_\beta \underbrace{W W^T}_{I_M} D_\beta^{-1} = -\frac{1}{4} Q A_M Q. \tag{3.32}$$

So, by following the steps described above, one may end up with a matrix $\widehat{\mathbb{P}}$ that (up to the multiplicative constant $-1/4$) is unitarily equivalent to $A_M$. Let us also note that in the full array case the orthonormality of the $X_n$'s implies that $A_{\text{arr}}$ is the identity matrix, $s_j(x) = X_j(x)$ and $W = I_M$, thus we recover the previous definition of $\widehat{\mathbb{P}}$, see (2.9).

### 3.2.2 Implementation aspects

We feel that the previous approach may be useful for theoretical purposes mainly. The main reason for that hinges on the fact that the data that we have in our disposal is the $N^2$ values tabulated in $\widehat{\Pi}$. Hence the integrals over $\mathcal{A}$ in (3.28) and (3.29) have to be evaluated numerically whereas the validity of (3.32) relies crucially on the fact that (3.29) holds. In practice, (3.29) holds only approximately due to inherent errors in the course of numerical integration; as a result those errors 'pollute' (3.32) as well.

In order to avoid these difficulties we propose the following implementation of our method in order to work on the matrix level. To this end we consider the real, symmetric matrix $h(V^T V)$, where $V$ is the $N \times M$ matrix with entries

$$V_{mn} = X_n(x_m), \quad m = 1, \ldots, N, n = 1, \ldots, M, \tag{3.33}$$

and we let $S$ to be the $M \times N$ matrix with

$$S_{ij} = s_i(x_j), i = 1, \ldots, M, \quad j = 1, \ldots, N, \tag{3.34}$$

where $x_k$, $k = 1, \ldots, N$, are the elements of the now-truncated array, and $s_i(x_j)$ is the $i$–th trigonometric polynomial defined in (3.27) evaluated at the cross-range of the $j$–th transducer. Now, by abusing slightly the notation, $\nu_j$ and $\boldsymbol{w}^j = (w_1^j, w_2^j, \ldots, w_M^j)^T$ are the eigenvalues and corresponding orthonormal eigenvectors of the Gram matrix $h(V^T V)$. Notice that the scaling factor $h$ is used here just to push the $\nu_i$'s to cluster near one and zero (instead of near $h^{-1}$ and zero) as we shall see later.

It is easy to show that

$$SV = h^{-1} D_\nu W^T, \quad \text{where } D_\nu = \operatorname{diag}(\nu_1, \ldots, \nu_M),$$

(a matrix equivalent of (3.29)), and since $W$ is orthogonal we deduce that

$$W D_\nu^{-1} S V = h^{-1} I_M.$$

Therefore, if we define the matrix $\hat{\mathbb{P}}$ as

$$\widehat{\mathbb{P}} = D_\beta^{-1}\, W\, D_\nu^{-1}\, S\, \hat{\Pi}\, S^T\, D_\nu^{-1}\, W^T\, D_\beta^{-1},$$

we get that

$$\widehat{\mathbb{P}} = -\frac{1}{4} D_\beta^{-1} \underbrace{W\, D_\nu^{-1}\, S\, V}_{h^{-1} I_M} D_\beta Q A_M Q D_\beta \underbrace{V^T\, S^T\, D_\nu^{-1}\, W^T}_{h^{-1} I_M}\, D_\beta^{-1} = -\frac{1}{4h^2} Q A_M Q,$$

so $\widehat{\mathbb{P}}$ is again unitarily equivalent to $A_M$ (up to the multiplicative constant $-1/(4h^2)$). We summarize these in the following definition

**Definition 2** *Given the array response matrix $\widehat{\Pi}$ for the scattered field, we first consider the $M \times N$ matrix*

$$\tilde{S} = D_\nu^{-1}\, S, \tag{3.35}$$

*where*

$$S_{ij} = s_i(x_j),\ i = 1, \ldots, M,\ j = 1, \ldots, N, \quad \text{and } D_\nu = \operatorname{diag}(\nu_1, \ldots, \nu_M),$$

*and next, we define $\widehat{\mathbb{P}}$ by*

$$\widehat{\mathbb{P}} = D_\beta^{-1}\, W\, \tilde{S}\, \hat{\Pi}\, \tilde{S}^T\, W^T\, D_\beta^{-1}. \tag{3.36}$$

*Then we use $\widehat{\mathbb{P}}$ in $\widetilde{\mathcal{I}}^{\mathrm{KM}}$ (as defined in (2.12)), i.e.,*

$$\widetilde{\mathcal{I}}^{\mathrm{KM}}(\vec{\boldsymbol{y}}^{\mathrm{s}}, \omega) = -\frac{1}{4h^2} \sum_{m,n=1}^{M} \mathrm{e}^{-\mathrm{i}(\beta_m + \beta_n)|z_{\mathrm{a}} - z^{\mathrm{s}}|} X_n(x^{\mathrm{s}}) X_m(x^{\mathrm{s}}) \widehat{\mathbb{P}}_{mn}(\omega),$$

*for imaging.*

In order to assess the performance of $\widetilde{\mathcal{I}}^{\mathrm{KM}}$, as defined above, we apply our methodology in the test case that we have considered in the beginning of the present section. In the leftmost subplot of Figure 3.5 we show $\widetilde{\mathcal{I}}^{\mathrm{KM}}$ images for full array, while the other three subplots correspond to array lengths $l_{\mathrm{arr}} = 0.9D,\ 0.7D,\ 0.5D$, respectively. In all cases the length of the array is reduced symmetrically from both ends. We observe that there is no loss of information, even when we use an array with half of its original length. This falls in line with the theory, which suggests that the projected array response matrix $\widehat{\mathbb{P}}$ for the partial aperture array, as it is defined for example in (3.30) and (3.31), is identical to the projected matrix for an array that spans the whole vertical cross-section $[0, D]$. Of course, as we have already remarked, this holds under the assumption that all computations are exact and there is no need for regularization in our calculations, as will be the case for smaller array lengths, which we will examine in the next subsection.

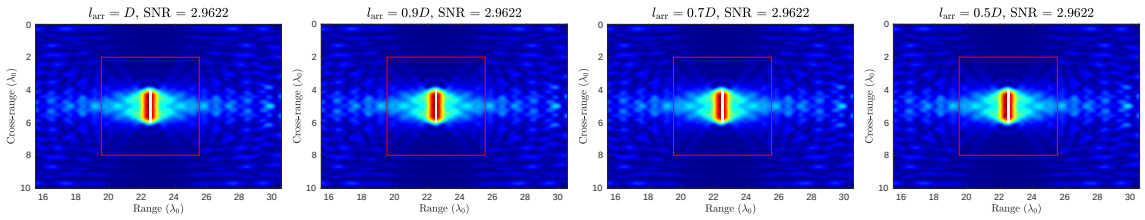


Figure 3.5: Imaging with $\widetilde{\mathcal{I}}^{\mathrm{KM}}$ for the screen, when $l_{\mathrm{arr}} = D,\ 0.9D,\ 0.7D,\ 0.5D$, for $k = 0.975k_0$.

Next, in Figure 3.6, we plot selective imaging results obtained with the functional $\widetilde{\mathcal{I}}_J^{\mathrm{KM}}$, for $J = 1, 2, 3, 4$, when $l_{\mathrm{arr}} = 0.9D$. Selective imaging with $\widetilde{\mathcal{I}}_J^{\mathrm{KM}}$ performs as if we were using the full-aperture array; all four images are very good with high SNR $> 1.9$, and projection on the first singular vector results in focusing on the middle of the screen while projection on the second to fourth singular vectors provides information about the location of its edges. These images remain identical until we reduce by half the length of the array (symmetrically from both ends).

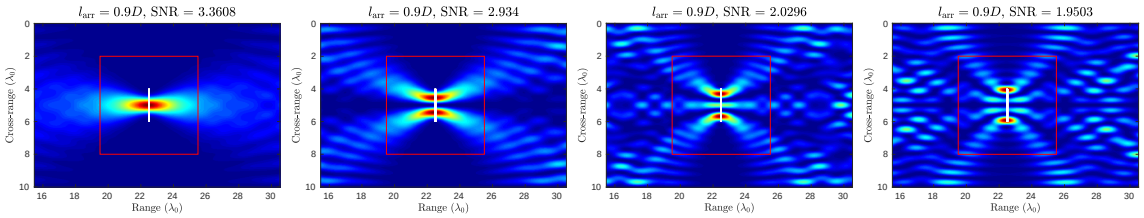


Figure 3.6: Imaging with $\widetilde{\mathcal{I}}_J^{\rm KM}$ for the screen, for $J = 1, 2, 3, 4$ when $l_{\rm arr} = 0.9D$, for $k = 0.975k_0$.

The results in Figures 3.5 and 3.6 are in perfect agreement with the theory in this ideal case; they are excellent and in some sense counter intuitive, since there is no loss of information despite the fact that we decrease the array length. Note that this is certainly not true for the functional that we have used to create the images in Figure 3.4, where the quality of the images deteriorates as the array aperture decreases.

### 3.2.3 Numerical experiments: Partial-aperture array imaging for the model problem

#### The noiseless data case

So far we have seen that for the screen model problem and under the assumption that all arithmetic operations are exact (i.e. they are performed with infinite precision), the spectral properties of $\widehat{\mathbb{P}}$ (as defined by (3.36)) are determined by those of $A_M$, thus we expect $\widetilde{\mathcal{I}}^{\rm KM}$ to perform in exactly the same way as if we were using a full-aperture array. However, in practice we use finite precision arithmetic so we have to examine whether and how this affects the performance of our method.

A quite obvious cause of potential numerical instabilities is the presence of the reciprocals $\nu_i^{-1}$ of the eigenvalues of the matrix $h(V^TV)$ in the definition of $\tilde{S}$, see (3.35). Hence it is important to examine the behavior of the $\nu_i$'s, and how it is related to the length of the array $\mathcal{A}$. An important remark in this direction is that $h(V^TV)$ may be considered as an approximation of the $M \times M$ matrix Toeplitz-minus-Hankel matrix $A_{\rm arr}$. Therefore we would expect $\nu_i$ to cluster near 0 and 1 and, specifically, roughly $[l_{\rm arr}/(\lambda/2)]$ of them to lie near 1, and the rest $M - [l_{\rm arr}/(\lambda/2)]$ to approach zero. Moreover, as $l_{\rm arr}$ decreases, more singular values tend to zero, and in fact $h(V^TV)$ will become practically singular as soon as its minimum eigenvalue $\nu_{\rm min}$ falls below a certain threshold.

In some cases there do exist theoretical bounds for the minimum eigenvalues of Toeplitz

matrices. For example, Serra in [54] shows that if $T$ is an $(n+1)\times(n+1)$ Toeplitz matrix with generating function a real integrable function on $[-\pi,\pi]$, which is strictly positive in a closed interval $J\subset I$ and zero elsewhere, then for $n$ sufficiently large, and for any $\epsilon\in(0,t)$, its minimum eigenvalue $\lambda_{\min}$ is bounded as

$$c_1\,(t-\epsilon)^{n(n+1)/2} < \lambda_{\min} < c_2\,t^n,$$

where $c_1, c_2$ are positive constants (independent of $n$), and $t$ is a constant less than one that depends on the width of the interval $J$; specifically $t=\sin^2(|J|/4)$, see also [52]. In our case, we may apply these bounds in the case where the array is attached on the top of the waveguide. Then the generating function of the Toeplitz-minus-Hankel matrix $A_{\text{arr}}$ is the indicator function $\mathbb{1}_{\tilde{J}}(x)$ of $\tilde{J}=[-l_{\text{arr}}, l_{\text{arr}}]$, and the minimum eigenvalue of $A_{\text{arr}}$ is equal to the minimum odd eigenvalue of its associated $(2M+1)\times(2M+1)$ Toeplitz counterpart. Hence, we expect its minimum eigenvalue to decrease to zero like $\tau^{2M}$, where

$$\tau=\sin^2\left(\frac{\pi l_{\text{arr}}}{2D}\right).$$

As already said, we expect that the eigenvalues of $h(V^TV)$ behave like those of $A_{\text{arr}}$. In Figure 3.7 we plot (using a logarithmic scale on the vertical axis) the minimum eigenvalue $\nu_{\min}$ of the $M\times M$ matrix $h(V^TV)$ (computed in MATLAB) and the values predicted by the bounds $\tau^{2M}$ and $\tau^{2M(2M+1)/2}$ as $l_{\text{arr}}$ decreases. As an indication of the relative error due to floating point arithmetic we use the so-called machine epsilon $\varepsilon$ (implemented in MATLAB and printed as a blue dashed line in the figure). Here, we have $k=0.975k_0$, $M=19$ modes propagate, and the array pitch is $h=2.5$ m $\simeq\lambda/8$. The results shown in Figure 3.7 suggest that the minimum eigenvalue of $h(V^TV)$ drops below $\varepsilon$ when the length of the array is less than $0.6D$.

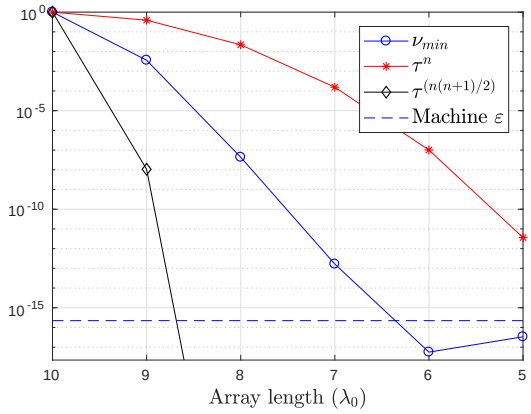


Figure 3.7: The minimum eigenvalue of $h(V^TV)$ (blue circles) vs. $\tau^n$ (red asterisks) and $\tau^{n(n+1)/2}$ (black diamonds) for $k = 0.975k_0$ and $n = 2M$, when we decrease the length of the array from below.

In Figure 3.8 we plot the minimum eigenvalue of $h(V^TV)$ as we decrease $l_{\text{arr}}$ and for various values of the array pitch $h$. In the left subplot the length of the array is reduced symmetrically with respect to the mid-width of the waveguide, while in the right one the lower part of the array is cut off. The different markers (also typed in different colors) shown in Figure 3.8 correspond to arrays with different densities; the value of $h$ that corresponds to each marker is reported in the legend of the figure in terms of the reference wavelength $\lambda_0$. We observe that the decay rate is much faster in the non-symmetric case (right subplot) than in the symmetric one (left). Moreover, the density of the array seems to affect the rate at which $\nu_{\min}$ drops below $\varepsilon$; these results indicate that the magnitude of $\nu_{\min}$ is stabilized with an inter-element array distance of approximately $\lambda_0/8$.

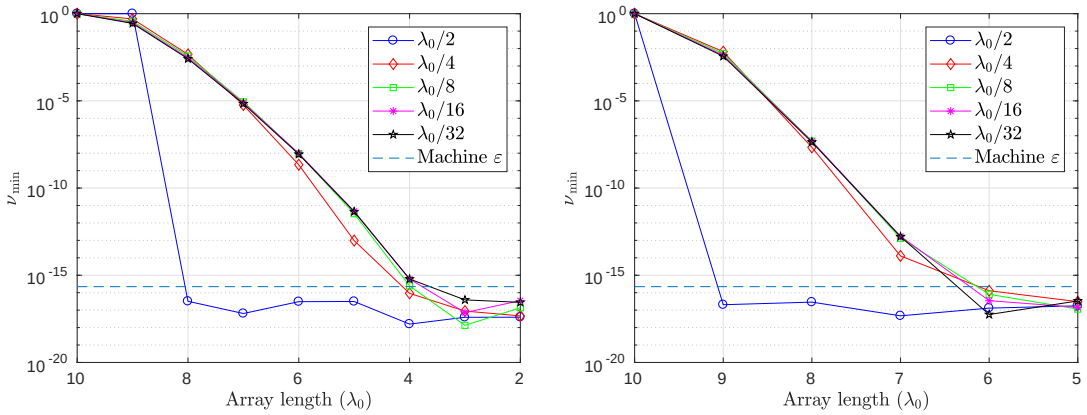


Figure 3.8: Behavior of $\nu_{\min}$ when we decrease the length of the array symmetrically from both ends (left subplot) and just from below (right subplot), for $k = 0.975k_0$.

By inspecting the plots in Figure 3.8 we expect no loss in image resolution or signal to noise ratio (SNR) in our images with $\widetilde{\mathcal{I}}^{\text{KM}}$ as long as $\nu_{\min}$ stays above some threshold $\varepsilon^+$. However, as $\nu_{\min}$ approaches machine $\varepsilon$, most likely one will experience numerical instabilities. As a regularization procedure we may try the following filtering:

> Consider some threshold $\varepsilon^+$.
> Then if $\nu_c > \varepsilon^+ > \nu_{c+1}$, for some $c \in \{1, \ldots, M\}$, we set $1/\nu_i = 0$, for $i \geq c+1$.

Notice that the reciprocals $\nu_i^{-1}$ of these small eigenvalues, which are in fact very big, multiply the lower $(M-c) \times N$ part of the matrix $S$; let us call it $S_c$. Intuitively we expect the entries of $S_c$ to be very small since, for example, the $j$-th row contains the values of the trigonometric polynomial $s_j$ calculated on the receivers' depths, and recall that our results in Section 3.1 suggest that when $\nu_j$ is small then $s_j$ is mainly supported on the exterior of $\mathcal{A}$ (see, for example, Figures 3.2 and 3.3 that exhibit the behavior of the trigonometric polynomials with coefficients the eigenvectors of the matrix $A_M$ defined in (3.7), and recall that the matrix $h(V^TV)$ approximates $A_{\text{arr}}$ defined in (3.26) which is of the same form as $A_M$). Indeed, it is not hard to prove that

$$\|S_c\|_{\text{F}}^2 = (\sum_{i=c+1}^{M} \nu_i)/h < (M-c)\varepsilon^+/h,$$

where $\|\cdot\|_{\text{F}}$ is the Frobenius matrix norm, to give grounds to the proposed regularization technique. Of course, in the case we employ this filtering technique we do not expect a

unitary equivalence relation between $\widehat{\mathbb{P}}$ and $A_M$ to hold any more.

We clarify the above by giving some examples. We decrease the length of the array at $l_{\text{arr}} = 0.3D$ (symmetrically from both ends ), i.e. the array covers 30% of the waveguide depth. In order to form $\widehat{\mathbb{P}}$ we use a threshold $\varepsilon^+ = 10^{-15}$ that forces the reciprocals of the last three eigenvalues of $h(V^TV)$ to be equal to zero. One may verify the good quality of the image shown on the top right corner of Figure 3.9 that is obtained with the proposed filtering. On the top left corner we plot the singular values of $\widehat{\mathbb{P}}$. The bottom row in Figure 3.9 shows the corresponding results when we do not use any filtering and demonstrates the catastrophic effect of roundoff errors during the computation of $\widehat{\mathbb{P}}$.

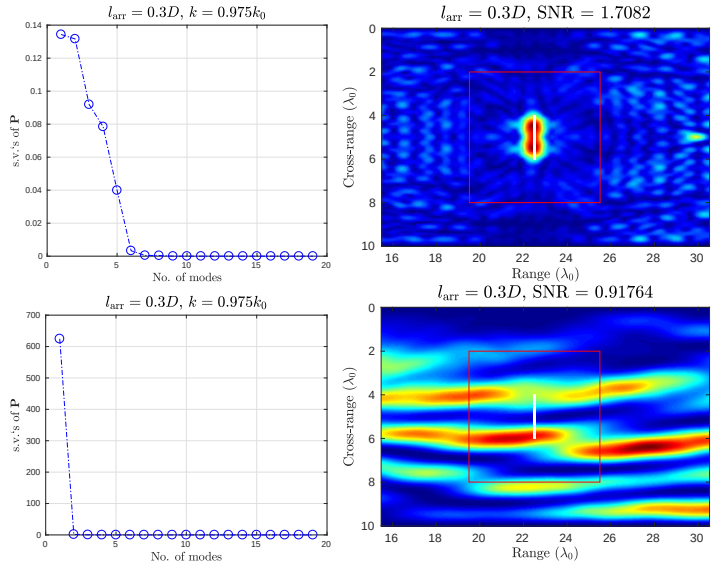


Figure 3.9: Top: The singular values of $\widehat{\mathbb{P}}$ (left) and the associated $\widetilde{\mathcal{I}}^{\text{KM}}$ image (right) that we obtain with threshold $\varepsilon^+ = 10^{-15}$. Bottom: The same as in the top row but without using $\varepsilon^+$. Here $l_{\text{arr}} = 0.3D$, $h = \lambda_0/8$ and $k = 0.975k_0$.

Figure 3.10 depicts selective imaging results with $\widetilde{\mathcal{I}}_J^{\text{KM}}$, where again in the course of constructing $\widehat{\mathbb{P}}$ we employ the threshold $\varepsilon^+ = 10^{-15}$. Here, selective imaging with $\widetilde{\mathcal{I}}_J^{\text{KM}}$ fails, in the sense that the usual ordering in focusing does not hold anymore. To be precise, this means that we lose the property that when we project on the singular vector that corresponds to the largest singular value we get an image that provides information about the bulk of the object, while projection on the singular vectors that correspond to smaller singular values carry information about its edges. This is something to be expected since

filtering prevents to establish a unitary equivalence relation between $\widehat{\mathbb{P}}$ and $A_{\mathrm{M}}$. However, the images for $J = 2,\ 3$ and 4 still have good SNR and provide useful information about the object.

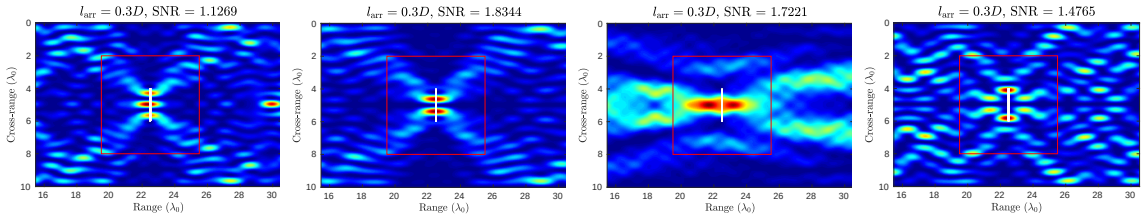


Figure 3.10: Imaging with $\widetilde{\mathcal{I}}_J^{\mathrm{KM}}$ for the screen with $\varepsilon^+ = 10^{-15}$, for $J = 1, 2, 3, 4$, when $l_{\mathrm{arr}} = 0.3D$, for $h = \lambda_0/8$ and $k = 0.975k_0$.

In order to push $\widetilde{\mathcal{I}}^{\mathrm{KM}}$ to the limit for this model problem we decrease (symmetrically) the length of the array to be equal to $l_{\mathrm{arr}} = \lambda_0$ (this is just 10% of the total waveguide depth). In this case, we make the array denser by setting the pitch $h = \lambda_0/20$. The image shown in Figure 3.11 is generated with a threshold equal to $\varepsilon^+ = 10^{-15}$ that removes the reciprocals of the last 8 singular values of $h(V^TV)$. We observe that the $\widetilde{\mathcal{I}}^{\mathrm{KM}}$ image gives us very good information about the object, although its SNR value is quite low, about 1.2, due to the presence of the small artifact that is visible on the right side of the image.

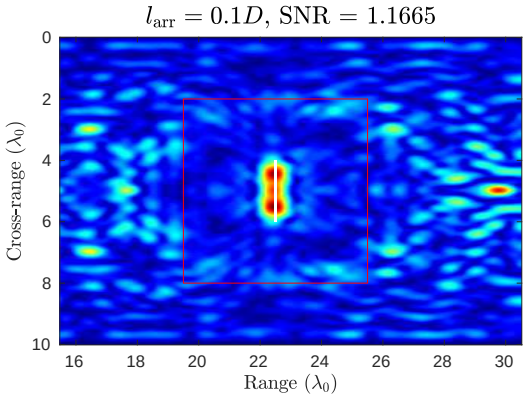


Figure 3.11: Imaging with $\widetilde{\mathcal{I}}^{\mathrm{KM}}$ for the screen with $\varepsilon^+ = 10^{-15}$ when $l_{\mathrm{arr}} = 0.1D$, for $h = \lambda_0/20$ and $k = 0.975k_0$.

We close this paragraph with a few remarks.

**Remark 7** *1. In all results that we have shown thus far we have reduced the length of the array symmetrically from both ends and we have placed the screen centered in the*

*mid-depth of the waveguide. We have experimented with various other configurations altering the way we reduce the array and/or the position of the screen. Our results suggest that in some cases we may have to use filtering for larger array lengths than before. For example, when we reduce the length of the array from below the eigenvalues of $h(V^TV)$ decrease towards zero much faster, see Figure 3.8, and indeed in this case we have to employ some threshold $\varepsilon^+$ for larger arrays than those reported in the examples shown here.*

2. *One may try different approaches to construct a weighted projection of the array response matrix in the partial array case. For example, we may define*

$$\widehat{\mathbb{P}} = D_\beta^{-1}\, V^+\, \hat{\Pi}\, (V^T)^+\, D_\beta^{-1},$$

*where $V^+$ is the Moore-Penrose pseudoinverse of $V$. Then it is immediate to check that in the screen model problem, and under the assumption that all computations are performed with infinite precision, $\widehat{\mathbb{P}}$ is unitarily equivalent to $A_M$. However, as we decrease the length of the array we still have to use a regularized pseudoinverse that treats as zero any singular values of $V$ less than some suitable threshold.*

3. *So far we have seen that when we decrease $l_{\rm arr}$ beyond some level and we employ some thresholding to the $\nu_i^{-1}$ the nice 'ordering' property of the selective imaging functional $\widetilde{\mathcal{I}}_J^{\rm KM}$ does not hold. However, in a post-processing stage, one may still have some benefit in imaging using the functional $\widetilde{\mathcal{I}}^{\rm KM,f}$, see (2.16), where in the filtered version of $\widehat{\mathbb{P}}$ we may take into account those of its singular vectors that correspond to 'good' $\widetilde{\mathcal{I}}_J^{\rm KM}$ images.*

### Adding noise to the data

In the previous subsection, we found that $\widetilde{\mathcal{I}}^{\rm KM}$ seems to work very well under ideal conditions that allow us to derive $\widehat{\Pi}$ analytically in the special form (3.4). Now we shall examine the performance of our method under the effect of measurement noise. Specifically, we model measurement noise, as in [10], adding a noise matrix $W(\omega)$ with zero mean uncorrelated Gaussian distributed entries with variance $\epsilon p_{\rm avg}$, *i.e.* $W_{r,s}(\omega) \sim \mathcal{N}(0, \epsilon p_{\rm avg})$. Here the

average power received per source and receiver is given by

$$p_{\text{avg}} = \frac{1}{N^2}\|\widehat{\Pi}(\omega)\|_{\text{F}}^2,$$

where $\|\cdot\|_{\text{F}}$ is the Frobenius matrix norm. The expected power of the noise $W(\omega)$ over all receivers and sources is

$$\mathbb{E}\left[\|W(\omega)\|_{\text{F}}^2\right] = \epsilon N^2\, p_{\text{avg}}.$$

Since the total power of the signal received over all receivers and sources is $N^2\, p_{\text{avg}}$, the normalized noise power in dB is $-10\log_{10}\epsilon$.

In Figure 3.12 we superimpose the singular values of $\widehat{\Pi}$ and $\widehat{\Pi}+W$ when we add noise of 10 dB to our data, and the array is reduced symmetrically to have length equal to $l_{\text{arr}} = 0.7D$. We use a linear scale for the $y$-axis in the left subplot and a $\log_{10}$ scale in the right one. As one may immediately verify the largest singular values of $\widehat{\Pi}+W$ remain close to those of $\widehat{\Pi}$, while the noise severely affects the smaller ones.

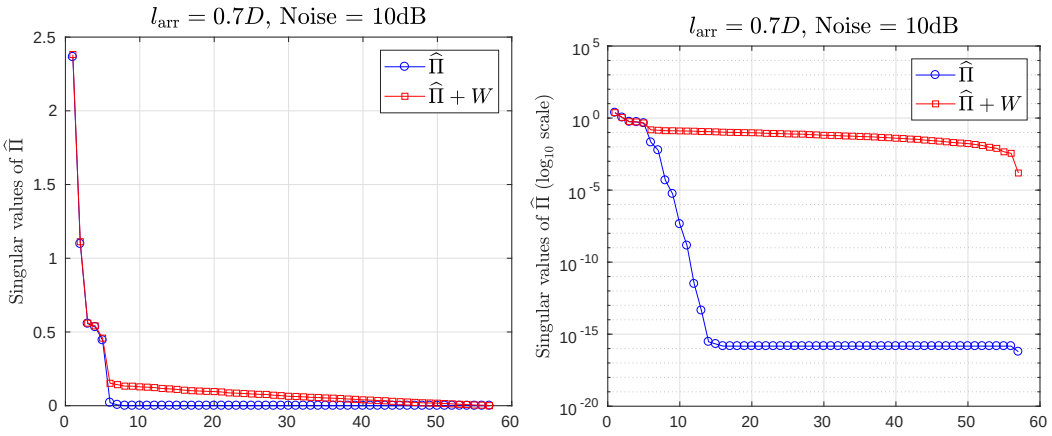


Figure 3.12: The singular values of $\widehat{\Pi}$ and $\widehat{\Pi}+W$ using a linear scale for the $y$-axis (left) and a $\log_{10}$ scale (right). Here $l_{\text{arr}} = 0.7D$ and $k = 0.975k_0$.

Next, we present the outcome of some of the experiments that we have performed with noise power 10 dB, keeping the rest of the parameters the same as in the previous sections. We begin with an array with $l_{\text{arr}} = 0.7D$. In Figure 3.13 we plot the singular values of $h(V^TV)$ using a linear scale for the vertical axis in the left subplot and a $\log_{10}$ scale in the right one. Note that the smallest singular value is greater than $10^{-6}$, hence all the singular values of $h(V^TV)$ are well above the threshold $\varepsilon^+ = 10^{-15}$ that we have used so

far. However, as one may see in the top left subplot of Figure 3.14 the SVD of $\widehat{\mathbb{P}}$ does not follow the usual pattern. Specifically, the first singular value of $\widehat{\mathbb{P}}$ is 53.7, the second 33.15, while the rest are less than 1. This is an indication that something goes wrong and, indeed, the corresponding image shown in the bottom left subplot is just noise. In order to improve this unsatisfactory result we employ some threshold $\varepsilon^+$ during the computation of $S$ in order to remove gradually those $\nu_i^{-1}$ that correspond to the smaller $\nu_i$'s, one at a time. The $\widetilde{\mathcal{I}}^{\text{KM}}$ images obtained by removing those $\nu_i^{-1}$ that correspond to the smallest one, or two, $\nu_i$ are also very bad and we do not show them here. In the middle subplots of Figure 3.14 we present the singular values of $\widehat{\mathbb{P}}$ (top) and the corresponding $\widetilde{\mathcal{I}}^{\text{KM}}$ image (bottom) for a threshold $\varepsilon^+ = 10^{-2}$; with this value we treat as zero the $\nu_i^{-1}$ that correspond to the smaller three $\nu_i$'s, see Figure 3.13. Things are also well by choosing $\varepsilon^+ = 5 \cdot 10^{-2}$, thus setting one more $\nu_i^{-1}$ equal to zero.

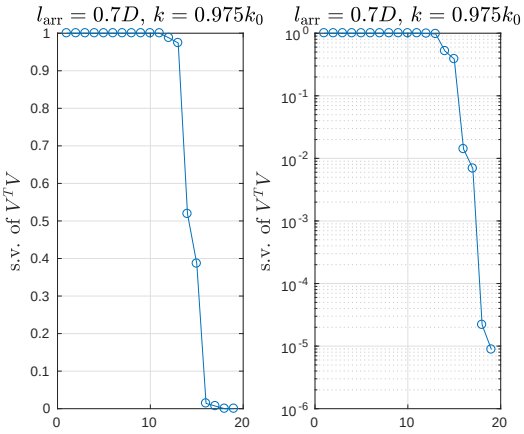


Figure 3.13: The singular values of $h(V^TV)$ using a linear scale for the $y$-axis (left) and a $\log_{10}$ scale (right). Here $l_{\text{arr}} = 0.7D$ and $k = 0.975k_0$.

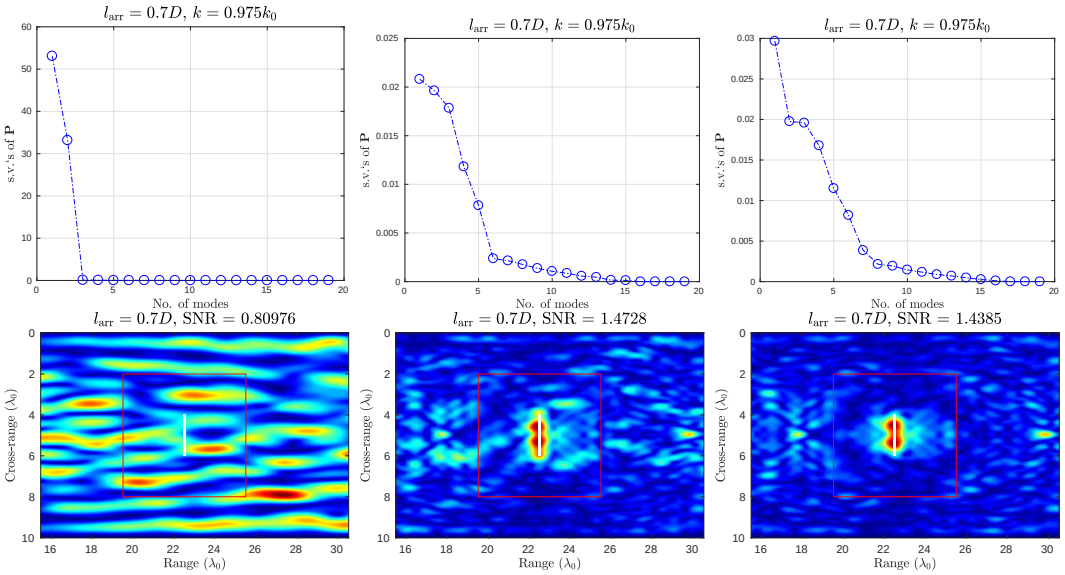


Figure 3.14: Singular values of $\widehat{\mathbb{P}}$ (top row) and $\widetilde{\mathcal{I}}^{\rm KM}$ images (bottom row) for the screen, without a threshold (left subplots) and with a threshold $\varepsilon^+ = 10^{-2}$ that removes 3 (middle subplots) and $\varepsilon^+ = 5 \cdot 10^{-2}$ that removes 4 (right subplots) of the smallest $\nu_i^{-1}$, respectively (compare with Figure 3.13). Here $l_{\rm arr} = 0.7D$ m, and $k = 0.975k_0$.

Looking once again at Figure 3.13, and recalling the results of Section 3.1, we realise that the choice of the threshold value $\varepsilon^+ = 5 \cdot 10^{-2}$ does in fact dictate to project the array response matrix $\widehat{\Pi}$ just on the trigonometric polynomials that are supported on $\mathcal{A}$; also recall that their number is expected to be roughly $l_{\rm arr}/(\lambda/2)$. Keeping this in mind, we next examine whether in order to obtain good images for various lengths of the array it suffices to compute $\widehat{\mathbb{P}}$ using a threshold $\varepsilon^+$ that excludes those trigonometric polynomials with coefficients the eigenvectors of $A_{\rm arr}$ that belong to the noise subspace; these are supported on the exterior of $\mathcal{A}$. To this end, we plot in Figure 3.15 the singular values of $h(V^T V)$ (top line) and the corresponding $\widetilde{\mathcal{I}}^{\rm KM}$ images (bottom line) for the screen, with $l_{\rm arr} = 0.6D$ (left subplots), $l_{\rm arr} = 0.5D$ (middle subplots), and $l_{\rm arr} = 0.45D$ (right subplots). In all cases we take $\varepsilon^+ = 5 \cdot 10^{-2}$ that removes 6, 8 and 8 of the smallest $\nu_i^{-1}$, respectively. As one may see, and as it is expected, the quality of the images deteriorates as we decrease the length of the array but it remains acceptable even if we place symmetrically in the waveguide an array that covers more or less the half of its depth.

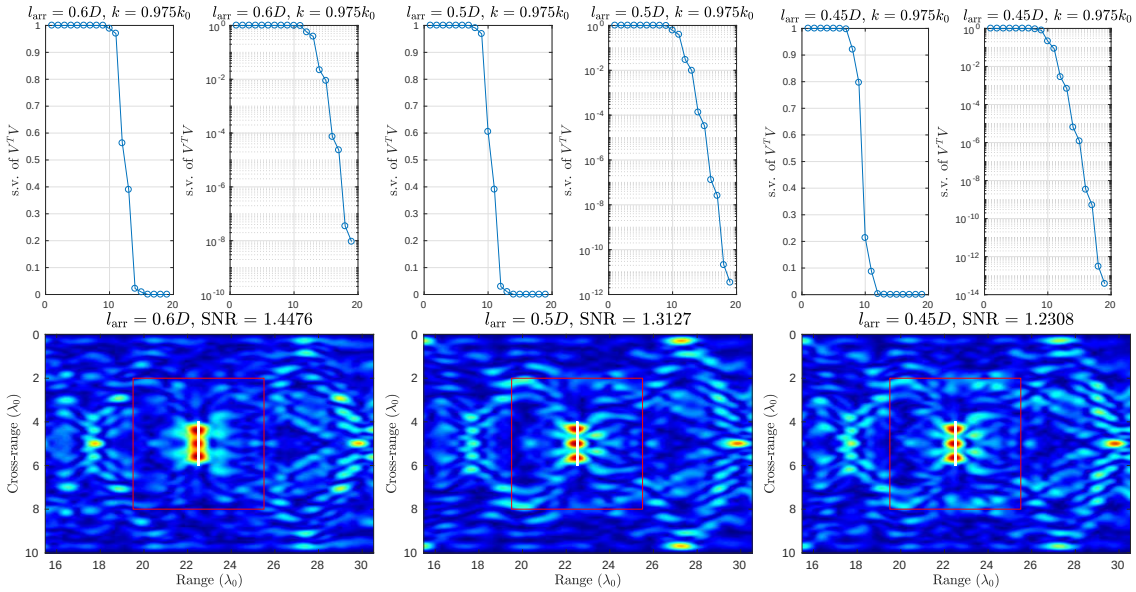


Figure 3.15: Singular values of $h(V^TV)$ (top row) and $\widetilde{\mathcal{I}}^{\text{KM}}$ images (bottom row) for the screen, with $l_{\text{arr}} = 0.6D$ (left subplots), $l_{\text{arr}} = 0.5D$ (middle subplots), and $l_{\text{arr}} = 0.45D$ (right subplots). In all cases $\varepsilon^+ = 5 \cdot 10^{-2}$ that removes 6, 8 and 8 of the smallest $\nu_i^{-1}$, respectively.

Finally, on both subplots of Figure 3.16, instead of using the whole matrix $\widehat{\mathbb{P}}$, as it is obtained with thresholding with $\varepsilon^+ = 5 \cdot 10^{-2}$, we project on certain of its singular vectors. On the left subplot $l_{\text{arr}} = 0.5D$ and we project on the second and third singular vectors of $\widehat{\mathbb{P}}$, while on the right one $l_{\text{arr}} = 0.45D$ and we project just on the second singular vector. Both images exhibit better SNR compared to their counterparts in Figure 3.15, albeit with a worse range resolution.

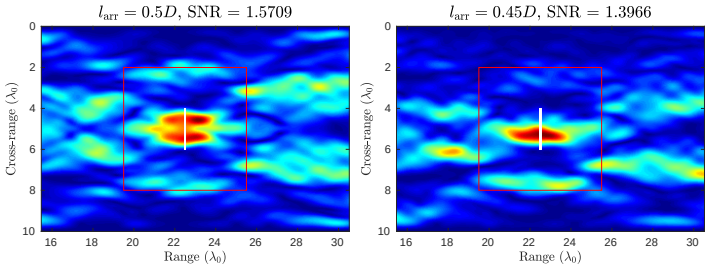


Figure 3.16: $\widetilde{\mathcal{I}}^{\text{KM,f}}$ images for the screen, with $l_{\text{arr}} = 0.5D$ where we project on the second and third singular vectors of $\widehat{\mathbb{P}}$ (left subplot) and $l_{\text{arr}} = 0.45D$ where we project on the second singular vector. In both cases $\widehat{\mathbb{P}}$ was derived with $\varepsilon^+ = 5 \cdot 10^{-2}$.

## 3.3 A semicircular scatterer

So far, we have analyzed our proposed imaging method for the case of a vertical screen, where we have explored the good properties of the projected response matrix $\widehat{\mathbb{P}}$ and established a connection between its singular vectors and the prolate spheroidal wave functions. Now, we want to see whether the properties that we have observed for the screen model problem carry over for different scatterer geometries. Specifically, we wish to examine if the relation between the number of 'significant' singular values and the size of the object still holds and if the usual ordering in focusing is preserved when we use selective imaging, *i.e.* do our images still focus on the bulk of the object when we deploy the singular vectors that correspond to singular values in the signal subspace, and towards the edges when we use singular vectors that correspond to singular values that lie in the transient subspace? We are also going to assess the performance of imaging with a partial array-aperture for this shape of the reflector.

To this end, we assume that the reflector is a semicircle, in a setup as the one shown in Figure 3.17. As it can be seen in Appendix A.3, the array response matrix $\widehat{\Pi}$ for the semicircle problem may be written as

$$\widehat{\Pi} = -\frac{1}{4}\, V\, D_\beta\, Q\, B_M\, Q\, D_\beta\, V^T, \tag{3.37}$$

where the matrices $D_\beta, Q, V$ are the same as in (3.5) and (3.6), and $B_M$ is given by

$$(B_M)_{mn} = \int_0^\pi \mathrm{e}^{i(\beta_m+\beta_n)\rho(1-\sin t)} X_m(x_0-\rho\cos t) X_n(x_0-\rho\cos t)\,\rho\,dt, \quad m,n=1,2,\ldots.$$

Note that $B_M$ does not possess the special Toeplitz-minus-Hankel structure, as was the case for $A_M$ in the screen problem. Although we cannot find explicit expressions for the singular vectors of $B_M$, we are going to experiment with $\widetilde{\mathcal{I}}^{\mathrm{KM}}$ through some numerical examples.

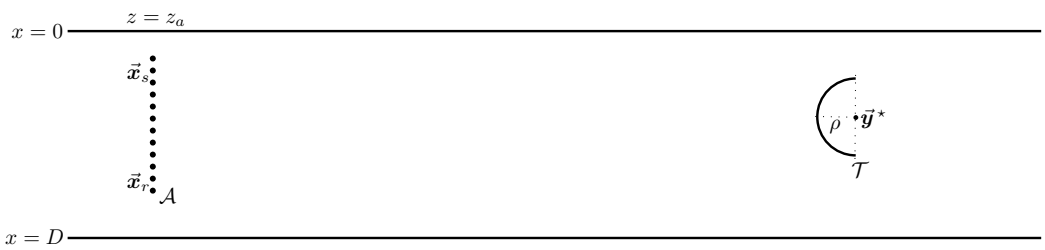


Figure 3.17: Active imaging setup for a semicircle, in an infinite strip.

As in the previous section, we assume a reference wavenumber $k_0 = \pi/10$ that corresponds to a reference wavelength $\lambda_0$ and we consider a waveguide with depth equal to $D = 10\lambda_0$ and constant sound speed $c_0$. We use a single frequency with associated wavenumber $k = 0.975k_0$. The diameter of the semicircle is taken equal to $b = 2\lambda_0$ and is centered at $\vec{\boldsymbol{y}}^\star = (22, 5)\lambda_0$. In Figure 3.18 we plot the imaging results for $\widetilde{\mathcal{I}}^{\mathrm{KM}}$, for the semicircle. We observe again that our image mainly focuses on the leftmost side of the reflector.

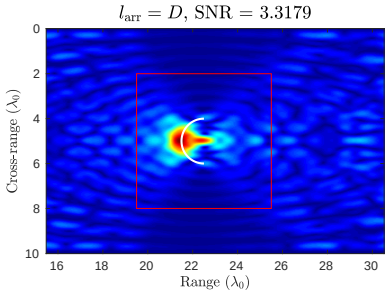


Figure 3.18: Values of $\widetilde{\mathcal{I}}^{\mathrm{KM}}$ for the semicircle, for $b = 2\lambda_0$, and $k = 0.975k_0$.

In Figure 3.19, we plot the normalized singular values of $\widehat{\mathbb{P}}$ for the semicircle. Now we see that the first 3 singular values are above 0.7 and there are also 2 singular values slightly above 0.3. Recall that for the screen model problem the special structure of $A_M$ allowed us to obtain a theoretical estimate for the number of significant singular values; it was approximately equal to $[2b/\lambda]$, where $b$ was the length of the screen. Unfortunately, we cannot prove something like that in the case of the semicircle. However, using the formula $[2b/\lambda]$ as 'a rule of thumb' for the typical length $b = 2\lambda_0$, that corresponds to the diameter of the semicircle, we would expect to have roughly 4 significant singular values. This is a quite good 'guess' since the number of significant singular values appears here to be equal to 3. Therefore, it seems that a similar relation between the size of the object and the number of significant singular values like the one we have for the screen model problem is still valid for this geometry.

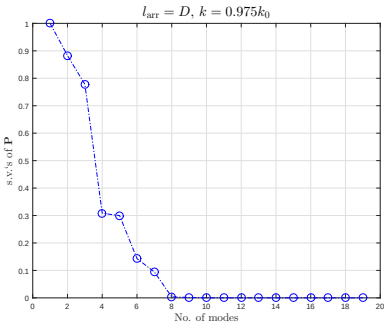


Figure 3.19: Normalized singular values of $\widehat{\mathbb{P}}$ for the semicircle, for $b = 2\lambda_0$ and $k = 0.975k_0$.

In Figure 3.20 we present the results for selective imaging with $\widetilde{\mathcal{I}}_J^{\text{KM}}$ for the semicircle, for $J = 1, 2, 3, 4$. We see that the selective imaging results in this case follow the same trend with those obtained for the screen case, i.e. when we project on the first singular vector we locate the center of the target, while projection on subsequent singular vectors results in images that are focusing towards the edges of the object.

Notice that, in this case, the use of selective imaging is more helpful than in the screen case in the sense that, apart from enabling us to focus on specific parts of the reflector, we have the added benefit of getting images that provide information for parts of the object that are not illuminated in the images that we get when we use the full matrix. We see that although in Figure 3.18 we recover the leftmost part of the scatterer, when we do selective imaging with $\widetilde{\mathcal{I}}_J^{\text{KM}}$ we achieve focusing towards the edges of the vertical diameter of the object for $J = 2, 3$. This illustrates the benefits of selective imaging that allows us to focus on the edges of the object and, therefore, to obtain more information about its shape and size.

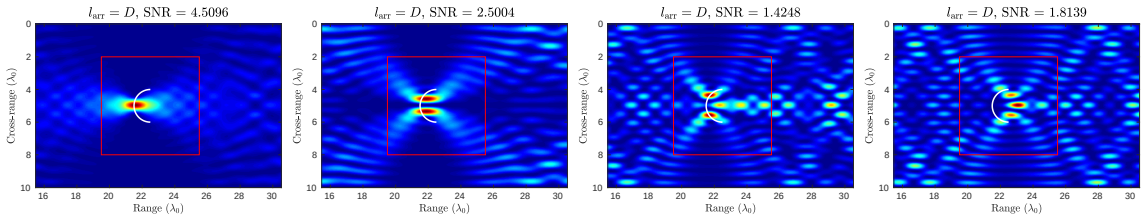


Figure 3.20: Values of $\widetilde{\mathcal{I}}^{\text{KM}}$ for the semicircle, for $b = 2\lambda_0$, and $k = 0.975k_0$, for $J = 1, 2, 3, 4$.

The last results showed us that despite not having the special Toeplitz-minus-Hankel form for the scattering matrix $B_M$ for the semicircle we still get the desired selective focusing behavior.

Lastly, we assess the performance of partial-aperture imaging for the semicircle. To this end, we first want to check whether we can extract results that display the same behavior as the one in Figure 3.5. Therefore, in Figure 3.21, we use the same parameters and indeed we see that as long as the minimum singular value $\nu_{\min}$ stays above machine epsilon (see Figure 3.8), the images that we obtain with a partial array-aperture are the same as if we were imaging with a full array-aperture.

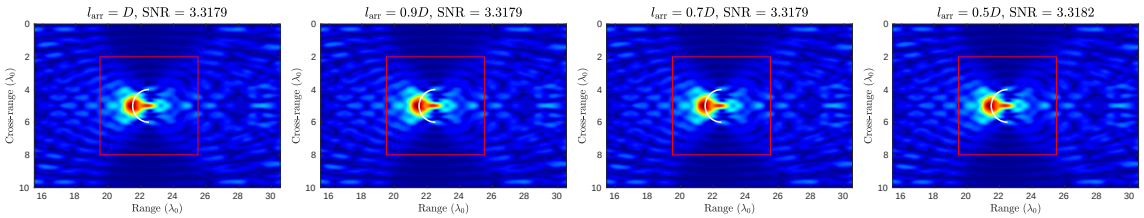


Figure 3.21: Imaging with $\widetilde{\mathcal{I}}^{\text{KM}}$ for the semicircle, when $l_{\text{arr}} = D,\ 0.9D,\ 0.7D,\ 0.5D$, for $k = 0.975k_0$.

In Figure 3.22 we present three cases where some of the smaller singular values fall below machine epsilon. Here, as we also saw in the screen case, we have to employ a threshold $\varepsilon^+$ that removes the reciprocals of those singular values. Specifically, we have $l_{\text{arr}} = 0.4D$ in the left subplot, $0.3D$ in the middle, and $0.2D$ in the right. We observe that as the array length decreases and we have to remove more and more singular values that fall below the machine epsilon, the quality of the image deteriorates in terms of both reconstruction and SNR.

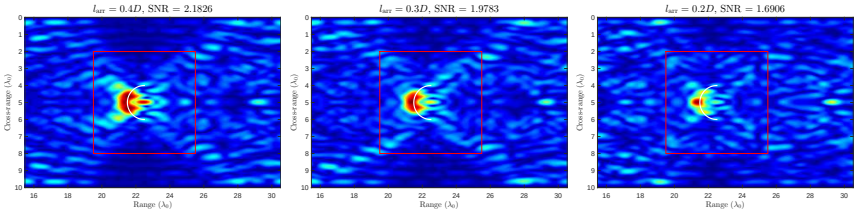


Figure 3.22: Imaging with $\widetilde{\mathcal{I}}^{\text{KM}}$ for the semicircle with $\varepsilon^+ = 10^{-15}$ when $l_{\text{arr}} = 0.4D$ (left), $0.3D$ (middle) and $0.2D$ (right), for $k = 0.975k_0$.

Lastly, in Figure 3.23 we present the limiting case where, similar to the result shown in Figure 3.11, we have that $l_{\text{arr}} = 0.1D$ and a reduced $h = \lambda_0/20$. We again recover information about the object, even after removing 90% of the array's original size.

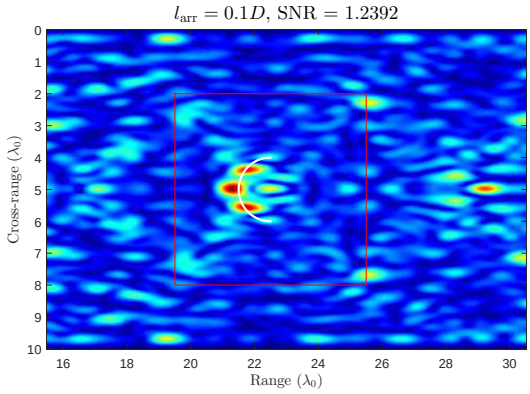


Figure 3.23: Imaging with $\widetilde{\mathcal{I}}^{\text{KM}}$ for the semicircle with $\varepsilon^+ = 10^{-15}$ when $l_{\text{arr}} = 0.1D$, for $h = \lambda_0/20$ and $k = 0.975k_0$.

**Remark 8** *In (3.4) and (3.37) we can split the array response matrix $\widehat{\Pi}$ into three parts. First, the product $V\,D_\beta\,Q$ forms a matrix that describes the propagation of the field from the array to the scatterer's location. This then interacts with a matrix that contains information about its geometry; this is the matrix $A_M$ for the screen problem and $B_M$ for the semicircle. Then, the field is propagated back to the array with the transpose of the propagating matrix. This structure is important since it allows us to relate directly the properties of the projected matrix $\widehat{\mathbb{P}}$ with those of the scattering matrices $A_M$ and $B_M$. Let us also note that we expect that all results shown in this section still hold for scatterers whose array response matrix may be written in a form such as (3.37), i.e. under the Born approximation.*

## 3.4 Algorithm for imaging

To close this chapter, we summarize the process for imaging with partial arrays, in the form of an algorithm. First, let us recall the basic components of our imaging method.

- We first compute the eigenvalues $\nu_j$, $j = 1, 2, \ldots, M$, and the corresponding orthonormal eigenvectors $\boldsymbol{w}^j = (w_1^j, w_2^j, \ldots, w_M^j)^T$ of the $M \times M$ Gram matrix $h(V^TV)$, and we form the $M \times M$ orthogonal matrix $W = (\boldsymbol{w}^1, \ldots, \boldsymbol{w}^M)$ and the diagonal matrix $D_\nu = \text{diag}(\nu_1, \ldots, \nu_M)$.

- Then we construct the trigonometric polynomials

$$s_j(x) = \sum_{i=1}^{M} w_i^j X_i(x), \quad j = 1, 2, \ldots, M,$$

and we consider the $M \times N$ matrix

$$\tilde{S} = D_\nu^{-1}\, S, \tag{3.38}$$

where

$$S_{ij} = s_i(x_j),\ i = 1, \ldots, M,\ j = 1, \ldots, N.$$

- Next, given the array response matrix $\widehat{\Pi}$ for the scattered field,we define $\widehat{\mathbb{P}}$ by

$$\widehat{\mathbb{P}} = D_\beta^{-1}\, W\, \tilde{S}\, \hat{\Pi}\, \tilde{S}^T\, W^T\, D_\beta^{-1}. \tag{3.39}$$

- Finally, we use $\widehat{\mathbb{P}}$ in $\widetilde{\mathcal{I}}^{\mathrm{KM}}$ (as defined in (2.12)), i.e.,

$$\widetilde{\mathcal{I}}^{\mathrm{KM}}(\vec{\boldsymbol{y}}^{\mathrm{s}}, \omega) = -\frac{1}{4h^2} \sum_{m,n=1}^{M} \mathrm{e}^{-\mathrm{i}(\beta_m+\beta_n)|z_{\mathrm{a}}-z^{\mathrm{s}}|} X_n(x^{\mathrm{s}}) X_m(x^{\mathrm{s}}) \widehat{\mathbb{P}}_{mn}(\omega), \tag{3.40}$$

for imaging.

Now, we are in a position to present our algorithm for imaging with $\widetilde{\mathcal{I}}^{\mathrm{KM}}$.

**Algorithm 1** *1. We compute the matrix $\tilde{S}$ in (3.38), and filter the matrix $D_\nu^{-1}$, by setting $1/\nu_i = 0$ for those indices $i$ that correspond to eigenvalues $\nu_i$ that are below a certain threshold $\varepsilon^+$.*

*2. Given the $N \times N$ array response matrix $\widehat{\Pi}$, we compute the $M \times M$ weighted projected response matrix $\widehat{\mathbb{P}}$ by means of (3.39).*

*3. We compute the imaging functional $\widetilde{\mathcal{I}}^{\mathrm{KM}}$, given by (3.40) for each point of our search domain $\mathcal{S}$ and graphically display its modulus.*

To summarize, in this chapter we examined the properties of the weighted projected response matrix $\widehat{\mathbb{P}}$ for the vertical screen model problem by deriving a relation between $\widehat{\mathbb{P}}$ and the Toeplitz-minus-Hankel matrix $A_M$ that describes the scattering of the screen. Through this, we found a link between the singular vectors of $A_M$ and prolate (or prolate-like) spheroidal wave functions, which allowed us to characterize the behavior of the selective imaging functional $\widetilde{\mathcal{I}}_J^{\mathrm{KM}}$. We also derived a relation between the size of the screen and the number of *significant* singular values of $A_M$. We also tested the performance of our imaging

method for a semicircular scatterer and observed that the properties of $\widetilde{\mathcal{I}}^{\mathrm{KM}}$ and $\widetilde{\mathcal{I}}_J^{\mathrm{KM}}$ seem to hold in general for different scatterers' geometries and not only for the screen. This will be further illustrated with more examples of different scatterers' geometries in Chapter 5.

# Chapter 4

# Resolution analysis

In this chapter we present the resolution analysis of our imaging method that is based on the evaluation of the functional $\widetilde{\mathcal{I}}^{\text{KM}}$ in points of the search domain. The analysis relies on the study of the behavior of the *point spread function (PSF)*, that is the behavior of the proposed imaging functional for a *point source* (passive case) or a *point scatterer* (active case). The PSF is a fundamental measure of the quality of an imaging functional since it determines its resolution. Specifically, we are going to examine the passive case since, as we will show, it turns out that the imaging functional for a point scatterer is the square of the functional for a point source.

This chapter is organised as follows: we first perform a resolution analysis for a single frequency. Next, we examine the 'response' of the proposed imaging functional to the use of multiple frequencies. We close this chapter with a result that concerns the partial-apreture array case.

## 4.1 Single frequency resolution analysis

In this section we consider a single frequency and we are interested in analyzing the behavior of $\widetilde{\mathcal{I}}^{\text{KM}}$ for a point scatterer. However, as we are going to show in a while, it suffices to examine the passive imaging case, *i.e.* the way the imaging functional behaves in the case of a point source.

**Passive case**

We consider the problem of imaging a point source placed at $\vec{\boldsymbol{x}}^\star = (z^\star, x^\star)$, using an array $\mathcal{A}$ that is vertically placed at a range equal to $z = z_a$ and spans the whole width of the waveguide. As we have seen in Chapter 2 (see (2.1)), the data that we have in our disposal, for a single frequency $\omega$, come in the form of the $N \times 1$ array response vector $\widehat{\Pi}(\vec{\boldsymbol{x}}_r; \omega)$, where

$$\widehat{\Pi}(\vec{\boldsymbol{x}}_r; \omega) = \widehat{G}(\vec{\boldsymbol{x}}_r, \vec{\boldsymbol{x}}^\star). \tag{4.1}$$

Next, we define the projected response vector $\widehat{\mathbb{P}}$ for the passive case, in a similar way as in the active case (see (2.9)),

$$\widehat{\mathbb{P}}_n(\omega) = \beta_n \int_0^D \mathrm{d}x_r \, \widehat{\Pi}(\vec{\boldsymbol{x}}_r, \omega) X_n(x_r). \tag{4.2}$$

Then, we define $\widetilde{\mathcal{I}}^{\mathrm{KM}}$ (see (2.12)) for the passive case, which we denote hereinafter by $\widetilde{\mathcal{I}}^{\mathrm{KM}}_{\mathrm{p}}$, as

$$\widetilde{\mathcal{I}}^{\mathrm{KM}}_{\mathrm{p}}(\vec{\boldsymbol{y}}^{\mathrm{s}}, \omega) = \sum_{n=1}^{M} \overline{\widehat{\mathbb{P}}_n(\omega)} \widetilde{G}_n(z_a, \vec{\boldsymbol{y}}^{\mathrm{s}}), \tag{4.3}$$

where $\widetilde{G}_n$ are the weighted projections of the Green's function on the propagating modes, as in (2.11).

Inserting (4.1) into (4.2), we get that

$$\widehat{\mathbb{P}}_n(\omega) = \beta_n \int_0^D \mathrm{d}x_r \, \widehat{G}_n(z_a, \vec{\boldsymbol{x}}^\star) X_n(x_r) = \widetilde{G}_n(z_a, \vec{\boldsymbol{x}}^\star). \tag{4.4}$$

Therefore, the passive imaging functional for a point source, is given by

$$\widetilde{\mathcal{I}}^{\mathrm{KM}}_{\mathrm{p}}(\vec{\boldsymbol{y}}^{\mathrm{s}}, \omega) = \sum_{n=1}^{M} \overline{\widetilde{G}_n(z_a, \vec{\boldsymbol{x}}^\star)} \widetilde{G}_n(z_a, \vec{\boldsymbol{y}}^{\mathrm{s}}). \tag{4.5}$$

**Active case**

Now, let us "consider" the active imaging case, where we now try to image a point scatterer placed at $\vec{\boldsymbol{x}}^\star = (z^\star, x^\star)$. We will show that the active imaging functional $\widetilde{\mathcal{I}}^{\mathrm{KM}}$ is simply the square of the passive imaging functional $\widetilde{\mathcal{I}}^{\mathrm{KM}}_{\mathrm{p}}$. Indeed, as stated in (2.6), the array response

matrix in this case is given by

$$\widehat{\Pi}(\vec{\boldsymbol{x}}_s, \vec{\boldsymbol{x}}_r; \omega) = \widehat{G}(\vec{\boldsymbol{x}}^\star, \vec{\boldsymbol{x}}_s)\widehat{G}(\vec{\boldsymbol{x}}_r, \vec{\boldsymbol{x}}^\star). \tag{4.6}$$

Similar to what we just did for the passive case, it is easy to show that the projected response matrix $\widehat{\mathbb{P}}$ is given by

$$\widehat{\mathbb{P}}_{mn}(\omega) = \widetilde{G}_m(z_a, \vec{\boldsymbol{x}}^\star)\widetilde{G}_n(z_a, \vec{\boldsymbol{x}}^\star). \tag{4.7}$$

Therefore, we have that for a point scatterer, the imaging functional $\widetilde{\mathcal{I}}^{\mathrm{KM}}$ has the form

$$\begin{aligned}
\widetilde{\mathcal{I}}^{\mathrm{KM}}(\vec{\boldsymbol{y}}^{\mathrm{s}}; \omega) &= \sum_{m,n=1}^{M} \overline{\widetilde{G}_m(z_a, \vec{\boldsymbol{x}}^\star)}\, \overline{\widetilde{G}_n(z_a, \vec{\boldsymbol{x}}^\star)}\widetilde{G}_m(z_a, \vec{\boldsymbol{y}}^{\mathrm{s}})\widetilde{G}_n(z_a, \vec{\boldsymbol{y}}^{\mathrm{s}}) \\
&= \left(\sum_{n=1}^{M} \overline{\widetilde{G}_n(z_a, \vec{\boldsymbol{x}}^\star)}\widetilde{G}_n(z_a, \vec{\boldsymbol{y}}^{\mathrm{s}})\right)^2 \\
&= \left(\widetilde{\mathcal{I}}_{\mathrm{p}}^{\mathrm{KM}}(\vec{\boldsymbol{y}}^{\mathrm{s}}, \omega)\right)^2.
\end{aligned}$$

Having this in mind, we perform the resolution analysis for $\widetilde{\mathcal{I}}_{\mathrm{p}}^{\mathrm{KM}}$, instead of performing it for $\widetilde{\mathcal{I}}^{\mathrm{KM}}$. Hence, for the rest of the chapter, we assume that the array is placed at $z_a = 0$ and we seek a point source placed far enough from the array at $\vec{\boldsymbol{x}}^\star = (z^\star, x^\star)$. Then, if we replace the expression for the Green's function given by (1.15) into (4.1), taking into account only the propagating modes since we have assumed that $z^\star$ is large enough, we get

$$\widehat{\Pi}(\vec{\boldsymbol{x}}_r; \omega) = \frac{i}{2}\sum_{k=1}^{M} \frac{\mathrm{e}^{\mathrm{i}\beta_k z^\star}}{\beta_k} X_k(x_r)X_k(x^\star). \tag{4.8}$$

We also have that

$$\widehat{\mathbb{P}}_n(\omega) = \widetilde{G}_n(0, \vec{\boldsymbol{x}}^\star) = \mathrm{e}^{\mathrm{i}\beta_n z^\star} X_n(x^\star). \tag{4.9}$$

Hence, in view of the above relation, (4.3) reduces to

$$\widetilde{\mathcal{I}}_{\mathrm{p}}^{\mathrm{KM}}(\vec{\boldsymbol{y}}^{\mathrm{s}}, \omega) = \frac{\mathrm{i}}{2}\sum_{n=1}^{M} \mathrm{e}^{\mathrm{i}\beta_n(z^* - z^{\mathrm{s}})} X_n(x^*)X_n(x^s) \tag{4.10}$$

### 4.1.1 Cross-range resolution for $\widetilde{\mathcal{I}}_{\mathrm{p}}^{\mathrm{KM}}$

To examine the resolution in cross-range, we assume that the wavelength $\lambda$ is much smaller than the depth ($\lambda \ll D$) and that the search point is located at the correct range, *i.e.*, $z^{\mathrm{s}} = z^{\star}$. Then, recalling (1.11), (4.10) simplifies to

$$\widetilde{\mathcal{I}}_{\mathrm{p}}^{\mathrm{KM}}(\vec{\boldsymbol{y}}^{\mathrm{s}};\omega) = \frac{i}{D}\sum_{n=1}^{M} \sin\frac{n\pi x^{\star}}{D}\sin\frac{n\pi x^{\mathrm{s}}}{D}. \tag{4.11}$$

Then we prove the following:

**Proposition 7 (Cross-range resolution)** *Assume that the search point is located at the correct range, i.e.,* $\vec{\boldsymbol{y}}^{\mathrm{s}} = (z^{*}, x^{\mathrm{s}})$. *Then*

$$\widetilde{\mathcal{I}}_{\mathrm{p}}^{\mathrm{KM}}(\vec{\boldsymbol{y}}^{\mathrm{s}};\omega) \approx \frac{\mathrm{i}}{\lambda}\left[\mathrm{sinc}\left(\frac{2}{\lambda}(x^{*}-x^{\mathrm{s}})\right) - \mathrm{sinc}\left(\frac{2}{\lambda}(x^{*}+x^{\mathrm{s}})\right)\right], \tag{4.12}$$

*where the* sinc *function is defined as*

$$\mathrm{sinc}(x) := \frac{\sin(\pi x)}{\pi x}. \tag{4.13}$$

**Proof:** Letting $\xi_n = \lambda n/(2D)$ we may view the right-hand side of (4.11) as a Riemann sum that approximates an integral. Therefore, from (4.11) we have

$$\begin{aligned}
\widetilde{\mathcal{I}}_{\mathrm{p}}^{\mathrm{KM}}(\vec{\boldsymbol{y}}^{\mathrm{s}};\omega) &\approx \frac{2\mathrm{i}}{\lambda}\int_{0}^{1}\sin\left(\frac{2\pi x^{*}\xi_n}{\lambda}\right)\sin\left(\frac{2\pi x^{s}\xi_n}{\lambda}\right)d\xi_n \\
&= \frac{\mathrm{i}}{\lambda}\int_{0}^{1}\left[\cos\left(\frac{2\pi(x^{*}-x^{s})}{\lambda}\xi_n\right) - \cos\left(\frac{2\pi(x^{*}+x^{s})}{\lambda}\xi_n\right)\right]d\xi_n \\
&= \frac{\mathrm{i}}{\lambda}\left[\mathrm{sinc}\left(\frac{2}{\lambda}(x^{*}-x^{\mathrm{s}})\right) - \mathrm{sinc}\left(\frac{2}{\lambda}(x^{*}+x^{\mathrm{s}})\right)\right].
\end{aligned}$$

□

Now we are going to check the validity of these expressions and illustrate the PSF for a specific numerical example. To this end, we consider a reference wavelength $\lambda_0$ with a corresponding wavenumber $k_0 = \pi/10$ and we assume that our waveguide has width $D = 10\lambda_0$, constant sound speed $c_0$, and a source placed at $x^{*} = 4\lambda_0$. We use a single frequency with a corresponding wavenumber $k = 0.975k_0$. In Figure 4.1 we plot the normalized absolute values of (4.11) with a solid blue line and (4.12) with a dashed red line. We

confirm good agreement between the two expressions. We observe a clear focusing on the true location of the source and the presence of side lobes that decay as we move further away from the source. Defining the resolution as the width of the main lobe at its mid-height, we obtain here $\lambda/2$ resolution depicted in the plot with a green segment.

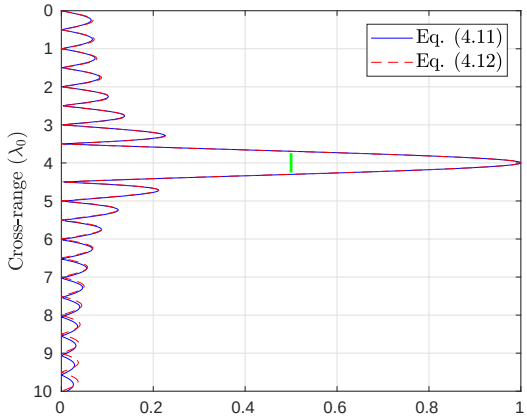


Figure 4.1: The absolute value of (4.11) (blue line) and (4.12) (dashed red line) for $D = 10\lambda_0$, $k = 0.975k_0$, $x^\star = 4\lambda_0$. The green segment indicates length equal to $\lambda/2$.

In Figure 4.2 we also compare the cross-range resolution of $\widetilde{\mathcal{I}}_{\mathrm{p}}^{\mathrm{KM}}$ given by (4.12), shown in a solid blue line, with the resolution of $\widetilde{\mathcal{I}}^{\mathrm{KM}}$, which is simply its square, plotted with a dashed red line. As expected, we observe an increase in the SNR of the image. There also appears to be no significant change in the resolution of the image, which remains equal to $\lambda/2$ for both the passive and the active case.

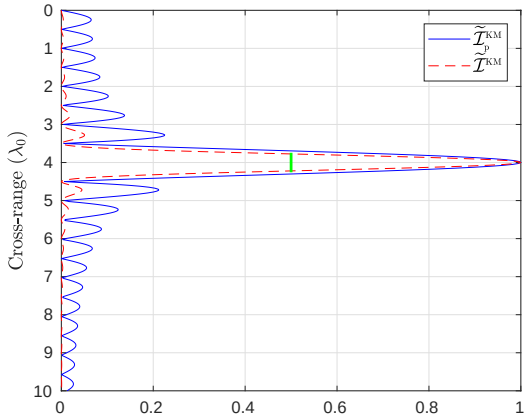


Figure 4.2: Cross-range resolution of $\widetilde{\mathcal{I}}_{\mathrm{p}}^{\mathrm{KM}}$ (blue line) and $\widetilde{\mathcal{I}}^{\mathrm{KM}}$(dashed red line) for $D = 10\lambda_0$, $k = 0.975k_0$, $x^\star = 4\lambda_0$. The green segment indicates length equal to $\lambda/2$.

### 4.1.2 Range resolution for $\widetilde{\mathcal{I}}_{\mathrm{p}}^{\mathrm{KM}}$

In order to estimate the resolution in range we assume that the search point is located at the correct depth, i.e. at $\vec{\boldsymbol{y}}^{\mathrm{s}} = (z^{\mathrm{s}}, x^{\star})$, so (4.10) becomes

$$\widetilde{\mathcal{I}}_{\mathrm{p}}^{\mathrm{KM}}(\vec{\boldsymbol{y}}^{\mathrm{s}}, \omega) = \frac{\mathrm{i}}{D} \sum_{n=1}^{M} \mathrm{e}^{\mathrm{i}\beta_n (z^* - z^{\mathrm{s}})} \sin^2\left(\frac{n\pi x^{\star}}{D}\right). \tag{4.14}$$

If we follow the same process as we did for the cross-range case in order to derive an analytical expression for the range resolution, we end up with an expression that is too complex and proves too hard to analyze. In an effort to simplify that expression, we assume that the source is placed at half the width of the waveguide, *i.e.* $x^{\mathrm{s}} = x^{\star} = D/2$. Then, (4.14) has the form

$$\widetilde{\mathcal{I}}_{\mathrm{p}}^{\mathrm{KM}}(\vec{\boldsymbol{y}}^{\mathrm{s}}, \omega) = \frac{\mathrm{i}}{D} \sum_{n=0}^{\lceil \frac{M}{2} \rceil - 1} \mathrm{e}^{\mathrm{i}\,\beta_{2n+1}(z^* - z^{s})}. \tag{4.15}$$

For this special case, we may prove the following:

**Lemma 1** *Assume that the point source is placed at half the width of the waveguide and the search point is located at the correct cross-range, i.e.,* $\vec{\boldsymbol{y}}^{\mathrm{s}} = (z^{\mathrm{s}}, x^{*})$, $x^{*} = D/2$. *Then*

$$\widetilde{\mathcal{I}}_{\mathrm{p}}^{\mathrm{KM}}(\vec{\boldsymbol{y}}^{\mathrm{s}}, \omega) \approx \frac{\mathrm{i}}{\lambda} \left[ 1 - \frac{\pi}{2} \mathbf{H}_1\left(\frac{2\pi}{\lambda}(z^* - z^{\mathrm{s}})\right) + \mathrm{i}\,\frac{\pi}{2} J_1\left(\frac{2\pi}{\lambda}(z^* - z^{\mathrm{s}})\right) \right], \tag{4.16}$$

*where* $J_1(x)$ *and* $\mathbf{H}_1(x)$ *denote the Bessel and Struve functions of order one, respectively.*

**Proof:** Let $\left(n + \frac{1}{2}\right)\frac{\lambda}{D} = \xi_n$. Then $\beta_{2n+1} = \frac{2\pi}{\lambda}\sqrt{1 - \xi_n^2}$ and the sum in the right-hand side of (4.15) may be seen as a Riemman sum that approximates the integral

$$\widetilde{\mathcal{I}}_{\mathrm{p}}^{\mathrm{KM}}(\vec{\boldsymbol{y}}^{\mathrm{s}}, \omega) \approx \frac{\mathrm{i}}{\lambda} \int_0^1 \mathrm{e}^{\mathrm{i}\frac{2\pi}{\lambda}(z^* - z^{s})\sqrt{1 - x^2}}\, dx. \tag{4.17}$$

We let $\alpha = 2\pi(z^* - z^{s})/\lambda$, hence we want to evaluate the integral $\int_0^1 \mathrm{e}^{\mathrm{i}\alpha\sqrt{1-x^2}}\, dx$. To this end, letting $x = \sin\theta$ we have

$$\begin{aligned} \int_0^1 \mathrm{e}^{\mathrm{i}\,\alpha\sqrt{1-x^2}}\, dx &\approx \int_0^{\pi/2} \mathrm{e}^{\mathrm{i}\alpha\cos\theta} \cos\theta\, d\theta \\ &= \int_0^{\pi/2} \cos(\alpha\cos\theta)\cos\theta\, d\theta + \mathrm{i}\int_0^{\pi/2} \sin(\alpha\cos\theta)\cos\theta\, d\theta =: I_1 + \mathrm{i}\, I_2. \end{aligned}$$

In $I_2$ we change variables $\theta = \frac{\pi}{2} - x$ to obtain

$$I_2 = \int_0^{\pi/2} \sin(\alpha \sin x) \sin x \, dx = \frac{\pi}{2} J_1(\alpha),$$

where the integral is found in [30, (3.715.2)].

For $I_1$ we integrate by parts

$$I_1 = \int_0^{\pi/2} \cos(\alpha \cos\theta) \, (\sin\theta)' \, d\theta = 1 - \alpha \int_0^{\pi/2} \sin(\alpha \cos\theta) \sin^2\theta \, d\theta = 1 - \frac{\pi}{2} \mathbf{H}_1(\alpha).$$

For the last integral above see [30, (3.716.16)]. Finally, we have that

$$\widetilde{\mathcal{I}}_{\mathrm{p}}^{\mathrm{KM}}(\vec{\boldsymbol{y}}^{\mathrm{s}}, \omega) \approx \frac{\mathrm{i}}{\lambda} \left( 1 - \frac{\pi}{2} \mathbf{H}_1(\alpha) + i \frac{\pi}{2} J_1(\alpha) \right). \tag{4.18}$$

□

Next, similar to what we did in the cross-range case, we illustrate (4.15) and its approximation (4.16) for a specific example. In Figure 4.3 we plot the modulus of the imaging functional (4.15) with a blue line and the modulus of (4.16) with a dashed red line, normalized with respect to their maximum values, using the same values for the parameters $D, k_0$ and $k$ as in the cross-range case, and assuming that a source is placed at $(z^\star, x^\star) = (22, 5)\lambda_0$. We observe that while the theoretical expression given by (4.16) fails to describe the oscillations away from the source's location in range, it captures the behavior of the main lobe really well. Also, similar to what we did for the cross-range case, we plot a green segment at the mid-height of the main lobe to indicate the resolution in range. In this case, its length is $2\lambda$.

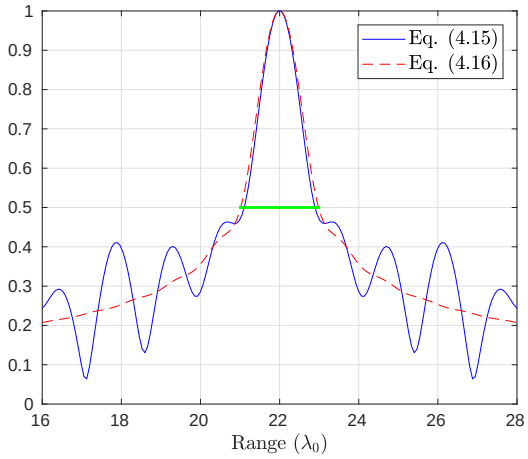


Figure 4.3: The modulus of (4.15) (blue line) and (4.16) (dashed red line) for $D = 10\lambda_0$, $k = 0.975k_0$, $(z^\star, x^\star) = (22, 5)\lambda_0$. The green segment indicates length equal to $2\lambda$.

Having seen that we may describe the resolution in range by a theoretical expression for the special case where the source is in the middle of the waveguide, we want to make sure that the resolution is the same for other cross-range locations of the source. Therefore, in Figure 4.4 we plot the modulus of (4.14) for the case where $x^\star = 5\lambda_0$ with a blue line, $x^\star = 8\lambda_0$ with a dashed red line and $x^\star = 2.5\lambda_0$ with a dash-dotted black line. We see that in all cases the behavior of the main lobe is very similar, despite the fact that the oscillations far from the source differ. Let us note that this test is not necessary for the cross-range case since when we are at the correct range, the exponential term in (4.10) vanishes and, therefore, the result we get does not depend on $z^\star$.

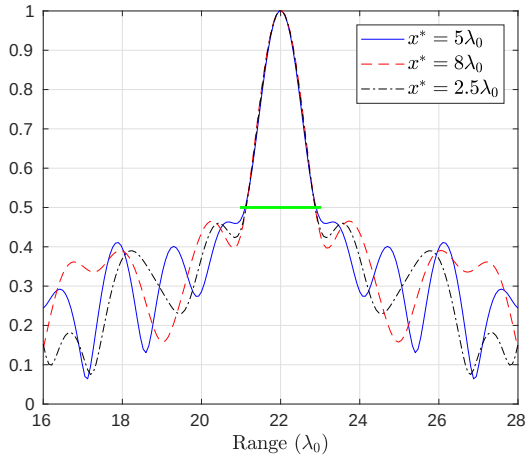


Figure 4.4: The absolute value of (4.14) for $D = 10\lambda_0$, $k = 0.975k_0$, $z^\star = 22\lambda_0$ and for $x^\star = 5\lambda_0$ (blue line), $8\lambda_0$ (dashed red line) and $2.5\lambda_0$ (dash-dotted black line). The green segment indicates length equal to $2\lambda$.

Lastly, in Figure 4.5 we compare the range resolution of $\widetilde{\mathcal{I}}_{\mathrm{p}}^{\mathrm{KM}}$, shown in a blue line and $\widetilde{\mathcal{I}}^{\mathrm{KM}}$ plotted with a dashed red line. The green segment has width $2\lambda$ and the black segment has width $\lambda$. Therefore, aside from the expected SNR gain for the active case which, as already stated, is the square of the passive case, we also seem to have a better resolution in range.

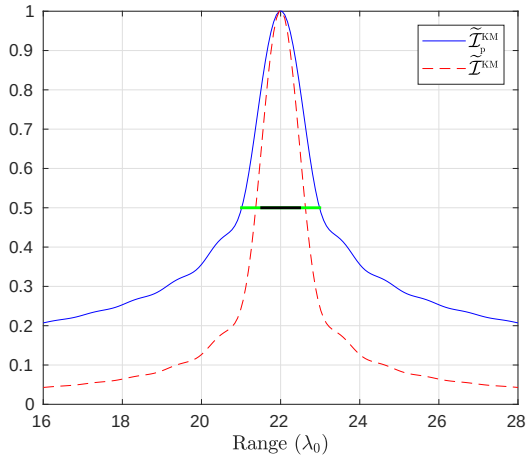


Figure 4.5: Range resolution of $\widetilde{\mathcal{I}}_{\mathrm{p}}^{\mathrm{KM}}$ (blue line) and $\widetilde{\mathcal{I}}^{\mathrm{KM}}$(dashed red line) for $D = 10\lambda_0$, $k = 0.975k_0$, $x^\star = 4\lambda_0$. The green segment indicates length equal to $2\lambda$ and the black segment length equal to $\lambda$.

**Remark 9** *As a summary of this section, let us note that the plots in Figures 4.2 and 4.5*

*show the point spread function (PSF) of $\widetilde{\mathcal{I}}_{\mathrm{p}}^{\mathrm{KM}}$ and $\widetilde{\mathcal{I}}^{\mathrm{KM}}$ as a function of cross-range and range, respectively. We observe that the PSF is centered at the correct location and the resolution of the imaging method can be determined using these plots. If we define, for example, the resolution as the width of the PSF at half its maximal value we obtain a cross-range resolution of $\lambda/2$ for both $\widetilde{\mathcal{I}}_{\mathrm{p}}^{\mathrm{KM}}$ and $\widetilde{\mathcal{I}}^{\mathrm{KM}}$ (see Figure 4.2) and a range resolution of $2\lambda$ for $\widetilde{\mathcal{I}}_{\mathrm{p}}^{\mathrm{KM}}$ case and $\lambda$ for $\widetilde{\mathcal{I}}^{\mathrm{KM}}$ (see Figure 4.5).*

## 4.2 Resolution analysis in the multiple frequency case

In this section, we investigate the performance of $\widetilde{\mathcal{I}}_{\mathrm{p}}^{\mathrm{KM}}$ when we use multiple frequencies. Recalling the definition given in (2.13), the multiple frequency version of $\widetilde{\mathcal{I}}_{\mathrm{p}}^{\mathrm{KM}}$ is simply an addition over frequencies, hence

$$\widetilde{\mathcal{I}}_{\mathrm{p}}^{\mathrm{KM}}(\vec{\boldsymbol{y}}^s) := \sum_{l=1}^{N_f} \widetilde{\mathcal{I}}_{\mathrm{p}}^{\mathrm{KM}}(\vec{\boldsymbol{y}}^s; f_l) \tag{4.19}$$

where $f_l$, $l = 1, \ldots, N_f$ are discrete frequencies that span the available frequency interval $[f_{\min}, f_{\max}]$. For the purposes of this chapter, we will assume that we have a continuous spectrum of frequencies, covering the interval $[f_{\min}, f_{\max}]$. Then, we may replace the sum in (4.19) with an integral, and write

$$\widetilde{\mathcal{I}}_{\mathrm{p}}^{\mathrm{KM}}(\vec{\boldsymbol{y}}^s) := \int_{f_{\min}}^{f_{\max}} \widetilde{\mathcal{I}}_{\mathrm{p}}^{\mathrm{KM}}(\vec{\boldsymbol{y}}^s; f)\, df \tag{4.20}$$

We call the length of the interval $B = f_{\max} - f_{\min}$ the bandwidth and we assume that $f_{\min} = f_c - B/2$ and $f_{\max} = f_c + B/2$, where $f_c = (f_{\min} + f_{\max})/2$ is the central frequency. Let us note here that in (4.20) we use the frequency $f$ as an argument instead of the angular frequency $\omega$.

### 4.2.1 Cross-range resolution

First, we start with the behavior of $\widetilde{\mathcal{I}}_{\mathrm{p}}^{\mathrm{KM}}$ in the cross-range direction. As shown in (4.12), the expression for the resolution in cross-range is

$$\widetilde{\mathcal{I}}_{\mathrm{p}}^{\mathrm{KM}}(\vec{\boldsymbol{y}}^{\mathrm{s}}; \omega) \approx \frac{\mathrm{i}}{\lambda} \left( \operatorname{sinc}\left( \frac{2}{\lambda}(x^* - x^{\mathrm{s}}) \right) - \operatorname{sinc}\left( \frac{2}{\lambda}(x^* + x^{\mathrm{s}}) \right) \right), \tag{4.21}$$

where $\text{sinc}(x) = (\sin(\pi x))/(\pi x)$.

In fact, we may further simplify (4.21), by ignoring the second sinc function, since we expect that it takes values that are approximately zero, due to its large argument ($\sim 4x^*/\lambda$) for values of $x^{\text{s}}$ near the source location. Therefore we can write that the resolution in cross-range is determined by

$$\widetilde{\mathcal{I}}_{\text{p}}^{\text{KM}}(\vec{\boldsymbol{y}}^{\text{s}};\omega) \approx \frac{\text{i}}{\lambda}\text{sinc}\left(\frac{2}{\lambda}(x^* - x^{\text{s}})\right). \tag{4.22}$$

We can verify this numerically, as shown in Figure 4.6, where we plot the absolute values of (4.21) with a blue line and (4.22) with a dashed red line. It is immediate to see that the two lines are in excellent agreement and, therefore, we may use (4.22) for our computations.

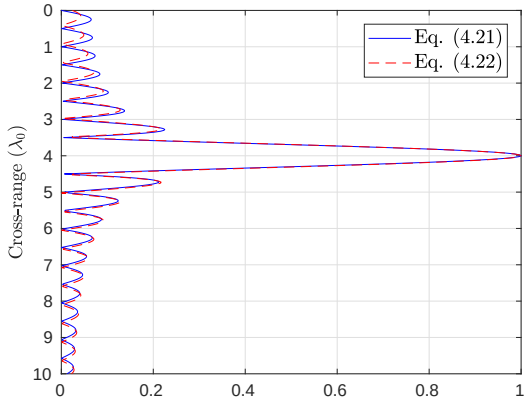


Figure 4.6: The absolute value of (4.21) (blue line) and (4.22) (dashed red line) for $D = 10\lambda_0$, $k = 0.975k_0$, $x^\star = 4\lambda_0$.

Using (4.22), when imaging with multiple frequencies, we may prove the following:

**Lemma 2** *For multiple frequencies $f_l$, $l = 1, \ldots, N_f$, that span the frequency range $[f_{\min}, f_{\max}]$, the imaging functional $\widetilde{\mathcal{I}}_{\text{p}}^{\text{KM}}$ (defined in (4.19)) evaluated at the correct range is approximated by*

$$\widetilde{\mathcal{I}}_{\text{p}}^{\text{KM}}(\vec{\boldsymbol{y}}^{\text{s}}) \approx \frac{Bf_c}{2c_0}\ \text{sinc}\left(\frac{B}{c_0}(x^\star - x^s)\right)\text{sinc}\left(\frac{2f_c}{c_0}(x^\star - x^s)\right), \tag{4.23}$$

*where $B$ is the bandwidth and $f_c$ is the central frequency.*

**Proof:** As a first step, we will perform some additional calculations and re-write (4.22) in

terms of $f$, instead of $\lambda$:

$$\widetilde{\mathcal{I}}_{\mathrm{p}}^{\mathrm{KM}}(\vec{\boldsymbol{y}}^{\mathrm{s}}; f) \approx \frac{1}{2\lambda}\mathrm{sinc}\left(\frac{2}{\lambda}(x^* - x^{\mathrm{s}})\right) \tag{4.24}$$

$$= \frac{1}{4\pi(x^\star - x^s)}\sin\left(\frac{2\pi}{c_0}f(x^\star - x^s)\right). \tag{4.25}$$

To get from (4.24) to (4.25) we simply replaced the expression for the sinc function given earlier in (4.13) and the fact that $\lambda = c_0/f$.

To investigate the PSF behaviour with multiple frequencies, we integrate (4.22) with respect to frequency $f$ over an interval with bandwidth $B$. We slightly abuse notation by letting $\widetilde{\mathcal{I}}_{\mathrm{p}}^{\mathrm{KM}}(x; B)$ denote the PSF for multiple frequencies at the correct range. Then we have

$$\begin{aligned}\widetilde{\mathcal{I}}_{\mathrm{p}}^{\mathrm{KM}}(x; B) &= \int_{f_{\min}}^{f_{\max}} \widetilde{\mathcal{I}}_{\mathrm{p}}^{\mathrm{KM}}(z^\star, x; f)df \approx \int_{f_{\min}}^{f_{\max}} \frac{1}{4\pi(x^\star - x^s)}\sin\left(\frac{2\pi}{c_0}f(x^\star - x^s)\right) df \\ &= \frac{1}{2}\int_{f_{\min}}^{f_{\max}} \frac{1}{\alpha_x}\sin\left(\frac{\alpha_x}{c_0}f\right) df, \end{aligned} \tag{4.26}$$

where

$$\alpha_x := 2\pi(x^* - x^s).$$

Then, we get that (4.26) becomes

$$\widetilde{\mathcal{I}}_{\mathrm{p}}^{\mathrm{KM}}(x; B) \approx \frac{c_0}{2\alpha_x^2}\left[\cos\left(\frac{\alpha_x}{c_0}f_{\min}\right) - \cos\left(\frac{\alpha_x}{c_0}f_{\max}\right)\right]. \tag{4.27}$$

Using the trigonometric identity

$$\cos a - \cos b = -2\sin\frac{a-b}{2}\sin\frac{a+b}{2}$$

where $a = \frac{\alpha_x}{c_0}f_{\min}$ and $b = \frac{\alpha_x}{c_0}f_{\max}$, as well as the fact that

$$\frac{f_{\min} - f_{\max}}{2} = -B/2 \quad \text{and} \quad \frac{f_{\min} + f_{\max}}{2} = f_c,$$

we finally get that

$$\begin{aligned}\widetilde{\mathcal{I}}_{\mathrm{p}}^{\mathrm{KM}}(x;B) &\approx \frac{c_0}{\alpha_x^2}\,\sin\left(\frac{B}{2c_0}\alpha_x\right)\sin\left(\frac{f_c}{c_0}\alpha_x\right)\\ &= \frac{Bf_c}{2c_0}\,\mathrm{sinc}\left(\frac{B}{c_0}(x^\star - x^s)\right)\mathrm{sinc}\left(\frac{2f_c}{c_0}(x^\star - x^s)\right). \end{aligned} \tag{4.28}$$

□

In Figure 4.7 we examine how (4.28) behaves for various bandwidths. We consider a reference wavelength $\lambda_0$ with a corresponding wavenumber $k_0 = \pi/10$ and we have that our waveguide has width $D = 10\lambda_0$, while our source is placed in cross-range at $x^\star = 4\lambda_0$. In our experiment, we have a central frequency $f_c$ with a corresponding wavenumber $k_c = 0.975k_0$ and we consider three different bandwidths: $B = 0.1f_c$, shown with the blue line, $B = 0.5f_c$ shown in red, and $B = f_c$ shown in the black line. We observe that when we increase the bandwidth the amplitudes of the side lobes decrease, thus resulting in an SNR increase.

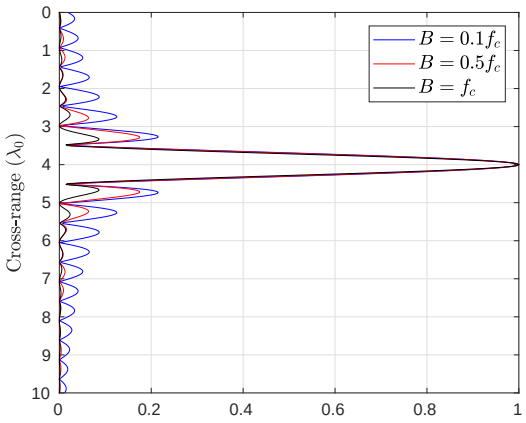


Figure 4.7: Cross-range resolution for $\widetilde{\mathcal{I}}_{\mathrm{p}}^{\mathrm{KM}}$ for multiple frequencies for a source placed at $x^\star = 4\lambda_0$ and $B = 0.1f_c$ (blue line), $B = 0.5f_c$ (red line) and $B = f_c$ (black line), with $k_c = 0.975k_0$.

Specifically, we may quantify the SNR gain in each image by computing the ratio of the maximum value to the second taller peak. The maximum value is taken at $x^s = x^\star$, while the latter is a root of $\frac{d}{dx}\big(\widetilde{\mathcal{I}}_{\mathrm{p}}^{\mathrm{KM}}(x;B)\big) = 0$ for $x \neq x^\star$. In Table 4.1 we present the SNR values for the cases we examined in Figure 4.7, where the numerical values were extracted from the associated graphs. We observe that we have a slight increase in SNR between $B = 0.1f_c$ and $B = 0.5f_c$, while when we take the bandwidth equal to the central frequency the SNR increases by a factor of two compared to the bandwidth $B = 0.5f_c$.

| $B$ | SNR |
|---|---|
| $0.1f_c$ | 4.6468 |
| $0.5f_c$ | 5.7143 |
| $f_c$ | 11.6063 |

Table 4.1: SNR values in cross-range for various bandwidths.

Let us also note that the results shown in Figure 4.7 suggest that the resolution of our imaging method remains the same, regardless of the bandwidth we choose and is in fact determined by the central frequency.

### 4.2.2 Range resolution

Next, we move to the case where we are located at the correct cross-range and, specifically, we assume that $x^\star = D/2$. Then the expression of $\widetilde{\mathcal{I}}_{\mathrm{p}}^{\mathrm{KM}}$ evaluated at the correct cross-range is given by

$$\widetilde{\mathcal{I}}_{\mathrm{p}}^{\mathrm{KM}}(\vec{\boldsymbol{y}}^{\mathrm{s}},\omega) \approx \frac{1}{2\lambda h}\left(1-\frac{\pi}{2}\mathbf{H}_1(\frac{2\pi}{\lambda}(z^\star-z^s))+i\frac{\pi}{2}J_1(\frac{2\pi}{\lambda}(z^\star-z^s))\right). \tag{4.29}$$

**Lemma 3** *For multiple frequencies $f_l$, $l=1,\ldots,N_f$, that span the frequency range $[f_{\min},f_{\max}]$, the imaging functional $\widetilde{\mathcal{I}}_{\mathrm{p}}^{\mathrm{KM}}$ (defined in (4.19)) evaluated at the correct cross-range is approximated by*

$$\begin{aligned}\widetilde{\mathcal{I}}_{\mathrm{p}}^{\mathrm{KM}}(\vec{\boldsymbol{y}}^{\mathrm{s}}) = \frac{\Gamma(5/2)(4\pi+24)-3\sqrt{\pi}\alpha^2}{96c_0\Gamma(5/2)}\Bigg\{ & f_{\max}^2-f_{\min}^2 \\ & -f_{\max}^4\ {}_2F_3\left(1,2;\frac{3}{2},\frac{5}{2},3;-\frac{\alpha^2f_{\max}^2}{4}\right)+f_{\min}^4\ {}_2F_3\left(1,2;\frac{3}{2},\frac{5}{2},3;-\frac{\alpha^2f_{\min}^2}{4}\right) \\ & +\mathrm{i}\left[\alpha f_{\max}^3\ {}_1F_2\left(\frac{3}{2};2,\frac{5}{2};-\frac{\alpha^2f_{\max}^2}{4}\right)-\alpha f_{\min}^3\ {}_1F_2\left(\frac{3}{2};2,\frac{5}{2};-\frac{\alpha^2f_{\min}^2}{4}\right)\right]\Bigg\},\end{aligned} \tag{4.30}$$

*where ${}_pF_q$ is called a Generalized Hypergeometric Series [4] and has the formula*

$${}_pF_q\left(\alpha_1,\alpha_2,\ldots,\alpha_p;\rho_1,\ldots,\rho_q;z\right)=\sum_{n=0}^{\infty}\frac{(\alpha_1)_n(\alpha_2)_n\cdots(\alpha_p)_n}{n!(\rho_1)_n(\rho_2)_n\cdots(\rho_q)_n}z^n,$$

*and*

$$(a)_n=a(a+1)(a+2)\cdots(a+n-1),\quad (a)_0=1.$$

*The values $\alpha_i,\ i=1,\dots,p$ are called the numerator parameters, while $\rho_j,\ j=1,\dots,q$ are the denominator parameters.*

**Proof:** First, let us write (4.29) with respect to $f$:

$$\widetilde{\mathcal{I}}_{\mathrm{p}}^{\mathrm{KM}}(\vec{\boldsymbol{y}}^{\mathrm{s}},f)\approx\frac{f}{2c_0}-\frac{\pi f}{4c_0}\mathbf{H}_1\left(\frac{2\pi f}{c_0}(z^\star-z^s)\right)+i\frac{\pi f}{4c_0}J_1\left(\frac{2\pi f}{c_0}(z^\star-z^s)\right). \tag{4.31}$$

We want to integrate (4.31) over $f$, hence

$$\widetilde{\mathcal{I}}_{\mathrm{p}}^{\mathrm{KM}}(\vec{\boldsymbol{y}}^{\mathrm{s}})=\int_{f_{\min}}^{f_{\max}}\frac{f}{2c_0}-\frac{\pi f}{4c_0}\mathbf{H}_1\left(\frac{2\pi f}{c_0}(z^\star-z^s)\right)+i\frac{\pi f}{4c_0}J_1\left(\frac{2\pi f}{c_0}(z^\star-z^s)\right)\ df \tag{4.32}$$

and we will perform the integration part by part, so

$$\begin{aligned}\widetilde{\mathcal{I}}_{\mathrm{p}}^{\mathrm{KM}}(\vec{\boldsymbol{y}}^{\mathrm{s}})=&\int_{f_{\min}}^{f_{\max}}\frac{f}{2c_0}\ df-\int_{f_{\min}}^{f_{\max}}\frac{\pi f}{4c_0}\mathbf{H}_1\left(\frac{2\pi f}{c_0}(z^\star-z^s)\right)\ df\\&+i\int_{f_{\min}}^{f_{\max}}\frac{\pi f}{4c_0}J_1\left(\frac{2\pi f}{c_0}(z^\star-z^s)\right)\ df\\&:=I_1-I_2+\mathrm{i}I_3\end{aligned}$$

The computation of

$$I_1=\int_{f_{\min}}^{f_{\max}}\frac{f}{2c_0}\ df$$

trivially gives

$$I_1=\frac{f_{\max}^2-f_{\min}^2}{4c_0}. \tag{4.33}$$

Next, we wish to compute

$$I_2=\int_{f_{\min}}^{f_{\max}}\frac{\pi f}{4c_0}\mathbf{H}_1\left(\frac{2\pi f}{c_0}(z^\star-z^s)\right)\ df. \tag{4.34}$$

Following [16, 1.4.1.1], for $\nu=\lambda=1$ and $\alpha=2\pi(z^\star-z^s)/c_0$, we have that

$$I_2=\frac{\sqrt{\pi}\alpha^2}{32c_0\Gamma(5/2)}\left[f_{\max}^4\ {}_2F_3\left(1,2;\frac{3}{2},\frac{5}{2},3;-\frac{\alpha^2f_{\max}^2}{4}\right)-f_{\min}^4\ {}_2F_3\left(1,2;\frac{3}{2},\frac{5}{2},3;-\frac{\alpha^2f_{\min}^2}{4}\right)\right]. \tag{4.35}$$

Lastly, we compute

$$I_3 = \int_{f_{\min}}^{f_{\max}} \frac{\pi f}{4c_0} J_1\left(\frac{2\pi f}{c_0}(z^\star - z^s)\right) \, df, \tag{4.36}$$

which, evaluated by `Mathematica`, gives us

$$I_3 = \frac{\pi}{24c_0}\left[\alpha f_{\max}^3 \, {}_1F_2\left(\frac{3}{2}; 2, \frac{5}{2}; -\frac{\alpha^2 f_{\max}^2}{4}\right) - \alpha f_{\min}^3 \, {}_1F_2\left(\frac{3}{2}; 2, \frac{5}{2}; -\frac{\alpha^2 f_{\min}^2}{4}\right)\right]. \tag{4.37}$$

By combining (4.33), (4.35), and (4.37), we end up with (4.30). □

**Remark 10** *Although (4.30) offers an analytic expression for the behavior of $\widetilde{\mathcal{I}}_{\mathrm{p}}^{\mathrm{KM}}$ in the range direction when we use multiple frequencies, this expression is rather complicated. Therefore, for this case, we will extract our information by its graphical representation.*

In Figure 4.8 we examine how the modulus of (4.30) behaves for various bandwidths. We consider the same setup as in Figure 4.7, while our scatterer is placed at $\vec{\boldsymbol{x}}^\star = (22, 5)\lambda_0$. We observe that for the smallest bandwidth $B = 0.1f_c$, plotted with a blue line the main lobe seems very wide and has no roots in our imaging window. As we move to larger bandwidths we observe an improvement in resolution and a significant increase in SNR. Let us also note that for $B = 0.5f_c$ and $B = f_c$ we seem to have a sinc-like behavior which reminds us of the cross-range plots, albeit with a worse resolution.

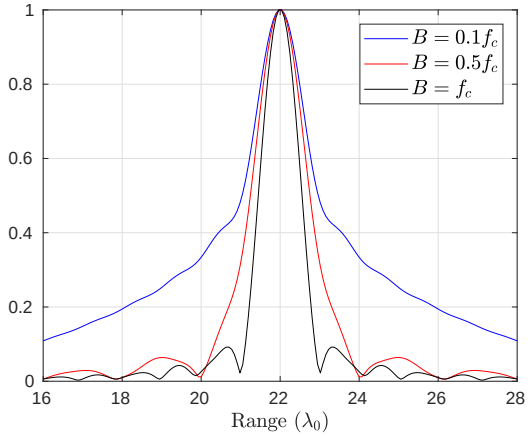


Figure 4.8: Range resolution for $\widetilde{\mathcal{I}}_{\mathrm{p}}^{\mathrm{KM}}$ for multiple frequencies for a source placed at $x^\star = 4\lambda_0$ and $B = 0.1f_c$ (blue line), $B = 0.5f_c$ (red line) and $B = f_c$ (black line), with $k_c = 0.975k_0$.

## 4.3 A result for partial aperture

In this section, we will prove that in the case of a point scatterer, the projected response matrix $\widehat{\mathbb{P}}$ created by (3.30) and (3.31) for the partial aperture case, is the same as for the full-aperture case.

**Proposition 8** *Let a single point scatterer of unit reflectivity be located at $\vec{\boldsymbol{x}}^\star = (z^\star, x^\star)$. We assume that the array $\mathcal{A}$ is at range $z = z_a$, and far enough from the scatterer so that the evanescent part of the wave field may be neglected. Then the projected array response matrix $\widehat{\mathbb{P}}$ defined by (3.30) and (3.31) for a partial aperture array is equal to the projected matrix $\widehat{\mathbb{P}}$ for an array that spans the whole vertical cross-section $[0, D]$.*

**Proof:** For a single point scatterer the $(s, r)$ entry of the array response matrix $\widehat{\Pi}$ is given by

$$\widehat{\Pi}(\vec{\boldsymbol{x}}_s, \vec{\boldsymbol{x}}_r; \omega) = \widehat{G}(\vec{\boldsymbol{x}}^\star, \vec{\boldsymbol{x}}_s)\widehat{G}(\vec{\boldsymbol{x}}_r, \vec{\boldsymbol{x}}^\star). \tag{4.38}$$

Moreover, note that for each $\vec{\boldsymbol{x}}$ far enough from $\vec{\boldsymbol{x}}^\star$, the Green's function may be written as

$$\widehat{G}(\vec{\boldsymbol{x}}, \vec{\boldsymbol{x}}^\star) \approx \sum_{i=1}^{M} C_i X_i(x), \tag{4.39}$$

since the evanescent modes can be neglected for large propagation distances. Obviously $C_i = \widehat{G}_i(z, \vec{\boldsymbol{x}}^\star)$, where $\widehat{G}_i(\cdot, \vec{\boldsymbol{x}}^\star)$ is defined in (2.10).

In the full-aperture array case, using (2.11) and (4.7), it is immediate to see that

$$\widehat{\mathbb{P}}_{nm} = \beta_n \beta_m C_n C_m.$$

If the array has partial aperture, then using (4.38) in (3.30) we get

$$\begin{aligned}
\widehat{\mathbb{S}}_{nm} &= \frac{1}{\nu_n \nu_m} \int_{\mathcal{A}} \int_{\mathcal{A}} \widehat{G}(\vec{\boldsymbol{x}}^*, \vec{\boldsymbol{x}}_s)\, \widehat{G}(\vec{\boldsymbol{x}}_r, \vec{\boldsymbol{x}}^*)\, s_n(x_s)\, s_m(x_r)\, dx_s dx_r \\
&= \frac{1}{\nu_n \nu_m} \sum_{k=1}^{M} \sum_{l=1}^{M} C_k C_l \int_{\mathcal{A}} s_n(x_s) X_k(x_s) dx_s \int_{\mathcal{A}} s_m(x_r) X_l(x_r) dx_r \\
&\overset{(3.29)}{=} \sum_{k=1}^{M} C_k w_k^n \sum_{l=1}^{M} C_l w_l^m.
\end{aligned}$$

Hence

$$\begin{aligned}\widehat{\mathbb{P}}_{nm} &\overset{(3.31)}{=} (D_\beta^{-1} W \widehat{\mathbb{S}} W^T D_\beta^{-1})_{nm} = \beta_n \beta_m \sum_{j=1}^{M} w_n^j \sum_{i=1}^{M} s_{ji} w_m^i \\ &= \beta_n \beta_m \sum_{j=1}^{M} w_n^j \sum_{i=1}^{M} \sum_{k=1}^{M} \sum_{l=1}^{M} C_k C_l w_k^j w_l^i w_m^i = \beta_n \beta_m \sum_{k=1}^{M} \sum_{l=1}^{M} C_k C_l \sum_{j=1}^{M} w_n^j w_k^j \sum_{i=1}^{M} w_l^i w_m^i \\ &= \beta_n \beta_m \sum_{k=1}^{M} \sum_{l=1}^{M} C_k C_l (WW^T)_{nk} (WW^T)_{lm} = \beta_n \beta_m C_n C_m,\end{aligned}$$

where the last equality holds since $W$ is orthogonal. □

**Remark 11**

*(a) An analogous result to that stated in Proposition 8 is expected to hold also for extended scatterers under the linearized Born approximation.*

*(b) In practice, Proposition 8 holds only as long as all relevant computations are performed exactly, i.e. with infinite precision. However, as we already saw in Section 3.2.3, numerical instabilities occur when the length of the array decreases and some of the smaller in magnitude eigenvalues $\nu_j$ drop below some small threshold $\epsilon$. In these cases, one may resort to a regularizing procedure like the one described in Section 3.2.3 in order to compensate the apparent loss of information compared with the full aperture array case.*

# Chapter 5

# Numerical experiments with data generated by a full wave model

In the previous chapters we have theoretically analyzed the proposed imaging methods and we have numerically examined their behavior in simplified model problems with data generated under the Born approximation. In this chapter we want to assess the performance of our methods in more realistic scatterer geometries with data that are generated by a full wave model. Specifically, we will examine two scatterer shapes: a square and a disc-shaped scatterer. We will present how imaging with $\widetilde{\mathcal{I}}^{\mathrm{KM}}$ and $\widetilde{\mathcal{I}}_J^{\mathrm{KM}}$ work for these scatterers, compare the results with their respective 1-D model problems and see that there are significant similarities that allow us to understand very well what we see. Then, we will examine the partial aperture case and demonstrate the major improvement that the use of multiple frequencies brings upon the performance of the method.

## 5.1 Numerical solution of the wave equation

Throughout this chapter, we will present numerical experiments for two scatterer geometries: a square and a disc shaped scatterer. In order to construct the array response matrix for each case, we compute numerically the solution of the wave equation problems (1.2) and (1.3). To this end, we use Montjoie [44], a high-order finite element C++ code developed at INRIA, which is designed to solve problems that arise in wave propagation phenomena.

### 5.1.1 Numerical setup

Following the setup that was presented in the previous chapters, we consider a homogeneous infinite waveguide of width $D$ that forms an infinite strip, *i.e.* $\Omega = (-\infty, \infty) \times (0, D)$. We assume a reference wavenumber $k_0 = \pi/10$ that corresponds to a reference wavelength $\lambda_0$, and take $D = 10\lambda_0$. The vertical array is placed at $z_{\rm a} = 2\lambda_0$ and consists of $N = 39$ transducers uniformly distributed in the water column with a pitch $h = \lambda_0/4$, thus spanning the whole depth of the waveguide. Let us note that in the partial array-aperture case the related array response matrix is extracted from the matrix that corresponds to the full aperture array, by removing the appropriate lines and columns.

The originally infinite (in the $z$-direction) domain is truncated by introducing two perfectly matched layers (PML) [6, 26], as shown in Figure 5.1. Each PML has a width of $5\lambda_0$, which was enough to absorb the waves efficiently so that there are no discernible wave reflections occurring from the PML. The resulting bounded computational domain has size $[0, 25]\lambda_0 \times [0, 10]\lambda_0$ and is discretized, in general, with quadrilaterals on which the usual basis functions of the $\mathbb{Q}_n$ family are used, where

$$\mathbb{Q}_n = \text{span}\{x^\ell y^m,\ 0 \le \ell, m \le n\}.$$

Specifically, for the square scatterer we discretize our domain using squares of side $\lambda/2$ and we use $\mathbb{Q}_8$ polynomials, while for the disc we use quadrilaterals in a neighborhood of the scatterer, and squares with side $\lambda$ elsewhere; in this case, we use $\mathbb{Q}_{12}$ polynomials. Numerical quadrature in space is based on Gauss-Lobatto rules, while for the time discretization, we use a fourth–order leapfrog scheme.

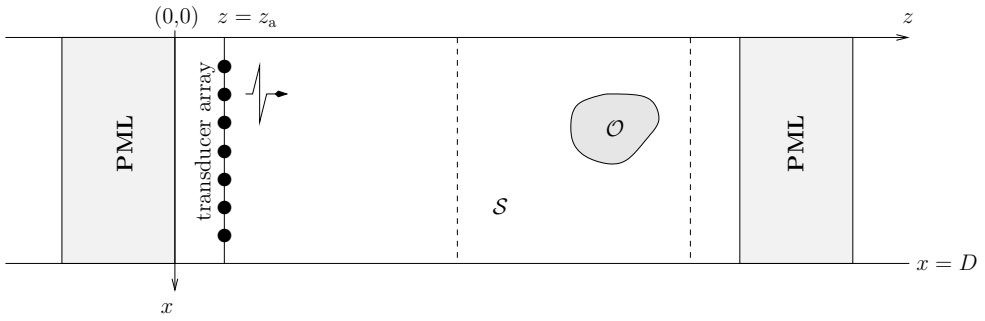


Figure 5.1: Schematic representation of a waveguide truncated near and far from the array with two perfectly matched layers.

In the previous chapters, we presented results that were based on the assumption that the sources used to generate the wavefield were point sources, both in space and time, hence

$$f(t,x) = \delta(\vec{\boldsymbol{x}} - \vec{\boldsymbol{x}}_s)\delta(t),$$

where $\vec{\boldsymbol{x}}_s$ is the location of the source. For the solution of (1.2) and (1.3) with Montjoie, we simulate point sources by considering the source term to be of the form

$$f(t,\vec{\boldsymbol{x}}) = h(t)\, g(\vec{\boldsymbol{x}};\vec{\boldsymbol{x}}_s).$$

Here $h(t)$ is a Ricker function of time, given by

$$h(t) = \sqrt{2} f_0 \left[1 - 4\pi^2 f_0^2 (t - t_c))^2\right] \exp\left\{-[\sqrt{2}\pi f_0 (t - t_c)]^2\right\},$$

where $f_0$ is the central frequency of the pulse and $t_c$ is the time at which the source attains its maximum. Here, we take $t_c = 0.01$ s and the final computation time is taken equal to $T = 4$ s.

The function $g(\vec{\boldsymbol{x}};\vec{\boldsymbol{x}}_s)$ is a Gaussian, given by

$$g(\vec{\boldsymbol{x}};\vec{\boldsymbol{x}}_s) = \sqrt{\alpha/\pi}\exp(-\alpha|\vec{\boldsymbol{x}} - \vec{\boldsymbol{x}}_s|^2),$$

where $\alpha = \ln(10^6)/r^2$; $r$ determines the support of the Gaussian and is taken equal to $\lambda_0/2$.

In Figure 5.2, we plot snapshots of the solution (total field) in our waveguide, for a disc-shaped scatterer of diameter $\delta = 2\lambda_0$, centered at $\vec{\boldsymbol{x}}^\star = (22,3)\lambda_0$. In these results the emitting source is the twentieth array element, *i.e.* $\vec{\boldsymbol{x}}_{20} = (2,10)\lambda_0$. On the top left subplot we have the solution at $t = 3.75 \cdot 10^{-2}$ s, slightly after the source's emission. On the top right, we have $t = 1.625 \cdot 10^{-1}$ s and we observe a wavefront, followed by the reflections of the wave on the horizontal boundaries, propagating towards the scatterer. On the bottom left at $t = 3.125 \cdot 10^{-1}$ s the wave is scattered by the disc, while on the bottom right at $t = 5.125 \cdot 10^{-1}$ s we see the reflections traveling towards the array where they get recorded.

Finally, let us note that the solution is computed with Montjoie in the time domain, so, in turn, we use the fast Fourier transform (FFT) to obtain the array response matrix $\widehat{\Pi}$ for the scattered field in the frequency domain.

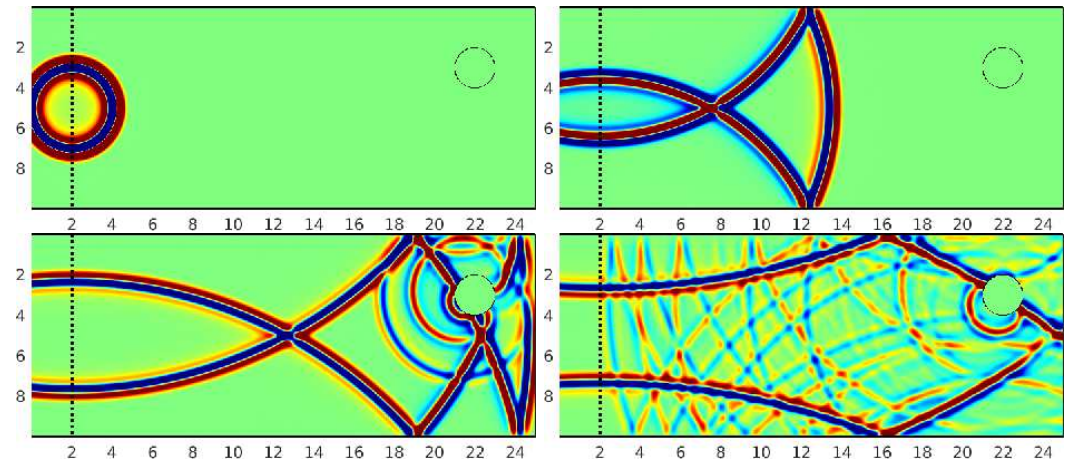

Figure 5.2: Total field solution for a disc-shaped scatterer with diameter $\delta = 2\lambda_0$, centered at $\vec{\boldsymbol{x}}^\star = (22, 3)\lambda_0$ and for the 20th source element. From left to right and top to bottom: $t = 3.75 \cdot 10^{-2},\ 1.625 \cdot 10^{-1},\ 3.125 \cdot 10^{-1},\ 5.125 \cdot 10^{-1}$ s.

## 5.2 Square scatterer

In this section, we will illustrate imaging results for the square scatterer. In fact, this was one of the first problems that we have dealt with, and it was the need of gaining a deeper understanding on this problem that motivated us to consider the screen model problem, which we have studied in detail in Chapter 3. To be more precise, we have considered the screen model problem in order to simulate the left side of a square scatterer like the one shown in Figure 5.3. Therefore, we will start this section with a comparison between the screen and square scatterers and see that the behavior we have observed in the screen case carries over to the square. We will also examine the partial aperture case and see how multiple frequencies improve the performance of the imaging method.

As before, we assume a reference wavenumber $k_0 = \pi/10$, that corresponds to a wavelength $\lambda_0$. The waveguide's geometry is as described in the previous section, where we now have a square scatterer of side $b = 2\lambda_0$ centered at $\vec{\boldsymbol{x}}^\star = (23.5, 3.5)\lambda_0$, as shown in Figure 5.3. Lastly, our search domain is $\mathcal{S} = [17, 30]\lambda_0 \times [0, 10]\lambda_0$.

### 5.2.1 Comparison between screen and square - Full aperture

We start with a comparison between the screen and the square. We assume that the screen and the left side of the square are located at the same place, specifically we take them both

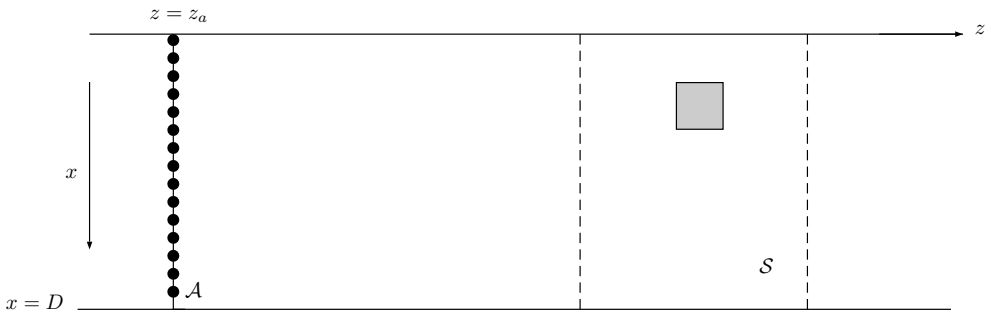


Figure 5.3: Active imaging setup for the square scatterer.

centered at $\vec{\boldsymbol{x}}^{\star} = (22.5, 3.5)\lambda_0$. On the top row of Figure 5.4 we plot the singular values of the matrix $\widehat{\mathbb{P}}$ for the screen (left subplot) and for the square scatterer (right subplot), for a single frequency that corresponds to a wavenumber equal to $k = 0.973k_0$. They are both normalized by their maximum values. Based on the theory that we have presented in Chapter 3 and, specifically, using (3.17) for the current frequency and size of the object, we expect to have 4 'significant' singular values for the screen. This is confirmed by the top-left plot, where we identify 3 singular values clustered close to 1, and one more that is above 0.6, as well as a 'transient' singular value that is slightly below 0.3. A similar behavior can also be observed on the top-right plot for the square, where now the three larger singular values are less clustered near 1 and the fourth is above 0.4.

On the bottom row of Figure 5.4, we also plot the modulus of $\widetilde{\mathcal{I}}^{\mathrm{KM}}$ for the screen in the left subplot and for the square in the right subplot. We see that we recover the left side of the square; this fact follows our intuition since it is this side that faces our array. Lastly, both images display a high SNR. As a reminder, we define SNR as

$$\mathrm{SNR} = \frac{\max\limits_{\vec{\boldsymbol{x}}^{\mathrm{s}} \in \mathcal{R}} |\widetilde{\mathcal{I}}^{\mathrm{KM}}(\vec{\boldsymbol{x}}^{\,\mathrm{s}})|}{\max\limits_{\vec{\boldsymbol{x}}^{\mathrm{s}} \in \mathcal{S} \setminus \mathcal{R}} |\widetilde{\mathcal{I}}^{\mathrm{KM}}(\vec{\boldsymbol{x}}^{\,\mathrm{s}})|},$$

where $\mathcal{R}$ is a subset of our search domain $\mathcal{S}$ that contains the reflector. In our tests we define $\mathcal{R}$ as a $6\lambda_0 \times 6\lambda_0$ box around the scatterer.

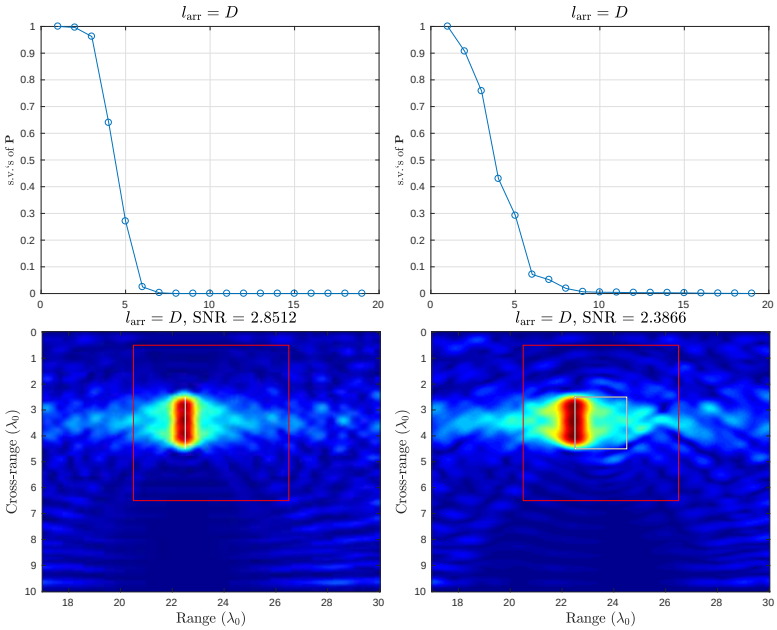


Figure 5.4: Top: Normalized singular values of $\widehat{\mathbb{P}}$ for the screen (left) and square (right). Bottom: Modulus of $\widetilde{\mathcal{I}}^{\text{KM}}$ for the screen (left) and for the square (right), for $b = 2\lambda_0$ and $k = 0.973k_0$.

Next, in Figure 5.5, we plot imaging results when we use $\widetilde{\mathcal{I}}_J^{\text{KM}}$ for the screen on the top row, and the square on the bottom. Going from left to right, we use $J = 1, 2, 3, 4$. We observe that selective imaging for the square follows our theoretical results for the screen, *i.e.* the image focuses on the center of the illuminated edge for $J = 1$, while when moving to the next singular vectors, we observe a focusing that progressively moves towards the edges of the object. Additionally, we have a clear focusing on the scatterer for both the screen and the square, with the exception of $J = 4$ for the square, where some strong artifacts, especially one on the bottom left of the image, lower its SNR to around 1.

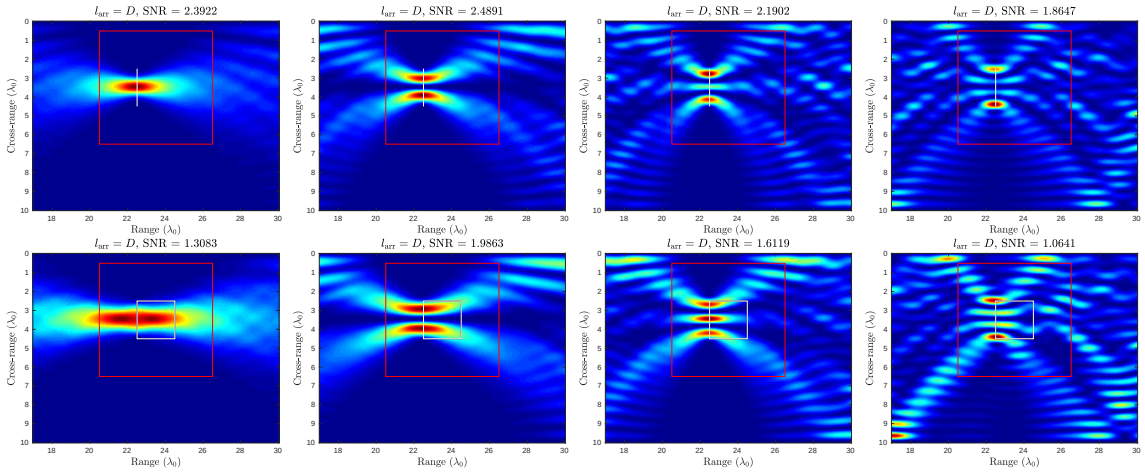


Figure 5.5: Modulus of $\widetilde{\mathcal{I}}_J^{\text{KM}}$ for the screen (top) and square (bottom), for $b = 2\lambda_0$ and $k = 0.973k_0$, for $J = 1, 2, 3, 4$.

### 5.2.2 Partial aperture case

Next, we examine the partial aperture case for the square scatterer. As a reminder, we have seen that for the screen model problem, as long as we do not need to employ a threshold $\varepsilon^+$ in the computation of $\widehat{\mathbb{P}}$ (see Section 3.4), we create images that are identical to those that we obtain with a full array-aperture. For the data that comes from the Born approximation, this was true up until $|\mathcal{A}| = 0.5D$; for these results, we refer to Figure 3.5. However, for the square scatterer, we need to employ a threshold for an array length that equals $0.8D$. For all partial aperture results for the square, shown in this section, we take $\varepsilon^+ = 0.1$.

In Figure 5.6, we plot the partial aperture results for the square scatterer, for an array with length $|\mathcal{A}| = 0.8, 0.6, 0.4, 0.3\ D$, as we move from left to right, respectively. In all cases the array is centered at the midpoint of the vertical cross-section of the waveguide. We observe that for the first two images we get a good reconstruction of the object, with high SNR. In the case where $|\mathcal{A}| = 0.4\ D$, we observe an increased background noise, which lowers the image's SNR to roughly 1.4, while when $|\mathcal{A}| = 0.3\ D$ the noise is almost as large as the values of the image on the object.

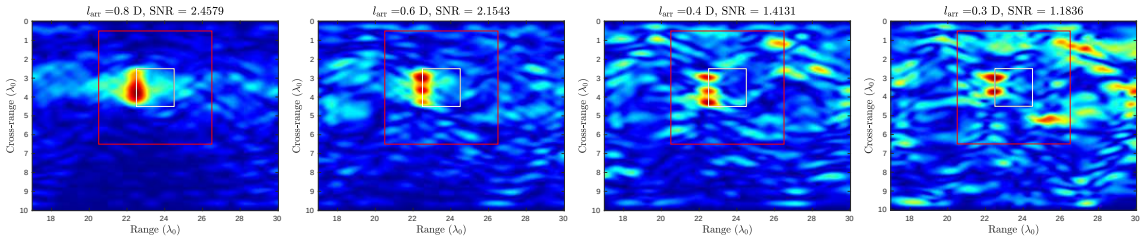


Figure 5.6: Modulus of $\widetilde{\mathcal{I}}^{\mathrm{KM}}$ for a square with $b = 2\lambda_0$ and $k = 0.973k_0$, for $|\mathcal{A}| = 0.8, 0.6, 0.4, 0.3\ D$

### Using multiple frequencies

At this point, there are two comments regarding Figure 5.6, that are worth mentioning. First, by using only a *single* frequency, we are able to create a good quality image that indicates the presence of a scatterer, with an array that spans only 40% of the waveguide's vertical cross-section. Secondly, despite the high level of background noise in the last case, we can see that our image indeed focuses on the scatterer. Using this fact, and following the results of our resolution analysis in Section 4.2, we will proceed to use multiple frequencies, in order to improve the SNR of the image and to create images with even smaller arrays.

In Figure 5.7 we now employ the use of multiple frequencies. Specifically, we consider our previous single frequency as a central frequency, *i.e.* $k_c = 0.973k_0$, and we use a bandwidth equal to $B = 0.92f_c$. The images shown in Figure 5.7 from left to right correspond to array lengths equal to $|\mathcal{A}| = 0.3, 0.2, 0.1, 0.05\ D$, respectively. Once more, in all cases, the array is centered at the midpoint of the vertical cross-section of the waveguide. It is immediate to see the vast improvement of the leftmost image of Figure 5.7, when it is compared with the rightmost image of Figure 5.6 that corresponds to the same array length. What is also extraordinary, is the fact that even with an array that spans just 5% of the waveguide's width (see the rightmost image) we are still able to create an image that focuses on the scatterer and has a high SNR. Let us note here that an array with pitch $h = \lambda_0/4$ that spans 5% of the width of the specific waveguide, as a matter of fact, consists of just three transducers.

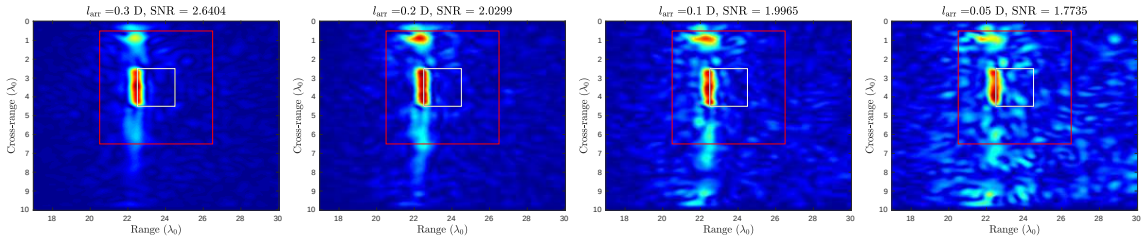


Figure 5.7: Modulus of $\widetilde{\mathcal{I}}^{\text{KM}}$ for a square with $b = 2\lambda_0$ and $k_c = 0.973k_0$ and $B = 0.92f_c$, for $|\mathcal{A}| = 0.3, 0.2, 0.1, 0.05\ D$

## 5.3 Disc-shaped scatterer

We also consider a disc-shaped scatterer and the corresponding semicircle model problem. We expect to observe similar results as the ones shown before for the square and screen problems. We present these results to indicate that the behavior we observe for the vertical screen and the square, it also holds for more general scatterer geometries. Aside from the disc that we will show here, similar results have been obtained for a rhombus shaped scatterer, which will not be shown here, for brevity.

The disc and the semicircle that we consider they both have diameter $\delta = 2\lambda_0$ and are centered at $\vec{\boldsymbol{x}}^\star = (22, 5)\lambda_0$. The waveguide's characteristics remain the same as in the previous section, while now we have slightly shifted the search domain to be $\mathcal{S} = [15.5, 28.5]\lambda_0 \times [0, 10]\lambda_0$.

Following the format of the previous section, we begin by comparing the disc and the semicircle. On the top row we plot the normalized singular values of $\widehat{\mathbb{P}}$ for the semicircle on the left and the corresponding ones for the disc on the right. The singular values are distributed in a somewhat similar manner to the screen/square case, where now we may distinguish three significant singular values. On the bottom we have the $\widetilde{\mathcal{I}}^{\text{KM}}$ images which show great agreement, and they both focus on the leftmost part of the scatterer.

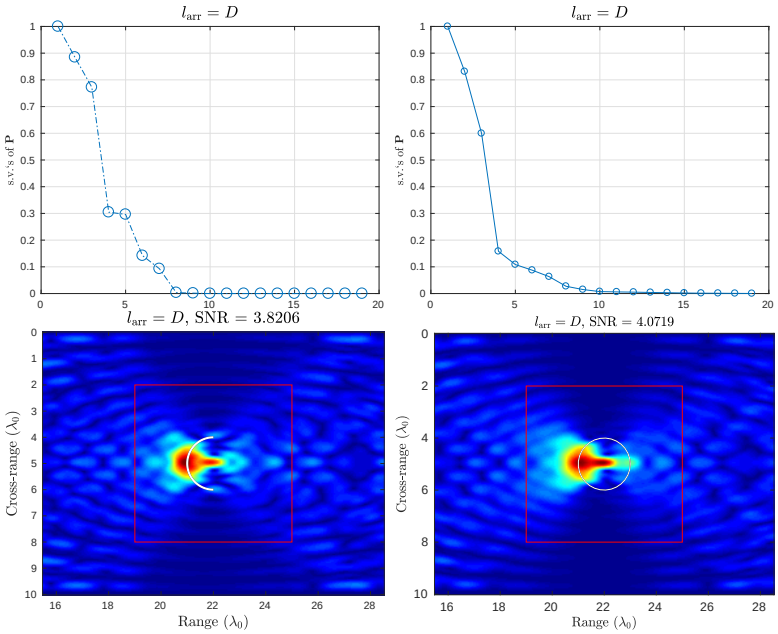


Figure 5.8: Top: Singular values of $\widehat{\mathbb{P}}$ for the screen (left) and square (right). Bottom: Modulus of $\widetilde{\mathcal{I}}^{\text{KM}}$ for the screen (left) and for the square (right), for $b = 2\lambda_0$ and $k = 0.973k_0$.

Let us remark here that in the case of the square scatterer, selectivity did not offer, in general, any important additional information in the sense that, for example, as one may verify in Figure 5.4 the whole left side of the square is recovered without using any selective technique. However, this is not the case for the disc, where the $\widetilde{\mathcal{I}}^{\text{KM}}$ image is focused on the leftmost part. As we shall see immediately, the use of selective imaging functionals helps us to recover additional information about the scatterer. In Figure 5.9, we plot the imaging results for a single frequency with a corresponding wavenumber $k = 0.973k_0$, when we use $\widetilde{\mathcal{I}}_J^{\text{KM}}$ for the semicircle, shown on top, and the disc at the bottom, for $J = 1, 2, 3$. In all images we observe a very good agreement between the semicircle and disc results, as well as the expected focusing order when using $\widetilde{\mathcal{I}}_J^{\text{KM}}$, with the first singular value focusing in the leftmost part of the scatterer, and the next ones moving towards the upper and lower edges of the scatterer.

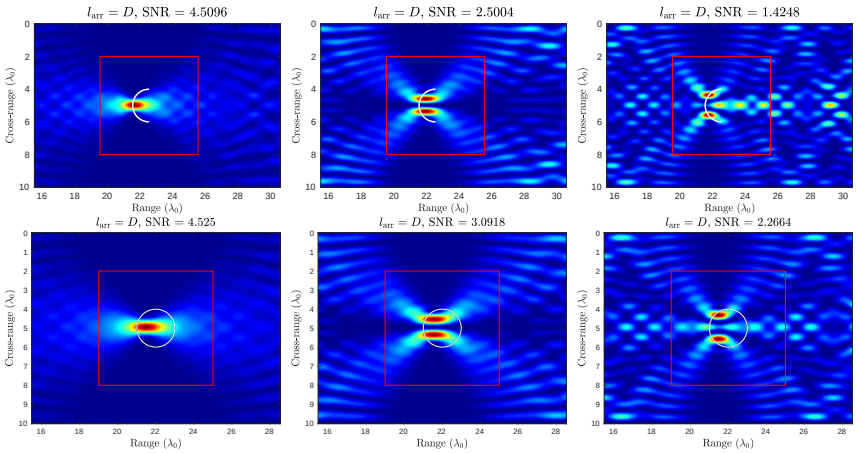


Figure 5.9: Modulus of $\widetilde{\mathcal{I}}_J^{\mathrm{KM}}$ for the semicircle (top) and disc (bottom), for $b = 2\lambda_0$ and $k = 0.973k_0$, for $J = 1, 2, 3$.

Next, in Figure 5.10 we test the performance of our imaging functional $\widetilde{\mathcal{I}}^{\mathrm{KM}}$ in locating the disc-shaped scatterer when we use a partial-aperture array centered at the midpoint of the vertical cross-section of the waveguide. We use a single frequency, and we plot our images from left to right for array lengths equal to $|\mathcal{A}| = 0.8, 0.6, 0.4, 0.3\ D$, respectively. We see that as we move to smaller arrays the focus of the image is mainly on the leftmost part of the scatterer, while for $|\mathcal{A}| = 0.3\ D$ we have an image that focuses in the center of the scatterer.

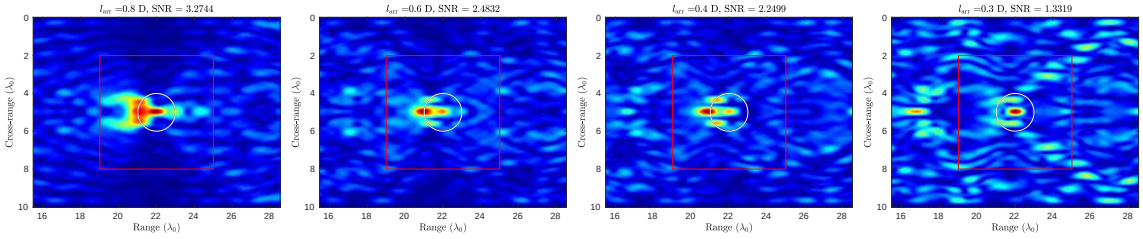


Figure 5.10: Modulus of $\widetilde{\mathcal{I}}^{\mathrm{KM}}$ for a disc with $\delta = 2\lambda_0$ and $k = 0.973k_0$, for $|\mathcal{A}| = 0.8, 0.6, 0.4, 0.3\ D$

Finally, in Figure 5.11 we again use multiple frequencies, and specifically with a central frequency that corresponds to the wavenumber $k_c = 0.973k_0$ and a bandwidth $B = 0.92f_c$, we image using arrays with length $|\mathcal{A}| = 0.3, 0.2, 0.1, 0.05\ D$. Again, the use of multiple frequencies significantly improves the quality of the image, and if we look at the rightmost plot we see again that even with an array that spans only 5% of the waveguide's cross-

section, we create an image with a very clear focusing on the scatterer.

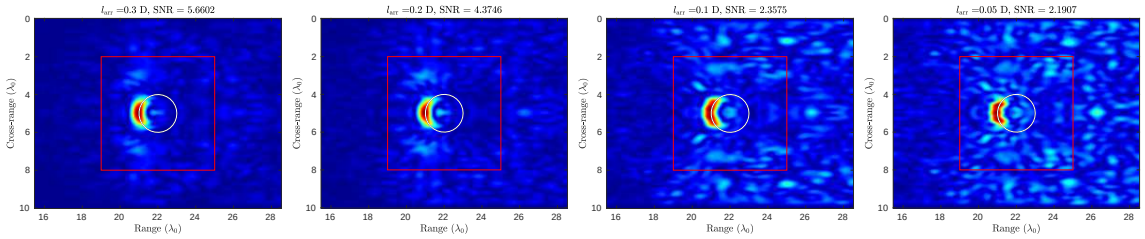


Figure 5.11: Modulus of $\widetilde{\mathcal{I}}^{\text{KM}}$ for a disc with $\delta = 2\lambda_0$ and $k_c = 0.973k_0$ and $B = 0.92f_c$, for $|\mathcal{A}| = 0.3, 0.2, 0.1, 0.05\ D$

## 5.4 Variable speed case

Lastly, in this section, as a step towards a more realistic environment, we assume that the sound speed is a function of the cross-range variable $x$, *i.e.* $c = c(x)$. In this case, we no longer have an analytic expression for the eigenvalues and the vertical eigenfunctions $X_n$. We obtain them by numerically solving the associated vertical eigenvalue problem. However, the $X_n$'s still form an orthonormal basis of $L^2[0, D]$. Therefore, the theoretical results that we have proven for the homogeneous case carry over to this case, thus we expect that the results of the numerical experiments that we have presented in the previous section to carry over as well. The sound speed profile that we consider in our experiments is shown in Figure 5.12, and is adapted from [33] to fit the current waveguide setup.

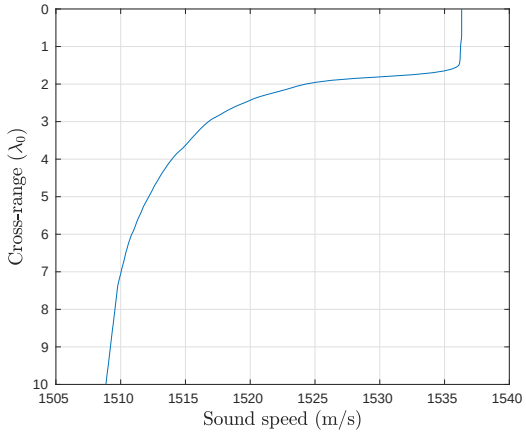


Figure 5.12: Variable speed profile for our waveguide.

We consider a square scatterer of side $b = 2\lambda_0$, centered at $\vec{\boldsymbol{x}}^\star = (23.5, 5)\lambda_0$. In this

section, we will compare imaging results between the homogeneous waveguide and the waveguide with a variable wave speed, as we just described. The results for the disc are very similar so we do not present them, for the sake of brevity. First, in Figure 5.13 we plot on the top row the normalized singular values of $\widehat{\mathbb{P}}$ and on the bottom the $\widetilde{\mathcal{I}}^{\mathrm{KM}}$ image, for a single frequency with a corresponding wavenumber $k = 0.973k_0$. On the left column we have the homogeneous waveguide, while on the right we have the variable speed case. We observe that the distribution of the singular values in both cases is very similar, while the $\widetilde{\mathcal{I}}^{\mathrm{KM}}$ images seem visually identical, and the corresponding SNR values are very close.

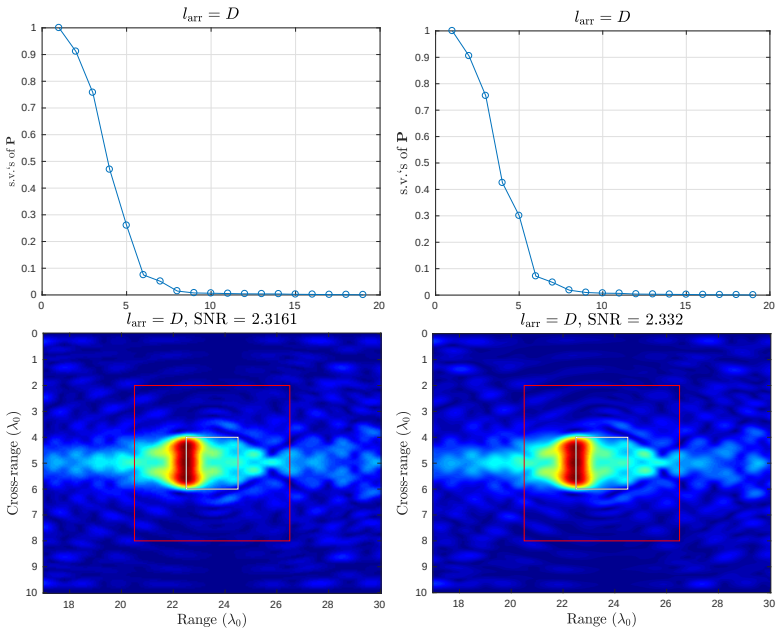


Figure 5.13: Normalized singular values of $\widehat{\mathbb{P}}$ (top) and modulus of $\widetilde{\mathcal{I}}^{\mathrm{KM}}$ (bottom) for the square in a waveguide with constant (left panel) and variable (right panel) wave speed, for $b = 2\lambda_0$ and $k = 0.973k_0$.

Next, in Figure 5.14 we present selective imaging results for the homogeneous waveguide plotted on top, and for the variable speed case shown on the bottom. As before, both cases show an excellent agreement, with their only difference being apparent at the rightmost image, for $J = 4$, where the artifacts that are the causes of a low SNR-value on the homogeneous case seem to be less pronounced in the variable speed case, thus the SNR of the image increases.

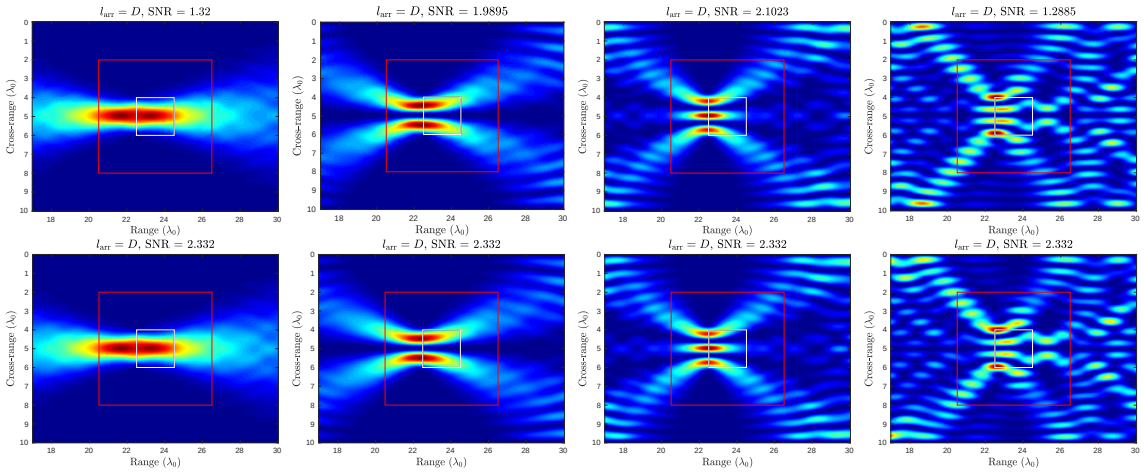


Figure 5.14: Modulus of $\widetilde{\mathcal{I}}_J^{\mathrm{KM}}$ for square in a waveguide with constant (top) and variable (bottom) wave speed, for $b = 2\lambda_0$ and $k = 0.973k_0$, for $J = 1, 2, 3, 4$.

In Figure 5.15 we consider the partial aperture case, with $|\mathcal{A}| = 0.8, 0.6, 0.4, 0.3\ D$. Again, the results between the homogeneous and variable speed case are similar, with the image for $|\mathcal{A}| = 0.4D$ having a focus on the left side of the square but a relatively low SNR and when $|\mathcal{A}| = 0.3D$ we have an image with SNR close to 1 for both cases.

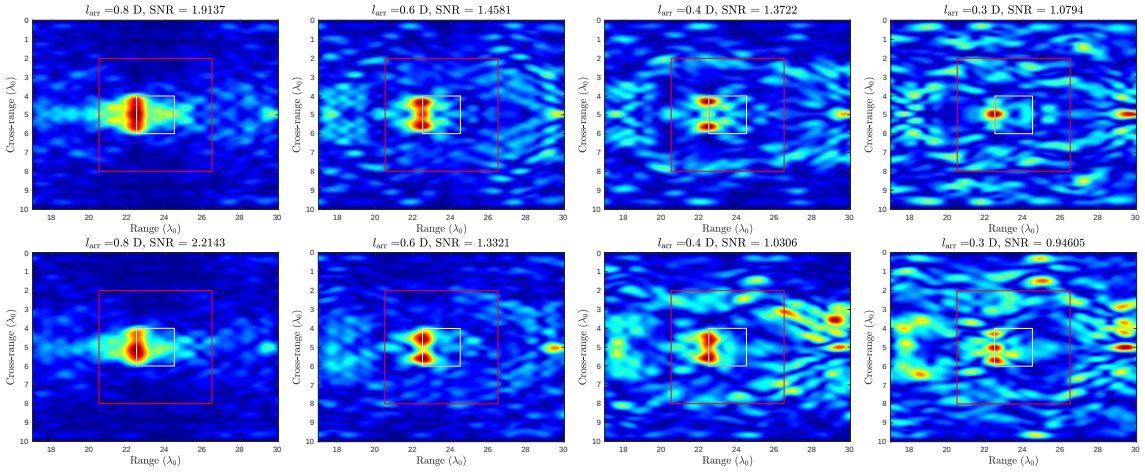


Figure 5.15: Modulus of $\widetilde{\mathcal{I}}^{\mathrm{KM}}$ for a square in a waveguide with constant (top) and variable (bottom) wave speed, for $b = 2\lambda_0$ and $k = 0.973k_0$, for $|\mathcal{A}| = 0.8, 0.6, 0.4, 0.3\ D$

Finally, in Figure 5.16 we use multiple frequencies to improve the performance of the imaging functional, having $k_c = 0.973k_0$ and $B = 0.92f_c$. Here we observe the only significant difference between the homogeneous waveguide and our current case, where for the

limiting case at $|\mathcal{A}| = 0.05D$ the quality of the rightmost bottom image seems to deteriorate, compared to the corresponding image on the top.

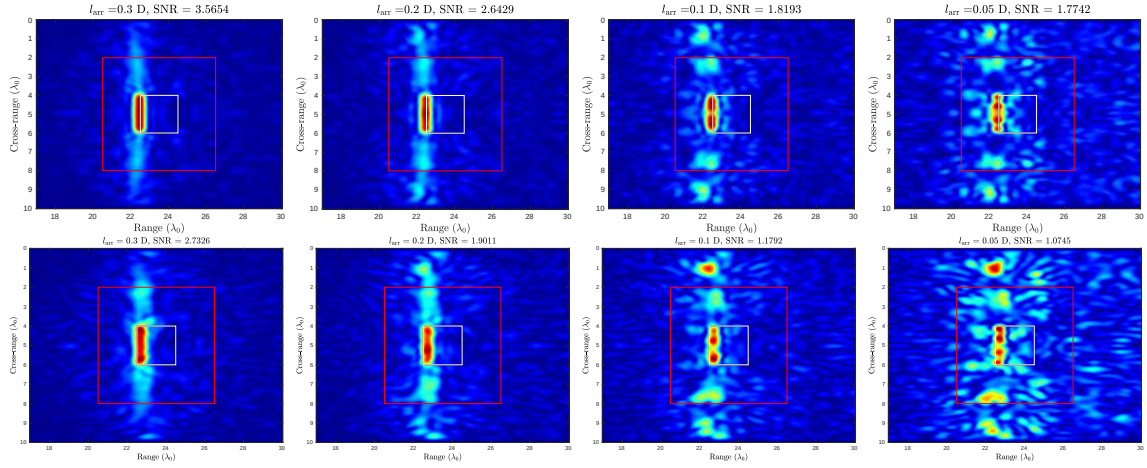


Figure 5.16: Modulus of $\widetilde{\mathcal{I}}^{\mathrm{KM}}$ for a square in a waveguide with constant (top) and variable (bottom) wave speed, for $b = 2\lambda_0$ and $k_c = 0.973k_0$ and $B = 0.92f_c$, for $|\mathcal{A}| = 0.3, 0.2, 0.1, 0.05\ D$

To summarize, in this chapter we assessed the performance of our imaging method for more realistic scatterer geometries with data that were generated by a full wave model. First, we compared the model problems for the one-dimensional scatterers with the problems for their two-dimensional counterparts and we have observed an excellent agreement. We also examined the partial array-aperture case. There, we saw that for a *single* frequency we are able to create good images with 40% of the original array, while when we use multiple frequencies we are able to push our method way past that length and we are able to locate the scatterers using an array with length $|\mathcal{A}| = 0.05D$. Lastly, we examined a more realistic case where the wave speed depends on the cross-range variable $x$, we have compared the results with the corresponding ones for the homogeneous case, and we have verified that our method works equally well in this cross-range dependent wave speed environment.

# Chapter 6

# Imaging in a terminating waveguide

In this chapter, we consider the problem of imaging extended reflectors in a terminating waveguide, as the one depicted in Figure 6.1. The main reason we consider this waveguide geometry is because, as we will see, more information about the extended reflector's support/shape can be obtained in this case compared to the infinite waveguide geometry. This is due to multiple-scattering reflections that bounce off the terminating boundary of the waveguide providing multiple views of the reflector that are not available in the infinite waveguide case. To benefit from this multipathing we need to know or determine the boundary of the waveguide prior to imaging the reflector. Here, we consider that the waveguide's boundary is known.

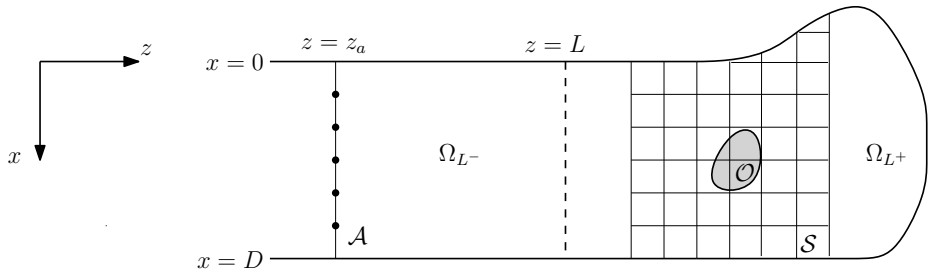


Figure 6.1: Schematic representation of the semi-infinite waveguide.

The main body of this chapter has been the object of publication [60]. Here, we essentially present the contents of this publication. Specifically, in Section 6.1 we present

the formulation of the problem and describe our imaging methodology inspired by phase conjugation for both the passive and active imaging. In Section 6.2 we carry out the resolution analysis for single and multiple frequency imaging and in Section 6.3 we illustrate the performance of our approach with numerical simulations in two and three dimensions.

## 6.1 Problem setup and imaging methodology

In this section, we briefly describe our problem and introduce our imaging methodology. The terminating waveguide $\Omega$ consists of two subdomains: the semi-infinite strip $\Omega_{L^-} = (-\infty, L) \times (0, D)$ and a bounded domain in $\mathbb{R}^2$ denoted by $\Omega_{L^+}$, see Figure 6.1. Let us also assume that all the inhomogeneities of the medium are contained in $\Omega_{L^+}$ while the medium is homogeneous in the semi-infinite strip $\Omega_{L^-}$, i.e. the wave speed may depend on range and cross-range in $\Omega_{L^+}$, and varies smoothly to the constant value that has for $z \leq L$. Note that the assumption of a constant wave speed in $\Omega_{L^-}$ may be relaxed by requiring the speed to depend on the cross-range variable $x$. However, to facilitate the presentation we assume here that $\Omega_{L^-}$ is filled with a homogeneous medium.

As with the infinite waveguide case, we have an active vertical array $\mathcal{A}$ in $\Omega_{L^-}$, composed of $N$ transducers, that may span the whole vertical cross-section of the waveguide or part of it. Our data are stored in the $N \times N$ response matrix $\widehat{\Pi}$ for the scattered field, which is determined by subtracting the incident field from the total field. The incident and scattered fields are the solution of (1.5) and (1.6) respectively with the radiation conditions adjusted accordingly, stating that '$p$ is outgoing as $z \to -\infty$'.

We assume here that these BVPs are well-posed. For example, in the case where $\eta(\vec{\boldsymbol{x}}) = 1$ everywhere in $\Omega$, it has been proved in [28] that the problem for the incident field is well-posed under the assumption that $k^2 \notin \Lambda \cup \{\mu_n\}_{n=1}^{\infty}$, where $\Lambda$ is the point spectrum of the negative Dirichlet Laplacian acting on $L^2(\Omega)$. This set $\Lambda$, which may be empty in some cases, is known to be at most countable, with no finite accumulation point, see [37]. For the total field there are examples in infinite waveguides that suggest existence of the so-called trapped modes, i.e. nonzero localized solutions of the associated homogeneous problem, see e.g. [23].

### 6.1.1 Imaging with a full-aperture array

Now, let us present the imaging method we will use for this waveguide geometry. We shall first consider the easier case where the array spans the whole vertical cross-section of the waveguide. Moreover, although we are interested in imaging extended reflectors we will first examine the so-called passive imaging problem in order to motivate the use of the imaging functional that we will introduce next.

#### Passive Imaging

So, let us assume that a point source of unit strength, located at the point $\vec{\boldsymbol{x}}_s = (z_s, x_s) \in \Omega$, emits a signal that is recorded on a vertical array $\mathcal{A}$ located in $\Omega_{L^-}$. Moreover, we assume that the array $\mathcal{A} = \{\vec{\boldsymbol{x}}_r = (z_a, x_r)\}_{r=1}^N$, $(z_a < L)$, spans the whole vertical cross-section of the waveguide as illustrated in Figure 6.2. Our aim is to find the location of the source. In this case the array response matrix $\widehat{\Pi}$ at frequency $\omega$ reduces to a $N \times 1$ vector, whose $r$-th component equals the Green's function evaluated at receiver $\vec{\boldsymbol{x}}_r$ due to the source $\vec{\boldsymbol{x}}_s$, i.e.

$$\widehat{\Pi}(\vec{\boldsymbol{x}}_r; \omega) = \widehat{G}(\vec{\boldsymbol{x}}_r, \vec{\boldsymbol{x}}_s; \omega). \tag{6.1}$$

In what follows we consider a monochromatic source and to simplify the notation we suppress parameter $\omega$ from the imaging functional and the Green's function. The dependence on $\omega$ will be recalled in Section 6.2.2, where imaging with multiple frequency data is considered.

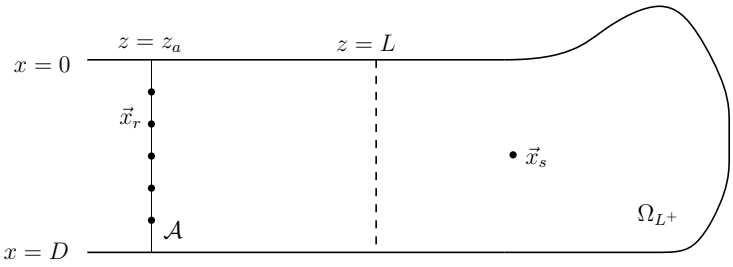


Figure 6.2: Passive imaging setup in a terminated waveguide.

The imaging functional that we propose to use is based on the concept of phase conjugation, which may be physically interpreted by virtue of the Huygen's principle. As pointed out in [35], Huygen's principle states that a propagating wave may be viewed as superpo-

sition of wavelets reemitted from a fictitious surface with amplitudes proportional to those of the original wave. In phase conjugation, which may be seen as the equivalent of time reversal in the frequency domain, the reemitted wavelets' amplitudes are proportional to the complex conjugate of the corresponding ones in the original wave. These remarks lead naturally one to define the following classical phase conjugation imaging functional

$$\mathcal{I}^{\text{pc}}(\vec{\boldsymbol{y}}^s) = \int_{\mathcal{A}} \overline{\widehat{G}(\vec{\boldsymbol{x}}_r, \vec{\boldsymbol{x}}_s)} \widehat{G}(\vec{\boldsymbol{y}}^s, \vec{\boldsymbol{x}}_r) dx, \tag{6.2}$$

where $\vec{\boldsymbol{x}}_r = (z_a, x) \in \mathcal{A}$ and $\vec{\boldsymbol{y}}^s \in \mathcal{S}$. However, if we assume for a moment that apart from recording the value of the field on the array we would be able to record its normal derivative as well, then we may define the following imaging functional, which as we will show next has very nice theoretical properties. So let

$$\mathcal{I}(\vec{\boldsymbol{y}}^s) := \int_{\mathcal{A}} \left( \overline{\widehat{G}(\vec{\boldsymbol{x}}_r, \vec{\boldsymbol{x}}_s)} \nabla \widehat{G}(\vec{\boldsymbol{x}}_r, \vec{\boldsymbol{y}}^s) - \widehat{G}(\vec{\boldsymbol{x}}_r, \vec{\boldsymbol{y}}^s) \overline{\nabla \widehat{G}(\vec{\boldsymbol{x}}_r, \vec{\boldsymbol{x}}_s)} \right) \cdot \nu \, dx, \tag{6.3}$$

where $\nu$ is the outward-pointing unit normal vector to $\mathcal{A}$. Of course this functional is more complicated than phase conjugation but the following proposition shows that in order to compute $\mathcal{I}(\vec{\boldsymbol{y}}^s)$ in a terminating waveguide it is required to know only the values of the wave field on the array and not its derivatives. Let us remark here that the form of the integral that appears in the right-hand side of (6.3) is also met in the context of the so-called reciprocity gap method, see, e.g., [19, 43].

**Proposition 9 (Kirchhoff-Helmholtz identity)** *Assume that a point source is located in the terminating waveguide that we have described in Section 6.1 (see, also, Figure 6.2), and that a vertical array $\mathcal{A}$, which spans the whole vertical cross-section of the waveguide, is located in $\Omega_{L^-}$. Then, the imaging functional that we have defined in (6.3) satisfies the following Kirchhoff-Helmholtz identity:*

$$\mathcal{I}(\vec{\boldsymbol{y}}^s) = \widehat{G}(\vec{\boldsymbol{y}}^s, \vec{\boldsymbol{x}}_s) - \overline{\widehat{G}(\vec{\boldsymbol{y}}^s, \vec{\boldsymbol{x}}_s)} = 2i \operatorname{Im} \widehat{G}(\vec{\boldsymbol{y}}^{\text{s}}, \vec{\boldsymbol{x}}_s). \tag{6.4}$$

*Moreover, we can show that,*

$$\mathcal{I}(\vec{\boldsymbol{y}}^s) = 2i \sum_{n=1}^{M} \beta_n \, \overline{\widehat{G}_n(z_a, \vec{\boldsymbol{x}}_s)} \, \widehat{G}_n(z_a, \vec{\boldsymbol{y}}^s), \tag{6.5}$$

*where* $\widehat{G}_n(z_a,\cdot)$, $n=1,\dots,M$, *denote the first* $M$ *Fourier coefficients of the Green's function (which correspond to the propagating modes) with respect to the orthonormal basis of* $L^2(0,D)$ *that is formed by the vertical eigenfunctions* $X_n$, *i.e.*

$$\widehat{G}_n(z_a,\cdot)=\int_0^D \widehat{G}((z_a,x'),\cdot)\,X_n(x')\,dx'. \tag{6.6}$$

**Proof.** See Section 1.7. □

**The passive imaging functional** Motivated by Proposition 9 we define here our imaging functional for the passive case. Assuming that the array elements are dense enough, so that we may think of the array as being continuous, we define

$$\widehat{\mathbb{Q}}_n=\int_0^D \widehat{\Pi}\big(\vec{\boldsymbol{x}}_r;\omega\big)X_n(x)\,dx,\quad n=1,\dots,M, \tag{6.7}$$

to be the projection of the recorded field on the first $M$ eigenfunctions $X_n$, $n=1,\dots,M$, of the vertical eigenvalue problem (1.10). Let us remark here that the definition of $\widehat{\mathbb{Q}}_n$ in (6.7) entails an idealized continuous array; this is convenient mainly for theoretical purposes. In practice, we work with arrays that consist of discrete elements and then we may define

$$\widehat{\mathbb{Q}}_n:=h\sum_{r=1}^{N}\widehat{\Pi}\big((z_a,x_r);\omega\big)X_n(x_r),\quad n=1,\dots,M,$$

where $h$ is the array inter-element distance.

Notice that using (6.1), $\mathbb{Q}_n$ may be written as

$$\widehat{\mathbb{Q}}_n=\int_0^D \widehat{G}\big((z_a,x),\vec{\boldsymbol{x}}_s\big)X_n(x)\,dx=\widehat{G}_n(z_a,\vec{\boldsymbol{x}}_s).$$

In view of (6.5) we define our imaging functional as:

$$\mathcal{I}^{\mathrm{p}}(\vec{\boldsymbol{y}}^s):=\sum_{n=1}^{M}\beta_n\overline{\widehat{\mathbb{Q}}_n}\,\widehat{G}_n(z_a,\vec{\boldsymbol{y}}^s). \tag{6.8}$$

Note that the evaluation of $\mathcal{I}^{\mathrm{p}}(\vec{\boldsymbol{y}}^s)$, for $\vec{\boldsymbol{y}}^s\in\mathcal{S}$, requires only recordings of the wave

field. Moreover, (6.4) and (6.5) ensure that

$$\mathcal{I}^{\mathrm{P}}(\vec{\boldsymbol{y}}^{\mathrm{S}}) = \operatorname{Im} \widehat{G}(\vec{\boldsymbol{y}}^{\mathrm{S}}, \vec{\boldsymbol{x}}_s). \tag{6.9}$$

This last equation is a very interesting result, and says that the quality of the focusing in the image is determined by the imaginary part of the Green's function in our waveguide. Therefore, a resolution analysis for $\mathcal{I}^{\mathrm{P}}$ will entail the study of the behaviour of $\operatorname{Im} \widehat{G}$.

**Example 1:** (Imaging a point source) In order to provide to the reader a sense of how $\mathcal{I}^{\mathrm{P}}(\vec{\boldsymbol{y}}^{\mathrm{S}})$ behaves, we consider the simple case of imaging a source in a homogeneous terminating waveguide that forms a semi-infinite strip, i.e. $\Omega = (-\infty, R) \times (0, D)$. We assume a reference wavenumber $k_0 = \pi/10$ that corresponds to a reference wavelength $\lambda_0$, and take $D = 10\lambda_0$ while the vertical (terminating) boundary is placed at $R = 27.5\lambda_0$. In Figure 6.3, we plot the modulus of equation (6.8), for a source placed at $\vec{\boldsymbol{x}}_s = (19, 5)\lambda_0$ (shown in the plot as a white asterisk) and for a single frequency $f$ that corresponds to a wavenumber $k = 0.973k_0$. This results to a number of propagating modes $M = 19$. Finally our search domain is $\mathcal{S} = [11.5, 26.5] \times [0, 10]$, where all distances are expressed in terms of the reference wavelength $\lambda_0$.

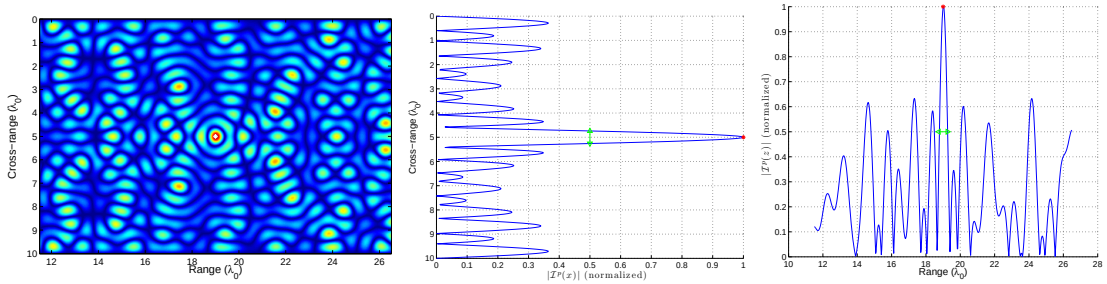


Figure 6.3: Normalized modulus of $\mathcal{I}^{\mathrm{P}}$ for a point source located at $\vec{\boldsymbol{x}}_s = (19, 5)\,\lambda_0$ and for a single frequency corresponding to $k = 0.973k_0$. Imaging on the whole search domain (left), for search points fixed at the correct range $z = z_s$ (middle) and at the correct cross-range $x = x_s$ (right). The green arrowed segment indicates length equal to $\lambda/2$ and a red asterisk points to the location of the source.

We observe that the $\mathcal{I}^{\mathrm{P}}(\vec{\boldsymbol{y}}^{\mathrm{S}})$ image, despite the presence of relatively high secondary peaks, displays a clear peak around $\vec{\boldsymbol{x}}_s$, which is a key property for an imaging functional.

### Active Imaging

As a step forward to the general case of an extended scatterer, we will now deal with the active imaging problem where we are interested in locating a single point scatterer of unit reflectivity that is situated at $\vec{\boldsymbol{x}}^* = (z^*, x^*)$, while the array $\mathcal{A}$ is like the one in the passive imaging case as illustrated in Figure 6.4.

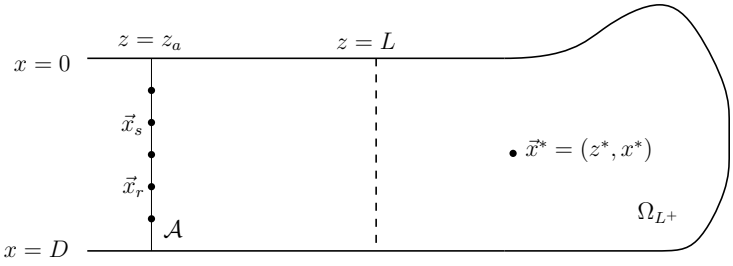


Figure 6.4: Active imaging setup in a terminated waveguide.

Then, the $(s, r)$ entry of the array response matrix:

$$\widehat{\Pi}(\vec{\boldsymbol{x}}_s, \vec{\boldsymbol{x}}_r; \omega) = k^2 \widehat{G}(\vec{\boldsymbol{x}}^*, \vec{\boldsymbol{x}}_s; \omega) \widehat{G}(\vec{\boldsymbol{x}}_r, \vec{\boldsymbol{x}}^*; \omega),$$

corresponds to the scattered signal received at $\vec{\boldsymbol{x}}_r$ when the point reflector at $x^*$ is illuminated by a unit amplitude signal emitted at frequency $\omega$ from a point source located at $\vec{\boldsymbol{x}}_s$. In what follows we suppress the multiplicative constant $k^2$, hence we assume that

$$\widehat{\Pi}(\vec{\boldsymbol{x}}_s, \vec{\boldsymbol{x}}_r; \omega) = \widehat{G}(\vec{\boldsymbol{x}}^*, \vec{\boldsymbol{x}}_s; \omega) \widehat{G}(\vec{\boldsymbol{x}}_r, \vec{\boldsymbol{x}}^*; \omega). \tag{6.10}$$

In the mutiple-frequency case we can also remove this factor by rescaling the data matrix $\widehat{\Pi}(\vec{\boldsymbol{x}}_s, \vec{\boldsymbol{x}}_r; \omega)$ to be equal to $k^{-2}\widehat{\Pi}(\vec{\boldsymbol{x}}_s, \vec{\boldsymbol{x}}_r; \omega)$.

Assuming again that the array is continuous we define the projected response matrix $\widehat{\mathbb{Q}}$ as

$$\widehat{\mathbb{Q}}_{nm} = \int_0^D \int_0^D \widehat{\Pi}(\vec{\boldsymbol{x}}_s, \vec{\boldsymbol{x}}_r; \omega) X_n(x_s) X_m(x_r)\, dx_s\, dx_r, \quad n, m = 1 \ldots, M, \tag{6.11}$$

where $X_n$, $n = 1 \ldots, M$, are the first $M$ eigenfunctions of problem (1.10) as before.

**The active imaging functional** A natural generalization of the imaging functional that we have proposed in the passive case (see (6.8)), is the following active imaging functional

$$\mathcal{I}^{\mathrm{a}}(\vec{\boldsymbol{y}}^{\mathrm{s}}) := \sum_{n=1}^{M}\sum_{m=1}^{M} \beta_n \beta_m \overline{\widehat{\mathbb{Q}}_{nm}}\, \widehat{G}_n(z_a, \vec{\boldsymbol{y}}^{\mathrm{s}})\, \widehat{G}_m(z_a, \vec{\boldsymbol{y}}^{\mathrm{s}}), \tag{6.12}$$

defined for each point $\vec{\boldsymbol{y}}^{\mathrm{s}}$ in the search domain $S$.

Note that by replacing (6.10) into (6.11) and using the expression of $\widehat{G}_n$ given in (6.6), it is easy to show that

$$\widehat{\mathbb{Q}}_{nm} = \widehat{G}_n(z_a, \vec{\boldsymbol{x}}^*)\, \widehat{G}_m(z_a, \vec{\boldsymbol{x}}^*). \tag{6.13}$$

In turn, (6.12) now becomes,

$$\mathcal{I}^{\mathrm{a}}(\vec{\boldsymbol{y}}^{\mathrm{s}}) = \sum_{n=1}^{M} \beta_n\, \overline{\widehat{G}_n(z_a, \vec{\boldsymbol{x}}^*)}\, \widehat{G}_n(z_a, \vec{\boldsymbol{y}}^{\mathrm{s}}) \sum_{m=1}^{M} \beta_m\, \overline{\widehat{G}_m(z_a, \vec{\boldsymbol{x}}^*)}\, \widehat{G}_m(z_a, \vec{\boldsymbol{y}}^{\mathrm{s}}),$$

and Proposition 9 ensures that

$$\mathcal{I}^{\mathrm{a}}(\vec{\boldsymbol{y}}^{\mathrm{s}}) = \Big(\operatorname{Im} \widehat{G}(\vec{\boldsymbol{y}}^{\mathrm{s}}, \vec{\boldsymbol{x}}^*)\Big)^2. \tag{6.14}$$

Thus we deduce that the imaging functional (6.12) for a point scatterer behaves like the square of the imaginary part of the Green's function.

**Example 2:** (Imaging a point scatterer) To illustrate how $\mathcal{I}^{\mathrm{a}}(\vec{\boldsymbol{y}}^{\mathrm{s}})$ behaves we consider a point scatterer in the homogeneous terminating waveguide that we have described in Example 1. The scatterer is placed at $\vec{\boldsymbol{x}}^* = (19, 5)\,\lambda_0$ while all the other parameters are the same as in the previous example. In Figure 6.5 we plot the modulus of (6.12). As one may immediately verify this image has better signal-to-noise (SNR) ratio than the one shown in Figure 6.3. This is something to be expected since $\mathcal{I}^{\mathrm{a}}$ is just the square of $\mathcal{I}^{\mathrm{p}}$.

### 6.1.2 Imaging with a partial-aperture array

We now turn our attention to the case where the array does not span the whole vertical cross-section of the waveguide. In Section 3.2, we have presented a way to construct a projection of the array response matrix that is well suited to the infinite waveguide case. Here we briefly repeat the basic idea and necessary notation, in order to apply them in our current setup.

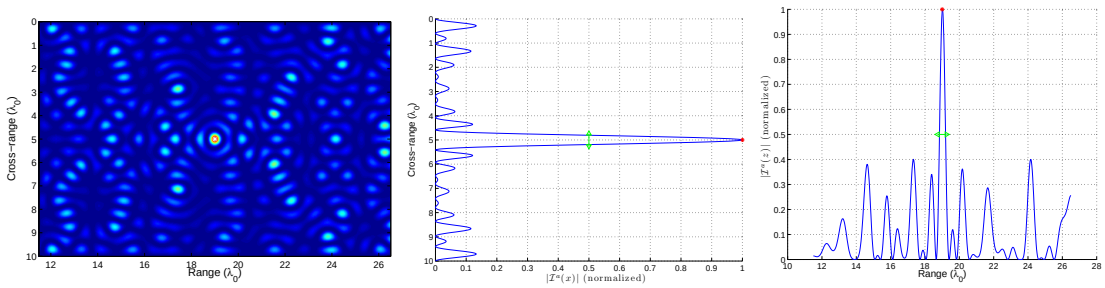


Figure 6.5: Normalized modulus of $\mathcal{I}^{\rm a}$ for a point scatterer located at $\vec{\boldsymbol{x}}^* = (19, 5)\,\lambda_0$ and for a single frequency corresponding to $k = 0.973k_0$. Imaging on the whole search domain (left), for search points fixed at the correct range $z = z^*$ (middle) and at the correct cross-range $x = x^*$ (right). The green arrowed segment indicates length equal to $\lambda/2$ and a red asterisk points to the location of the scatterer.

Let $A_{\rm arr}$ be the $M \times M$ matrix with entries

$$(A_{\rm arr})_{mn} = \int_{\mathcal{A}} X_m(x) X_n(x) \mathrm{d}x, \quad m, n = 1, \ldots, M, \tag{6.15}$$

where $M$ is the number of propagating modes in $\Omega_{L^-}$. We have shown that $A_{\rm arr}$ is a real, symmetric Toeplitz-minus-Hankel matrix and its eigenvalues $\nu_j$, $j = 1, \ldots, M$, are clustered near 0 and 1. Let, also, $\boldsymbol{w}^j = (w_1^j, w_2^j, \ldots, w_M^j)^T$ be the corresponding orthonormal eigenvectors, which turn out to be discrete prolate (or prolate-like) spheroidal sequences, and $W$ be the $M \times M$ orthogonal matrix $W = (\boldsymbol{w}^1, \boldsymbol{w}^2, \ldots, \boldsymbol{w}^M)$. Then we introduce the trigonometric polynomials

$$s_j(x) = \sum_{i=1}^{M} w_i^j X_i(x), \quad j = 1, 2, \ldots, M. \tag{6.16}$$

Next, we project $\widehat{\Pi}$ onto the first $M$ trigonometric polynomials $s_n$, $n = 1, \ldots, M$ instead of projecting onto the eigenfunctions $X_n$. Specifically, we define $\widehat{\mathbb{S}}$ to be the $M \times M$ matrix with entries

$$\widehat{\mathbb{S}}_{mn} = \frac{1}{\nu_m \nu_n} \int_{\mathcal{A}} \int_{\mathcal{A}} \widehat{\Pi}(\vec{\boldsymbol{x}}_s, \vec{\boldsymbol{x}}_r, \omega)\, s_m(x_s)\, s_n(x_r)\, dx_s\, dx_r, \;\; m, n = 1, \ldots, M. \tag{6.17}$$

It is easy to check that

$$\int_{\mathcal{A}} s_k(x) X_m(x)\, dx = \nu_k\, w_m^k, \quad k, m = 1, \ldots, M. \tag{6.18}$$

Finally, we define $\widehat{\mathbb{Q}}$ as

$$\widehat{\mathbb{Q}} = W\, \widehat{\mathbb{S}}\, W^T. \tag{6.19}$$

As in the infinite waveguide case, for a full aperture array, we recover the definition of $\widehat{\mathbb{Q}}$ given in (6.11). Let us also note that the results and proof shown in Section 4.3 carry over in an analogous fashion; for a single point scatterer, the projected array response matrix $\widehat{\mathbb{Q}}$ defined by (6.17) and (6.19) for a partial aperture array is equal to the projected matrix $\widehat{\mathbb{Q}}$ for the full aperture case.

In the case of passive imaging with a partial-aperture array our methodology is modified as follows: We first construct the vector $\widehat{\mathbb{S}}$ with entries

$$\widehat{\mathbb{S}}_n = \frac{1}{\nu_n} \int_{\mathcal{A}} \widehat{\Pi}(\vec{\boldsymbol{x}}_r)\, s_n(x_r)\, dx_r, \quad n = 1, \ldots, M, \tag{6.20}$$

and then we define the vector

$$\widehat{\mathbb{Q}} = W \widehat{\mathbb{S}}, \tag{6.21}$$

where the matrix $W$ is as before. It is straightforward to show that the projected array response vector $\widehat{\mathbb{Q}}$ for a continuous array that spans the whole vertical cross-section $[0, D]$ is equal to the vector defined by (6.20) and (6.21) in the case of a partial-aperture array.

We conclude this section by proposing the following imaging algorithms for imaging one or more extended sources or scatterers located in $\Omega_{L^+}$.

**Algorithm 2 (Passive imaging)** *(a) Given the $N \times 1$ array response vector $\widehat{\Pi}$ we compute the $M \times 1$ projected vector $\widehat{\mathbb{Q}}$ by means of (6.20) and (6.21) .*

*(b) Next, we compute the imaging functional $\mathcal{I}^{\mathrm{p}}$ given in (6.8) for each point of a predefined search domain $S$ and we display graphically the modulus of these values.*

**Algorithm 3 (Active imaging)** *(a) Given the $N \times N$ array response matrix $\widehat{\Pi}$ we compute the $M \times M$ projected matrix $\widehat{\mathbb{Q}}$ by means of (6.17) and (6.19).*

*(b) Next, we compute the imaging functional $\mathcal{I}^{\mathrm{a}}$ given in (6.12) for each point of a predefined search domain $S$ and we display graphically the modulus of these values.*

In practice, we follow the same steps as Algorithm 1, where we now create the matrix $\widehat{\mathbb{Q}}$ instead of $\widehat{\mathbb{P}}$.

We close this section with a remark

**Remark 12** *The intuitive definition of the imaging functionals $\mathcal{I}^{\mathrm{p}}$ and $\mathcal{I}^{\mathrm{a}}$, as well as their nice resolution properties may raise the question as to why the same methodology was not used in the infinite waveguide case. To clarify this, we refer to Section 1.7, where the proof for the Kirchhoff-Helmholtz identity is given. The proof relies on second Green's identity which involves a boundary integral over a closed curve. For the terminating waveguide, that curve consists of the waveguide's boundaries and a single array on the left side. For the infinite waveguide case, the curve consists of the horizontal boundaries of the waveguide and two arrays on either side of the scatterer. So in order to use the same methodology in the infinite waveguide we need to record the scattered field on two arrays. Our objective in the previous chapters however, was to examine how well we can image an extended scatterer using a single array.*

## 6.2 Resolution analysis

In this section we present a detailed resolution analysis for the imaging functionals $\mathcal{I}^{\mathrm{p}}$ and $\mathcal{I}^{\mathrm{a}}$ defined in (6.8) and (6.12), respectively. As usual, this amounts in studying the behaviour of the point spread function (PSF), which is the imaging functional for a point source (passive case) or a point scatterer (active case). In fact, we are going to examine only the case of a point source since the results of the previous section ensure that the PSF for a point scatterer is just the square of the PSF for a point source.

Specifically, we restrict ourselves in the simple case of a homogeneous waveguide ($\eta(\vec{\boldsymbol{x}}) = 1$) which forms the semi-infinite strip $(-\infty, R) \times (0, D)$. The Green's function in this waveguide, hereafter denoted by $\widehat{G}^R$, may be found analytically; the derivation is given in Section 1.4.2. We have that for each $\vec{\boldsymbol{y}}^{\mathrm{s}} = (z, x) \in \Omega$,

$$\widehat{G}^R(\vec{\boldsymbol{y}}^s, \vec{\boldsymbol{x}}_s) = \begin{cases} \displaystyle\sum_{m=1}^{\infty} \frac{1}{\beta_m} \mathrm{e}^{i\beta_m(R-z_s)} \sin\beta_m(R-z)\, X_m(x)\, X_m(x_s), & z > z_s \\ \displaystyle\sum_{m=1}^{\infty} \frac{1}{\beta_m} \mathrm{e}^{i\beta_m(R-z)} \sin\beta_m(R-z_s)\, X_m(x)\, X_m(x_s), & z < z_s \end{cases}, \tag{6.22}$$

where the point source is located at $\vec{\boldsymbol{x}}_s = (z_s, x_s)$, the vertical eigenpairs $(\mu_n, X_n)$ are equal

to

$$\mu_n = (n\pi/D)^2, \quad X_n(x) = \sqrt{2/D}\sin(\sqrt{\mu_n}x),\ n = 1, 2, \dots, \tag{6.23}$$

and the horizontal wavenumbers $\beta_n$ are defined as

$$\beta_m = \begin{cases} \sqrt{k^2 - \mu_m}, & m = 1, \dots, M \\ i\sqrt{\mu_m - k^2}, & m \geq M + 1. \end{cases} \tag{6.24}$$

Then, as (6.9) suggests, the PSF for a point source is

$$\begin{aligned} \mathcal{I}^{\mathrm{p}}(\vec{\boldsymbol{y}}^{\mathrm{s}}) = \operatorname{Im}\widehat{G}^R(\vec{\boldsymbol{y}}^{\mathrm{s}}, \vec{\boldsymbol{x}}_s) &= \sum_{n=1}^{M} \frac{1}{\beta_n} \sin\beta_n(R - z_s)\, \sin\beta_n(R - z)\, X_n(x)\, X_n(x_s) \\ &= \frac{1}{2}\sum_{n=1}^{M} \frac{1}{\beta_n}\Big(\cos\beta_n(z - z_s) - \cos\beta_n(2R - z - z_s)\Big)\, X_n(x)\, X_n(x_s). \end{aligned} \tag{6.25}$$

### 6.2.1 Single frequency

The analysis in this subsection is carried out for a monochromatic source. The following two propositions provide analytical estimates of the PSF when we fix range or cross-range to that of the point source and look at a cross-section in the other direction.

**Proposition 10 (Cross-range resolution)** *Assume that the search point is located at the correct range, i.e., $\vec{\boldsymbol{y}}^{\mathrm{s}} = (z_s, x)$. Then, for $M$ sufficiently large, it holds that*

$$\mathcal{I}^{\mathrm{p}}(z_s, x) \approx \frac{1}{4}\left[\big(J_0(\alpha_x) - J_0(\beta_x)\big) - \big(J_0(\sqrt{\alpha_x^2 + \gamma_x^2}) - J_0(\sqrt{\beta_x^2 + \gamma_x^2})\big)\right], \tag{6.26}$$

*where*

$$\alpha_x = \frac{2\pi(x - x_s)}{\lambda}, \quad \beta_x = \frac{2\pi(x + x_s)}{\lambda}, \quad \gamma_x = \frac{4\pi}{\lambda}(R - z_s). \tag{6.27}$$

*Proof.* For $\vec{\boldsymbol{y}}^{\mathrm{s}} = (z_s, x)$, and in view of (6.23), (6.25) becomes

$$\mathcal{I}^{\mathrm{p}}(z_s, x) = \frac{1}{D}\sum_{n=1}^{M} \frac{1}{\beta_n}\Big(1 - \cos(2\beta_n(R - z_s))\Big)\, \sin\frac{n\pi x}{D} \sin\frac{n\pi x_s}{D}. \tag{6.28}$$

Letting $\xi_n = n\lambda/(2D)$ we may view the right-hand side of (6.28) as a Riemann sum approximation of the integral

$$\frac{1}{\pi}\int_0^1 \frac{1}{\sqrt{1 - \xi_n^2}}\Big(1 - \cos\big(\frac{4\pi}{\lambda}(R - z_s)\sqrt{1 - \xi_n^2}\big)\Big)\, \sin\Big(\frac{2\pi x}{\lambda}\xi_n\Big)\, \sin\Big(\frac{2\pi x_s}{\lambda}\xi_n\Big) d\xi_n.$$

Hence, using the simple trigonometric identity $\sin A \sin B = \frac{1}{2}(\cos(A-B) - \cos(A+B))$ we may approximate $\mathcal{I}^{\text{P}}$ as:

$$\mathcal{I}^{\text{P}}(x) \approx \frac{1}{\pi}\int_0^1 \frac{1}{\sqrt{1-\xi_n^2}}\Big(1-\cos\big(\frac{4\pi}{\lambda}(R-z_s)\sqrt{1-\xi_n^2}\big)\Big) \times \frac{1}{2}\Big(\cos\big(\frac{2\pi(x-x_s)}{\lambda}\xi_n\big) - \cos\big(\frac{2\pi(x+x_s)}{\lambda}\xi_n\big)\Big)\, d\xi_n,$$

where we have slightly extended the notation and used here $\mathcal{I}^{\text{P}}$ as a function of a single variable (cross-range). Now, with $\alpha_x, \beta_x$ and $\gamma_x$ given by (6.27), $\mathcal{I}^{\text{P}}$ can be written as

$$\begin{aligned}
\mathcal{I}^{\text{P}}(x) &\approx \frac{1}{2\pi}\int_0^1 \frac{1}{\sqrt{1-\xi_n^2}}\Big(1-\cos\big(\gamma_x\sqrt{1-\xi_n^2}\big)\Big)\Big(\cos(\alpha_x\xi_n) - \cos(\beta_x\xi_n)\Big)\, d\xi_n \\
&= \frac{1}{2\pi}\int_0^1 \frac{1}{\sqrt{1-\xi_n^2}}\cos(\alpha_x\xi_n)\, d\xi_n - \frac{1}{2\pi}\int_0^1 \frac{1}{\sqrt{1-\xi_n^2}}\cos(\beta_x\xi_n)\, d\xi_n \\
&+ \frac{1}{2\pi}\int_0^1 \frac{1}{\sqrt{1-\xi_n^2}}\cos(\alpha_x\xi_n)\cos\big(\gamma_x\sqrt{1-\xi_n^2}\big)\, d\xi_n \\
&- \frac{1}{2\pi}\int_0^1 \frac{1}{\sqrt{1-\xi_n^2}}\cos(\beta_x\xi_n)\cos\big(\gamma_x\sqrt{1-\xi_n^2}\big)\, d\xi_n \\
&=: I_1 - I_2 + I_3 - I_4. \qquad (6.29)
\end{aligned}$$

The integrals $I_i$, $i = 1, \ldots, 4$, in (6.29) may be evaluated analytically. We look at each term separately. For example, it is known, [30, (3.753.2)], that

$$\int_0^1 \frac{1}{\sqrt{1-\xi_n^2}}\cos(\alpha_x\xi_n)\, d\xi_n = \frac{\pi}{2}J_0(\alpha_x),$$

where $J_0(\cdot)$ is the Bessel function of the first kind of order 0. Therefore,

$$I_1 = \frac{1}{4}J_0(\alpha_x) \quad \text{and} \quad I_2 = \frac{1}{4}J_0(\beta_x).$$

Next, in order to evaluate $I_3$ we change variables, letting $\theta = \arcsin\xi_n$, and use the fact that $J_{-1/2}(t) = \sqrt{\frac{2}{\pi t}}\cos(t)$ (see, e.g., [22, (10.16.1)]) to write $I_3$ as

$$I_3 = \frac{1}{4}\sqrt{\alpha_x\gamma_x}\int_0^{\pi/2} J_{-1/2}(\alpha_x\sin\theta)J_{-1/2}(\gamma_x\cos\theta)(\sin\theta)^{1/2}(\cos\theta)^{1/2}d\theta.$$

Then, according to [30, (6.683.2)], $I_3 = \frac{1}{4}J_0(\sqrt{\alpha_x^2+\gamma_x^2})$. Similarly, $I_4 = \frac{1}{4}J_0(\sqrt{\beta_x^2+\gamma_x^2})$ and the proof is complete. □

**Proposition 11 (Range resolution)** *Assume that the search point is located at the correct cross-range, i.e.,* $\vec{\boldsymbol{y}}^{\,\mathrm{s}} = (z, x_s)$. *Then, for* $M$ *sufficiently large, it holds that*

$$\mathcal{I}^{\mathrm{p}}(z, x_s) \approx \frac{1}{4}\left[\big(J_0(\alpha_z) - J_0(\beta_z)\big) - \big(J_0(\sqrt{\alpha_z^2+\gamma_z^2}) - J_0(\sqrt{\beta_z^2+\gamma_z^2})\big)\right], \tag{6.30}$$

*where now*

$$\alpha_z = \frac{2\pi(z-z_s)}{\lambda}, \quad \beta_z = \frac{2\pi(2R-z-z_s)}{\lambda}, \quad \gamma_z = \frac{4\pi x_s}{\lambda}. \tag{6.31}$$

*Proof.* Since $\vec{\boldsymbol{y}}^{s}$ is placed at the correct cross-range we now let $x = x_s$ in (6.25). Thus, by a slight abuse of notation, $\mathcal{I}^{\mathrm{p}}(z)$ as a function of the range variable equals to

$$\mathcal{I}^{\mathrm{p}}(z) = \frac{1}{D}\sum_{n=1}^{M}\frac{1}{\beta_n}\Big(\cos\beta_n(z-z_s) - \cos\beta_n(2R-z-z_s)\Big)\,\sin^2\frac{n\pi x_s}{D}. \tag{6.32}$$

As in the proof of Proposition 10, we let $\xi_n = n\lambda/(2D)$ and approximate the right-hand side of (6.28) by an integral. Specifically, if $\alpha_z, \beta_z, \gamma_z$ are as in (6.31), and if we use that $\sin^2 A = \frac{1}{2}(1-\cos 2A)$, we may deduce that $\mathcal{I}^{\mathrm{p}}(z)$ is approximated as

$$\begin{aligned}\mathcal{I}^{\mathrm{p}}(z) \approx \frac{1}{2\pi}\int_0^1 \frac{1}{\sqrt{1-\xi_n^2}}\big(\cos(\alpha_z)\sqrt{1-\xi_n^2}) - \cos(\beta_z\sqrt{1-\xi_n^2})\big)\\ \times\big(1-\cos(\gamma_z\xi_n)\big)\,d\xi_n.\end{aligned} \tag{6.33}$$

The integral of the various terms of (6.33) are of the same type as those in (6.29) and they can be evaluated analytically resulting to (6.30). □

A first remark is that the approximate formulas (6.26) and (6.30) for the PSF when range or cross-range, respectively, is fixed at the correct location of the point-source suggest that the term that mainly contributes in defining the resolution in the vicinity of the source is $J_0(\alpha_x)$ or $J_0(\alpha_z)$, respectively. To illustrate this, in Figure 6.6 we superimpose the graphs of (6.26) multiplied by 4 (typed in blue) and of $J_0(a_x)$ (red dashed line), for a source located at $(z_s, x_s) = (19, 5)\,\lambda_0$ and for a single frequency corresponding to $k = 0.973k_0$. The reference wavenumber is $k_0 = \pi/10$.

Hence, if we define the resolution to be the width of the PSF at its half maximum, it is

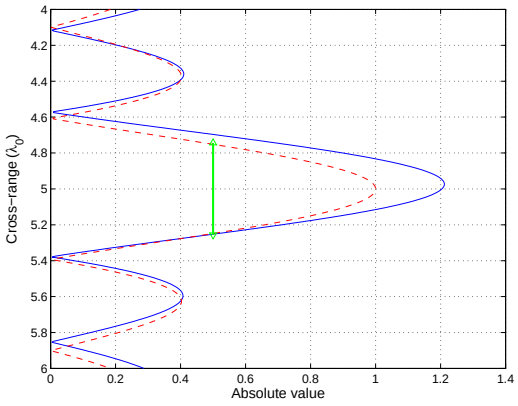


Figure 6.6: Comparison between (6.26) multiplied by 4 (blue line) and $J_0(a_x)$ (red dashed line), for a source located at $(z_s, x_s) = (19, 5)\,\lambda_0$ and for a single frequency corresponding to $k = 0.973k_0$, where the reference wavenumber is $k_0 = \pi/10$. The green arrowed segment indicates length equal to $\lambda/2$.

immediate to check that both cross-range and range resolution are approximately equal to $\lambda/2$.

Next, we plot in Figure 6.7, the absolute values of (6.26) (left subplot) and (6.30) (right subplot) for a point source located at $(z_s, x_s) = (19, 5)\,\lambda_0$. As before, the reference wavenumber is $k_0 = \pi/10$ and results are shown for a single frequency that corresponds to $k = 0.973k_0$. The analytical expressions we have derived for the cross-range and range resolution capture the behaviour of the imaging functional as we may check by comparing the plots in Figure 6.7 with the two rightmost subplots of Figure 6.3. The images shown in Figures 6.3 and 6.7, peak at the right position of $\vec{\boldsymbol{x}}_s$ and as predicted by the theoretical analysis they have a resolution of $\lambda/2$ in both range and cross-range directions. We observe however that they are quite oscillatory and their SNR is not very satisfactory.

### 6.2.2 Multiple frequencies

In this subsection we show that the SNR in our images can be significantly improved using multiple frequencies. For most practical purposes this is something feasible since in many applications sources are not monochromatic but they rather emit pulses. The multiple frequency version of the imaging functional defined in (6.8) is simply the summation over

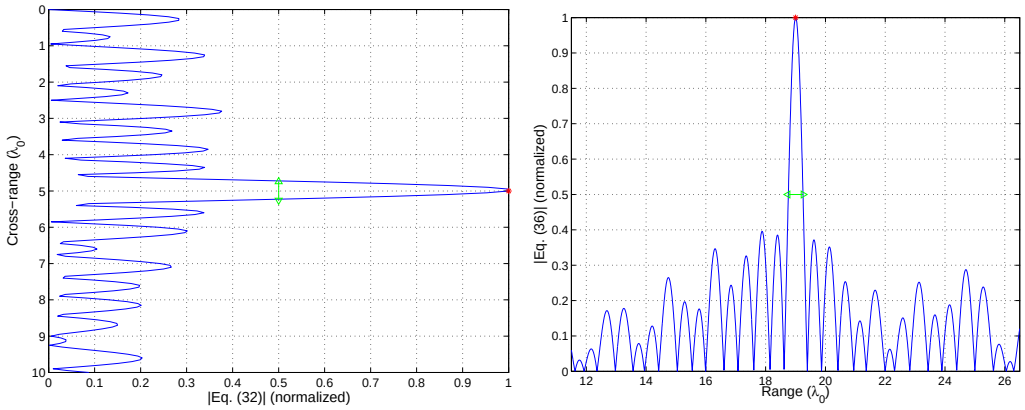


Figure 6.7: Normalized absolute value of (6.26) versus cross-range (left subplot) and normalized absolute value of (6.30) versus range (right subplot) for a point source located at $(z_s, x_s) = (19, 5)\,\lambda_0$. Here the reference wavenumber is $k_0 = \pi/10$ and results are shown for a single frequency that corresponds to $k = 0.973k_0$. The green arrowed segment indicates length equal to $\lambda/2$ and a red asterisk points to the location of the source.

frequencies of the corresponding monochromatic one

$$\mathcal{I}^{\mathrm{P}}(\vec{\boldsymbol{y}}^s) := \sum_{l=1}^{N_f} \mathcal{I}^{\mathrm{P}}(\vec{\boldsymbol{y}}^s; f_l) = \sum_{l=1}^{N_f} \sum_{n=1}^{M_l} \beta_n(f_l) \overline{\widehat{\mathbb{P}}_n}(f_l)\, \widehat{G}_n(z_a, \vec{\boldsymbol{y}}^s; f_l) \tag{6.34}$$

where $f_l$, $l = 1, \ldots, N_f$ are the discrete frequencies that span the available frequency interval $[f_{\min}, f_{\max}]$ in our data. Note that $M_l$ depends on the index $l$ since the number of propagating modes depends on the frequency $f_l$. The definition of the corresponding active imaging functional for multiple frequencies follows similarly.

Let us first look at the cross-range direction. To investigate the PSF behaviour with multiple frequencies in the ideal setting that we have examined thus far, we integrate (6.26) with respect to frequency $f$ over an interval with bandwidth $B$. Specifically, letting $\Psi(x; B)$

denote the PSF for multiple frequencies at the correct range, we have

$$\begin{aligned}\Psi(x;B) &= \int_{f_{\min}}^{f_{\max}} \mathcal{I}^{\mathrm{P}}(z_s,x;f)df \\ &\approx \frac{1}{4}\int_{f_{\min}}^{f_{\max}} \Big[\big(J_0(\alpha_x)-J_0(\beta_x)\big)-\big(J_0(\sqrt{\alpha_x^2+\gamma_x^2})-J_0(\sqrt{\beta_x^2+\gamma_x^2})\big)\Big]\,df \\ &\approx \frac{1}{4}\int_{f_{\min}}^{f_{\max}} J_0(\alpha_x)\,df, \end{aligned} \tag{6.35}$$

where now the parameters $\alpha_x, \beta_x$ and $\gamma_x$ (given in (6.27)) are written in terms of the frequency $f$ as

$$\alpha_x = \frac{2\pi}{c_0}(x-x_s)f, \quad \beta_x = \frac{2\pi}{c_0}(x+x_s)f, \quad \gamma_x = \frac{4\pi(R-z_s)}{c_0}f,$$

where $c_0$ is the constant wave speed, $f_c$ is the central frequency, and $[f_{\min}, f_{\max}] = [f_c - \frac{B}{2}, f_c + \frac{B}{2}]$. Note that we have numerically verified the validity of the last approximation in (6.35) at least in the frequency range that we have examined. Now, let $\zeta_x := \frac{2\pi}{c_0}(x-x_s)$. Then, [1, 11.1.7],

$$\Psi(x;B) \approx \frac{1}{4}\int_{f_{\min}}^{f_{\max}} J_0(\zeta_x f)\,df = \frac{1}{4\zeta_x}\Big(\Lambda_0\big(\zeta_x f_{\max}\big)-\Lambda_0\big(\zeta_x f_{\min}\big)\Big), \tag{6.36}$$

where

$$\Lambda_0(s) := sJ_0(s) + \frac{\pi s}{2}\Big(J_1(s)\mathbf{H}_0(s) - J_0(s)\mathbf{H}_1(s)\Big), \tag{6.37}$$

$J_n(\cdot)$ is the Bessel function of the first kind of order $n$, and $\mathbf{H}_n(\cdot)$, is the Struve function of order $n$, respectively. (For the definition of the Struve function see e.g. [1, Ch. 12].)

Let us consider a specific example. Assume a point source located at $(z_s, x_s) = (19, 5)\lambda_0$, a reference wavenumber equal to $k_0 = \pi/10$ and a central frequency $f_c$ corresponding to $k_c = 0.973k_0$. In Figure 6.8 we superimpose the modulus of the right-hand side of (6.36) for three different bandwidths that are equal to $B = 10\%, 50\%$ and $100\%$ of the central frequency $f_c$. All three are normalized with respect to their maximum value which, as may be immediately inferred from (6.36), is equal to $B/4$. Moreover, we observe that resolution is determined by the central frequency while SNR is improved as the bandwidth increases. Specifically, when $B = 0.10f_c$ the SNR seems to be of the same order as in the single

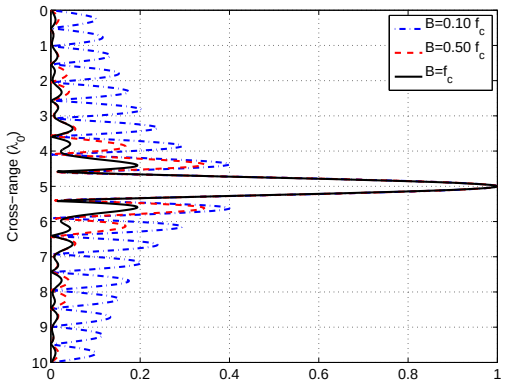


Figure 6.8: Modulus of (6.36) for bandwidth equal to $B = 0.10f_c$ (dash-dot blue line), $B = 0.50f_c$ (dashed red line) and $B = 1.00f_c$ (solid black line). The point source is placed at $(z_s, x_s) = (19, 5)\lambda_0$, the reference wavenumber is $k_0 = \pi/10$ and the central frequency $f_c$ corresponds to $k = 0.973k_0$.

frequency case (compare the blue dashed-dotted line with the one shown in the left plot in Figure 6.7), it is slightly improved when $B = 0.50f_c$ and it is considerably improved by a factor of 2 for the larger bandwidth $B = f_c$. Let us quantify these observations. Obviously the global maximum of $|\Psi(x; B)|$ is attained at $x = x_s$ and is equal to $B/4$. Then, for the bandwidths considered in the example referring to Figure 6.8, SNR is determined as the ratio of the maximum value to the second taller peak; assume that the latter is attained at $\rho(B)$. Hence (6.36) and (6.37) imply that $\zeta_\rho := \frac{2\pi}{c_0}(\rho(B) - x_s)$ satisfies the following equation

$$\begin{aligned} &f_{\max}\Big(J_1(\zeta_\rho f_{\max})\mathbf{H}_0(\zeta_\rho f_{\max}) - J_0(\zeta_\rho f_{\max})\mathbf{H}_1(\zeta_\rho f_{\max})\Big) \\ &-f_{\min}\Big(J_1(\zeta_\rho f_{\min})\mathbf{H}_0(\zeta_\rho f_{\min}) - J_0(\zeta_\rho f_{\min})\mathbf{H}_1(\zeta_\rho f_{\min})\Big) = 0. \end{aligned} \tag{6.38}$$

Moreover, it is immediate to check that since $\zeta_\rho$ is a root of (6.38) then

$$\Psi(\rho(B); B) = \frac{1}{4}\big(f_{\max}J_0(\zeta_\rho f_{\max}) - f_{\min}J_0(\zeta_\rho f_{\min})\big),$$

hence $\text{SNR} = B/|f_{\max}J_0(\zeta_\rho f_{\max}) - f_{\min}J_0(\zeta_\rho f_{\min})|$.

We compute numerically $\rho(B)$ for the various bandwidths reported above and our results are summarized in table 6.1.

Table 6.1: SNR in cross-range for various bandwidths.

| $B$ | $\rho(B)$ | SNR |
|---|---|---|
| $0.10f_c$ | $5.62521\lambda_0$ | 2.4981 |
| $0.50f_c$ | $5.61865\lambda_0$ | 2.9097 |
| $1.00f_c$ | $5.59433\lambda_0$ | 5.1513 |

The situation in the range direction is completely similar so we do not present it here.

We observe the same behaviour when we work with the actual imaging functional $\mathcal{I}^{\mathrm{p}}$. For example, in Figure 6.9 we plot the modulus of $\mathcal{I}^{\mathrm{p}}(\vec{\boldsymbol{y}}^{\mathrm{s}})$ for a point source located (as before) at $(z_s, x_s) = (19, 5)\lambda_0$, a reference wavenumber equal to $k_0 = \pi/10$ and a central frequency $f_c$ that corresponds to $k_c = 0.973k_0$. The left image is obtained when the bandwidth $B \approx 0.15f_c$, in the middle one $B \approx 0.51f_c$, and the one on the right corresponds to $B = 0.92f_c$. The advantage of using multiple frequencies is evident when we compare these images with the one shown in the left plot of Figure 6.3. Moreover, using a bandwidth of the same order as the central frequency greatly improves the SNR in the image.

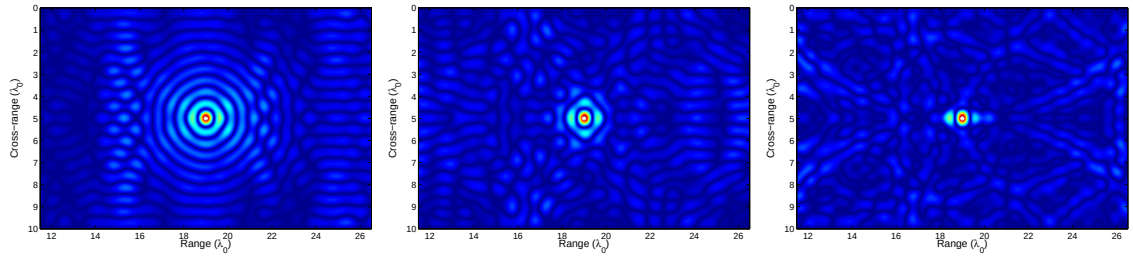


Figure 6.9: Imaging with $\mathcal{I}^{\mathrm{p}}$ for multiple frequencies for a point source placed at $(z_s, x_s) = (19, 5)\lambda_0$. The reference wavenumber equals $k_0 = \pi/10$ and the central frequency $f_c$ corresponds to $k_c = 0.973k_0$. Left image: Bandwidth $B = 0.15f_c$, Middle image: $B = 0.51f_c$, Right image: $B = 0.92f_c$.

Finally, in Figure 6.10, we plot the $(\mathrm{Im}\,\widehat{G}^R(\vec{\boldsymbol{y}}^{\mathrm{s}}; \vec{\boldsymbol{x}}_s))^2$ which, as (6.14) suggests, is equal to $\mathcal{I}^{\mathrm{a}}(\vec{\boldsymbol{y}}^{\mathrm{s}})$. We examine the same cases as in Figure 6.9 and, while the noise levels are lower even at the single frequency case (compare with the left plot in Figure 6.5), again we have a clear SNR improvement as the bandwidth increases. As we will see in the next section, this effect is of greater importance when one deals with extended scatterers.

To summarize, in this section we derived analytical formulas that approximate the PSF

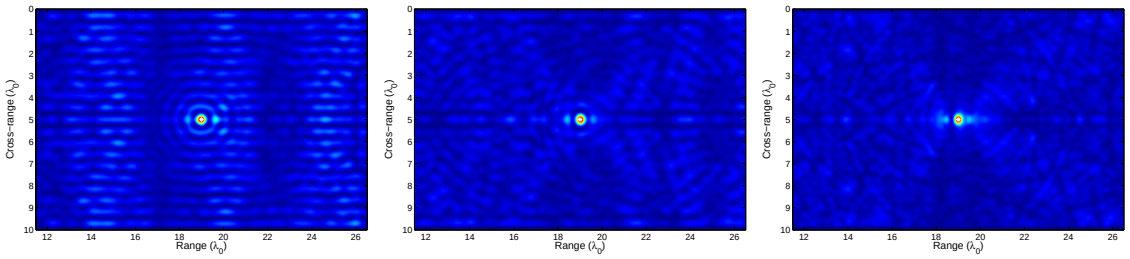


Figure 6.10: Imaging with $\mathcal{I}^{\mathrm{a}}$ for multiple frequencies for a point scatterer placed at $(z_s, x_s) = (19, 5)\lambda_0$. The central frequency $f_c$ is the same as in Figure 6.9. Left image: Bandwidth $B = 0.15 f_c$, Middle image: $B = 0.51 f_c$, Right image: $B = 0.92 f_c$.

for a point source in cross-range and range. We have concluded that both range and cross-range resolution equal to $\lambda/2$ in the monochromatic case. Moreover, we addressed the improvement in SNR that brings upon the images the use of multiple frequencies, and we have shown that the resolution in the multiple frequency case is $\lambda_c/2$, where $\lambda_c$ is the wavelength that corresponds to the central frequency of the available bandwidth. Let us note that the resolution analysis carries over to the partial aperture case at least for array apertures such that the minimum eigenvalue $\nu_{\min}$ of $A_{\mathrm{arr}}$ is larger than $\epsilon$.

## 6.3 Numerical experiments

In this section we focus on the active imaging case and assess the performance of $\mathcal{I}^{\mathrm{a}}$ for imaging extended reflectors in terminating waveguides. We start with a model problem for which the scattered data are computed using the linearized Born approximation and then consider several extended reflectors for which the scattered data are computed by solving the full wave equation. In all cases we will show imaging results obtained using $\mathcal{I}^{\mathrm{a}}$ with multiple frequencies. We first show numerical results for a full aperture array and then consider the more challenging case of a partial aperture array.

### 6.3.1 Linearized Born scattered data

We consider a one-dimensional scatterer $\mathcal{C}$, which is a semicircle placed in a homogeneous waveguide with flat horizontal boundaries and a vertical terminating boundary at $z = R$, i.e. $\Omega = (-\infty, R) \times (0, D)$. The response matrix is computed using the Born approximation

and is given by

$$\widehat{\Pi}(\vec{\boldsymbol{x}}_s, \vec{\boldsymbol{x}}_r; \omega) = \int_{\mathcal{C}} \widehat{G}^R(\vec{\boldsymbol{x}}, \vec{\boldsymbol{x}}_s; \omega) \widehat{G}^R(\vec{\boldsymbol{x}}_r, \vec{\boldsymbol{x}}; \omega) d\vec{\boldsymbol{x}}, \tag{6.39}$$

with $\widehat{G}^R(\vec{\boldsymbol{x}}, \vec{\boldsymbol{y}}; \omega)$ as in (6.22). Note that in (6.39) we have suppressed the multiplicative factor $k^2$ that usually appears in its right-hand side. As already mentioned in section 6.1.1, this can be performed in practice by rescaling the data matrix $\widehat{\Pi}(\vec{\boldsymbol{x}}_s, \vec{\boldsymbol{x}}_r; \omega)$ as $k^{-2}\widehat{\Pi}(\vec{\boldsymbol{x}}_s, \vec{\boldsymbol{x}}_r; \omega)$.

Recall also that our imaging functional $\mathcal{I}^{\mathrm{a}}$ is given by

$$\mathcal{I}^{\mathrm{a}}(\vec{\boldsymbol{y}}^{\mathrm{s}}) = \sum_{l=1}^{N_f} \sum_{n=1}^{M_l} \sum_{m=1}^{M_l} \beta_n(f_l)\beta_m(f_l) \overline{\widehat{\mathbb{Q}}_{nm}(f_l)}\, \widehat{G}_n^R(z_a, \vec{\boldsymbol{y}}^{\mathrm{s}}; f_l)\, \widehat{G}_m^R(z_a, \vec{\boldsymbol{y}}^{\mathrm{s}}; f_l), \tag{6.40}$$

where $\widehat{\mathbb{Q}}$ is the projected array response matrix (see (6.17) and (6.19)) and $\widehat{G}_n^R$, $n = 1, \ldots, M_l$ is the projection of the Green's function on the first $M_l$ vertical eigenfunctions, cf. (6.6). To demonstrate the effect of the terminating boundary of the waveguide on imaging, we compare the results obtained when the same reflector is placed in a terminating and in an open-ended (infinite-strip) waveguide. For both the open ended and the terminating waveguide the array is placed at $z_a = 0$ and spans the whole vertical cross-section of the waveguide. The semicircular scatterer $\mathcal{C}$ is centered at $(z^*, x^*) = (19, 5)\lambda_0$ with diameter $b = 2\lambda_0$ and we use frequencies $f \in [f_c - B/2, f_c + B/2]$, where the central frequency $f_c$ corresponds to the wavenumber $k_c = 0.975k_0$, the reference wavenumber, as before, equals $k_0 = \pi/10$, and the bandwidth is equal to $B = 0.92f_c$. For the terminating waveguide, the vertical boundary is placed at $R = 27.5\lambda_0$.

To compute the data and the image for the open ended waveguide, we simply replace $\widehat{G}^R(\vec{\boldsymbol{y}}, \vec{\boldsymbol{x}}_s; \omega)$ in (6.39) and (6.40) by the Green's function for the infinite waveguide, hereafter denoted by $\widehat{G}^0(\vec{\boldsymbol{y}}, \vec{\boldsymbol{x}}_s; \omega)$. Recall that $\widehat{G}^0$ is given by (see e.g. (1.15))

$$\widehat{G}^0(\vec{\boldsymbol{y}}, \vec{\boldsymbol{x}}_s; \omega) = \frac{i}{2} \sum_{m=1}^{\infty} \frac{1}{\beta_m} \mathrm{e}^{i\beta_m|z-z_s|}\, X_m(x)\, X_m(x_s), \tag{6.41}$$

where $\vec{\boldsymbol{y}} = (z, x) \in \Omega$ and $\vec{\boldsymbol{x}}_s = (z_s, x_s)$, the vertical eigenpairs $(\mu_n, X_n)$ are as in (6.23), and the horizontal wavenumbers $\beta_n$ are defined in (1.14).

In Figure 6.11 we plot the modulus of $\mathcal{I}^{\mathrm{a}}$ for the case of an open-ended waveguide (plots shown in the first and third columns), and a terminating waveguide (second and fourth columns). We have used two different bandwidths. The images shown in the first two columns were obtained with bandwidth $B = 0.51f_c$, while $B$ was taken equal to $B = 0.92f_c$

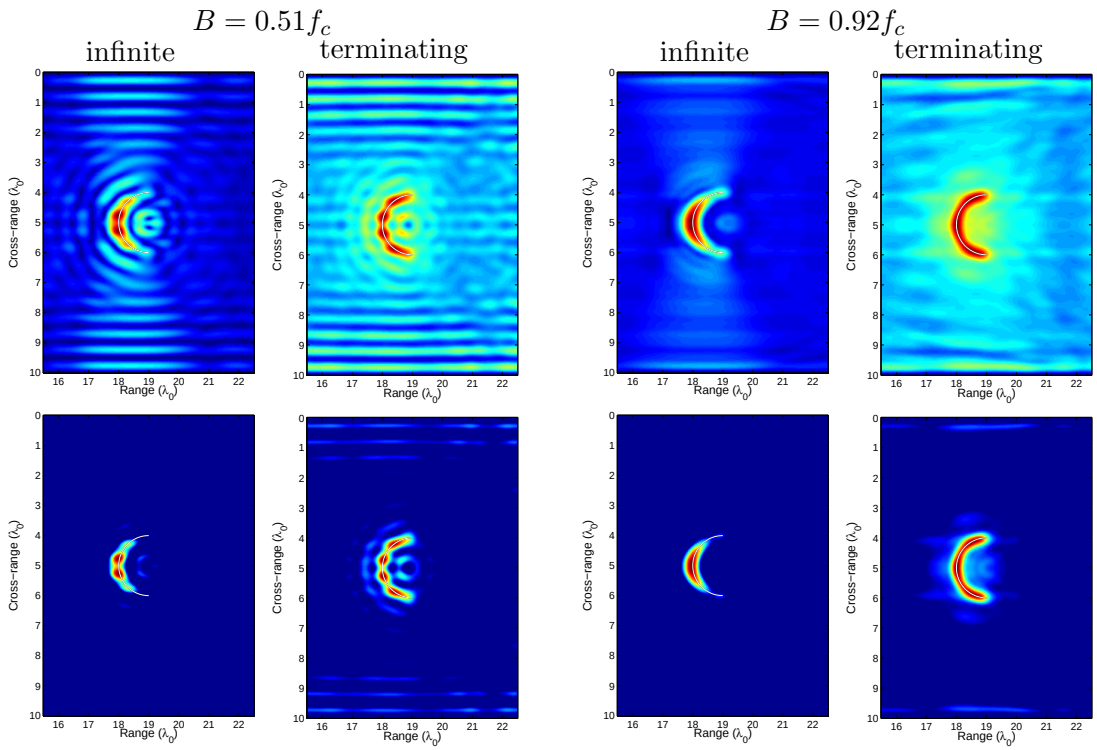


Figure 6.11: Multiple frequency imaging with $\mathcal{I}^{\mathrm{a}}$ of a semicircular reflector centered at $(z^*, x^*) = (19, 5)\lambda_0$. Specifically, $f \in [f_c - B/2, f_c + B/2]$ with $k_c = 0.975 k_0$, $k_0 = \pi/10$. For the first two columns the bandwidth is equal to $B = 0.51 f_c$, while a larger bandwidth $B = 0.92 f_c$ is used for the two columns on the right. The images shown in the first and and in the third column correspond to the open-ended waveguide while those depicted in the second and fourth to the terminating waveguide. On the top row we plot the modulus of the image normalized by its maximum value, while on the bottom row we use a threshold that sets to zero the values of the image with normalized modulus less than $\ell = 0.4$.

for the images shown in the third and fourth columns. These results are in perfect agreement with our theoretical analysis that suggests that SNR improves as we increase the bandwidth. In the remaining part of this section we fix the bandwidth to $B = 0.92 f_c$. In all plots, the image is normalized with respect to its maximum value. Looking carefully at the images shown in Figure 6.11, we observe that these in the open ended waveguide exhibit a lower noise compared to the corresponding ones in the terminating waveguide, while the latter offer a better reconstruction of the entire scatterer shape compared to those in the infinite waveguide which focus mainly around the midpoint of the semicircle. This can be seen more clearly in the images displayed on the bottom row, where we threshold the normalized

modulus of the values of the image that are less than $\ell = 0.4$. From now on we will refer to this process as thresholding with parameter $\ell$.

### 6.3.2 Full wave scattered data

Next, we want to test our approach in imaging extended scatterers without using any simplifying approximation for the forward model. To this end, we now construct the array response matrix $\widehat{\Pi}$ by solving the wave equation (1.3) numerically, with the aid of the high-order finite element C++ code Montjoie [44], which was developed at INRIA. The originally semi-infinite waveguide is truncated with a perfectly matched layer (PML), as shown in Figure 6.12, that ranges between $-5\lambda_0$ and 0, a width sufficient to absorb waves propagating to $-\infty$. We discretize the finite computational domain using quadrangles, in which we use $\mathbb{Q}_{12}$ polynomials ($\mathbb{Q}_n = \text{span}\{x^l y^m,\ 0 \le l, m \le n\}$), while we use a fourth-order leapfrog scheme for the time domain discretization.

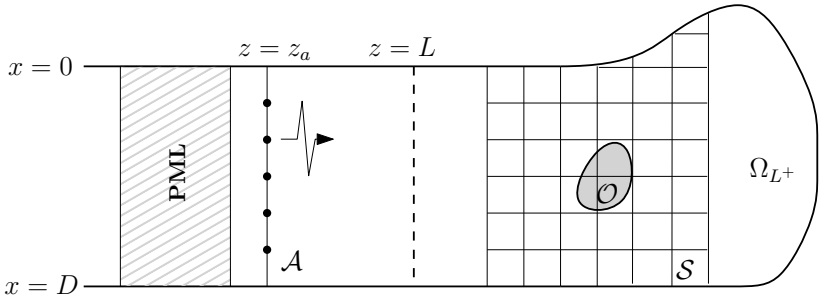


Figure 6.12: Sketch of a waveguide that is truncated near the array with a PML.

The array imaging setup is similar to the one used in the previous subsection, with the exception that now our vertical array is placed at $z_{\text{a}} = 2\lambda_0$ and has a pitch $h = \lambda_0/4$. First, we consider the case of the semi-infinite strip, i.e. $\Omega = (-\infty, R) \times (0, D)$, where now the terminating vertical boundary is located at $R = 28\lambda_0$ and a disc-shaped scatterer of diameter $b = 2\lambda_0$ is centered at $(z^*, x^*) = (20.5, 5)\lambda_0$. A Neumann condition is imposed on the circular boundary of the scatterer. In the right subplot of Figure 6.13(a) (second image in the panel) we plot the modulus of $\mathcal{I}^{\text{a}}$ normalized by its maximum value. As one may immediately verify, even though the SNR of the image is a bit low, the location, size and shape of the scatterer are fully recovered. For the image in the left subplot (first image in the panel) we pretend that we are not aware of the fact that the waveguide has a closed end, and we back propagate the same data with the "wrong" Green's function, i.e. the one

for the open-ended waveguide. We implement this by replacing in (6.40) the terms $\widehat{G}_m^R$, $\widehat{G}_n^R$ by $\widehat{G}_m^0$, $\widehat{G}_n^0$, respectively, i.e., by the Fourier coefficients of the Green's function for the infinite waveguide (see (6.41)) with respect to the orthonormal basis $\{X_n\}_{n=1}^{\infty}$ of $L^2(0, D)$. As a result, only the left part of the scatterer is recovered. In an attempt to improve the SNR of these images we plot in Figure 6.13(b) the corresponding images after thresholding with $\ell = 0.4$.

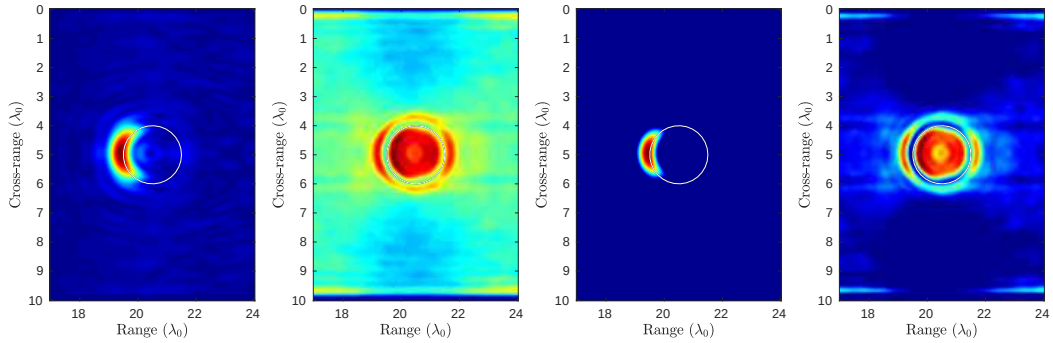


(a) No threshold used. (b) Threshold equal to 0.4.

Figure 6.13: Imaging with $\mathcal{I}^{\mathrm{a}}$ of a disc-shaped scatterer centered at $(z^*, x^*) = (20.5, 5)\lambda_0$, for $k_c = 0.9733k_0$, $k_0 = \pi/10$ and $B = 0.92f_c$. (a) Data are back propagated with the Green's function for the open ended (left subplot) and the terminating waveguide (right subplot), where we do not use thresholding. (b) Same setup as in (a) but we use thresholding with $\ell = 0.4$.

As a second example, we place in the previously described waveguide a rhombus-shaped scatterer of diameter $b = 2\lambda_0$, centered at $(z^*, x^*) = (20.5, 3)\lambda_0$. Figure 6.14 is the analogous of Figure 6.13. As before, on the left subplot of each subfigure we present the image obtained when we back propagate our data with the Green's function for the open-ended waveguide; again we observe that only the left part of the scatterer can be reconstructed. When we use the correct Green's function, the corresponding images on the right subplots of each subfigure exhibit a good reconstruction of the scatterer.

Finally, to demonstrate the robustness and the generality of our imaging approach we consider a waveguide $\Omega$ with a more complex geometry. Specifically, the waveguide has constant width in the cross-range direction equal to $10\lambda_0$ until $z = 17\lambda_0$ and, then, it expands vertically by $2\lambda_0$ on both sides and keeps a new constant width of $14\lambda_0$ until it is terminated by a vertical boundary located at $z = 28\lambda_0$. The geometry of part of the waveguide is depicted in the imaging results shown in Figure 6.15. A disc-shaped scatterer

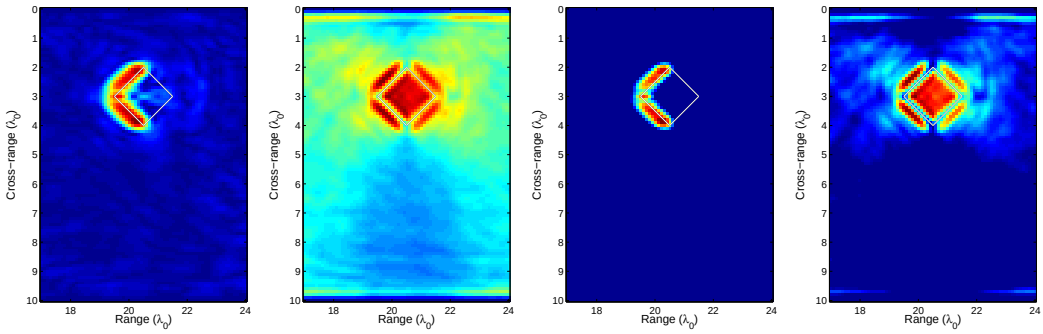


(a) No threshold used. (b) Threshold equal to 0.4.

Figure 6.14: Imaging with $\mathcal{I}^{\mathrm{a}}$ of a rhombus-shaped scatterer centered at $(z^*, x^*) = (20.5, 3)\lambda_0$, for $k_c = 0.9733k_0$, $k_0 = \pi/10$ and $B = 0.92f_c$. (a) Data are back propagated with the Green's function for the open ended (left subplot) and the terminating waveguide (right subplot), where we do not use thresholding. (b) Same setup as in (a) but we use thresholding with $\ell = 0.4$.

with diameter $b = 2\lambda_0$ is centered at $(z^*, x^*) = (22.5, 7)\lambda_0$ and is depicted in Figure 6.15 with a white continuous line.

For this waveguide geometry, we do not have an analytic expression for the Green's function $\widehat{G}(\vec{\boldsymbol{y}}^s, \vec{\boldsymbol{x}}_s)$, which is needed to form the image, hence we compute it numerically. To be more precise, $\widehat{G}(\vec{\boldsymbol{y}}^s, \vec{\boldsymbol{x}}_s)$ is obtained by solving the wave equation in $\Omega$ in the absence of the scatterer for all sources' locations $\vec{\boldsymbol{x}}_s$, $s = 1, \ldots, N$ and the solution is stored for all search points $\vec{\boldsymbol{y}}^s$ in the imaging window. The computations are performed in the time domain and we use FFT to transform the data in the frequency domain.

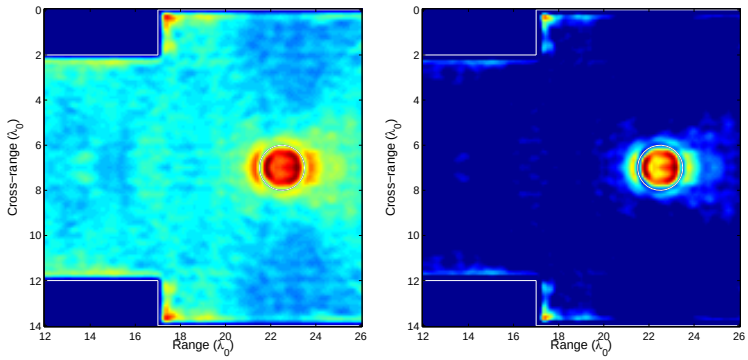


Figure 6.15: Imaging with $\mathcal{I}^{\mathrm{a}}$ for a disc scatterer centered at $(z^*, x^*) = (22.5, 7)\lambda_0$, for $k_c = 0.9733k_0$, $k_0 = \pi/10$ and $B = 0.92f_c$. On the left we use no threshold, while on the right we have a threshold $\ell = 0.4$.

The imaging results are shown in Figure 6.15 where we plot on the left the normalized modulus of $\mathcal{I}^{\mathrm{a}}$ without a threshold, and on the right using a threshold $\ell = 0.4$. The reconstruction is successful since it provides good estimates for the size and shape of the reflector.

### 6.3.3 Imaging with partial aperture

We consider now the more challenging problem of imaging a reflector with an array that does not span the entire vertical cross-section of the waveguide. As we have described in algorithm 3, our imaging method requires the evaluation of the functional $\mathcal{I}^{\mathrm{a}}$ in each point of the search domain. Recall that in the case of multiple frequencies $\mathcal{I}^{\mathrm{a}}$ is given in (6.40) and let us remark that this expression applies for any array aperture size. What alters is the way we construct the $M_l \times M_l$ modal projected matrix $\widehat{\mathbb{Q}}$, which in the case of a partial-aperture array uses the trigonometric polynomials $s_j$, $j = 1, \ldots, M_l$, as in (6.17) and (6.19) that account for the partial array aperture through the eigenvectors of the array matrix $A_{\mathrm{arr}}$.

We show in Figures 6.16 and 6.17 imaging results obtained for the same configurations as in Figures 6.13 and 6.15, respectively. The difference is that here we consider array apertures $|\mathcal{A}| = 0.75D$, $0.5D$ and $0.25D$ where $D$ is the total width of the waveguide in the cross-range direction. As illustrated in these figures the image quality deteriorates as the array aperture decreases but rather moderately. Indeed, comparing these images with the corresponding ones in Figure 6.13, one may confirm that the images for $|\mathcal{A}| = 0.75D$ are almost indistinguishable from the full aperture ones, and they are still quite good for $|\mathcal{A}| = 0.25D$!

Next, we present an example of the performance of our algorithm under the effect of measurement noise. Specifically, we consider the waveguide environment and the circular scatterer that concern the results shown in Figure 6.13. We model measurement noise as in [10], by adding to the response matrix $\widehat{\Pi}$ a noise matrix $W(\omega) \in \mathbb{C}^{N \times N}$ with entries that are normally distributed with mean zero and variance $\epsilon p_{\mathrm{avg}}$. Here $\epsilon$ is a positive constant and $p_{\mathrm{avg}}$ denotes the average power received per source, receiver, and frequency. Then it turns out that the normalized noise power in dB is equal to $-10 \log_{10} \epsilon$. For details of the implementation we refer to [61]. In Figure 6.18, we present our results for two noise levels: 10 dB, shown on the top row, and 0 dB, shown on the bottom. The length of the array decreases from full-aperture (leftmost column panel) to $|\mathcal{A}| = 0.25D$ (right column panel).

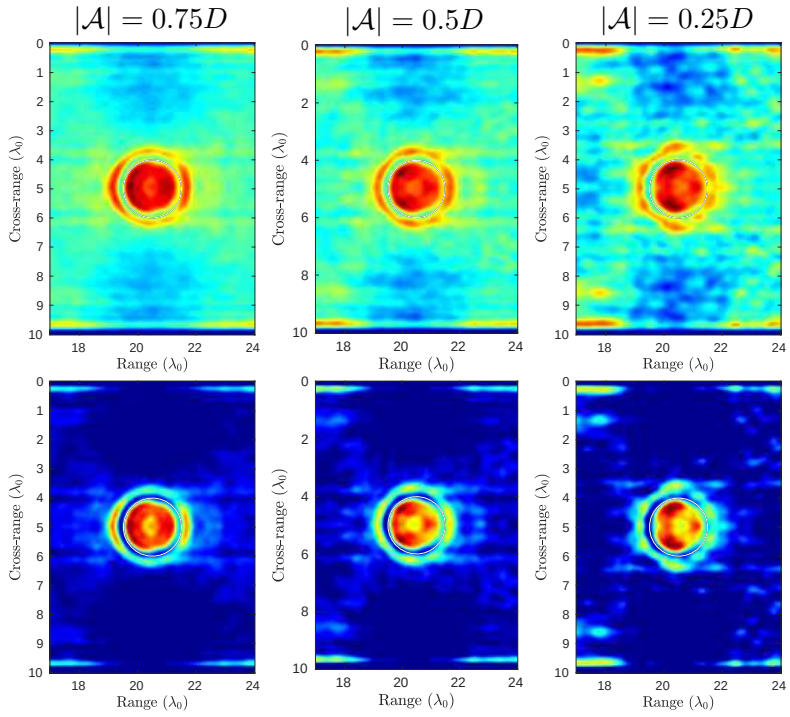


Figure 6.16: From left to right: Imaging with $\mathcal{I}^{\mathrm{a}}$ for a disc scatterer centered at $(z^*, x^*) = (21.5, 5)\lambda_0$, for different array apertures $|\mathcal{A}| = 0.75D,\ 0.5D$ and $0.25D$, for $k_c = 0.9733k_0$, $k_0 = \pi/10$ and $B = 0.92f_c$. On the top row plots we use no threshold, while for the plots in the bottom row we have a threshold $\ell = 0.4$.

On all plots we use a threshold $\ell = 0.4$. Comparing these images with the analogous in Figure 6.16, where there is no noise, we observe that noise for both levels does not seem to affect the quality of the images. Remark that the 0 dB level corresponds to very noisy data since in this case the power of the noise is equal to the power of the signal. These results illustrate the robustness of the proposed imaging methodology to uncorrelated measurement noise. For similar results concerning the case of an infinite waveguide with a full aperture array we refer to [61].

To synopsize, our numerical results indicate that the imaging method based on $\mathcal{I}^{\mathrm{a}}$ can be used for reconstructing extended scatterers that are located in terminating waveguides of complex geometry. The data used is the usual array response matrix which may cover only part of the vertical cross-section of the waveguide. The array response matrix is then projected on the propagating modes in an adequate way using the trigonometric polynomials on the array aperture as in (6.17) and (6.19). We note that the same procedure can be

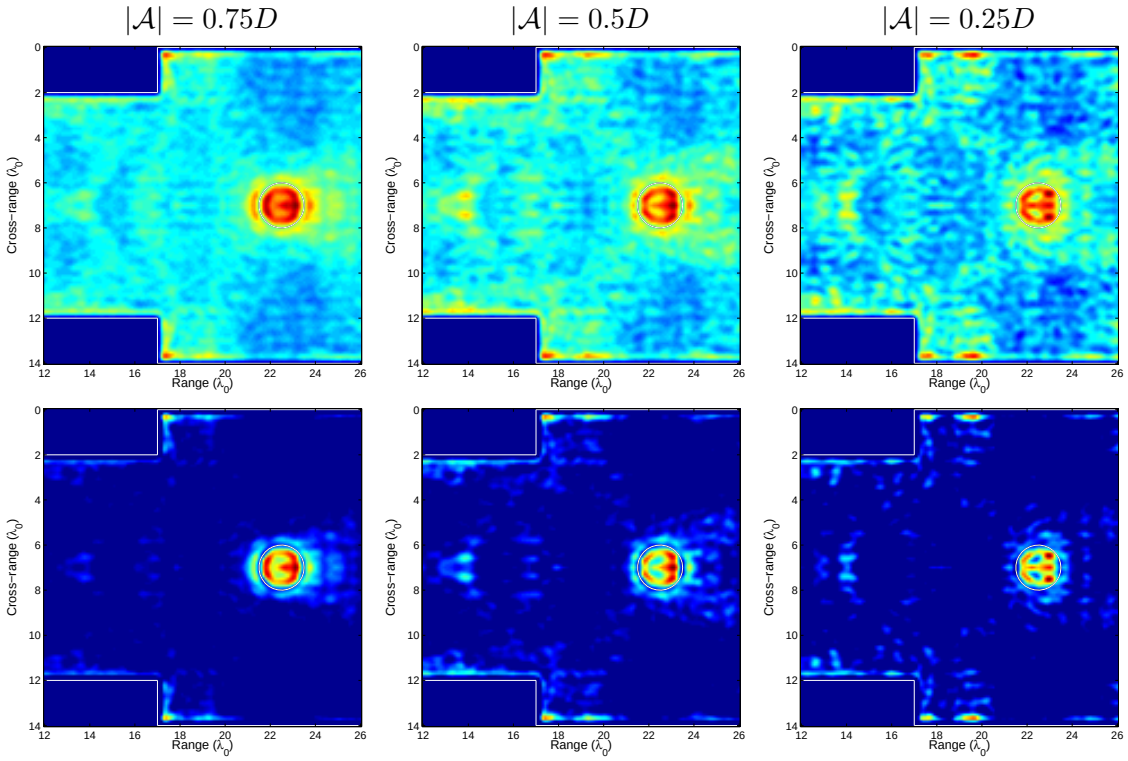


Figure 6.17: From left to right: Imaging with $\mathcal{I}^{\mathrm{a}}$ for a disc scatterer centered at $(z^*, x^*) = (22.5, 7)\lambda_0$, for different array apertures $|\mathcal{A}| = 0.75D,\ 0.5D$ and $0.25D$, for $k_c = 0.9733k_0$, $k_0 = \pi/10$ and $B = 0.92f_c$. On the top row plots we use no threshold, while for the plots in the bottom row we have a threshold $\ell = 0.4$.

followed for synthetic aperture data collected by a single transmit/receive element. In the latter case the data consist only of the diagonal entries of the array response matrix. We have numerically observed that the image resolution remains the same in this case while the SNR is worse; this is expected since the number of measurements is reduced to $N$ for the synthetic aperture instead of $N^2$ that are tabulated in the array response matrix. As an example, we show in Figure 6.19 full and partial aperture imaging results for the same imaging configuration as in Figure 6.16 but with a synthetic aperture that is formed with a single transmit/receive element.

Note that to form the image with $\mathcal{I}^{\mathrm{a}}$ we need the Green's function in the semi-infinite waveguide, which can be computed numerically assuming that the geometry and background velocity in the waveguide are known. This is necessary for complex geometries and/or propagation media in which case it is not possible to derive an analytical expression for the

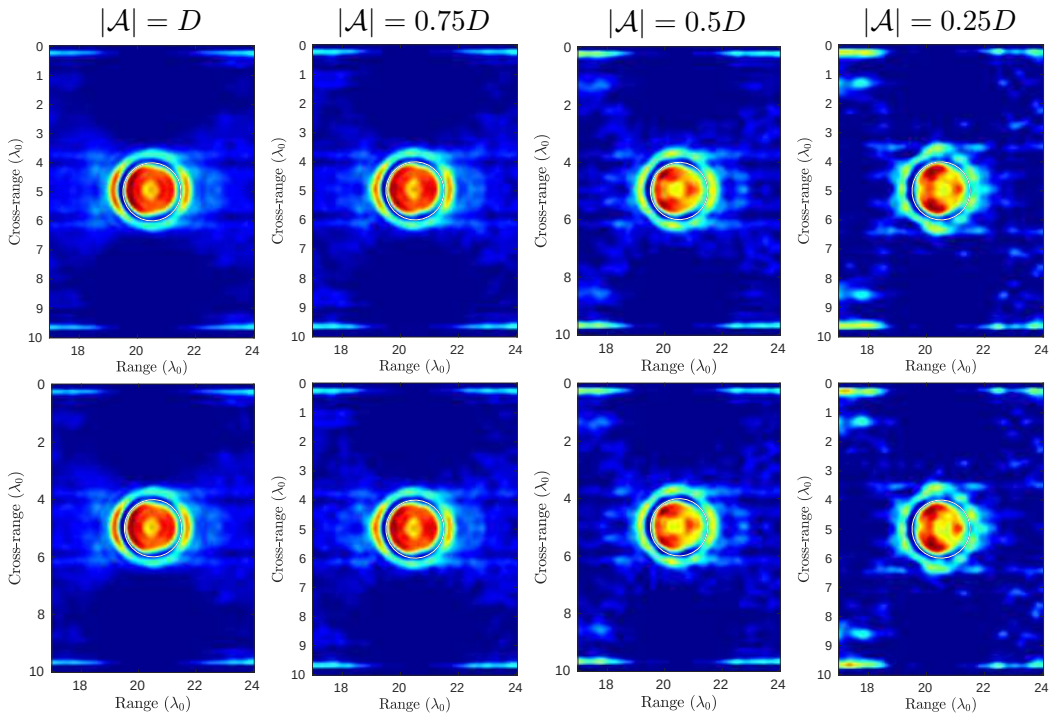


Figure 6.18: From left to right: Imaging with $\mathcal{I}^{\mathrm{a}}$ for noisy measurements for a disc scatterer centered at $(z^*, x^*) = (21.5, 5)\lambda_0$, for different array apertures $|\mathcal{A}| = D$, $0.75D$, $0.5D$ and $0.25D$, for $k_c = 0.9733k_0$, $k_0 = \pi/10$ and $B = 0.92f_c$. The normalized noise power $-10\log_{10}\epsilon$ is equal to 10 dB on the top row, and 0 dB on the bottom row. On all plots, we have a threshold $\ell = 0.4$.

Green's function. We have also assessed the performance of the imaging method with fully non-linear scattering data and in the presence of additive uncorrelated measurement noise.

### 6.3.4 Imaging in a three-dimensional terminating waveguide

We finally consider the problem of imaging an extended reflector in a three-dimensional terminating waveguide with a bounded rectangular cross-section. The imaging setup is illustrated in Figure 6.20. We denote as before, with $z$ the range variable and with $x$, $y$ the two cross-range variables. The vertical cross-section of the waveguide (xy-plane) is the rectangle $(0, D) \times (0, Y)$ and the terminating boundary is at $z = R$. Homogeneous Dirichlet boundary conditions are imposed on all of the waveguide's boundaries.

For a homogeneous waveguide with a simple geometry as the one depicted in Figure 6.20, the analytic expression for the Green's function in the waveguide may be retrieved in

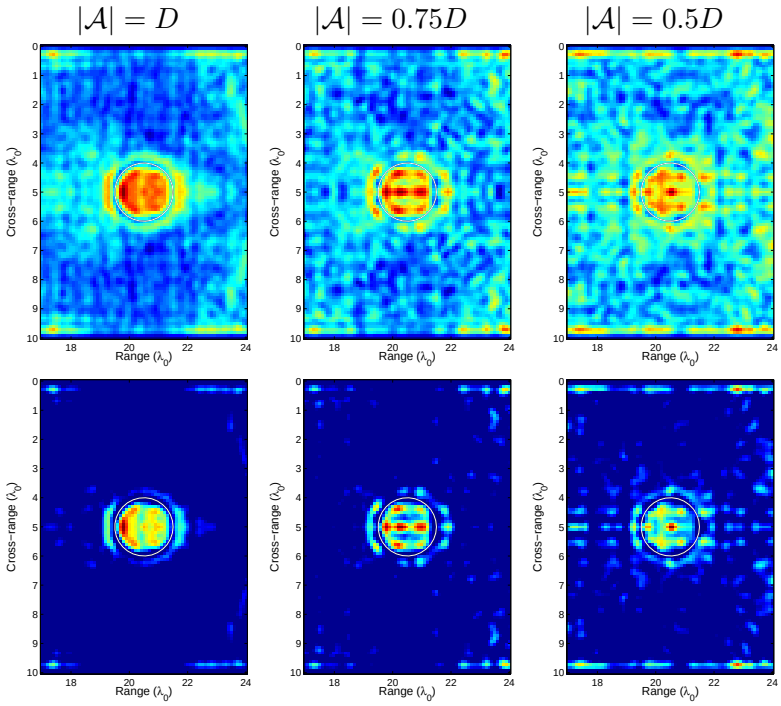


Figure 6.19: From left to right: Imaging with $\mathcal{I}^{\mathrm{a}}$ for a disc scatterer centered at $(z^*, x^*) = (20.5, 5)\lambda_0$, using a synthetic aperture array with length $|\mathcal{A}| = D$, $0.75D$ and $0.5D$, for $k_c = 0.9733k_0$, $k_0 = \pi/10$ and $B = 0.92f_c$. On the top row plots we use no threshold, while for the plots in the bottom row we have a threshold $\ell = 0.4$.

straightforward way from the analogous two-dimensional expressions. Consequently, the linearized scattered acoustic field may be computed on the array of receivers $\mathcal{A}$ that span the bounded cross-section of the waveguide. Imaging is performed by the functional $\mathcal{I}^{\mathrm{a}}$ as in (6.12) with the projected response matrix $\widehat{\mathbb{Q}}$ defined by adequately modifying (6.11) so that the integrals are taken over the two-dimensional array aperture.

Without giving the details of the computations we present as a proof of concept in the following figures some preliminary results that illustrate how this imaging methodology performs in the three-dimensional case. In Figure 6.21 we show the reconstruction for a point reflector located at $\vec{\boldsymbol{x}}^* = (19, 5, 10)\,\lambda_0$. The vertical cross-section has size $[0, 10\lambda_0] \times [0, 20\lambda_0]$ and the terminating boundary is placed at $z = 28\lambda_0$. This is a single frequency result for $k = 0.973k_0$ ($k_0 = \pi/10$), and essentially depicts the point spread function of $\mathcal{I}^{\mathrm{a}}$ in three dimensions. We observe that the resolution is $\lambda/2$ in all directions as expected from our resolution analysis.

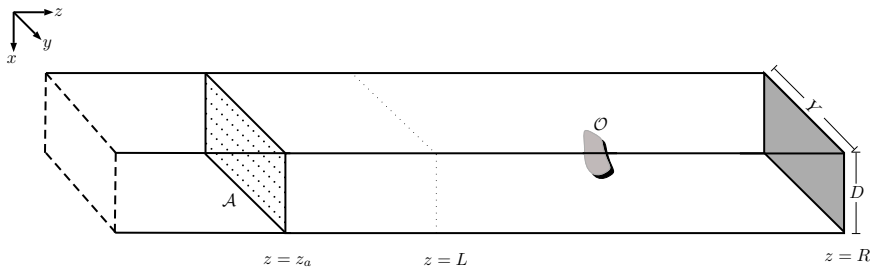


Figure 6.20: Schematic representation of the imaging setup in a three-dimensional waveguide.

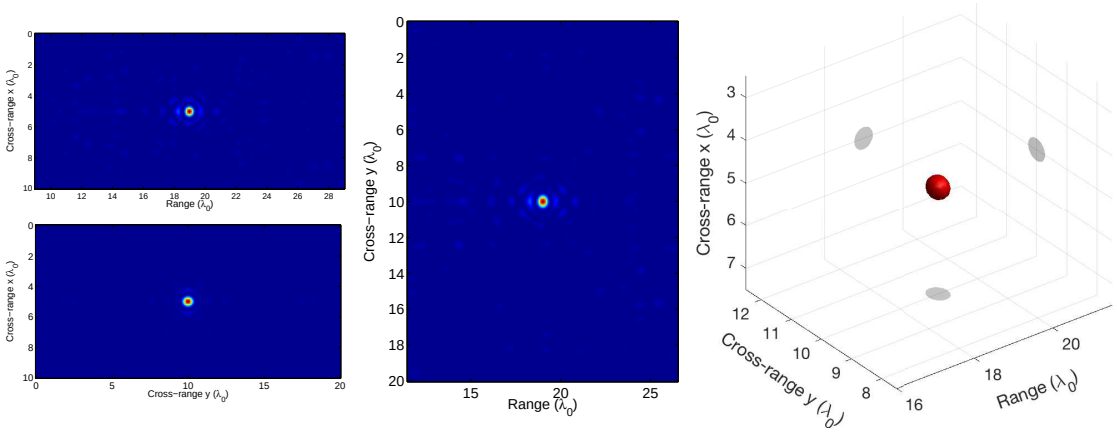


Figure 6.21: Modulus of $\mathcal{I}^{\mathrm{a}}$ for the $zx$-plane (top left), $yx$-plane (bottom left) and $zy$-plane (middle), for a single frequency $k = 0.973k_0$, $k_0 = \pi/10$, for a point reflector placed at $\vec{\boldsymbol{x}}^* = (19, 5, 10)\ \lambda_0$. On the right plot we show the three dimensional reconstruction of the point reflector.

In Figure 6.22 we display the modulus of $\mathcal{I}^{\mathrm{a}}$ for a square-shaped screen reflector. We observe that the reconstructions are very good and the shape of the reflector can be retrieved with accuracy.

A more challenging example is considered in Figure 6.23 where we seek to reconstruct a hemisphere with diameter $b = 2\lambda_0$, centered at $\vec{\boldsymbol{x}}^* = (19, 5, 10)\lambda_0$. The reconstruction shown on the right plot is very close to the true reflector's geometry shown on the left plot. These preliminary three-dimensional results are very promising. Of course, more experiments with full wave scattered data and noise should be carried out to fully assess the performance of the method in three-dimensions. Also, we leave for future work the adequate modification of the imaging functional for the partial-aperture case in three dimensions.

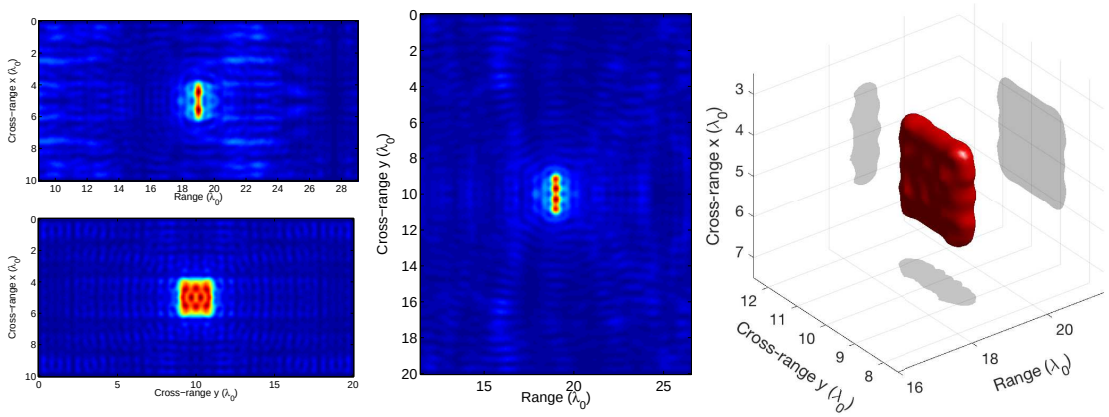


Figure 6.22: Modulus of $\mathcal{I}^{\mathrm{a}}$ for the $zx$-plane (top left), $yx$-plane (bottom left) and $zy$-plane (middle), for a single frequency $k = 0.973k_0$ for a square reflector $[9, 11]\lambda_0 \times [4, 6]\lambda_0$ placed at $z = 19\lambda_0$. On the right plot we show the three dimensional reconstruction of the square reflector.

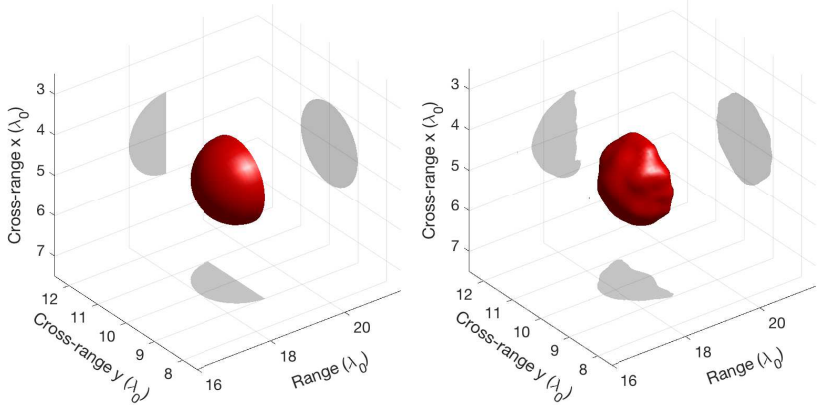


Figure 6.23: Imaging a hemisphere with diameter $b = 2\lambda_0$, centered at $\vec{\boldsymbol{x}}^* = (19, 5, 10)\lambda_0$. The true reflector is shown on the left. The modulus of $\mathcal{I}^{\mathrm{a}}$ for a single frequency $k_c = 0.9733k_0$ is on the right plot.

# Appendix A

# The response matrix for model problems

## A.1 Point scatterer

Consider a homogeneous infinite waveguide that forms an infinite strip, i.e. $\Omega = (-\infty, \infty) \times (0, D)$ and a point scatterer placed at $\vec{\boldsymbol{x}}^\star = (z^\star, x^\star)$, as shown in Figure A.1. Then, as mentioned previously, the response matrix in this case is given by

$$\widehat{\Pi}(\vec{\boldsymbol{x}}_s, \vec{\boldsymbol{x}}_r; \omega) = \widehat{G}(\vec{\boldsymbol{x}}^\star, \vec{\boldsymbol{x}}_s)\widehat{G}(\vec{\boldsymbol{x}}_r, \vec{\boldsymbol{x}}^\star), \tag{A.1}$$

where $\widehat{G}$ is given by the formula

$$\widehat{G}(\vec{\boldsymbol{x}}, \vec{\boldsymbol{x}}_s) = \frac{i}{2} \sum_{m=1}^{\infty} \frac{\mathrm{e}^{\mathrm{i}\beta_m |z - z_s|}}{\beta_m} X_m(x) X_m(x_s). \tag{A.2}$$

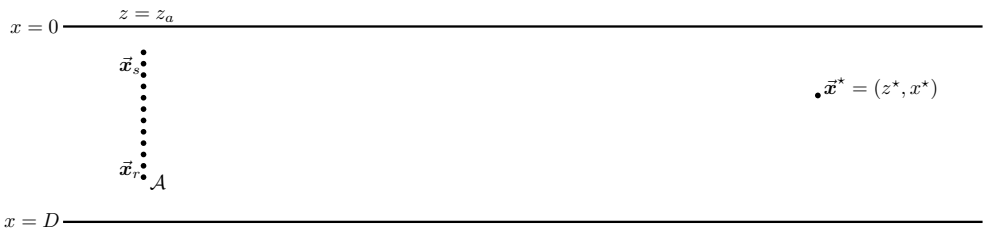


Figure A.1: Active imaging setup for a point scatterer, in an infinite strip.

If we replace the expression (A.2) into (A.1), we get that the analytic expression for the

response matrix $\widehat{\Pi}$ for a point scatterer in the homogeneous strip is given by

$$\widehat{\Pi}(\vec{\boldsymbol{x}}_r, \vec{\boldsymbol{x}}_s, \omega) = -\frac{1}{4} \sum_{m,n=1}^{M} \frac{\mathrm{e}^{\mathrm{i}\beta_m L}}{\beta_m} X_m(x_s) \frac{\mathrm{e}^{\mathrm{i}\beta_n L}}{\beta_n} X_n(x_r) X_m(x^\star) X_n(x^\star), \tag{A.3}$$

where $L = z^\star - z_a$ is the distance between the scatterer and the array and is considered large enough, so that we only consider the propagating modes in the computation of the Green's function.

## A.2 Vertical screen

Next, we consider a vertical screen $\mathcal{T}$, located at range $z = z^\star$, see Figure A.2. Let the coordinates of its endpoints be $(z^\star, \alpha)$ and $(z^\star, \beta)$, hence its width equals $b = \beta - \alpha$.

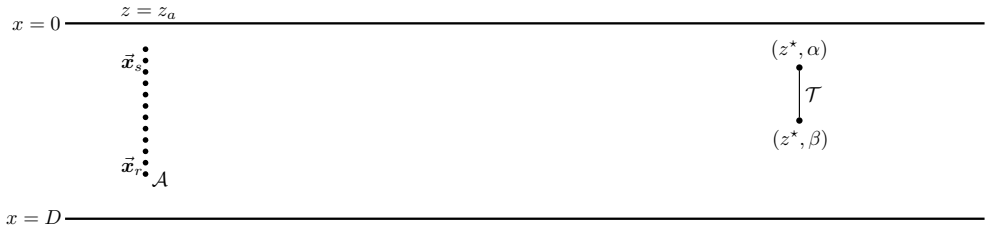


Figure A.2: Active imaging setup for a vertical screen, in an infinite strip.

Then, the response matrix is given by

$$\widehat{\Pi}(\vec{\boldsymbol{x}}_s, \vec{\boldsymbol{x}}_r; \omega) = \int_{\mathcal{T}} \widehat{G}(\vec{\boldsymbol{y}}, \vec{\boldsymbol{x}}_s) \widehat{G}(\vec{\boldsymbol{x}}_r, \vec{\boldsymbol{y}})\, d\vec{\boldsymbol{y}}. \tag{A.4}$$

Again, by replacing the expression for the Green's function given by (A.2) into (A.4) and considering $L$ large enough, we get

$$\widehat{\Pi}(\vec{\boldsymbol{x}}_r; \vec{\boldsymbol{x}}_s, \omega) = -\frac{1}{4} \sum_{m,n=1}^{M} \frac{\mathrm{e}^{\mathrm{i}\beta_m L}}{\beta_m} X_m(x_s) X_n(x_r) \frac{\mathrm{e}^{\mathrm{i}\beta_n L}}{\beta_n} \int_{\beta}^{\alpha} X_m(x) X_n(x) dx, \tag{A.5}$$

or, equivalently, as a matrix product of the form

$$\widehat{\Pi} = -\frac{1}{4}\, V\, D_\beta\, Q\, A\, Q\, D_\beta\, V^T, \tag{A.6}$$

where

$$D_\beta = \mathrm{diag}(1/\beta_1, \ldots, 1/\beta_M), \quad Q = \mathrm{diag}(\mathrm{e}^{\mathrm{i}\beta_1 L}, \ldots, \mathrm{e}^{\mathrm{i}\beta_M L}), \tag{A.7}$$

$V$ is the $N \times M$ matrix with

$$V_{k\ell} = X_\ell(x_k), \quad k = 1, \ldots, N, \ell = 1, \ldots, M, \tag{A.8}$$

and $A$ is the matrix with entries

$$a_{mn} = \int_\alpha^\beta X_m(x) X_n(x) dx, \quad m, n = 1, 2, \ldots, M. \tag{A.9}$$

## A.3 Semicircle

Lastly, we assume that the target $\mathcal{T}$ is a semicircular arc (with diameter parallel to the $x$ axis) of radius $\rho$, centered at $\vec{\boldsymbol{y}}^\star = (z^\star, x^\star)$. Let us also denote $\vec{\boldsymbol{y}}_1^\star = (z^\star, x^\star - \rho)$ and $\vec{\boldsymbol{y}}_2^\star = (z^\star, x^\star + \rho)$ the endpoints of the arc.

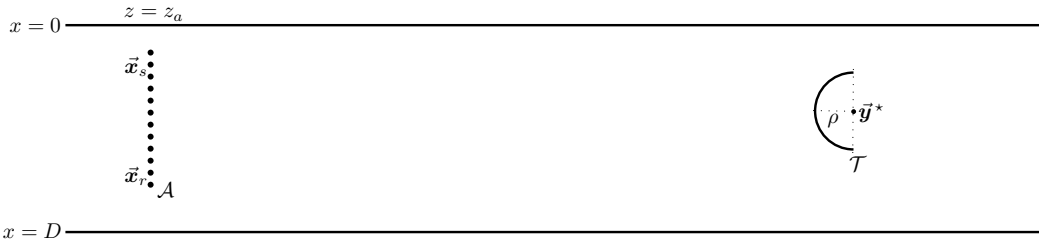


Figure A.3: Active imaging setup for a semicircle, in an infinite strip.

We parametrize $\mathcal{T}$ as follows. Let

$$z = z^\star - \rho \sin t, \quad x = x^\star - \rho \cos t.$$

Then the line integral (A.4) with respect to arc length equals

$$\begin{aligned}
\widehat{\Pi}(\vec{\boldsymbol{x}}_r, \vec{\boldsymbol{x}}_s, \omega) &= \int_0^\pi \widehat{G}\Big((z^\star - \rho\sin t, x^\star - \rho\cos t), (z_a, x_r)\Big) \\
&\times \quad \widehat{G}\Big(z^\star - \rho\sin t, x^\star - \rho\cos t), (z_a, x_s)\Big)\sqrt{\left(\frac{dz}{dt}\right)^2 + \left(\frac{dx}{dt}\right)^2}\, dt \\
&= -\frac{1}{4}\int_0^\pi \sum_{m=1}^{\infty}\sum_{n=1}^{\infty} \frac{1}{\beta_m} \mathrm{e}^{i\beta_m(L+\rho(1-\sin t))} X_m(x^\star - \rho\cos t) X_m(x_r) \\
&\times \quad \frac{1}{\beta_n} \mathrm{e}^{i\beta_n(L+\rho(1-\sin t))} X_n(x^\star - \rho\cos t) X_n(x_s)\, \rho\, dt \\
&= -\frac{1}{4}\sum_{m=1}^{\infty}\sum_{n=1}^{\infty} \frac{1}{\beta_m}\frac{1}{\beta_n} X_m(x_r) X_n(x_s) \\
&\times \quad \int_0^\pi \mathrm{e}^{i(\beta_m+\beta_n)(L+\rho(1-\sin t))} X_m(x^\star - \rho\cos t) X_n(x^\star - \rho\cos t)\, \rho\, dt \\
&= -\frac{1}{4}\sum_{m=1}^{\infty}\sum_{n=1}^{\infty} \frac{1}{\beta_m}\frac{1}{\beta_n} X_m(x_r) X_n(x_s) \\
&\times \quad \int_0^\pi \mathrm{e}^{i\beta_m(L+\rho(1-\sin t))} X_m(x^\star - \rho\cos t)\, \mathrm{e}^{i\beta_n(L+\rho(1-\sin t))} X_n(x^\star - \rho\cos t)\, \rho\, dt
\end{aligned}$$

where $L = z^\star - z_a - \rho$ is the distance between the array and the leftmost part of the semicircle. Passing the terms $\mathrm{e}^{i\beta_m L}$ and $\mathrm{e}^{i\beta_n L}$ outside the integral we get

$$\begin{aligned}
\widehat{\Pi}(\vec{\boldsymbol{x}}_r, \vec{\boldsymbol{x}}_s, \omega) = -\frac{1}{4}\sum_{m=1}^{\infty}\sum_{n=1}^{\infty} \frac{\mathrm{e}^{i\beta_m L}}{\beta_m}\frac{\mathrm{e}^{i\beta_n L}}{\beta_n} X_m(x_r) X_n(x_s) \\
\times \quad \int_0^\pi \mathrm{e}^{i(\beta_m+\beta_n)\rho(1-\sin t)} X_m(x^\star - \rho\cos t) X_n(x^\star - \rho\cos t)\, \rho\, dt.
\end{aligned}$$

Now, let $B$ be the matrix with entries

$$B_{mn} = \int_0^\pi \mathrm{e}^{i(\beta_m+\beta_n)\rho(1-\sin t)} X_m(x^\star - \rho\cos t) X_n(x^\star - \rho\cos t)\, \rho\, dt, \quad m, n = 1, 2, \ldots.$$

Then $\widehat{\Pi}$ may be written as

$$\widehat{\Pi} = -\frac{1}{4}\, V\, D_\beta\, Q\, B\, Q\, D_\beta\, V^T, \tag{A.10}$$

where the matrices $V, D_\beta, Q$ are the same matrices as in (A.6), which describes the scattered field for the screen.

# Bibliography


[1] M. Abramowitz and I. A. Stegun. *Handbook of Mathematical Functions with Formulas, Graphs, and Mathematical Tables*. Dover, 1964.

[2] A. L. Andrew. Eigenvectors of certain matrices. *Linear Algebra and Appl.*, 7:151–162, 1973.

[3] T. Arens, D. Gintides, and A. Lechleiter. Direct and inverse medium scattering in a three-dimensional homogeneous planar waveguide. *SIAM Journal on Applied Mathematics*, 71(3):753–772, 2011.

[4] W. N. Bailey. Generalized hypergeometric series. 1935.

[5] A. Bendali and Ph. Guillaume. Non-reflecting boundary conditions for waveguides. *Math. Comput.*, 68(225):123–144, 1999.

[6] J.-P. Berenger. A perfectly matched layer for the absorption of electromagnetic waves. *Journal of Computational Physics*, 114:185 – 200, 1994.

[7] N. Bleistein. *Mathematical methods for wave phenomena*. Computer Science and Applied Mathematics. Academic Press Inc., Orlando, FL, 1984.

[8] N. Bleistein, J. K. Cohen, and J. W. Stockwell, Jr. *Mathematics of multidimensional seismic imaging, migration, and inversion*, volume 13 of *Interdisciplinary Applied Mathematics*. Springer-Verlag, New York, 2001. Geophysics and Planetary Sciences.

[9] L. Borcea and D.-L. Nguyen. Imaging with electromagnetic waves in terminating waveguides. *Inverse Problems and Imaging*, 10:915–941, 2016.

[10] L. Borcea, G. Papanicolaou, and F. Guevara Vasquez. Edge illumination and imaging of extended reflectors. *SIAM J. Imaging Sci.*, 1:75–114, 2008.

[11] L. Borcea, G. Papanicolaou, and C. Tsogka. Optimal waveform design for array imaging. *Inverse Problems*, 23(5):1973–2020, 2007.

[12] L. Borcea, G. Papanicolaou, and C. Tsogka. Subspace projection filters for imaging in random media. *Comptes Rendus Mecanique*, 338:390–401, 2010.

[13] L. Bourgeois, F. Le Louer, and E. Lunéville. On the use of lamb modes in the linear sampling method for elastic waveguides. *Inverse Problems*, 27:055001, 2011.

[14] L. Bourgeois and E. Lunéville. The linear sampling method in a waveguide: a modal formulation. *Inverse problems*, 24(1):015018, 2008.

[15] L. Bourgeois and E. Lunéville. On the use of sampling methods to identify cracks in acoustic waveguides. *Inverse Problems*, 28(10):105011, 2012.

[16] Yu A. Brychkov, O. I. Marichev, and A. P. Prudnikov. Integrals and series, vol 3: more special functions. *Gordon and Breach science publishers*, 1986.

[17] J. L Buchanan, R. P Gilbert, A. Wirgin, and Y. Xu. *Marine acoustics: direct and inverse problems*. Siam, 2004.

[18] D.K. Cheng. *Field and wave electromagnetics*. The Addison-Wesley series in electrical engineering. Addison-Wesley Publishing Company, 1989.

[19] D. Colton and H. Haddar. An application of the reciprocity gap functional to inverse scattering theory. *Inverse Problems*, 21:383–398, 2005.

[20] D. Colton and A. Kirsch. A simple method for solving inverse scattering problems in the resonance region. *Inverse Problems*, 12:383–393, 1996.

[21] S. Dediu and J. R. McLaughlin. Recovering inhomogeneities in a waveguide using eigensystem decomposition. *Inverse Problems*, 22(4):1227–1246, 2006.

[22] *NIST Digital Library of Mathematical Functions*. http://dlmf.nist.gov/, Release 1.0.16 of 2017-09-18. F. W. J. Olver, A. B. Olde Daalhuis, D. W. Lozier, B. I. Schneider, R. F. Boisvert, C. W. Clark, B. R. Miller and B. V. Saunders, eds.

[23] DV Evans and R Porter. Trapped modes embedded in the continuous spectrum. *The Quarterly Journal of Mechanics and Applied Mathematics*, 51(2):263–274, 1998.

[24] D. Fasino. Spectral properties of Toeplitz-plus-Hankel matrices. *Calcolo*, 33:87–98, 1996.

[25] M. Fink, C. Prada, F. Wu, and D. Cassereau. Self focusing in inhomogeneous media with time reversal acoustic mirrors. In *Proceedings., IEEE Ultrasonics Symposium,*, pages 681–686 vol.2, Oct 1989.

[26] S.D. Gedney. An anisotropic perfectly matched layer-absorbing medium for the truncation of FDTD lattices. *IEEE Transactions on Antennas and Propagation*, 44:1630 –1639, 1996.

[27] D. Givoli. *Numerical methods for problems in infinite domains*. Elsevier, 1992.

[28] C. I. Goldstein. A finite element method for solving Helmholtz type equations in waveguides and other unbounded domains. *Math. Comp.*, 39(160):309–324, 1982.

[29] G. H. Golub and C. F. Van Loan. *Matrix computations*. Johns Hopkins Studies in the Mathematical Sciences. Johns Hopkins University Press, Baltimore, MD, third edition, 1996.

[30] I. S. Gradshteyn and I. M. Ryzhik. *Table of integrals, series, and products*. Elsevier/Academic Press, Amsterdam, seventh edition, 2007.

[31] U. Grenander and G. Szegő. *Toeplitz forms and their applications*. Chelsea Publishing Co., New York, second edition, 1984.

[32] C. Hazard and K. Ramdani. Selective acoustic focusing using time-harmonic reversal mirrors. *SIAM J. Appl. Math.*, 64:1057–1076 (electronic), 2004.

[33] J.-P. Hermand and P. Gerstoft. Inversion of broad-band multitone acoustic data from the yellow shark summer experiments. *IEEE J. Ocean. Eng.*, 21:324–346, 1996.

[34] M. Ikehata, G. N. Makrakis, and G. Nakamura. Inverse boundary value problem for ocean acoustics using point sources. *Mathematical Methods in the Applied Sciences*, 27(12):1367–1384, 2004.

[35] D. R. Jackson and D. R. Dowling. Phase conjugation in underwater acoustics. *J. Acoust. Soc. Amer.*, 89(1):171–181, 1991.

[36] F.B. Jensen, W.A. Kuperman, M.B. Porter, and H. Schmidt. *Computational Ocean Acoustics*. Modern Acoustics and Signal Processing. Springer, 2011.

[37] D. S. Jones. The eigenvalues of $\nabla^2 u + \lambda u = 0$ when the boundary conditions are given on semi-infinite domains. *Mathematical Proceedings of the Cambridge Philosophical Society*, 49(4):668–684, 1953.

[38] A. Kirsch. Characterization of the shape of a scattering obstacle using the spectral data of the far field operator. *Inverse Problems*, 14:1489–1512, 1998.

[39] W.A. Kuperman and D. Jackson. Ocean acoustics, matched-field processing and phase conjugation. Topics in Applied Physics, pages 43–97. Springer Berlin / Heidelberg, 2002.

[40] H. J. Landau and H. O. Pollak. Prolate spheroidal wave functions, fourier analysis and uncertainty – II. *Bell System Technical Journal*, 40(1):65–84, 1961.

[41] H. J. Landau and H. O. Pollak. Prolate spheroidal wave functions, fourier analysis and uncertainty – III: The dimension of the space of essentially time- and band-limited signals. *Bell System Technical Journal*, 41(4):1295–1336, 1962.

[42] J.L. Lions and E. Magenes. *Non-homogeneous boundary value problems and applications*. Number v. 3 in Non-homogeneous Boundary Value Problems and Applications. Springer-Verlag, 1972.

[43] P. Monk and V. Selgas. Sampling type methods for an inverse waveguide problem. *Inverse Problems and Imaging*, 6(4):709–747, 2012.

[44] Montjoie user's guide, http://montjoie.gforge.inria.fr/.

[45] I. C. Moore and M. Cada. Prolate spheroidal wave functions, an introduction to the Slepian series and its properties. *Appl. Comput. Harmon. Anal.*, 16(3):208–230, 2004.

[46] N. Mordant, C. Prada, and M. Fink. Highly resolved detection in a waveguide using the D.O.R.T. method. *J. Acoust. Soc. Amer.*, 105:2634–2642, 1999.

[47] J. A. Morrison. On the eigenfunctions corresponding to the bandpass kernel, in the case of degeneracy. *Quart. Appl. Math.*, 21:13–19, 1963.

[48] B. Pinçon and K. Ramdani. Selective focusing on small scatterers in acoustic waveguides using time reversal mirrors. *Inverse Problems*, 23:1–25, 2007.

[49] F. Podd, M. Ali, K. Horoshenkov, A. Wood, S. Tait, J. Boot, R. Long, and A. Saul. Rapid sonic characterisation of sewer change and obstructions. *Water Science and Technology*, 56:131 – 139, 2007.

[50] C. Prada, J. de Rosny, D. Clorennec, J.-G. Minonzio, A. Aubry, M. Fink, L. Berniere, P. Billand, S. Hibral, and T. Folegot. Experimental detection and focusing in shallow water by decomposition of the time reversal operator. *J. Acoust. Soc. Amer.*, 122:761–768, 2007.

[51] C. Prada and M. Fink. Eigenmodes of the time reversal operator: a solution to selective focusing in multiple-target media. *Wave Motion*, 20:151–163, 1994.

[52] M. Rosenblatt. Some purely deterministic processes. *J. Math. Mech.*, 6:801–810, 1957.

[53] I. SenGupta, B. Sun, W. Jiang, G. Chen, and M. C. Mariani. Concentration problems for bandpass filters in communication theory over disjoint frequency intervals and numerical solutions. *J. Fourier Anal. Appl.*, 18(1):182–210, 2012.

[54] S. Serra. On the extreme eigenvalues of hermitian (block) toeplitz matrices. *Linear Algebra and its Applications*, 270(1–3):109 – 129, 1998.

[55] D. Slepian. Prolate spheroidal wave functions, fourier analysis and uncertainty – IV: Extensions to many dimensions; generalized prolate spheroidal functions. *Bell System Technical Journal*, 43(6):3009–3057, 1964.

[56] D. Slepian. Prolate spheroidal wave functions, fourier analysis, and uncertainty – V: The discrete case. *Bell System Technical Journal*, 57(5):1371–1430, 1978.

[57] D. Slepian. Some comments on Fourier analysis, uncertainty and modeling. *SIAM Rev.*, 25(3):379–393, 1983.

[58] D. Slepian and H. O. Pollak. Prolate spheroidal wave functions, Fourier analysis and uncertainty – I. *Bell System Tech. J.*, 40:43–63, 1961.

[59] W. F. Trench. Asymptotic distribution of the even and odd spectra of real symmetric Toeplitz matrices. *Linear Algebra Appl.*, 302/303:155–162, 1999. Special issue dedicated to Hans Schneider (Madison, WI, 1998).

[60] C. Tsogka, D. Mitsoudis, and S. Papadimitropoulos. Imaging extended reflectors in a terminating waveguide. *SIAM Journal on Imaging Sciences*, 11(2):1680–1716, 2018.

[61] C. Tsogka, D. A. Mitsoudis, and S. Papadimitropoulos. Selective imaging of extended reflectors in two-dimensional waveguides. *SIAM J. Imaging Sci.*, 6(4):2714–2739, 2013.

[62] Y. Xu, C. Mawata, and W. Lin. Generalized dual space indicator method for underwater imaging. *Inverse Problems*, 16:1761 – 1776, 2000.